Active vibration control in a specific zone of smart structures

Peng Wang

N° d'ordre NNT : 2019LYSEC007

THÈSE DE DOCTORAT DE L'UNIVERSITÉ DE LYON

opérée au sein de

l'Ecole Centrale de Lyon

Spécialité: **"Automatique"**

préparée dans le laboratoire **Ampère et LTDS**

dans le cadre de l'École Doctorale EEA de Lyon **(ED160)**

par : **Peng WANG**

Active vibration control in a specific zone of smart structures

---

Soutenue publiquement le 25 Mars 2019 devant le jury composé de :

Rapporteur	M. Gilles Duc	Professeur, CentraleSupélec
Rapporteur	M. Jean-François Deü	Professeur, Conservatoire National des Arts et Métiers
Présidente	Mme. Isabelle Queinnec	Directeur de Recherche, CNRS, LAAS
Examinatrice	Mme. Emeline Sadoulet	Maître de Conférences, Université de Franche Comté
Encadrant	M. Manuel Collet	Directeur de Recherche, CNRS
Encadrant	M. Xavier Bombois	Directeur de Recherche, CNRS
Encadrant	M. Anton Korniienko	Maître de Conférences, École Centrale de Lyon
Directeur de thèse	M. Gérard Scorletti	Professeur, École Centrale de Lyon

Acknowledgments

This dissertation is the conclusion of my three-year researches at the Laboratoire Ampère of École Centrale de Lyon (ECL) and the department of Laboratoire de Tribologie et Dynamique des Systèmes (LTDS). I am deeply indebted to a number of people without whose encouragement and assistance I would not have accomplished my researches. Now it is my pleasure to express my sincere gratitude to them all.

My deepest gratitude goes first and foremost to my superiors, Professor Gérard Scorletti, Director Manuel Collet, Director Xavier Bombois and Doctor Anton Korniienko for their constant guidance and invaluable supports throughout my researches in ECL. Professor Gérard Scorletti have guided me with illuminating instruction and expert advice. He always explains the knowledge and responds to my questions with great patience. His extensive knowledge, rigorous attitude of scholarship and open mind deeply influence me. Director Manuel Collet gives me great help and support on the modeling work and provides me with very useful experimental guidance. Without his help, I would not have obtained reliable models and satisfactory experimental results. Director Xavier Bombois gives me great instruction and help on the identification technique which greatly contributes to the success of my research. I also owe a special debt of gratitude to him for helping me redact and revise my article. Doctor Anton Korniienko gives me great assistance during my researches on robust control. We are like friends. I want thank him first for representing me to conduct the presentation at the conference in Brazil. And also thank him for inviting me to his home and experiencing a perfect dinner.

I would also like to thank the members of LTDS and Ampère for providing an enjoyable working environment of mutual interest in each others' researches in which many problems could be discussed and solved. Especially to Dr. Kaijun Yi, Doctor Ellen Skow, Kévin Colin, Daumas Amaury, Chuhan WANG for their sincere help to my work.

On a more personal note, I would like to thank my parents and my wife for their love, care, help and encouragements over these years. Without their supports, I would not have gone so far. Thank them for always being so supportive despite my choices in life.

At last, I gratefully acknowledge Chinese Scholarship Council (CSC) for providing the funding source and for supporting my doctor work.

Abstract

This research aims at solving a particular vibration control problem of smart structures. We aim at reducing the vibration in a specific zone of the smart structure under the disturbance that covers a wide frequency band. Moreover, at this specific zone, neither actuation nor sensing is possible.

Here we face several main challenges. First, we need to control the vibration of a specific zone of the structure while we only have access to measurements at other zones. Second, the wide bandwidth of the disturbance implies that numerous modes should be controlled at the same time which requires the use of multiple actuators and sensors. This leads to a MIMO controller which is difficult to obtain using classical controller design methods. Third, the so-called spillover problem must be avoided which is to guarantee the closed-loop stability when the model-based controller is applied on the actual setup. To tackle these challenges, we investigate two control strategies: the centralized control and the distributed control.

For centralized control, we propose a methodology that allows us to obtain a simple MIMO controller that accomplishes these challenges. First, several modeling and identification techniques are applied to obtain an accurate low-order model of the smart structure. Then, an H_∞ control based synthesis method with a particularly proposed H_∞ criterion is applied. This H_∞ criterion integrates multiple control objectives, including the main challenges. In particular, the spillover problem is transformed into a robust stability problem and will be guaranteed using this criterion. The obtained H_∞ controller is a standard solution of the H_∞ problem. The final controller is obtained by further simplifying this H_∞ controller without losing the closed-loop stability and degrading the performance. This methodology is validated on a beam structure with piezoelectric transducers and the central zone is where the vibration should be reduced. The effectiveness of the obtained controller is validated by simulations and experiments.

For distributed control, we consider the same beam structure and the same control objectives. There exist methods aiming at designing distributed controllers of spatially interconnected system. This research proposes a FEM based method, combined with several model reduction techniques, that allows to spatially discretize the beam structure and deduce the state-space models of interconnected

subsystems. The design of distributed controllers will not be tackled in this research.

Résumé

Cette recherche vise à résoudre un problème particulier de contrôle de vibration. L'objectif est de réduire les vibrations dans une zone spécifique de la structure intelligente avec une perturbation qui couvre une large gamme de fréquences. De plus, dans cette zone spécifique, ni l'actionnement, ni la mesure ne sont possibles.

Ici, nous faisons face à plusieurs défis principaux. Premièrement, nous devons contrôler les vibrations dans une zone spécifique, alors que nous n'avons accès aux mesures que dans d'autres zones. Deuxièmement, la large bande passante de la perturbation implique que nombreux modes doivent être contrôlés en même temps, ce qui nécessite l'utilisation de plusieurs actionneurs et capteurs. Cela conduit à un contrôleur MIMO difficile à obtenir pour les méthodes classiques de conception. Troisièmement, il faut éviter le problème de spill-over, qui consiste à garantir la stabilité en boucle fermée lorsque le contrôleur basé sur un modèle est appliqué à l'installation réelle. Pour relever ces défis, nous étudions deux stratégies de contrôle : le contrôle centralisé et le contrôle distribué.

Pour le contrôle centralisé, nous proposons une méthodologie qui nous permet d'obtenir un contrôleur MIMO simple. Tout d'abord, plusieurs techniques de modélisation, de réduction et d'identification sont appliquées pour obtenir un modèle précis d'ordre faible de la structure. Ensuite, une méthode de synthèse basée sur le contrôle H_∞ avec un critère H_∞ particulière est appliquée. Ce critère H_∞ intègre plusieurs objectifs de contrôle, y compris les défis principaux. En particulier, le problème de spill-over se transforme en un problème de stabilité robuste et sera garanti en utilisant ce critère. Le contrôleur H_∞ obtenu est une solution standard du problème H_∞. Le contrôleur final est obtenu en simplifiant ce contrôleur H_∞ sans perdre la stabilité en boucle fermée ni dégrader les performances. Cette méthodologie est validée sur une structure de poutre avec des transducteurs piézoélectriques et les vibrations dans la zone centrale doit être réduites. L'efficacité du contrôleur est validée par des simulations et des expériences.

Pour le contrôle distribué, on considère la même structure et les mêmes objectifs. Il existe des méthodes visant à concevoir des contrôleurs distribués pour les systèmes spatialement interconnectés. Cette recherche propose une méthode basée

sur la FEM, associée à plusieurs techniques de réduction de modèles, permettant de discrétiser spatialement la structure de la poutre et d'en déduire les modèles d'espace d'état des sous-systèmes interconnectés. La conception des contrôleurs distribués n'est pas abordée dans cette recherche.

Contents

Nomenclature

Symbols

M_{mode}	Normalized mass matrix
K_{mode}	Stiffness matrix relating to M_{mode}
$\mathcal{X}_{mode}$	Damping term relating to M_{mode}
E	Electromechanical coupling coefficients relating to M_{mode}
E_a	Electromechanical coupling coefficient of actuators
E_s	Electromechanical coupling coefficient of sensors
F	External force vector relating to M_{mode}
R	Capacitance matrix
R_c	Corrected capacitance matrix
R_s	Sensor capacitance matrix
r_i	Capacitance of the i^{th} PZT pair
Q	Electrode charge vector of PZT pairs
Q_s	Electrode charge vector of PZT pairs used as sensors
V	Voltage vector of PZT pairs
V_a	Voltage vector of PZT pairs used as actuators
V_s	Voltage vector of PZT pairs used as sensors
f	Force disturbance
φ	Eigenfunction
η	Modal coordinate
ω_i	Natural frequency of the i^{th} mode
ν_{node}	Velocity vector of the nodes in the central zone
κ_a	Viscous air damping constant
κ_s	Strain-rate damping constant
Y	Internal impedance of the control board
Y_s	Impedance matrix

E_{cent}	Central energy
E^p_{cent}	Proportional central energy
G^{full}	Full-order model
G_r	Reduced-order model
P	Augmented system
K	To-be-designed controller
K_{red}	Reduced-order controller
Ω	Frequency band of interest
r^p_e	Proportional central energy reduction rate
ρ	Density of the beam material
Y_{ang}	Young's Modulus
Δ	Uncertainty or modeling error
M_d	System with no uncertainty (nominal system)
T_s	Sampling time
$\Lambda(A)$	Eigenvalues of a matrix A
$G_{u\to y}$	Open-loop transfer function from input u to output y
$T_{u\to y}$	Closed-loop transfer function from input u to output y
$\mathcal{S}_u$	Power Spectrum Density (PSD) of a signal u
$diag\,(A_1, A_2, ..., A_n)$	Diagonal or block-diagonal matrix with $A_i, i = 1, 2, \cdots, n$ the diagonal terms or blocks
A^T	Transpose of a real matrix A
A^*	Conjugate transpose of a complex matrix A
$\overline{s(t)}$	Time domain average value of the real-time signal $s(t)$
$\|\|G\|\|_2$	H_2 norm of an LTI system G
$\|\|G\|\|_\infty$	H_∞ norm of an LTI system G
$\overline{\sigma}(T(j\omega))$	Maximal singular value of transfer function $T(j\omega)$
$\star$	Redheffer star product

Acronyms

PZT	Lead Zirconate Titanate
LTI	Linear Time Invariant
PPT	Positive Position Feedback
LQR	Linear Quadratic Regulator
LQG	Linear Quadratic Gaussian
SISO	Single Input Single Output

MIMO	Multi Input Multi Output
PSD	Power Spectrum Density
MFT	Modal Form Truncation
LMI	Linear Matrix Inequality
DAC	Digital-to-Analog Converter
ADC	Analog-to-Digital Converter
FEA	Finite Element Analysis
FEM	Finite Element Modeling
DOF	Degree of Freedom

Part I

Dissertation

Chapter 1

Introduction

This chapter introduces the motivation of this work. Then the objectives and the approaches are briefly discussed. Finally, an overview of the remaining chapters is presented.

1.1 Motivation of this research

Lighter structures and flexible manipulators have increasingly attracted attentions for many applications in many industrial domains (aerospace industry, automotive industry, manufacturing industry, etc.). The main advantages of light structures are their light weight and low production cost. With the development of more advanced technologies and materials in industry, it is possible to implement lightweight components in practice for miniaturization and efficiency especially in aerospace and automotive domain. However, light weight components are generally less rigid which makes the structure more flexible. This is reflected by a relatively small structural damping. Such flexible structure may suffer from considerable vibrations when they are excited by external disturbance around the resonant frequencies. The excessive vibrations problem will lead to unpleasant noises, unexpected stress, positioning error, material fatigue, malfunction, or even structure failure. Consequently, effectively controlling the vibrations in such structures is an objective of crucial economic importance which has motivated a huge amount of research in this field [1–4].

For the vibration control of flexible structures, passive vibration control first gained popularity in practical applications because of its practicability and reliability for example in [5–7]. As an alternative way, active vibration control [8] have drawn lots of attention in recent years. Different from passive vibration control methods where the control mechanisms work as the vibration absorber, active vibration control methods generally use a set of actuators and sensors (active structures) connected by a feedback loop. In this case, we exploit the main advantage of feedback which allows us to reduce the sensitivity of the output to parameter variations and to attenuate vibration disturbance within the bandwidth of the control system. Depending on the circumstances, active structures may be cheaper or lighter than passive structures (structures with passive control machenisums) of comparable performances and they may offer performances that no passive structure could offer [9]. This is possible because we can provide the control mechanisms with external energy to counteract more with the structural vibration.

Nowadays, active vibration control methods are becoming more and more cost efficient due to rapid development of electronic technologies which makes actuators and sensors more intelligent and efficient. We call such actuators and sensors the smart materials, such as piezoelectric materials, magnetostrictive materials, magneto-rheological, etc. Smart structures thus refer to the active structures integrated with such smart materials (used as actuators and sensors). A large part of the researches concerning the active vibration control of smart structures has used piezoelectric materials for actuation and sensing [10] because of the high precision and performance. Piezoelectric actuators have proven to be very useful in suppressing vibration and shape control of flexible structures [11–16]. Our objective is to design proper feedback controller to tackle a particular vibration problem on such smart structures (active vibration control) as explained bellow.

The active vibration control problem studied in this work has its particularities which reflect particular applications mainly in aerospace and automotive domain. First, the vibration energy must be particularly rejected in specific locations. For example, at the location of an antenna or a sensor on the aircraft envelope, at the location of the passenger's seat in a car (see Fig. 1.1), etc. In other words, we aim at focusing the control effort on specific locations. This allows us to achieve particular objectives for example giving more comfort to the passengers in a car. Second, we cannot place actuators or sensors at these specific locations. As there

are already multiple devices connecting with each other at these specific locations, it will thus be difficult to add extra actuation and sensing devices. The challenge will be to reduce the vibration in specific locations while only have access to the vibration state at other locations. This challenging objective requires the use of modern multivariable control design methods which allows us to tackle unmeasured performance variables. Third, we aim at reducing the vibration in a frequency band as wide as possible. All control systems have limited working bandwidth. The wider the bandwidth is, the more applicable the system will be. Fourth, the designed controller must avoid the so-called spill-over problem [17] which is the instability caused by the neglected model dynamics when the model-based controller is applied on the actual setup. As it will be discussed in the sequel, this spillover problem will be studied as a robust stability problem.

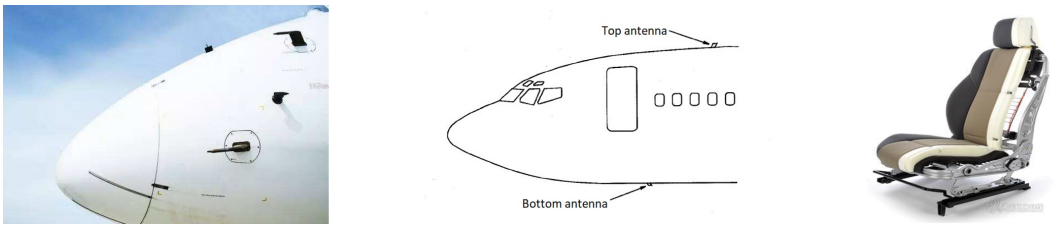

Figure 1.1: Examples of applications for particular vibration control problems

To reproduce the above vibration problem, we build an experimental setup which is composed of a free-free aluminum beam where a number of smart materials (here we use piezoelectric transducers) have already been patched except in the central zone of the beam. Details for this setup will be introduced in the sequel. A certain set of piezoelectric transducers will be used as sensors and another set as actuators. The objective is to compute feedback controllers that reduce the vibration energy in the central zone. In this research, we will first propose a methodology that allows us to design a satisfactory centralized controller. Then, considering the complexity of a centralized controller and its inconvenient physical connections, we then turn to distributed control. This research gives a modeling method for interconnected subsystems of the considered structure which will, in the future, allow us to synthesis distributed controllers.

1.2 Approaches of this research

The method proposed in this research is a model-based controller design process. We need a simple and accurate model of the structure and an efficient synthesis algorithm to compute the controller that achieves all the above objectives. The approaches used in this research is summarized as follows.

For centralized control, we propose a methodology which is the combination of several techniques that will finally lead to a satisfactory controller with guaranteed performance on the actual setup. First, we will build a mathematical model of the considered structure. As far as researches on active vibration control of flexible beams, most of the control design techniques make use of approximated finite-dimensional models [10] deduced using Finite Element Modeling (FEM) techniques [18–24]. FEM gives us the so-called governing equation (a partial differential equation) that contains the dynamics of the beam and the electromechanical coupling between the piezoelectric transducers and the beam. This modeling process can be done using commercial software that performs Finite Element Analysis for example ANSYS [25] and COMSOL [26]. Many researches use such software to build the model of the structure for active vibration control, see [20, 24] for ANSYS and [21, 22] for COMSOL. We here use COMSOL to perform Finite Element Analysis based on standard 3D elements which allows us to tackle the coupling effect between the beam and the piezoelectric transducers. However, the resulting governing equation will have a large number of Degree of Freedom (DOF) which is too complex for controller design. In this work, we apply Modal Displacement Method [27] which allows us to decompose the displacement field into modes and approximate the global behavior of the initial governing equation by a simpler one which neglects the higher frequency modes. The error introduced by this neglection is also corrected using the Static correction [28]. Finally, this governing equation is transformed into a state-space model. One of its outputs is a constructed velocity vector. Using this, we are able to deduce an expression of the vibration energy in the central zone of the beam. By controlling this velocity output, we are able to control the vibration in the central zone. Unfortunately, this model is then proved not accurate enough with the actual setup. Thus, Grey-box identification [29] is applied to optimize some of the parameters and finally gives a reliable identified model of the actual setup. This identified model (will be called the full-order model) actually

contains dynamics outside the frequency band of the disturbance. In order to further simplify it, we propose a multi-variable model reduction method which makes use of the Aggregation Technique [30] and the Linear Matrix Inequality (LMI) constraints [31]. For the controller design, we apply H_∞ control [32] on the reduced-order model obtained from the proposed model reduction method. We propose the H_∞ criterion for all the above objectives and compute a standard solution of the H_∞ problem. The robust stability criterion is satisfied using an important result in robust analysis, i.e. the Small Gain Theorem [33]. For the ease of the implementation, we also reduce the order of the controller by using the Balanced Truncation [34, 35] without loosing the closed-loop stability or degrading the performance. It should be noticed that the above approaches can be extended to any flexible structures such as plates and shells. However, in order to control the target modes, the number and position of piezoelectric transducers should be carefully chosen such that the target modes can be effectively excited/captured.

For distributed control, we will consider the structure as the interconnection of several subsystems. A subsystem will be a local part of the beam with few (or no) piezoelectric transducers on it, for example a section of the beam with two transducers (one actuator and one sensor). Distributed controllers will connect with the subsystems with actuation and sensing capabilities to achieve together a desired global behavior. In our case, it is to reduce the vibration energy in the central zone of the beam. In this work, we propose a modeling method which allows us to deduce these interconnected LTI subsystems (will be called the distributed model). First, according to the objective, we spatially discretize the structure into cells (a section of the beam with or without piezoelectic transducers). Using COMSOL, we are able to deduce the governing equation for each cell, however with large number of DOF. As the modes of one cell do not represent the modes of the entire structure, there will be no sense to apply the Modal Displacement Method to the cell equation. Here we will apply Guyan condensation [36] which approximates the initial governing equation by neglecting all the DOF free of external constraints. Kinematic assumption is also applied to further reduce the governing equation. Based on the simplified governing equations of the cells, we construct the state-space models for these subsystems such that there are no algebraic relations between the states of neighbor subsystems. In other words, all the subsystems are orthogonal which is very important for controller synthesis.

The identification of the distributed model and the controller synthesis will be the future works and will not be tacked in this dissertation.

1.3 Publications

• Journal paper:

P. Wang, A. Korniienko, X. Bombois, M. Collet, G. Scorletti, E. Skow, C. Wang, K. Colin, Active vibration control in specific zones of smart structures. Control Engineering practice (2018). doi:10.1016/j.conengprac.2018.12.005.

This paper concerns the proposed methodology for centralized controller design and its application. It introduces the modeling of the smart structure (see Chapter 4) and the proposed H_∞ criterion as well as some experimental results (see Chapter 5).

• Conference paper:

P. Wang, G. Scorletti, A. Korniienko, M. Collet, Multi-variable model reduction of smart structure in active vibration control, IFACPapersOnLine 51 (25) (2018) 441–446. doi:10.1016/j.ifacol.2018.11.152.

This paper concerns the proposed multi-variable model reduction method and its application (see Section 4.3).

1.4 Organization of this dissertation

The organization of the following chapters is as follows:

Chapter 2: Backgrounds

This chapter provides the backgrounds of this research. An extensive literature review on active vibration control is conducted for related techniques such as the employment of smart materials, the widely used active vibration control laws for centralized controller design. Different design methods are compared and discussed which gives the motivation of applying H_∞ control in this research.

Then, an overview of distributed control of the vibration problem on flexible structure is given.

Chapter 3: System description

This chapter gives a detailed explanation of the considered setup. The control objectives and all the other considerations are pointed out. These are the foundations of the proposed H_∞ criterion. Then, the choice of actuators and sensors as well as the implementation of the centralized controller is introduced. This is important because the controller design must take the actual control devices into account such that the performance can be guaranteed on the actual setup. For better understanding the centralized controller design process, we introduce the overview of the proposed methodology as a guide for the following chapters. We also introduce an overview of the modeling for distributed control.

Chapter 4: Modeling for centralized control

This chapter explains in details the modeling process of the beam-piezo system for centralized controller design. The governing equation is first deduced from Finite Element Modeling and then simplified and corrected to compensate the error introduced by the simplification. Based on this governing equation, a state-space model (the so-called full-order model) is deduced which contains a wider frequency band than the considered disturbance. Grey-box identification is first applied to optimize some of the parameters such that the full-order model match the benchmark. Then a multi-variable model reduction method is proposed and applied to the full-order model which gives a high quality reduced-order model. The reduced-order model is the to-be-controlled system for controller design.

Chapter 5: Centralized controller design

This chapter tackles the design process of the centralized controller. For better understanding, a brief introduction of the standard H_∞ control problem with respect to performance and robust stability is fist introduced. Then it is applied to solve our particular vibration problem by proposing the H_∞ criterion according to specified control objectives. The proposed criterion is applied on the considered structure by properly choosing weighting functions. For the ease of implementation, the obtained H_∞ controller is further reduced without losing closed-loop stability and degrading performance. The effectiveness of the reduced-order controller is verified by simulations and experiments. Finally, a

discussion is given to explain the limitation of a SISO controller with respect to our specific objectives.

Chapter 6: Modeling for distributed control

This chapter introduce our method for deducing a distributed model. The distributed model refers to the interconnection of LTI subsystems that correctly reflects the global dynamics of the structure. For this purpose, the structure is first discretized into cells. Multiple techniques are applied to obtain the governing equations of the cells. The state-space representations of subsystems are deduced from the local assembly of a small number of cells such that the neighbour subsystems are orthogonal. This method is validated by comparing the global responses of the distributed model with those of the model built for centralized control.

Chapter 7: Conclusions and future research

This chapter summarizes this research and outlines potential directions for future research.

Chapter 2

Background

This chapter provides the background of this research. It gives an extensive literature review on active vibration control including the employment of smart materials, the common used control laws for active vibration controller design (centralized) and an overview on distributed control of flexible structures.

2.1 Smart materials for active vibration control

Smart materials are materials that are able to generate strain based on the change of external physical environment such as temperature, electric field or magnetic field, etc. This is the result of the coupling effects described by constitutive equations. According to [9], there exist several popular smart materials such as *Shape Memory Alloys (SMA)*, *Magnetostrictive materials*, *Magneto-rheological (MR)* and *Piezoelectric materials*. Here, we will give a brief introduction of these smart materials as well as their properties which gives the choice of the type of material used in this research.

Shape Memory Alloys (SMA) are able to 'remember' its original shape and return to its predeformed shape when heated. They are only sensitive at low frequencies with low precision. As a result, they are little used in active vibration control. However, we could still find some applications, for example in [37].

Magnetostrictive materials generates strain under magnetic field. They can be used in compress situation as load carrying mechanisms [38] because it has maximum response when it is subjected to compress load. TERFENOL-D is the most popular magnetostrictive material. In some applications like sonar, TERFENOL-D can be an alternative choice of PZT.

Magneto-rheological (MR) is a particular viscous fluid that contains particles of magnetic material in micron-size. They are mainly used in semi-active vibration control of suspension systems [39].

Piezoelectric materials can be used as actuators as well as sensors because of its bidirectional piezoelectric effect. Ceramics and Polymers are two classes of piezoelectric materials mainly used in vibration control. The *piezopolymers* are not usually used as actuators because of the high voltage requirement and the limited control authority. Thus, they are mostly used as sensors. The best known piezopolymer is the Polyvinylidene Fluoride (PVDF). The application of PVDF in active vibration control can be seen for example in [40, 41]. The *piezoceramics* can be used as both actuators and sensors. They are applicable for a wide frequency band, till ultrasonic frquencies in some applications. They also have high precision up to the nanometer range[1] [9]. The most popular piezoceramic is the Lead Zirconate Titanate (PZT). PZT patches can be glued or co-fired on the target structures which makes it very applicable for light structures. *Piezoelectric materials* are the most commonly used smart materials in active vibration control [10].

Considering the properties of these smart materials, we conclude that the piezoelectric materials, especially the PZT patches, are the most suitable for active vibration of light weighted flexible structure such as an aluminum beam considered in this research. It has advantages over other materials in many aspects such as mechanical simplicity, small volume and lightweight, wide working frequency band, high precision, and the ability of high level integration in the structure.

As mentioned above, piezoelectric materials can be used to control the vibration because of its bidirectional piezoelectric effect which is first discovered by the Curie brothers in 1880 [42, 43]. In particular, they find that squeezing particular materials leads to the change of electric charge. This phenomenon allows piezoelectric materials to be used as strain sensors. On the other hand, the converse

[1] Up to $1nm = 10^{-9}m$

effect is also possible which means that it is able to generate a mechanical strain under the application of an electric voltage. This allows the use of piezoelectric materials as actuators. Active vibration control using piezoelectric materials has attracted considerable interest of the researches during the past few decades. To design efficient piezoelectric smart structures for active vibration control, both structural dynamics and control laws have to be investigated as introduced in the next section.

2.2 Active vibration control of flexible structures

As far as the researches about active vibration (centralized) control of flexible structures, various methods have been developed in the past few decades. Generally, the design process for an active vibration control problem involves many steps. A typical scenario is as follows [44]:

1. Analyze the property of the to-be-controlled structure.
2. Deduce a reliable mathematical model of the to-be-controlled structure by using techniques such as Finite Element Analysis or data-based modeling method (e.g. the identification techniques).
3. Reduce the model (if necessary) such that it has less degree of freedoms and lower dimension[2].
4. Analyze properties, dynamic characteristics of the resulting model. Properly define the disturbance.
5. Quantify requirements for sensors and actuators and decide their types as well as their locations on the structure.
6. Analyze the effect of the chosen actuators and sensors on the global dynamics of the structure.
7. According to the control objectives, quantify performance criterion and stability trade-offs.

[2] A simple model is always preferred for the purpose of control design

8. Decide the control law to be applied and design a controller to satisfy the quantified control requirements.

9. Validate the desired control requirements of the controlled system by simulations. If the controlled system fails to satisfy the requirements, adjust the requirements or modify the control law.

10. Choose proper hardware and the corresponding software and integrate them on an experimental benchmark.

11. Design experiments and perform system identification. Update the model if necessary.

12. Implement the obtained controller. Perform experiment and necessary measurements to evaluate the actual performance on the real-life system.

13. Repeat some of the above steps if the actual performance does not meet the control objectives.

In design process, depending on the circumstances, it is possible to follow different steps from the above scenario. However in any case, a reliable simplified mathematical model is first needed. Various modeling and model reduction techniques could be applied. Model updating is also necessary if the model does not have enough accuracy. Then, according to the control objectives, we need to quantify the requirements, choose the type of actuators and sensors and decide their positions. At last, apply proper control law and design a controller that satisfies specified performance criterion and stability trade-offs. Simulations and experiments are necessary to validate the obtained controller.

For the modeling part, a lot of researches concerning the modeling of piezoelectric materials incorporated into flexible structure apply the Finite Element Modeling (FEM) and the System Identification [45–51]. FEM is based on the principles of mechanics and physical laws and gives partial differential equations whose parameters possess actual physical sens. However, such equations will have a large number of DOF and dimensions. There exist various model reduction methods allowing us to reduce such finite element models for example the Modal Displacement Method [27], the Krylov Subspace Method [52], the Rayleigh–Ritz method [53], etc. On the contrary, System Identification ignores the mechanics and physical laws and builds the model in the perspective of systems and control.

It performs data matching and directly obtain the transfer function (or state-space representation) that reflects the input-output behavior of the structure. There also exist methods to reduce such models as discussed in [54]. In addition, It is also possible to combine these two modeling techniques as it is concerned in this research.

For the control part, there exists a lot of control laws applied under various circumstances and aimed at controlling different types of systems. For example the feedforward or feedback control employed for systems that are linear or non-linear, time-invariant or time-variant. To be specific, the smart structure studied in this research is considered as a Linear Time Invariant (LTI) system and we focus on the feedback control law for such LTI structures. In the literature on active vibration control for LTI systems, methods have first been developed to design Single Input Single Output (SISO) controllers to control one resonant mode with a collocated actuator-sensor pair. Such methods include PID control [55–57], Velocity Feedback control [9, 16, 58–60], Acceleration feedback control [13, 61, 62], Positive Position Feedback (PPF) control [63–66], etc. These methods have their limitations. First, as mentioned, they are only able to control one resonant mode. To control more modes, one have to design different controllers for each mode and combine them in parallel as discussed in [9, 65]. This is indeed a solution however with low efficiency and performance. Second, these methods require collocated actuator-sensor pair which limits the applicability. Otherwise, the closed-loop stability could not be guaranteed as evidenced in [9]. Third, if too many modes are concerned, one actuator-sensor pair will no longer be sufficient. A Multi Input Multi Output (MIMO) controller using multiple actuator-sensor pairs is thus required. There indeed exists modified version of the above mentioned methods which allows us to design a MIMO controller such as a modified version of PPF [67, 68]. However, it is not a systematic controller synthesis method and is not as efficient as the later developed modern control design methods. Recently, modern control design methods have been increasingly applied in active vibration control of flexible structures which allows us to design MIMO controllers that control multiple modes. Such methods include Pole Placement control [69], Linear Quadratic Gaussian/Regulator (LQG/LQR) [70–75], H_2 control [76], H_∞ control [77–82], etc. These modern control methods have the advantage over classical control methods in that they are applicable to both SISO and MIMO systems and do not require collocated actuator-sensor

pair. While H_∞ control has the advantage over other modern methods in that it provides satisfactory robustness properties in the presence of parametric and dynamic uncertainties [32] which are not easy to obtain with Pole Placement, LQG/LQR or H_2 control. The consideration in robustness properties allows us to avoid the spillover instability [83, 84], which is the most important motivation of applying H_∞ control in this research.

At last, it is important to notice that all these active vibration control methods are mainly applied to reduce the global vibration of a flexible structure with respect to an excitation over a relatively small frequency band (control one mode with SISO controller or control a few modes with MIMO controller). To the best of our knowledge, this research is the first one proposing a technique that allows to particularly reduce the vibration in a specific zone where there is no actuator or sensor and with respect to an excitation covering a large frequency band (containing as many as eleven modes). How to adapt H_∞ control to such objectives is thus a big challenge which constitutes the main scientific contribution of this work.

2.3 Distributed control of flexible structures

For the active vibration control problem, the general objective will always be controlling as many modes as possible with the best performance. Such objective could be achieved by giving smart structures more actuation and sensing capabilities which requires the use of more actuators and sensors. However, in the presence of a large number of actuators and sensors, designing a centralized controller will require high computational cost and high level of physical connectivity. An alternative way is to design distributed controllers which is referred to as the distributed control. Distributed controllers work in a different way from centralized controllers in that one controller only reacts with a local part of the structure, for example connects with a few number of actuators and sensors that are close to each other which forms a local control unit. Several such controllers working together to achieve a global control effect. For this purpose, the smart structure will be spatially discretized and thus can be considered as a spatially interconnected system (or spatially distributed system) [85]. Each

subsystem will have actuation and sensing capabilities which allow it to be connected with a distributed controller. Moreover, neighbor controllers will change information between each other which helps them to achieve global control objectives. Fig. 2.1 [85] shows the architecture of such spatially distributed control system where G denotes the interconnected subsystems of the smart structure and K the distributed controllers. There also exists a similar control architecture which is the so-called decentralized control [86] where different controllers do not communicate with each other. However, it has been proven on an actuated beam in [85, 87] that the distributed control can achieve better performance than the decentralized control.

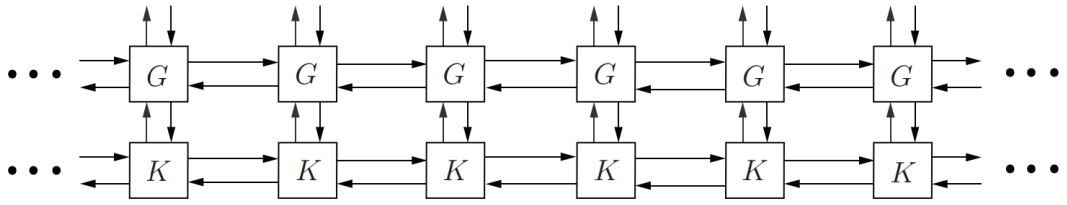

Figure 2.1: Architecture of a spatially distributed control system

In order to control such spatially interconnected system, methods have been developed in the recent few years to design distributed controllers. Raffaello and Geir [88] propose a state-space framework to design distributed controllers for systems with highly structured interconnection topology. Analysis and synthesis conditions are formulated in terms of Linear Matrix Inequality (LMI). Applications of this framework can be found in [85, 89–91]. In particular, this framework assumes that the interconnected architecture is spatially invariant. However, such architecture is typically not given in real-life applications where the architecture could be spatially variant as it will be concerned in this research. Thus, extended methods are developed for spatially variant systems [92–94] or heterogeneous systems [95–97]. To obtain the model of the spatially interconnected system, multiple techniques are available such as the Distributed identification [98, 99], the FEM [90], the combination of Distributed identification and FEM [100], etc.

2.4 Summary

This chapter gives an extensive literature review on active vibration control of smart structures. The review includes the employment of smart materials on flexible structures for the purpose of active vibration control, the modeling and control methods (centralized) as well as the typical scenario of the controller design process, and the overview of the distributed control. The focus of this review is on the centralized control.

Chapter 3

System description

This section will give a detailed introduction of the experimental setup and the control objectives. We will also explain the physical connections between the setup and the to-be-designed controller which will, in the sequel, be taken into account in the modeling part and the controller design process.

3.1 Experimental setup

The concerned system is a flexible structure with smart materials, the so-called smart structure. The used smart materials here are piezoelectric patches that will be used as sensors and actuators. The actuators generate certain efforts to counteract with the structural vibration in order to reduce it, which is considered as the active vibration control. In this dissertation, attention is focused on a particular situation where the vibration must be rejected in a specific location of the structure where smart materials cannot be placed. We thus aim at reducing the vibration in a specific zone by only using the measurements in other zones with a centralized or a distributed controller.

To reproduce the problem described above, the following experimental setup (beam-piezo system) is considered, see Fig. 3.1. It is made of a long thin aluminum beam with a number of piezoelectric transducers (PZT) and under the excitation of an electrodynamical shaker at the right end.

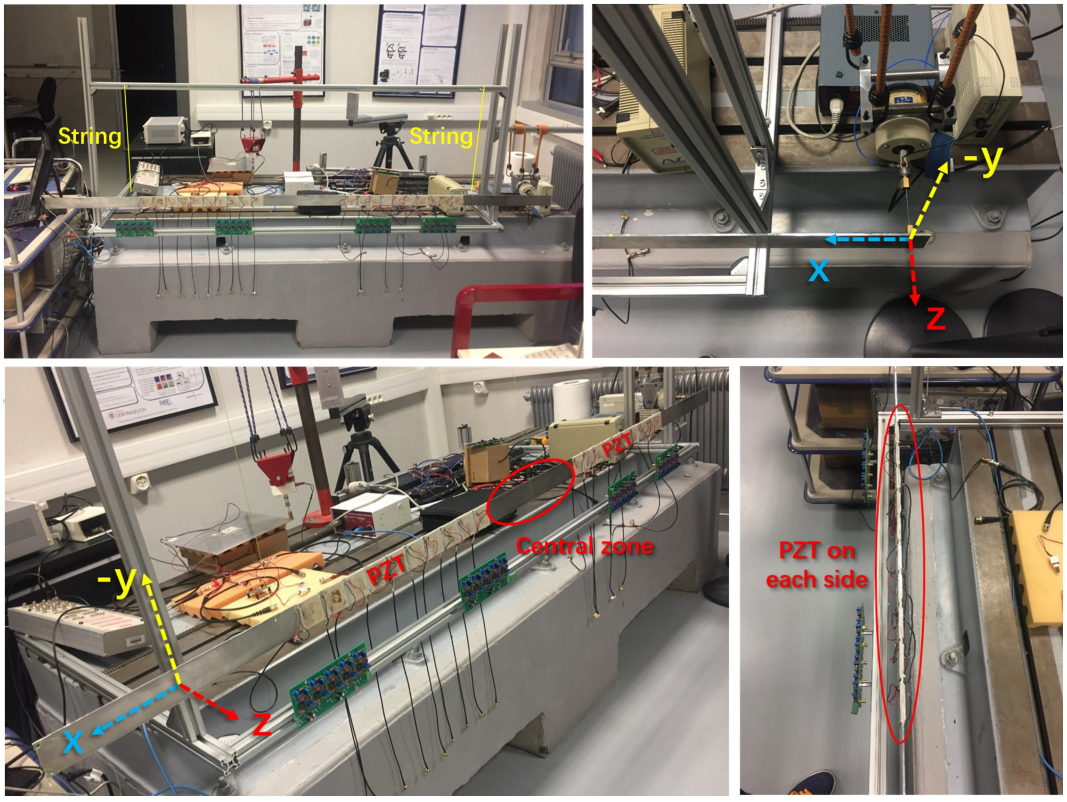

Figure 3.1: Setup pictures: a general view (top left), the shaker (top right), central zone and PZT locations (bottom left), PZT pairs (bottom right)

Fig. 3.2 is the schematic diagram of the setup on flat and top view which presents more details. The beam is hung on a solid shelf which creates a free-free boundary condition and which limits the displacement in y direction. Two times 10 pairs of PZT patches cover two zones L_3 around the central zone of the beam (zone L_2). These PZT are used in pairs which means that two PZT at the same location but on different sides of the beam are used together as one actuator (or sensor) in order to generate reversed force on two sides of the beam which gives a balanced control torque. For this purpose, the polarization of the two PZT as a pair must be towards the same direction as shown in Fig. 3.3 such that when a voltage is applied, the PZT on top and bottom of the beam deform in opposite directions which creates a balanced torque. There are in total 20 PZT pairs numbered from 1 to 20 (10 pairs on each side of the central zone). The excitation is a force disturbance applied by an electrodynamical shaker (top right figure in Fig. 3.1) along z-axis at the right end of the beam and the excitation point is in the middle of its height (h). This means that the disturbance will mainly excite the bending

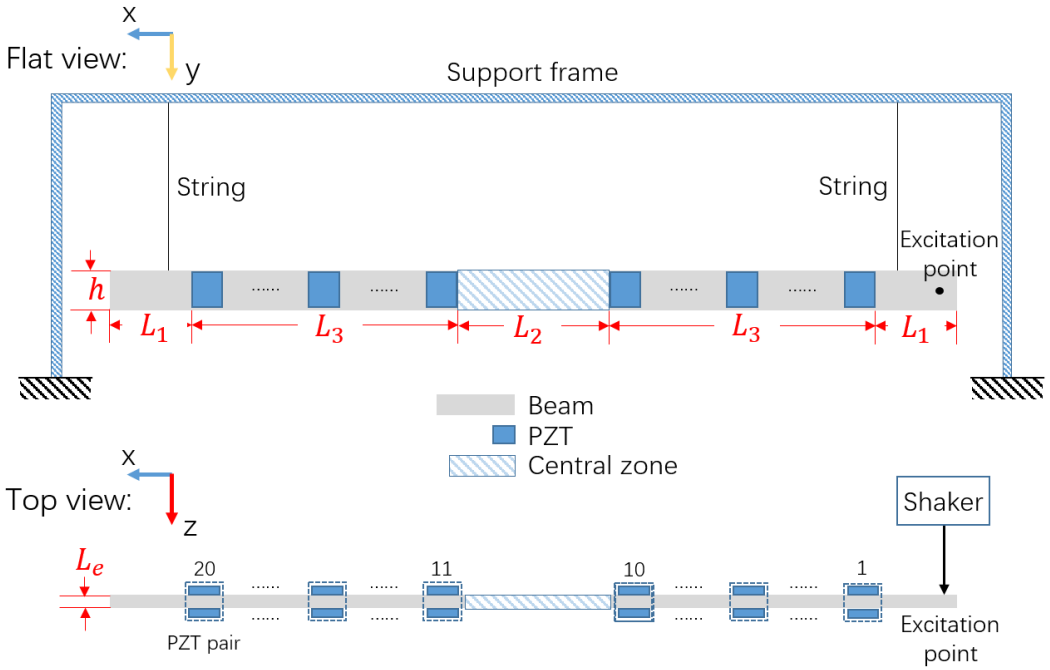

Figure 3.2: Schematic diagram of the setup: flat view (top); top view (bottom)

of $x-y$ plane which results in lateral displacement in z-axis. In addition, because of the high long-width ratio and the free-free boundary condition, Euler-Bernoulli assumptions [101] can be used where shear stress and rotational inertia can be neglected. This assumption will be considered in the modeling of the beam-piezo system as detailed in Chapter 4. This also corresponds to the way that the PZT pairs are pasted which makes the bending moment the most effective to be captured. The dimensions and the material parameters are listed in Table 3.1.

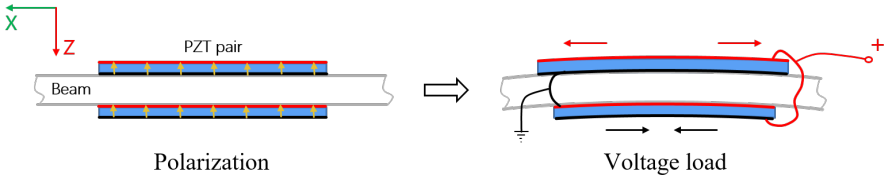

Figure 3.3: PZT polarization and the resulting balanced control torque under voltage load

Table 3.1: Setup dimensions and parameters

Property	**Value**
Beam density (Aluminum), ρ	$2720\,kg/m^3$
Beam total length, L	$2.5\,m$
Beam ends, L_1	$0.45\,m$
Beam center, L_2	$0.42\,m$
Beam middle with PZT, L_3	$0.59\,m$
Beam hight, h	$0.053\,m$
Beam thickness, L_e	$0.003\,m$
PZT material type	FerroPerm Pz26
PZT dimensions	$0.05m \times 0.05m \times 0.0005m$
Distance between PZT	$0.01\,m$
Maximum voltage for PZT (guideline)	$200\,VAC/mm$
Cross-section area of beam, A_S	$159\,mm^2$
Young's modulus (Aluminum), Y_{ang}	$69\,GPa$

3.2 Control objectives and considerations

The general objective is to use the smart materials as actuators and sensors to particularly reduce the vibration at a specific zone of a flexible structure by only using the measurements in other zones, which can be interpreted as to tackle unmeasured performance variables (see e.g. [102] for an example in another context). As to our experimental setup (Fig. 3.1), we aim at designing a feedback controller (centralized or distributed) that allows to significantly reject the vibration energy from the central zone (the part with length L_2 shown in Fig. 3.2) when the beam is subject to an external force disturbance at one end of the beam.

The disturbance is applied along z-axis and thus only the vibration in z-axis is of interest. As to the frequency band of the disturbance, if we forget the complexity of the feedback controller, the ideal goal is of course to reject a disturbance with a power spectrum density (PSD) which covers the largest possible frequency band, in other words, to control as many vibration modes as possible. However, the general control ability and the maximum possible performance will necessarily depend on the sensitivity of the actuator, which means that we can only effectively control the modes within the working range (sensitive range) of the actuator. In our case, the used piezoelectric material is Pz26 (see, Table 3.1)

which has a very large working range. The force disturbance applied by the electrodynamical shaker is chosen to have high PSD in $(600, 3000)$[1] rad/s which is within the working range of the PZT. This bandwidth covers 11 vibration modes[2] and the modes outside this bandwidth will thus not be controlled. Consequently, the disturbance is chosen to have large PSD in $(600, 3000)$ rad/s. To the best of our knowledge, this dissertation is the first one proposing a technique that aims to significantly reduce a vibration covering a frequency band with as many as 11 modes in a specific zone free of actuating and sensing transducers.

As to the controller design, the challenging objective of controlling such many modes requires the use of modern multi-variable control design methods. The first reason for this is that modern control design methods allow us to tackle unmeasured performance variables such as the vibration in the central zone where there is no sensor. Second, as it will be discussed in Section 3.3, in order to successfully control the 11 modes in $(600, 3000)$ rad/s, at least two sensors and two actuators are necessary for a centralized controller. We thus have to design a multi-variable (MIMO) controller. As for distributed control, all the 20 PZT pairs should be used which requires even more complex control design methods.

Some other considerations must also be taken into account. First, in order to guarantee the designed control effect on the actual setup, an accurate model is of crucial importance, especially for active vibration control. There are ways to build the theoretical model knowing the values of the physical parameters and geometry of the materials (i.e. Table 3.1). However, there are always errors and it will be further illustrated in Section 4.1.6 that the theoretical model is far from being accurate enough. Therefore, model correction is necessary, for example, using the identification technique which corrects the model using the measurement data from the actual setup and yields an updated model which will have much better accuracy. Second, to ensure a good feasibility of the implementation, the order of the controller should be relatively low, which implies that a low-order model containing only the modes in $(600, 3000)$ rad/s should be used to compute the controller because, as we will see in the sequel, the identified model will have to contain modes outside the frequency band of interest (called the full-order model in the sequel). This introduces a robust stability requirement that the low-order model based controller must also guarantee the

[1] About $(95, 477)$ Hz

[2] Only bending modes in z-axis are considered

stability when applied on the full-order model. This is also to avoid the so-called spill-over problem[3]. Third, the controller should have reasonably high magnitude in $(600, 3000)$ rad/s to ensure a high vibration reduction rate while relatively low magnitude outside $(600, 3000)$ rad/s to limit energy consumption. For the same reason, we should also take care that sensor/measurement noise (usually located at high frequencies) has limited effect on the control output.

3.3 Centralized controller implementation

The designed controller will be a centralized controller (a model-based feedback controller) which collects together all the measurements (sensing voltage) from the PZT pairs used as sensors and then computes control signals (actuation voltage) for all the PZT pairs used as actuators. Thus, the more PZT pairs we use, the more complex the controller will be, which increases computational burden and energy consumption of the control board. Thus, we need a minimum number of PZT pairs to obtain a maximum accessible performance. Considering the large bandwidth of the disturbance (i.e. $(600, 3000)$ rad/s), we show in Appendix A that we need at least two sensors and two actuators (a SISO controller is therefore not sufficient). In Appendix A, we also show that an appropriate choice for these two actuators and these two sensors is to select the 10^{th} and 16^{th} PZT pairs as actuators, the 5^{th} and 11^{th} PZT pairs as sensors (see Fig. 3.4 for the location of these PZT pairs).

The type of all the control devices are listed in Table 3.2 and their functions are detailed as follows. The designed controller will be implemented in a programmable digital control board which should be able to simulate the input-output behavior of transfer functions. Like all the other digital signal processors, this control board is equipped with ADC/DAC card in each input/output channel for sampling/constructing the actual input/output signal. However, it is not equipped with internal anti-aliasing filters. Therefore, extra anti-aliasing filters are necessarily used to sample the outputs of the PZT sensors and the filtered voltage signals are collected by the control board through its own ADC cards. The force disturbance is applied by an electrodynamical shaker which needs an

[3]Instability problem due to the effect of actuation to the unmodeled dynamics of the structure [17]

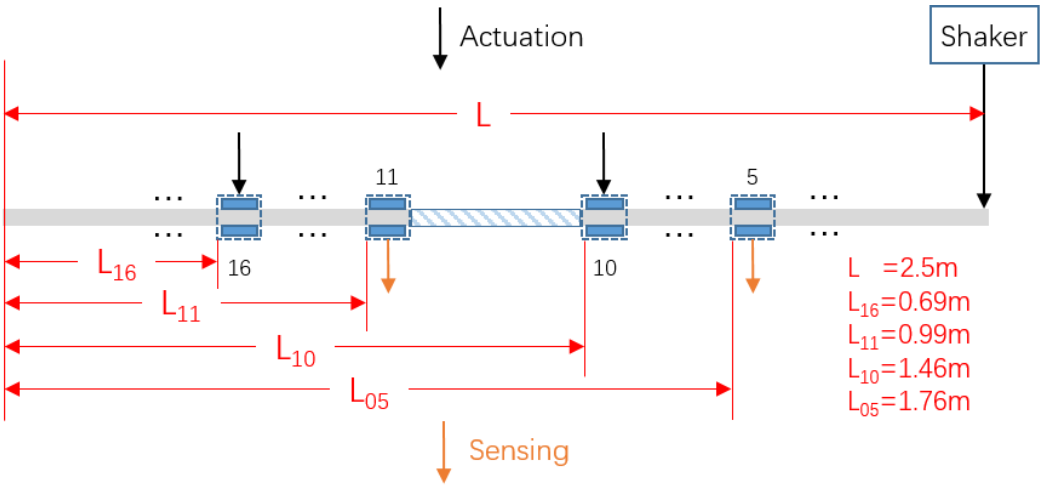

Figure 3.4: Actuators and sensors in the application

input signal as a reference to characterize the bandwidth and the magnitude of the output force. As to the actuation, the DAC cards of the control board do not have enough output power and thus power amplifiers are used to take control signals from the control board and then send power to the actuators. In general, the control system can be illustrated by Fig. 3.5 where f represents the disturbance force applied by the shaker and where the (digital) control board takes as input the sensor voltages V_s of the 5^{th} and the 11^{th} PZT pairs (that have been sampled after passing through anti-aliasing filters) and delivers as output the voltages V_a to be applied at the 10^{th} and the 16^{th} PZT pairs (through power amplifiers). These (amplified) voltages V_a on the PZT actuators will induce a force whose effect is to counteract the structural vibration (especially) in the central zone.

Table 3.2: List of the control devices

Control device	**Hardware type**
Digital control board	DSpace DS1104
Anti-aliasing filter	Nexus Conditioning Amplifier Type 2692
Power amplifier	PCB 790 Series Power Amplifier
Electrodynamical shaker	DP V4

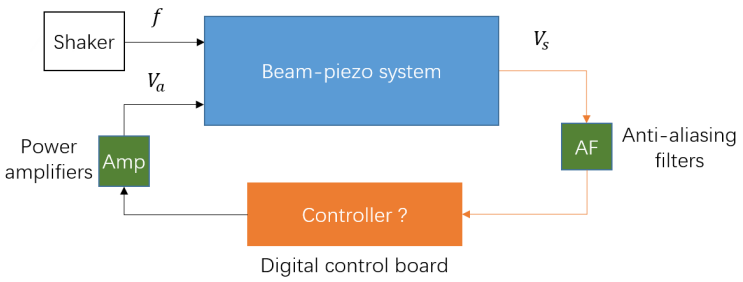

Figure 3.5: Block diagram of the controlled system

3.4 Methodology overview for centralized controller design

In order to design a centralized controller that achieve the control objectives described in Section 3.2 with a performance well guaranteed when applied on the actual setup, we propose the following methodology (based on H_∞ control and all other modern control design techniques).

Fig. 3.6 gives a general overview of this methodology and each step will be detailed in the following chapters. First, the theoretical model of the beam-piezo system is derived using the commercial software COMSOL which performs Finite Element Analysis and modal decomposition to a virtual 3D beam model. Only a finite number of vibration modes (chosen by the user) can be tackled. This results in a state-space model that is only valid up to a certain frequency band (corresponds to the user-chosen maximum vibration mode) which is here chosen slightly larger than the maximal frequency of the disturbance i.e. 3000 rad/s. In this state-space model, the output vector is not only made up of the voltages at the PZT pairs selected as sensors, but also of the (vibration) velocities at a number of locations in the central zone. An expression for the vibration energy in the central zone can indeed be derived from these velocities. Then, the model parameters, for which COMSOL gives a rough initial estimate, are tuned using grey-box identification in order to obtain a model with better accuracy[4], yielding the so-called full-order model of the system. The effect of all the control devices is also considered in the identification process. This (full-order) model covers a frequency band that is larger than the frequency band of interest (i.e.

[4]A grey-box identification approach is here preferred over a black-box approach to keep the model order low.

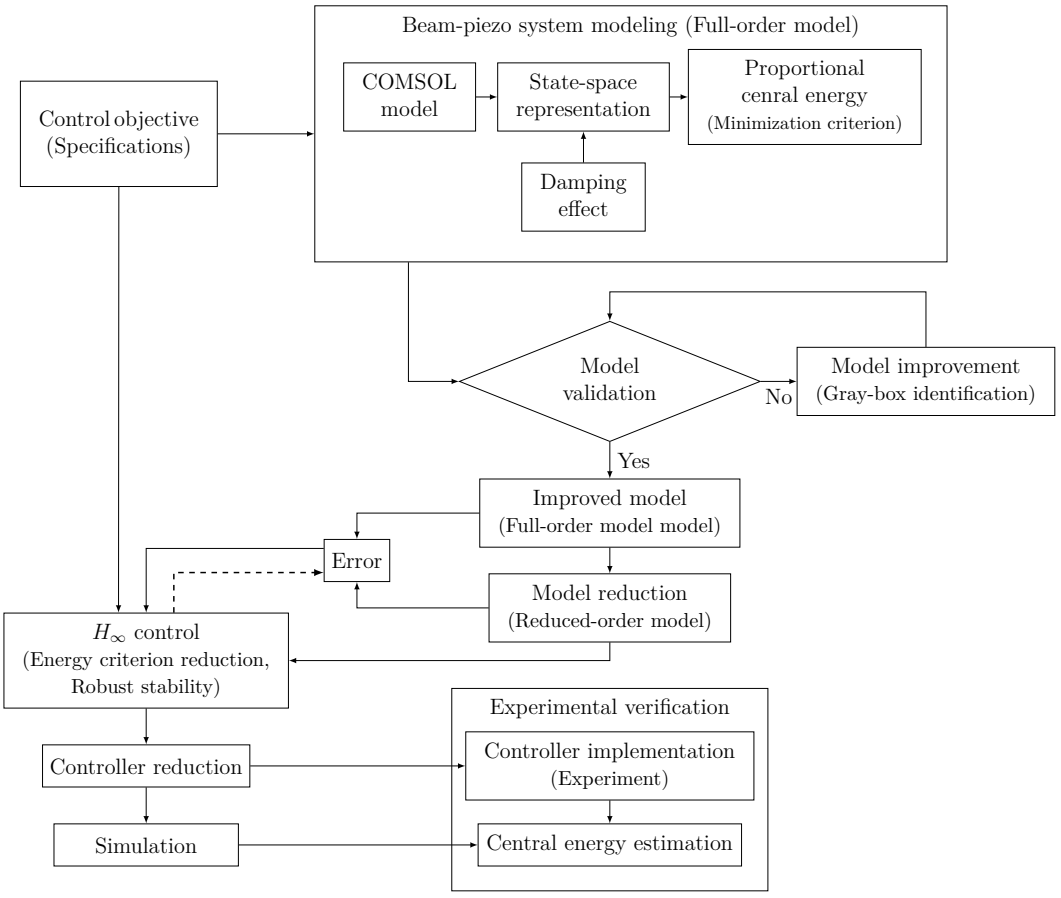

Figure 3.6: Overall design methodology

$(600, 3000)\ rad/s$). A model reduction method is therefore proposed and applied to obtain a reduced-order model that is close to the full-order model in the frequency band of interest. The reduced-order model is then used to design the controller using an H_∞ control design procedure. This control design procedure aims at minimizing the vibration energy in the central zone while keeping the control efforts in acceptable proportion and ensuring that the designed controller will stabilize the full-order model. This last objective is tackled by considering the difference between the full-order model and the reduced-order model as an uncertainty. Finally, for the ease of implementation, the obtained controller is reduced without impacting the stability or degrading the performance. We validate the proposed approach by simulation and by implementing the designed controller on the real setup.

Chapter 4 will introduce the modeling of the to-be-controlled system, where we will explain how to obtain an accurate full-order model and a high quality

reduced-order model with well defined expression of the central energy. Chapter 5 will present how to obtain a simple centralized controller satisfying all the control objectives using H_∞ control and reduction method. The simulation and experimental results are also introduced.

3.5 Overview of modeling for distributed control

For distributed control, we try to design several individual feedback controllers that locally react with the structure in order to achieve a global behavior. The desired global behavior is exactly our main objective, which is to particularly reduce the vibration in the central zone free of PZT pairs. For the implementation, each controller will only connect a small number of PZT pairs that are very closely located. As a result, we will consider a section of the beam with two neighbor PZT pairs as a to-be-controlled subsystem (one actuator and one sensor) which will be connected with a distributed controller as a local feedback control unit. In this dissertation, we will introduce the modeling method which allows us to deduce the state-space model of LTI subsystems such that the structure (beam with PZT pairs) can be considered as their interconnection, which will be called the distributed model. In particular, some of the subsystems will have actuation and sensing capabilities and will be connected with controllers forming a control unit. Other subsystems without actuation and sensing capabilities will only contribute to the global dynamics of the beam, for example the velocities of the points in the central zone which are also necessary for computing the vibration energy. Considering that the setup is a long thin beam, we will discretize the beam into sections along its length and will obtain several subsystems such that one subsystem only communicates with its left and right neighbours. Moreover, there should be no algebraic relations between the states of neighbour subsystems which is very important for distributed controller synthesis.

In the modeling part, we will first spatially discretize the structure according to the position of PZT pairs into different types of cells (cells with and without PZT pairs). The governing equation of each type of cell can be deduced using COMSOL and then be simplified by keeping the least number of DOF. Using

these governing equations, we perform local assembly and then deduce the state-space model of subsystems. It is important to note that in order to avoid algebraic relations, one subsystem and one cell will not be identical. Finally, to verify this method, the distributed model (interconnection of subsystems) and the model built for centralized control (before identification) should have the same global responses. The identification of the distributed model and the controller synthesis are the future works and will not be tackled in this dissertation.

3.6 Summary

This chapter gives a detailed picture of the experimental setup. The dimension of the beam and the piezoelectric material chosen for actuating and sensing as well as all the control devices are listed. The basic operating principle of the piezoelectric patches is also explained. We consider an excitation in a large frequency band that contains 11 vibration modes. The main control objective is to use these piezoelectric patches as actuators and sensors, compute a feedback controller that reduces the vibration energy in the central part of the structure free of actuating and sensing transducers. Other considerations are also taken into account for example the energy consumption of the controller, the ability of tolerating a certain level of measurement noise, avoiding spill-over problem (guarantee the robust stability), etc. In order to effectively control all the modes in the frequency band of interest, we carefully choose two PZT pairs as actuators and another two PZT pairs as sensors which requires a MIMO controller of 2×2. The design process for a centralized controller is generally explained as a guide for the discussion of the following chapters. We also point out that we will finally turn to distributed control with the same objective and we will introduce in this work our method for building interconnected LTI subsystems used for distributed controller design.

Chapter 4

Modeling for centralized control

In this chapter, we will build a state-space model of the beam-piezo system. The so-called beam-piezo system model is the model of the setup with the force disturbance f, the actuation voltage vector V_a as inputs and the sensing voltage vector V_s as output as illustrated in Fig. 3.5. Additionally, we will also construct another to-be-controlled output vector with which we can deduce an expression of the vibration energy in the central zone. Moreover, for model based controller design, we assume that the effects of the actual control devices in the control loop (i.e. the power amplifiers that provides V_a, the anti-aliasing filters used to sample V_s and the DAC/ADC card in each channel of the digital control board) can be considered as constant gain, phase shift and time delay. As we will see in the sequel, this phase shift will also be approximated by a pure time delay.

For the modeling of the beam-piezo system, we first perform Finite Element Modeling using COMSOL which gives us a global governing equation of the beam-piezo system with its parameters computed by COMSOL. The governing equation is then transformed into a state-space model (initial model). This model is actually a truncated model which ignores the dynamics at higher frequencies. To validate this model, we compare its frequency response with the response measured from the actual setup and find that this initial model is not accurate enough. Thus, model improvement using grey-box identification technique is performed to correct some of the model parameters. In this procedure, the effects of the actual control devices in the control loop are also taken into account in order to fit as much as possible the model with the actual setup. As to the controller design, the complexity of an H_∞ controller will always be larger than

the to-be-controlled model (it depends on the choice of the weighting functions). Thus, in order to obtain a simpler controller, the model should also be as simple as possible. However, the model deduced with COMSOL will contain the modes at lower frequencies that are outside of the frequency band of interest which should also be neglected. For this purpose, a model reduction method is proposed to further simplify the state-space model deduced from COMSOL by eliminating all the modes that are out of interest. The controller design will be based on the reduced-order state-space model.

4.1 State-space modeling of beam-piezo system

In this section, we will deduce a theoretical model of the beam-piezo system based on the Euler-Bernoulli assumptions, see the discussion in Section 3.1. In addition, the free-free boundary condition means that there will be no bending moments or shear forces at both ends of the beam. Note finally that the vibration is generated by a force disturbance applied at one end of the beam as shown in Fig. 3.2. Based on these assumptions and observations, finite element modeling is performed and leads to a coupling equation (or governing equation) that describes the beam dynamics and the electromechanical coupling between the beam and the PZT [75, 103]. However, the dimension of this governing equation is too large and it takes the displacement vector as the variable which contains an infinite number of modes. Knowing that we only choose to control a certain number of modes, we then apply Modal Displacement Method which decomposes the governing equation according to modes so that we can ignore (truncate) most of the modes that are out of interest. This leads to a much simpler governing equation which takes the modal coordinate as variable and which allows us to control the chosen modes. The commercial software COMSOL (a finite element analysis, solver and simulation software) allows us to derive an expression of the governing equation reflecting the first several number (user-chosen) of modes. In our case, the resonance frequency of the maximum number of mode have to be larger than the maximum frequency of the disturbance (i.e. 3000 rad/s) while higher modes are truncated. The error introduced by the truncation is eliminated by performing Static correction. Damping effect has also to be added because we do not include damping effect in COMSOL. The dynamic (differential equation) of the measurement circuit (the electric circuit used to measure the

sensing voltage on the PZT pair) is also considered. For the purpose of reducing the vibration energy in the central zone (central energy), we deduce a computable expression of the central energy out of the velocities at a number of points in the central zone. The model of the beam-piezo system is finally built in form of state-space representation for the purpose of controller design.

4.1.1 Governing equation deduced with COMSOL

4.1.1.1 Finite Element Modeling

COMSOL performs a finite element modeling of the structure and discretizes it into multiple sections based on a standard 3D elements. In this way, we are able to consider the coupling between the beam and the piezoelectric patches. Each element contains multiple degrees of freedom (e.g. the displacements along x, y and z axis, etc). However, we only focuses on the displacement along z axis. The displacements along x and y axis are thus removed because they are not excited or coupled with those along z axis. Denote $z(x,t)$ the displacement field along z axis with x the position and t the time, the governing equation is given as follows[1]

$$\begin{bmatrix} \widetilde{M} & 0 \\ 0 & 0 \end{bmatrix} \begin{bmatrix} \ddot{z}(x,t) \\ \ddot{V}(t) \end{bmatrix} + \begin{bmatrix} \widetilde{K} & \widetilde{E} \\ -\widetilde{E}^T & R \end{bmatrix} \begin{bmatrix} z(x,t) \\ V(t) \end{bmatrix} = \begin{bmatrix} \widetilde{F} \cdot f(t) \\ Q(t) \end{bmatrix}, \tag{4.1}$$

where $\widetilde{M} \in \mathbb{R}^{N_e \times N_e}$ the mass matrix with N_e the number of nodes created by Finite Element Analysis, $\widetilde{K} \in \mathbb{R}^{N_e \times N_e}$ the stiffness matrix, $R = diag(r_1, r_2, \cdots, r_{N_p})$ the capacitance matrix with r_i the capacitance of the i^{th} PZT pair and N_p the total number of the PZT pairs[2], $\widetilde{F} \in \mathbb{R}^{N_e}$ the force vector and $\widetilde{E} \in \mathbb{R}^{N_e \times N_p}$ the matrix representing the electro-mechanical coupling between the beam and the PZT. The scalar $f(t)$ represents the force disturbance applied by the shaker. The vector $V(t) = [v_1(t), \cdots, v_{N_p}(t)]^T$ and $Q(t) = [q_1(t), \cdots, q_{N_p}(t)]^T$ represent respectively the voltage and the charge on all the PZT pairs on the beam.

[1] Details for the derivation of the governing equation can be found in [75, 103].

[2] In our case, the PZT pairs are numbered from 1 to 20, see Fig. 3.2, and thus $N_p = 20$

For the displacement filed $z(x,t)$, according to the modal superposition principle, we use the modal coordinate $\widetilde{\eta}(t)$ and the shape function $\widetilde{\varphi}(x)$ to describe $z(x,t)$ as follows:

$$z(x,t) = \sum_{j=1}^{\infty} \varphi_j(x) \cdot \eta_j(t) = \widetilde{\varphi}(x) \cdot \widetilde{\eta}(t), \tag{4.2}$$

where $\widetilde{\eta}(t) = [\eta_1(t), \cdots, \eta_\infty(t)]^T$ and $\widetilde{\varphi}(x) = [\varphi_1(x), \cdots, \varphi_\infty(x)]$ with $\eta_j(t)$ and φ_j respectively the modal coordinate and the mode shape of the j^{th} vibration mode. φ_j is the solution of the eigenvalue problem with the following form (when $V = 0$):

$$\widetilde{K}\varphi_j = \omega_j^2 \widetilde{M}\varphi_j,$$

where ω_j is the natural frequency of the j^{th} mode.

Eq. (4.1) has two disadvantages for control objective. First, it has a huge dimension as we obtain a large number of nodes from Finite Element Analysis[3], i.e. very large N_e. A complex model will lead to a complex controller while we need to find a simple controller. Second, the displacement $z(x,t)$ is considered as the sum of a large number of modes which means that the information of the modes is hidden implicitly in $z(x,t)$. As only a chosen number of modes over a specified frequency band will be controlled, it will be better if the information of modes can be explicitly presented in the governing equation. For these purposes, we here introduce the Modal Displacement Method which allows us to explicitly present the modes and also to reduce the dimension of the governing equation.

4.1.1.2 Modal decomposition and truncation — Modal Displacement Method

As explained above, there are two benefits of applying the Modal Displacement Method [27]. First, Eq. (4.1) can be transformed into a form where the information of modes is explicitly presented. Second, it allows us to strongly simplify the

[3]The mesh used in Finite Element Analysis should be fine enough to avoid convergence problem. Fine mesh implies a large number of nodes which leads to an equation of large dimension

governing equation. These are achieved by truncating the displacement $z(x,t)$: only keeping the lower order modes while neglecting the higher order mode[4].

We should first choose, according to the control objective, the maximum number of modes that needs to be kept[5], denoted N. Then, the displacement $z(x,t)$ is truncated from mode N, which implies the following approximation:

$$z(x,t) \approx \sum_{j=1}^{N} \varphi_j(x) \cdot \eta_j(t) = \varphi(x) \cdot \eta(t), \tag{4.3}$$

where $\eta(t) = [\eta_1(t), \cdots, \eta_N(t)]^T$ and $\varphi(x) = [\varphi_1(x), \cdots, \varphi_N(x)]$. Replacing the $z(x,t)$ in Eq. (4.1) by Eq. (4.3), we thus obtain a simpler truncated governing equation:

$$\begin{bmatrix} M_{mode} & 0 \\ 0 & 0 \end{bmatrix} \begin{bmatrix} \ddot{\eta}(t) \\ \ddot{V}(t) \end{bmatrix} + \begin{bmatrix} K_{mode} & E \\ -E^T & R \end{bmatrix} \begin{bmatrix} \eta(t) \\ V(t) \end{bmatrix} = \begin{bmatrix} F \cdot f(t) \\ Q(t) \end{bmatrix}, \tag{4.4}$$

where

$$\begin{gathered} M_{mode} = \varphi^T \widetilde{M} \varphi = diag(m_1, \cdots, m_N), \\ K_{mode} = \varphi^T \widetilde{K} \varphi = diag(k_1, \cdots, k_N), \\ E = \varphi^T \widetilde{E}, \ F = \varphi^T \widetilde{F}. \end{gathered}$$

Usually, we consider a normalized truncated model (Eq. (4.4)) where $m_i = 1$ for $i = 1 \cdots, N$, i.e. $M_{mode} = I$ (identity), and k_i will be the resonance frequency of the i^{th} mode, denoted ω_i for $i = 1, \cdots, N$, i.e. $K_{mode} = diag(\omega_1^2, \cdots, \omega_N^2)$.

Eq. (4.4) has the modal coordinate $\eta(t)$ as variable and the dimension depends on the choice of the maximum mode N, much smaller than N_e which is the number of nodes.

Remark. *The above steps will keep all the modes at lower frequencies*[6]*. However, in our case, the modes below* 600 *rad/s are out of interest (see Section 3.2)*

[4]The structural vibration is always dominated by the modes of lower order

[5]This is necessary because only a finite number of modes can be numerically solved

[6]Indeed, we can also truncate the lower frequency modes. Consequently, we have to correct the model to take into consideration this low frequency truncation. This will make the modeling procedure more complicated.

which can be neglected. Further reduction should thus be made. For this purpose, we propose the multi-variable model reduction method, see Section 4.3.

COMSOL is a very powerful numerical solver that allows us to perform the Finite Element Analysis and compute an expression of governing equations. It not only allows us to compute the parameters in Eq. (4.1) (i.e. $\widetilde{M}$, $\widetilde{K}$, $\widetilde{E}$, $\widetilde{F}$) which are the direct results of Finite Element Analysis, but is also capable of integrating the Modal Displacement Method (with a user chosen maximum mode N) and gives directly the parameters in Eq. (4.4) (i.e. normalized M_{mode}, K_{mode}, E and F) as well as the corresponding mode shape $\varphi(x)$ relating to the modal coordinate $\eta(t)$ for all position x. The capacitance matrix R can be directly measured from the setup or obtained from the model. However, it is then corrected to compensate the error introduced by this modal truncation as explained below.

4.1.1.3 Piezoelectric capacitance correction — Static correction

It should be noticed that the truncation will inevitably introduce static reduction error [104] into the system, which should be considered. For this purpose, we perform Static correction [28]. The ideal is that we try to modify the capacitance matrix R such that when the system is free from external constraints, i.e. $f(t) = 0$, the charge generated by a constant voltage, e.g. $V(t) = 1$, of the finite element model (Eq. (4.1)) and the truncated model (Eq. (4.4)) are the same. As the excitation voltage stays constant, there will be no dynamic deformation, which means that the derivative term in the governing equation is neglected. Thus, the finite element model gives:

$$\begin{bmatrix} \widetilde{K} & \widetilde{E} \\ -\widetilde{E}^T & R \end{bmatrix} \begin{bmatrix} z(x,t) \\ V(t) \end{bmatrix} = \begin{bmatrix} \widetilde{F} \cdot f(t) \\ Q(t) \end{bmatrix}, \tag{4.5}$$

and the truncated model gives:

$$\begin{bmatrix} K_{mode} & E \\ -E^T & R_c \end{bmatrix} \begin{bmatrix} \eta(t) \\ V(t) \end{bmatrix} = \begin{bmatrix} F \cdot f(t) \\ Q(t) \end{bmatrix}, \tag{4.6}$$

where R_c is the unknown to-be-corrected capacitance matrix. With $f(t) = 0$ and $V(t) = 1$, we thus have two expression of the charge $Q(t)$ which should be equal. Thus, R_c is given by:

$$R_c = diag(\widetilde{E}^T \widetilde{K}^{-1} \widetilde{E} + R - E^T K_{mode}^{-1} E), \tag{4.7}$$

where $diag(\cdot)$ means to keep the diagonal terms of a matrix while set all the other terms to zero. As we ignore the capacitance factor between different PZT pairs, R_c should thus be kept diagonal.

4.1.2 Damping effect

Here we add viscous damping into the governing equation as it was not introduced in COMSOL. The viscous damping corresponds to the first-order derivative term of dynamic equations. Thus, the governing equation of the beam-piezo system that contains the damping effect should be as follow (normalized governing equation after modal decomposition with corrected capacitance matrix):

$$\begin{bmatrix} I & 0 \\ 0 & 0 \end{bmatrix} \begin{bmatrix} \ddot{\eta}(t) \\ \ddot{V}(t) \end{bmatrix} + \begin{bmatrix} \mathcal{X}_{mode} & 0 \\ 0 & 0 \end{bmatrix} \begin{bmatrix} \dot{\eta}(t) \\ \dot{V}(t) \end{bmatrix} + \begin{bmatrix} K_{mode} & E \\ -E^T & R_c \end{bmatrix} \begin{bmatrix} \eta(t) \\ V(t) \end{bmatrix} = \begin{bmatrix} F \cdot f(t) \\ Q(t) \end{bmatrix}, \tag{4.8}$$

where $\mathcal{X}_{mode}$ denotes the damping term. There are several models for $\mathcal{X}_{mode}$. In order to keep the model as simple as possible, we choose the Rayleigh Damping model [105] that defines $\mathcal{X}_{mode}$ as:

$$\mathcal{X}_{mode} = \kappa_a I + \kappa_s K_{mode}, \tag{4.9}$$

where κ_a and κ_s are two damping constants. As we will see in the sequel, such a simple model will indeed be sufficient to represent the dynamics of the system[7].

[7]There exist more general methods such as a modal damping model where each mode has a single damping parameter. However, the model contains many modes. Using this general damping model will increase its complexity, especially for the model correction step.

4.1.3 Measurement circuit

Some PZT pairs will be chosen as sensors whose voltages will be measured by the controller and used to compute control signals. Physically, these sensing voltages are measured through a measurement circuit, see Fig. 4.1, where one PZT sensor is equivalent to the parallel connection of a charge generator and a capacitance. The controller, with internal resistance $1/Y$, will connect the sensor and thus form a closed-loop electric circuit. The voltage of the PZT sensor equals to the voltage applied on the internal resistance which is measured through a voltmeter inside the controller. According to Ohm's law, we have:

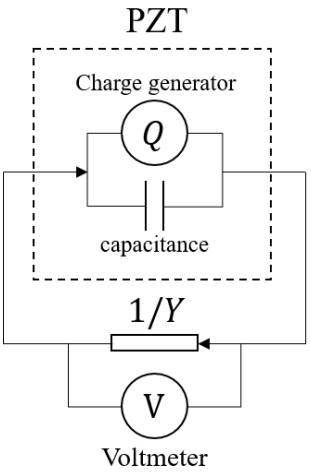

Figure 4.1: Measurement circuit

$$-Y_s V_s(t) = \dot{Q}_s, \tag{4.10}$$

where $V_s(t)$ and $Q_s(t)$ denote the voltage and charge vector of the PZT sensors. The diagonal matrix $Y_s = Y \cdot I_{N_s}$ is the impedance matrix of the controller where the scalar Y is the internal impedance[8] in each channel of the controller (supposed to be equal for different channels), N_s the total number of the chosen PZT sensors and I_{N_s} identity with dimension $N_s \times N_s$.

[8]The impedance is the inverse of the resistance. Normally, the internal resistance of a digital signal processor is between $100k$ $Ohms$ and 1 $MOhm$

4.1.4 Determination of the central energy

For the purpose of reducing the vibration energy (we only consider the kinetic energy) in the central zone, it is important to deduce an expression of the central energy using the variables of the above governing equation such that it can be constructed as an output of the state-space model. The kinetic central energy, denoted $E_{cent}(t)$, at time t is given by:

$$E_{cent}(t) = \frac{1}{2}\rho A_S \int_{x_1}^{x_2} \nu(x,t)^2 \, dx \tag{4.11}$$

where the interval (x_1, x_2) represents the location of the central zone, ρ the beam density, A_S the cross-section area. $\nu(x,t)$ is the vibration velocity for any location on the beam (thus also in the central zone) and using Eq. (4.3), we have:

$$\nu(x,t) = \dot{z}(x,t) \approx \varphi(x) \cdot \dot{\eta}(t). \tag{4.12}$$

If we assume a steady-state situation, the average central energy over time is given by:

$$\overline{E_{cent}} = \frac{1}{2}\rho A_S \lim_{T\to\infty} \frac{1}{T} \int_0^T \left(\int_{L_1}^{L_2} \nu(x,t)^2 \, dx \right) dt \tag{4.13}$$

Numerically, we will approximate the above integration of $\nu(x,t)$ over an area by the sum of velocity square at several chosen locations (nodes) x_i $(i = 1, \cdots, N_z)$ equally distributed in the central zone of the beam:

$$\int_{L_1}^{L_2} \nu(x,t)^2 dx \approx \nu_{node}(t)^T \cdot \nu_{node}(t) \cdot \Delta x, \tag{4.14}$$

where Δx denotes the distance between two nodes and $\nu_{node}(t)$ the velocity vector of the chosen nodes with:

$$\begin{gathered} \nu_{node}(t) = [\nu_{node_1}(t), \nu_{node_2}(t), \cdots, \nu_{node_{N_z}}(t)]^T, \\ \nu_{node_i} = \varphi_{node_i} \cdot \dot{\eta}(t) = \varphi(x_i) \cdot \dot{\eta}(t). \end{gathered} \tag{4.15}$$

By ignoring the scalar $\frac{1}{2}\rho A_S$ in Eq. (4.13), we define the so-called average proportional central energy $\overline{E^p_{cent}}$ as follow:

$$\overline{E^p_{cent}} = \lim_{T\to\infty} \frac{1}{T} \int_0^T \nu_{node}(t)^T \cdot \nu_{node}(t) \cdot dt \tag{4.16}$$

It is clear that $\overline{E_{cent}}$ and $\overline{E^p_{cent}}$ are (approximately) proportional. Thus, we can also conclude that reducing $\overline{E^p_{cent}}$ implies reducing $\overline{E_{cent}}$. Moreover, if we define the PSD of the disturbance f as $|L_f(j\omega)|^2$ with a transfer function $L_f(s)$, we can use Parseval's theorem to give the following computable expression of $\overline{E^p_{cent}}$:

$$\begin{aligned} \overline{E^p_{cent}} &= \frac{1}{2\pi} \int_{-\infty}^{+\infty} H^*(j\omega) H(j\omega) |L_f(j\omega)|^2 \, d\omega \\ &= \left\| H(s) L_f(s) \right\|_2^2 \end{aligned} \tag{4.17}$$

where $H(s)$ is the vector of transfer functions relating the force f and the vector ν_{node}.

It should be noted that the controller is computed using H_∞ control. It is thus the H_∞ norm of $H(s)L_f(s)$, $||HL_f||_\infty$, that is directly minimized. However, for our particular system, the reduction of $||HL_f||_\infty$ norm also leads to the reduction of $||HL_f||_2$. The main reason that we use H_∞ control is that it allows us to apply the Small Gain Theory in order to guarantee the robust stability which is to avoid the so-called spill-over problem. These considerations will be discussed later in Section 5.

4.1.5 State-space representation

Using the above equations, we can deduce the state-space representation of the beam-piezo system. Regrouping Eq. (4.8), Eq. (4.9), Eq. (4.10) and Eq. (4.15), we obtain a state-space model having disturbance force $f(t)$ and actuation voltage vector $V_a(t)$ (with dimension N_a) as inputs, sensing voltage vector $V_s(t)$ and velocity vector $\nu_{node}(t)$ as outputs and $x(t) = [\eta(t), \dot{\eta}(t), V_s(t)]^T$ as state vector:

$$\begin{cases} \dot{x}(t) = A \cdot x(t) + B_f \cdot f(t) + B_a \cdot V_a(t) \\ \nu_{node}(t) = C_e \cdot x(t) \\ V_s(t) = C_s \cdot x(t) \end{cases} \tag{4.18}$$

with

$$A = \begin{bmatrix} 0 & I & 0 \\ -K_{mode} & -\kappa_a I - \kappa_s K_{mode} & -E_s \\ 0 & R_s^{-1} \cdot E_s^T & -R_s^{-1} \cdot Y_s \end{bmatrix}, \quad B_a = \begin{bmatrix} 0 \\ -E_a \\ 0 \end{bmatrix}, \quad B_f = \begin{bmatrix} 0 \\ F \\ 0 \end{bmatrix}$$
$$C_s = \begin{bmatrix} 0 & 0 & I \end{bmatrix}, \quad C_e = \varphi_{node} \cdot \begin{bmatrix} 0 & I & 0 \end{bmatrix}, \quad \varphi_{node} = [\varphi_{node_1}^T, \varphi_{node_2}^T, \cdots, \varphi_{node_{N_z}}^T]^T$$

where E_s and E_a are two matrices (representing the electro-mechanical coupling between the piezo and the beam) respectively composed of the columns of the matrix E (see Eq. (4.8)) that correspond to V_s and V_a, R_s the capacitance matrix (diagonal) composed of the elements in R_c that relates to V_s.

For further reference, let us introduce the notation $G^{full}(s)$ for the transfer function matrix relating the inputs and outputs of the above model:

$$\begin{bmatrix} \nu_{node}(s) \\ V_s(s) \end{bmatrix} = G^{full}(s) \begin{bmatrix} f(s) \\ V_a(s) \end{bmatrix} = \left[\begin{array}{c|c} G^{full}_{f \to \nu_{node}} & G^{full}_{V_a \to \nu_{node}} \\ \hline G^{full}_{f \to V_s} & G^{full}_{V_a \to V_s} \end{array}\right] \begin{bmatrix} f(s) \\ V_a(s) \end{bmatrix} \tag{4.19}$$

An expression for $G^{full}(s)$ can easily be derived by applying the Laplace transform on the state-space model (4.18).

As discussed in Section 4.1.4, the central energy is computable using the velocity vector ν_{node}, see Eq. (4.17). In the open-loop situation, $H(s)$ is equal to $G^{full}_{f \to \nu_{node}}(s)$. In the closed-loop situation i.e. when the controller $K(s)$ is active, $H(s)$ is then equal to the closed-loop transfer vector between f and ν_{node} that will be denoted as $T^{full}_{f \to \nu_{node}}(s)$. This closed-loop transfer vector can be easily

determined by adding the relation[9] $V_a(s) = K(s)V_s(s)$ to Eq. (4.19), yielding: $\nu_{node}(s) = T^{full}_{f\to\nu_{node}}(s)f(s)$.

It is important to note that COMSOL provides us with a first estimate for all parameters[10] in the state-space model (4.18). In Section 4.2, we will nevertheless show that the values of some of these parameters will have to be refined using data collected on the system for the model described by the above equations to be a good representation of the actual dynamics of the system.

4.1.6 Application to the experimental setup

Now let us apply the above modeling procedure to the beam-piezo system representing the experimental setup. According to the control objectives described in Section 3.2, the frequency band of the considered force disturbance f is $(600, 3000)$ rad/s where there are 11 modes for our specific structure. Thus, the maximum mode N is chosen to be 20 because its resonance frequency ω_{20} is slightly larger than 3000 rad/s. As it has been discussed in Section 3.3, in order to effectively control these 11 modes with a least number of PZT pairs, we choose the 10^{th} and 16^{th} PZT pairs as actuators, the 5^{th} and 11^{th} PZT pairs as sensors. Thus, V_a and V_s will respectively pertain to the 10^{th}, 16^{th} PZT pairs and the 5^{th}, 11^{th} PZT pairs (i.e. $N_a = N_s = 2$). Consequently, the state vector x in the derived state-space model $G^{full}(\theta_{init})$ (see, Eq. (4.18)) is of dimension 42, where θ_{init} denotes the first estimate of its parameters using COMSOL and classical tests. For the central energy, we choose the dimension of the velocity vector ν_{node} to be 19 (i.e. $N_z = 19$).

To validate the state-space model, we compare the frequency response of $G^{full}(\theta_{init})$ and the one of the experimental setup. A very accurate non-parametric estimate of the latter can be derived using a frequency analyzer (an *HP 35652B* in our case). Such a frequency analyzer deduces an estimate of the frequency response of a SISO transfer function by averaging out the ratio of the cross-spectrum

[9] Note that, in Section 5, the notation $K(s)$ will in fact be used for the controller before amplification.

[10] The first estimates for κ_a, κ_s and Y_s are in fact not determined by COMSOL, but can instead be derived using measurement devices (for Y_s) and the half-power method [106] (for κ_a, κ_s).

between input and output measurements over the auto-spectrum of input measurement. In Fig. 4.2 (where we focus on the dynamics between V_a and V_s), we observe a large discrepancy between this accurate estimate of the frequency response of the setup (in blue) and the frequency response of the state-space model $G^{full}(\theta_{init})$ (in yellow). Such a discrepancy is also visible for other dynamics of the system. From the comparison, we find that COMSOL is indeed able to give a reasonable first estimate of the parameters for G^{full}. However, the accuracy is far from satisfactory. In order to improve the accuracy of the model parameters, we introduce Grey-box identification technique, which is detailed in Section 4.2.

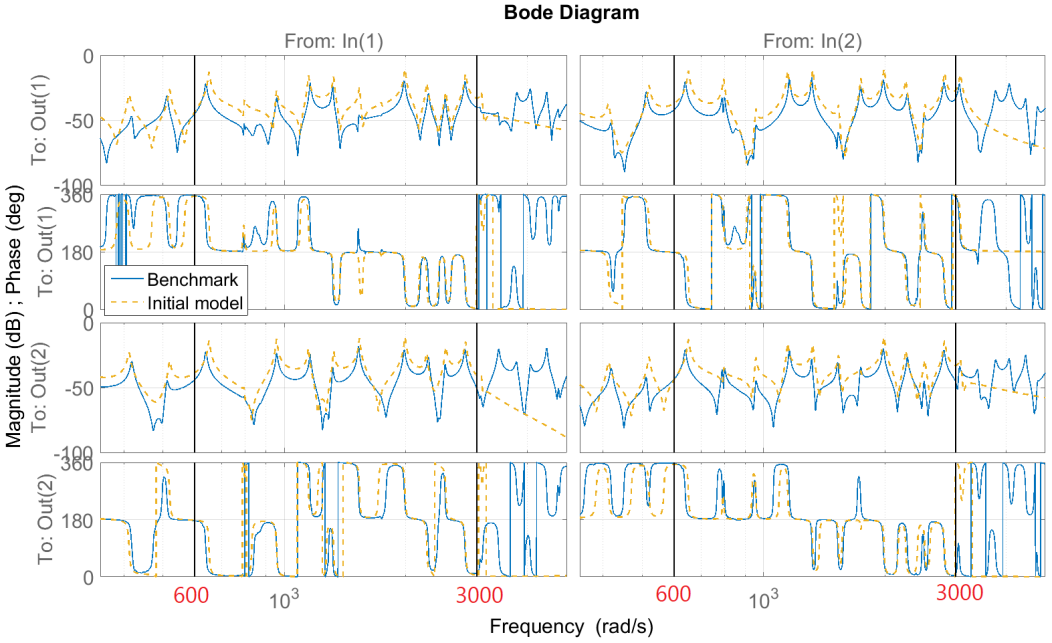

Figure 4.2: Comparison of the frequency response from V_a to V_s: non-parametric estimate obtained with the frequency analyzer (blue) and initial model $G^{full}_{V_a \to V_s}(\theta_{init})$ (yellow)

4.2 Model improvement using Grey-box identification

In Section 4.1, a physical model has been derived for the to-be-controlled system under the form of the state-space model (4.18) relating the system inputs (the disturbance force $f(t)$ and the actuator voltage vector $V_a(t)$) and the system outputs (the sensor vector $V_s(t)$ and the vector $\nu_{node}(t)$ containing the velocity

at a number of points in the central zone). As already mentioned, this physical model is parameterized by a number of physical parameters (i.e. K_{mode}, R_s, Y_s, κ_a, κ_s, E_a, E_s, F and φ_{node}) for which a first estimate can be derived using COMSOL or classical tests. The first estimate is relatively accurate for Y_s and R_s. However, the first estimate is much cruder for K_{mode}, κ_a, κ_s, E_a, E_s, F and φ_{node}. According to the discussion in Section 4.1.1.2, for a normalized governing equation, $K_{mode} = diag(\omega_1^2, \cdots, \omega_N^2)$ where ω_i is exactly the resonance frequency of the i^{th} mode, which corresponds to the location of the i^{th} peak in the frequency response (see for example the model response shown in Fig. 4.2). The discrepancies at peak locations can thus be easily corrected through replacing the elements of K_{mode} by the correct value of ω_i obtained from the non parametric estimate using a frequency analyzer (i.e. the benchmark in Fig. 4.2). For the rest of the parameters (i.e. κ_a, κ_s, E_a, E_s, F and φ_{node}), we will introduce Grey-box identification which allows us to correct them using the measurement data from the actual setup.

4.2.1 Grey-box identification theory

Grey-box identification is a data-based optimization algorithm. It allows us to use discrete-time sampling data to optimize the parameters of a continuous model with a predefined structure, for example the state-space representation [29]. It performs iterations based on the measured input and output data to find the best group of parameters with which the discrete-time output predictions of the optimized continuous model fit best the measured output with respect to the same input.

Now we consider a real continuous system $G_{reel}(s)$ and a candidate physical model $G_{mod}(s, \theta)$ with physic parameters θ. $G_{reel}(z)$ and $G_{mod}(z, \hat{\theta})$ are their corresponding discretizations. $\hat{\theta}$ is the estimator composed of all the parameters to be optimized. The optimization problem is shown in Fig. 4.3.

A certain $\hat{\theta}$ determines a candidate model. $y(t)$ and $y_{mod}(t)$ are respectively the output of the real system G_{reel} and of the candidate model G_{mod} with respect to the same input $u(t)$. Note that $u(t)$ and $y(t)$ must be measurable such that they can be recorded for computation. The error between $y(t)$ and $y_{mod}(t)$ is:

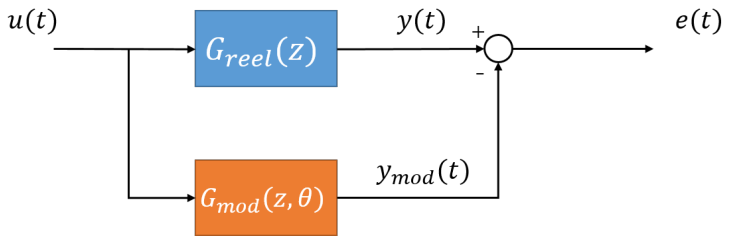

Figure 4.3: Grey-box optimization problem

$$e(t) = y(t) - y_{mod}(t) \tag{4.20}$$

The optimum solution is defined as $\hat{\theta}_{opt}$ that minimizes the average power of the error $e(t)$:

$$\begin{aligned} \hat{\theta}_{opt} &= \underset{\hat{\theta}}{argmin} \frac{1}{N} \sum_{i=1}^{N} e(t_i)^2 \\ &= \underset{\hat{\theta}}{argmin} \frac{1}{N} \sum_{i=1}^{N} \left(y(t_i) - y_{mod}(t_i)\right)^2 \\ &= \underset{\hat{\theta}}{argmin} \frac{1}{N} \sum_{i=1}^{N} \left(y(t_i) - G_{mod}(z, \hat{\theta}) u(t_i)\right)^2 \end{aligned} \tag{4.21}$$

Remark. *The expression $G_{mod}(z, \hat{\theta})u(t_i)$ is not very rigorous. It is just a way to represent the output of $G_{mod}(z, \hat{\theta})$ with respect to $u(t)$ at the instant t_i.*

Then the optimum solution θ_{opt} for $G_{mod}(s, \theta)$ could thus be obtained from transforming $G_{mode}(z, \hat{\theta}_{opt})$ into a continuous time system. There exist functions in Matlab that allows us to perform Grey-box identification directly in continuous time. The optimal solution is computed by iterations so that an initial value of the to-be-found parameters should be first given. For complex systems, the optimization criterion is always non-linear in θ. Consequently, a reasonable initialization is necessary.

4.2.2 Grey-box optimization of the beam-piezo system model

Grey-box identification is applied on the state-space model (4.18) to tune κ_a, κ_s, E_a, E_s, F and φ_{node}, which are gathered in a vector θ. We denote by θ_{init} its first estimate. The vector θ will be further divided in three terms $\theta^T = (\theta_1^T, \theta_2^T, \theta_3^T)$: θ_1 contains the scalar parameters κ_a, κ_s and the elements of the matrices E_a and E_s, θ_2 contains the elements of the vector F and θ_3 contains the elements in the matrix φ_{node}. Grey-box identification will be used to obtain a more accurate estimate of the unknown parameter vector θ, denoted $\theta_{id}^T = (\theta_{1,id}^T, \theta_{2,id}^T, \theta_{3,id}^T)$, which is initialized by $\theta_{init}^T = (\theta_{1,init}^T, \theta_{2,init}^T, \theta_{3,init}^T)$. For this purpose, experiments will be performed on the experimental setup and the corresponding input-output data will be collected. Due to the particular structure of the physical model (4.18), three different types of experiments will be performed and this will allow one to successively deduce accurate estimates for θ_1, θ_2 and finally θ_3. These separate identification experiments have the advantage to reduce the complexity of the identification criteria.

Experiment 1.

Let us first notice that, when f is forced to zero, the relation between V_a and V_s is only a function of the parameter vector θ_1 (see Eq. (4.18)). An experiment is performed on the experimental setup with $f = 0$ and with independent white noise signals applied to both actuators (i.e. V_a). Denote $V_{s,m_1}(t = nT_s)$ with $n = 1, 2, \cdots, N_d$ the corresponding output voltages measured at a sampling rate T_s after the application of an anti-aliasing filter. A more accurate estimate of θ_1 can then be deduced by solving the following output error identification criterion:

$$\theta_{1,id} = \arg\min_{\theta_1} \frac{1}{N_d} \sum_{n=1}^{N_d} \left(V_{s,m_1}(nT_s) - \hat{V}_s(nT_s, \theta_1)\right)^T \left(V_{s,m_1}(nT_s) - \hat{V}_s(nT_s, \theta_1)\right),$$

where $\hat{V}_s(nT_s, \theta_1)$ is the output voltage $V_s(t)$ predicted by Eq. (4.18) at $t = nT_s$ for an arbitrary value of θ_1 and for the input $V_a(t)$ applied during the experiment when $f(t) = 0$.

This criterion is of course nonlinear in θ_1. Consequently, the determination of $\theta_{1,id}$ requires an appropriate initialization which in our case can be taken equal to the first estimate of θ_1, i.e. $\theta_{1,init}$.

Experiment 2.

Seen from Eq. (4.18), when $V_a = 0$, the relation between f and V_s is function of θ_1 and θ_2. Since an accurate estimate of θ_1 has been determined in the first experiment (i.e. $\theta_{1,id}$), the relation between f and V_s can be reduced to a model which is only function of θ_2. An experiment is therefore performed on the experimental setup with $V_a = 0$ and with a force disturbance corresponding to a white noise signal. Denote $V_{s,m_2}(t = nT_s)$ with $n = 1, 2, \cdots, N_d$ the corresponding output voltages measured at a sampling rate T_s after the application of an anti-aliasing filter. A more accurate estimate of θ_2 can then be deduced by solving the output error identification criterion:

$$\theta_{2,id} = \arg\min_{\theta_2} \frac{1}{N_d} \sum_{n=1}^{N_d} \Big(V_{s,m_2}(nT_s) - \tilde{V}_s(nT_s, \theta_2, \theta_{1,id})\Big)^T \Big(V_{s,m_2}(nT_s) - \tilde{V}_s(nT_s, \theta_2, \theta_{1,id})\Big),$$

where $\tilde{V}_s(nT_s, \theta_2, \theta_{1,id})$ is the output voltage $V_s(t)$ predicted by Eq. (4.18) at $t = nT_s$ for an arbitrary value of θ_2 and for $\theta_1 = \theta_{1,id}$ and for the applied input force $f(t)$ when $V_a(t) = 0$.

This criterion is of course nonlinear in θ_2, but it can be initialized with the first estimate of θ_2 i.e. $\theta_{2,init}$.

Experiment 3.

Notice that the relation between f and ν_{node} is function of θ_1, θ_2 and θ_3 and that an accurate estimate of θ_1 and θ_2 has been deduced via **Experiments 1** and **2**. Consequently, using a similar approach as in **Experiment 2**, an estimate of θ_3 i.e. $\theta_{3,id}$ can be deduced by applying a white noise signal at the input $f(t)$ with $V_a(t) = 0$ and by measuring $v_{node_i}(t)$ $(i = 1, 2, \cdots, N_z)$ using a laser velocimeter. The laser velocimeter is necessary to measure $v_{node_i}(t)$ since there is no piezo-patches in the central zone[11]. In fact, since a laser velocimeter is only able to

[11]The fact that we can refine the parameter vector θ_3 using data collected from this laser velocimeter is the main reason for our choice to use ν_{node} as the physical signal to evaluate the central energy. Other approache such as the one in [107] does indeed not have this advantage.

measure the velocity of one point v_{node_i}, the experiment thus has to be repeated N_z times and each of these N_z experiments allows us to deduce a part of $\theta_{3,id}$ (i.e. the part containing the parameters in $\varphi_{node_i}, i = 1, 2, \cdots, N_z$).

The approach presented above allows to derive a model $G^{full}(\theta_{id})$ of the to-be-controlled system that is much more accurate than the model corresponding to θ_{init} (i.e. the model deduced by COMSOL). The improvement will be illustrated in Section 4.2.3 by comparing the frequency response of the parametric model $G^{full}(\theta_{id})$ with an accurate non-parametric estimate of the same response.

Remark. *In fact, for* **Experiment 3**, *it is also possible to apply a white noise at the actuators V_a with $f(t) = 0$. However, the dynamic between f and ν_{node} is related to the central energy which is thus more important than that between V_a and ν_{node}. For all these 3 experiments, note also that before proceeding to the identification of the parameter vector in each of them, the collected data can be pre-filtered using a band-pass filter focusing on the frequency band of interest.*

4.2.3 Application

Now, we will perform Grey-box identification to the state-space model (4.18) obtained in Section 4.1.6, i.e. $G^{full}(\theta_{init})$, using the measurement data collected from the actual setup. For data collection, we will perform the 3 experiments explained in Section 4.2.2. For **Experiment 2** and **3**, we will use the same frequency analyzer (i.e. *HP 35652B*) to excite the system and to record the excitation/response as the input/output data used for identification. In particular, the disturbance is measured through a force sensor (a *PCB 288D01*) and the velocity is sampled through a laser velocimeter (a *Polytec CLV-3D*). However for **Experiment 1**, particular considerations is taken in order to obtain a model close to the reality as much as possible because the accuracy of the response between the actuators and the sensors relates most closely to the final control effect in terms of stability and performance. This is explained as follows.

As presented in Section 3.3, for centralized control, we will use a digital control board (see Table 3.2 for its type) to implement the designed model-based controller. Two extra anti-aliasing filters are used to sample the output voltages of the 5^{th} and 11^{th} PZT pairs (i.e. V_s), and two power amplifiers are used to send power to the 10^{th} and 16^{th} PZT pairs (i.e. V_a), see Fig. 3.5. Therefore

in reality, there are several control devices (hardware) in the control loop between the designed model-based controller (i.e. $K(s)$) and the PZT pairs (i.e. $G^{full}_{V_a \to V_s}(s)$): extra anti-aliasing filters, internal DAC/ADC cards of the control board and power amplifiers. As mentioned at the beginning of this chapter and we will also see in Section 5 that the effects of these devices are simply considered as constant gains or pure time delay, which is of course the ideal case. However in reality, these devices may have some uncertainties and will possibly introduce other unexpected dynamics into the control loop, although the effect may be very small. As a consequence, for identification purpose, we will directly use the control board (instead of using the frequency analyzer) to excite the system and collect the excitation and the response. We will record the actual digital signals (independent white noise excitation) that enter the DAC cards of the control board and the direct sampling from its ADC cards (response) as inputs and outputs data used for identification. The benefit is that even though these control devices indeed introduce little unexpected dynamics into the control loop, we are able to integrate them into the state-space model (i.e. $G^{full}_{V_a \to V_s}$) by finding proper parameters (i.e. $\theta_{1,id}$) such that it is reasonable to only consider the effects of these control devices as constant gains or pure time delay.

Note also that we mainly focus on the response in $(600, 3000)$ rad/s. Thus, all the input-output data sets have been pre-filtered by a band-pass filter focusing on this frequency band[12].

Following the above procedure, we finally obtain an identified model $G^{full}(\theta_{id})$. In order to illustrate the improvement of the model accuracy, here we show three figures of comparison between different responses of the benchmark (the accurate non-parametric estimate using the frequency analyzer) in solid blue, of $G^{full}(\theta_{init})$ in dashed yellow and of $G^{full}(\theta_{id})$ in dotted red. Fig. 4.4 shows the frequency response between V_a and V_s (i.e. $G^{full}_{V_a \to V_s}$, result of **Experiment 1**). Fig. 4.5 shows the frequency response between f and V_s (i.e. $G^{full}_{f \to V_s}$, result of **Experiment 2**). Fig. 4.6 shows the singular value of the transfer function vector between f and ν_{node} (i.e. $G^{full}_{f \to \nu_{node}}$, result of **Experiment 3**). As seen from these 3 figures, we can conclude that Grey-box identification indeed greatly improve the model accuracy and gives us a much better model $G^{full}(\theta_{id})$. However, we

[12]For the identification of $G^{full}_{V_a \to V_s}$, the pass-band of the pre-filtering is in fact much larger than $(600, 3000\ rad/s)$ for the purpose of keeping as many dynamics as possible because $G^{full}_{V_a \to V_s}$ is actually a reference for verifying the robust stability.

still find relatively big discrepancies[13] in $G^{full}_{f\to\nu_{node}}$ (see Fig. 4.6). It seems that the overall magnitude of $G^{full}_{f\to\nu_{node}}(\theta_{id})$ is lower than the benchmark. However, in our case, this is not an issue because the response between f and ν_{node} somehow reflects the central energy (see Eq. (4.17)) and we mainly focus on its reduction rate instead of its actual value. Besides, this response is not as important as the response between V_a and V_s because it is not in the control loop and has no effect on the closed-loop stability. Some discrepancy like this is totally tolerable.

In conclusion, the identified model $G^{full}(\theta_{id})$ is a good representation of the actual setup. However, we will not directly use $G^{full}(\theta_{id})$ to design the controller because it still contains many modes outside $(600, 3000)$ rad/s. Therefore, model reduction step is necessary to simplify $G^{full}(\theta_{id})$ for the purpose of designing a simpler controller.

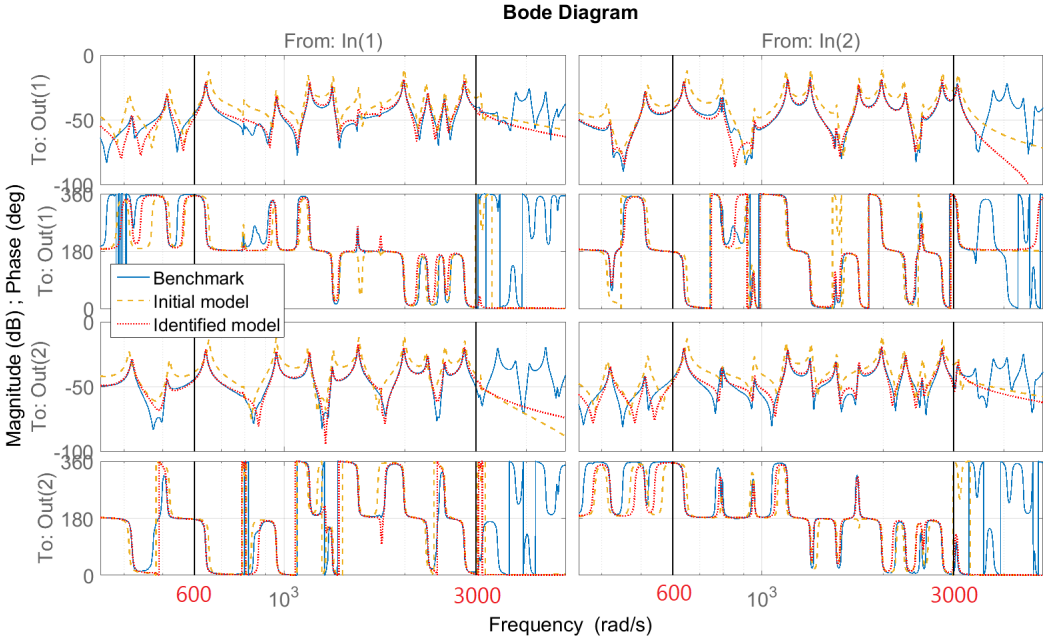

Figure 4.4: Frequency response: Benchmark (solid blue) vs $G^{full}_{V_a\to V_s}(\theta_{init})$ (dashed yellow) vs $G^{full}_{V_a\to V_s}(\theta_{id})$ (dotted red)

[13]To measure the velocities at different points, we have to move the laser velocimeter to each point by hand which will inevitably introduces error between the actual measuring position and the coordinate in the model. Thus, we may not find a perfect match between the test and the model

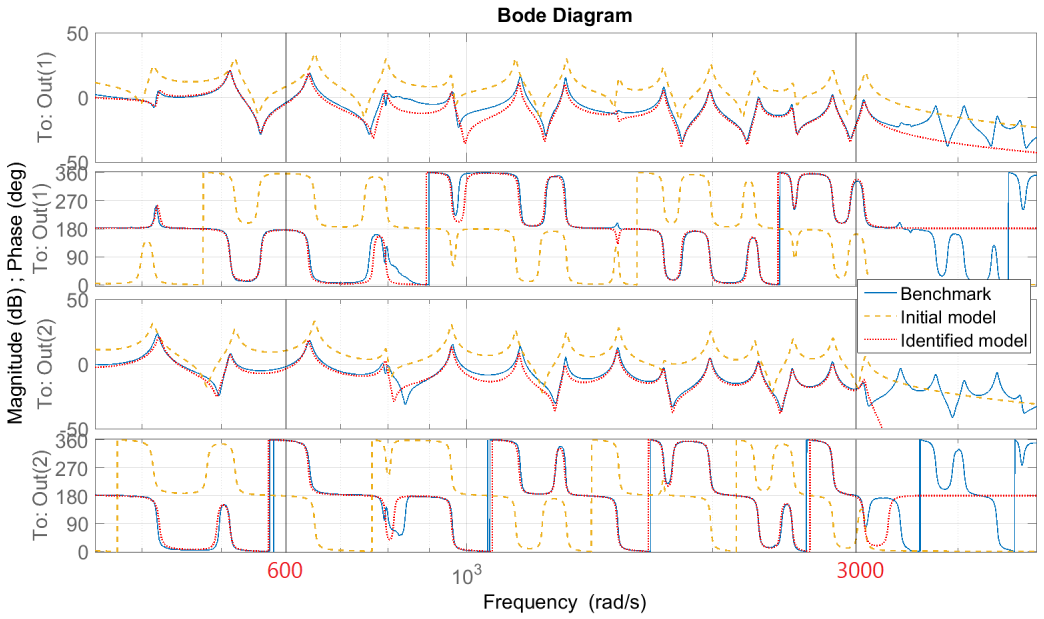

Figure 4.5: Frequency response: Benchmark (solid blue) vs $G^{full}_{f\to V_s}(\theta_{init})$ (dashed yellow) vs $G^{full}_{f\to V_s}(\theta_{id})$ (dotted red)

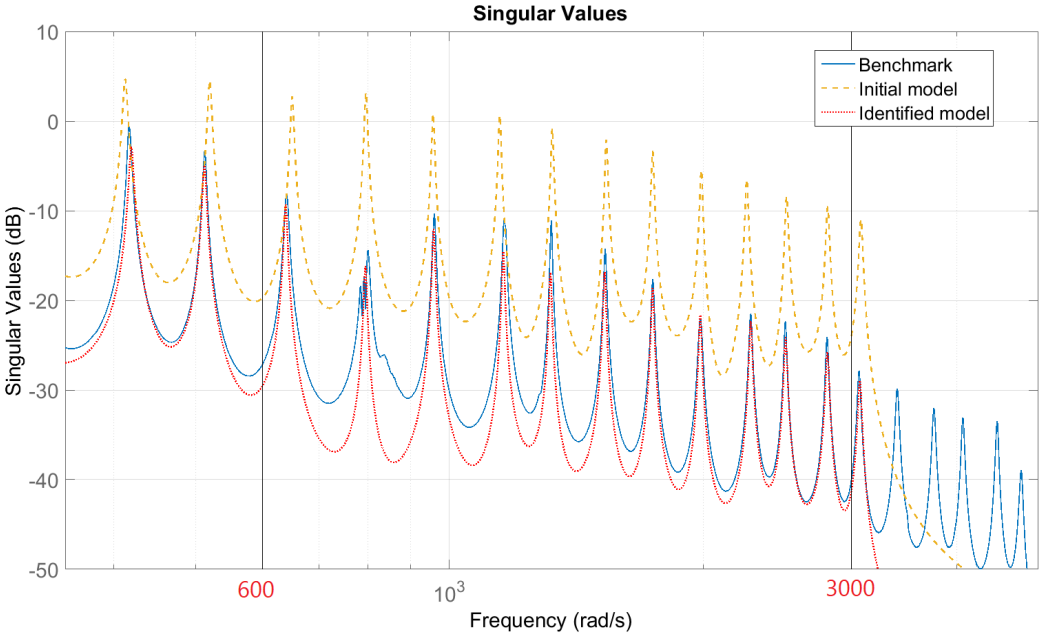

Figure 4.6: Frequency response: Benchmark (solid blue) vs $G^{full}_{f\to \nu_{node}}(\theta_{init})$ (dashed yellow) vs $G^{full}_{f\to \nu_{node}}(\theta_{id})$ (dotted red)

4.3 Multi-variable model reduction

The identified model $G^{full}(\theta_{id})$, the so-called full-order model, contains the modes outside the frequency band of interest, i.e. $(600, 3000)\ rad/s$ as we only truncate high frequency modes using Modal displacement Method (see Section 4.1.1). A model with high order will lead to a complex H_∞ controller. We thus need a low-order model which is close to the dynamics of $G^{full}(\theta_{id})$ only in $(600, 3000)\ rad/s$ while all the dynamics outside this frequency band should be ignored. This is not only for the resonances, but also the anti-resonances. Both are indeed very important for control as evidenced in [79]. Thus, model reduction technique is needed.

4.3.1 Overview of model reduction methods for mechanical structures

An actual mechanical structure has an infinite number of physical degree of freedom (DOF) and dimension. Finite Element Modeling (FEM) is always applied to model such a system by discretizing the structure into sections which gives a mathematical expression with finite DOF and very large dimension. Then, model reduction method, such as the Modal Displacement Method, is necessarily applied to reduce the complexity (size) of the model directly obtained from FEM. Except for Modal Displacement Method, there exist several other methods for the reduction of mechanical structure models. For example the methods based on the Petrov-Galerkin Projection [108] which performs base change of the initial state-space model using two modeling subspaces. There are different ways to construct such subspaces which leads to different model reduction method. For example the Krylov Subspace Method [52, 109, 110] which consider the Taylor Series Expansion of the transfer fucntion around a reference frequency. The coefficients of the Taylor Expansion are constructed using Krylov Subspace. Rational Interpolation [111, 112] is another Petrov-Galerkin Projection based method that approximates the initial model with respect to the H_∞ or H_2 norm around a reference frequency. Balanced Truncation [34, 35] is a common used model reduction method in the field of systems and control and could also be applied on mechanical structures, see [27, 108]. In this method, the initial model is first transformed into a so-called balanced realization and then the states that

have little contribution to the input-output behavior are truncated. There also exists a so-called the Hybrid Method [113] which is the combination of the Krylov Subspace Method and the Balanced Truncation. Rayleigh–Ritz method [53, 114] is particularly used to simplify the eigenfunction relating to the structure which makes it easier to be solved. However, the above mentioned methods have some limitations. First, some reduction aims at simplifying the computation of eigenvalue problems instead of approximating the input-output behavior of the system, for example the Rayleigh–Ritz method. Second, some of them are indeed able to approximate the input-output behavior with less DOF and smaller dimension, for example the Model Displacement Method and Balanced Truncation. However, they do not allow us to flexibly specify a certain frequency band which is the most important point in our case. Krylov Subspace Method and Rational Interpolation only focus on one reference frequency instead of a frequency band.

For our purpose, more powerful model reduction methods must be investigated in the field of systems and control which allows us to approximate the input-output behavior of the initial model (especially for the frequency response) over a specified frequency band. Many such methods can be found in [54]. The general idea is to find a reduced model that minimizes different types of norm of the error between the initial model and the reduced model. Different choices for the error are possible according to the control objective. Most importantly, these methods allow us to obtain a reduced model whose frequency response (at both resonances and anti-resonances) is close to the initial model as much as possible over a specified frequency band. As it will be discussed in the sequel, in order to satisfy the robust stability criterion, we will choose a particular type of error to minimize. However, the minimization of this particular error has not been discussed in [54]. Thus, we have to develop a new method aiming at finding a reduced model that minimizes this particular error following similar procedure proposed by [54]. The principle of our method as well as our choice for the error is explained in the sequel.

4.3.2 The proposed method

Consider a full-order LTI model G that contains dynamics outside of the frequency band of interest Ω. Our objective is to obtain a reduced-order model G_r that is close to G only in Ω. Our method has two steps. Knowing that

the dynamics of a system is characterized by its poles, having dynamics outside the frequency band of interest means having poles outside this frequency band. Therefore, in the first step, we will truncate the poles outside Ω which allows us to obtain a reduced-order model G_r that keeps well the resonances of G in Ω while no dynamics outside Ω. However, the truncation will introduce error in the frequency response mainly at anti-resonances which means that such a G_r may not be close enough to G in Ω. Thus, for the second step, we will modify some of the state matrices of G_r aiming at minimizing a particularly chosen error between G and G_r for all the frequencies in Ω. These two steps are detailed in the following sections.

4.3.3 Modal form truncation

The first step that we will call Modal Form Truncation (MFT) is actually an application of the Aggregation Technique [30] which allows us to eliminate the poles that are out of interest.

Denote the full-order model $G(A, B, C, D)$ in the following shorthand for state-space representation:

$$G = \left[\begin{array}{c|c} A & B \\ \hline C & D \end{array}\right] \tag{4.22}$$

with order n and $\Lambda(A)$ the set of eigenvalues of A which are also the poles of G.

First, the poles of G can be presented independently through base change which results in the so-called modal form, equivalently named the Diagonal Canonical Form in [115]. The modal form of G in the shorthand for state-space representation is as follows:

$$G = \left[\begin{array}{c|c} \hat{A} & \hat{B} \\ \hline \hat{C} & \hat{D} \end{array}\right] = \left[\begin{array}{ccccccc|c} \hat{A}_1 & & & & & & & \hat{B}_1 \\ & \ddots & & & & & & \vdots \\ \hdashline & & \hat{A}_p & & & & & \hat{B}_p \\ & & & \ddots & & & & \vdots \\ & & & & \hat{A}_q & & & \hat{B}_q \\ \hdashline & & & & & \ddots & & \vdots \\ & & & & & & \hat{A}_n & \hat{B}_n \\ \hline \hat{C}_1 & \cdots & \hat{C}_p & \cdots & \hat{C}_q & \cdots & \hat{C}_n & \hat{D} \end{array}\right] \tag{4.23}$$

where the dynamic matrix $\hat{A}$ is block-diagonal and $\Lambda(\hat{A}) = \Lambda(A)$. Each block $\hat{A}_i$ for $i = 1, 2, \cdots, n$ is either a 1×1 scalar or a 2×2 matrix. These blocks are in an increasing order of the corresponding eigenvalue modulus.

Define the frequency band of interest Ω as $\Omega = \{\omega | 0 < \underline{\omega} \leqslant \omega \leqslant \overline{\omega}\}$. Ω is of course covered by the pass-band of G. Denote $\hat{A}_j$ for $j = p, \cdots, q$ with $1 \leqslant p < q \leqslant n$ such that $\forall \lambda \in \Lambda(\hat{A}_j), |\lambda| \in \Omega$. Thus, $\{\lambda | \lambda = \Lambda(\hat{A}_j), j = p, \cdots, q\}$ should be the set of poles to be kept in the reduced-order model. The reduced-order model $G_r(A_r, B_r, C_r, D_r)$ is therefore obtained by truncating $G(\hat{A}, \hat{B}, \hat{C}, \hat{D})$ as illustrated by the dashed lines in Eq. (4.23) which gives:

$$G_r = \left[\begin{array}{c|c} A_r & B_r \\ \hline C_r & D_r \end{array}\right] = \left[\begin{array}{ccc|c} \hat{A}_p & & & \hat{B}_p \\ & \ddots & & \vdots \\ & & \hat{A}_q & \hat{B}_q \\ \hline \hat{C}_p & \cdots & \hat{C}_q & \hat{D} \end{array}\right] \tag{4.24}$$

The model G_r has lower order as the dimension of A_r is smaller than A.

4.3.4 Relative error minimization

It is important to note that the MFT in the first step generally introduces a mismatch between the full-order model $G(A, B, C, D)$ and the intermediate reduced-order model $G_r(A_r, B_r, C_r, D_r)$. As the poles of G_r belongs to the poles of G, the error around resonances will be relatively small so that the mismatch will mainly present around anti-resonances. In this second step, we will modify G_r

such that the error between G and G_r is minimized for all frequencies in Ω. Here we choose to minimize the relative error since the definition of the relative error gives similar weightings to both resonances and anti-resonances [116]. Moreover, according to [54], several definitions for the relative error could be chosen. We finally choose one of them as discussed bellow.

4.3.4.1 Relative error selection

Denote the relative error as Δ. The choice of Δ relates to the robust stability requirement in H_∞ criterion as will be presented later.

As presented in Section 3.2, in order to keep robust stability (i.e. to avoid the spill-over problem), we need to make sure that the reduced-order model based controller also guarantees the stability when applied on the full-order model. We will also see in Section 5.1.2 that this is achieved by considering Δ as an unstructured uncertainty and a corollary of the Small Gain Theorem [33] is applied where the closed-loop system is considered as the interconnection of an uncertain part Δ and a nominal part M_d, see Fig. 4.7. For different types of relative error Δ, M_d will have particular structures. Denote K the negative feedback controller designed based on the reduced-order model G_r. The definitions of different types of relative error Δ and the corresponding nominal part M_d are listed in Table 4.1 [54], where S and T respectively denote the input (subscript u) and output (subscript y) sensitivity function and the complementary sensitivity function. For the ease of discussion, denote L the open-loop transfer function (i.e. $L = KG_r$ or $L = G_rK$).

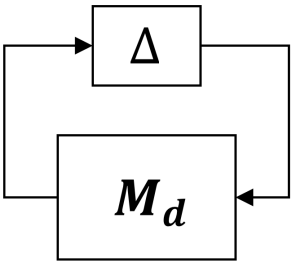

Figure 4.7: Interconnection of an uncertain part Δ and a nominal part M_d

Table 4.1: Different types of relative error Δ and the corresponding nominal part M_d

	Δ	M_d
Input inverse	$\Delta_{inv}^{In} = G^{-1}(G - G_r)$	$S_u = (I + KG_r)^{-1}$
Output inverse	$\Delta_{inv}^{Out} = (G - G_r)G^{-1}$	$S_y = (I + G_rK)^{-1}$
Input direct	$\Delta_{dir}^{In} = G_r^{-1}(G - G_r)$	$T_u = (I + KG_r)^{-1}KG_r$
Output direct	$\Delta_{dir}^{Out} = (G - G_r)G_r^{-1}$	$T_y = (I + G_rK)^{-1}G_rK$

First, let us discuss the inverse relative error Δ_{inv} (i.e. Δ_{inv}^{In} and Δ_{inv}^{Out}). The corresponding M_d is the sensitivity function S (i.e. S_u and S_y). In the frequency band of interest Ω, the open-loop system L will have high response which means:

$$\forall \omega \in \Omega,\ \underline{\sigma}(L(j\omega)) \gg 1 \tag{4.25}$$

Then we have:

$$\begin{aligned} &\forall \omega \in \Omega,\ \underline{\sigma}(I + L(j\omega)) \approx \underline{\sigma}(L(j\omega)) \gg 1 \\ \Leftrightarrow\ &\forall \omega \in \Omega,\ \overline{\sigma}(S(j\omega)) = \overline{\sigma}((I + L(j\omega))^{-1}) = \frac{1}{\underline{\sigma}(I + L(j\omega))} \ll 1 \end{aligned} \tag{4.26}$$

According to the sensitivity integral relations [117], if $\overline{\sigma}(S(j\omega))$ is smaller than 1 in Ω, it must be bigger than 1 for some frequencies outside Ω. Recall the stability condition of Small Gain Theorem in [33], the robust stability (stability when the controller K is applied on the full-order model G) is guaranteed if and only if $\forall \omega, \overline{\sigma}(S(j\omega))\overline{\sigma}(\Delta_{inv}(j\omega)) < 1$. Then we can conclude that $\overline{\sigma}(\Delta_{inv}(j\omega))$ could be be larger in Ω while it has to be small for some frequencies outside Ω. However, G_r is close to G in Ω which implies exactly the contrary. As a result, in case of inverse relative error, the stability condition can not be satisfied and thus the application of the Small Gain Theorem will fail to prove robust stability in this case.

However, for the direct relative error Δ_{dir} (i.e. Δ_{dir}^{In} and Δ_{dir}^{Out}), the corresponding M_d is the complementary sensitivity function T (i.e. T_u and T_y). The open-loop $L(j\omega)$ should have high magnitude in Ω and roll-off outside in order to obtain strong control effect and at the same time to limit the energy consumption and the effect of the measurement noise. This means that $\overline{\sigma}(T(j\omega))$ is close to 1 in

Ω and decreases outside[14]. This requires $\overline{\sigma}(\Delta_{dir}(j\omega))$ to be small in Ω and to be large outside Ω which is compatible with the objective of model reduction. In conclusion, the robust stability criterion should be applied on T and thus we should use the direct relative error Δ_{dir} as the minimization criterion.

Now, let us discuss the choice of Δ_{dir}^{In} and Δ_{dir}^{Out}. Using the expressions of these two errors, we draw the block diagram of the full-order model G as shown in Table 4.2. As it will be explained latter in H_∞ control problem, it is the H_∞ norm of the augmented system that is minimized and the augmented system is constructed by adding proper weighting transfer functions and eliminating the controller and the uncertainties. If Δ is removed from G, in Δ_{dir}^{In} case, it is possible to use the same weighting for the control input u and the uncertainty Δ. This allows, in other words, to combine two criterion together, i.e. limit energy consumption and guarantee robust stability (see Section 3.2). However, in Δ_{dir}^{Out} case, we have to use separate weightings for these two criterion which will increase the complexity of the augmented system and will finally result in complex controller. Therefore, for the purpose of obtaining simpler controller, we choose Δ_{dir}^{In} as the uncertainty and thus the minimization criterion for model reduction.

Table 4.2: Expression of G using the relative error Δ and the reduced-order model G_r

Δ	Expression of Δ	Block diagram of G
Δ_{dir}^{In}	$G_r^{-1}(G - G_r)$	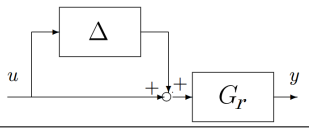
Δ_{dir}^{Out}	$(G - G_r)G_r^{-1}$	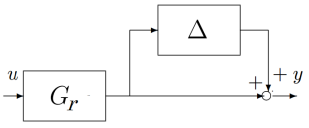

To sum up, for the second step of model reduction, we choose to minimize the relative error defined as follows:

$$\Delta(j\omega) = G_r^{-1}(j\omega)\left(G(j\omega) - G_r(j\omega)\right). \tag{4.27}$$

[14]In general, the magnitude of the weighting function for $\overline{\sigma}(T(j\omega))$ should be larger than 1 in the frequency band of interest in order to guarantee a strong control effect.

4.3.4.2 Formulation and solution of the minimization problem

Now let us reformulate the above minimization problem. We want to modify $G_r(A_r, B_r, C_r, D_r)$ such that the maximum singular value of the relative error defined by Eq. (4.27) is minimized for all frequencies in $\Omega = (\underline{\omega}, \overline{\omega})$. In our case, we will not modify A_r because it relates to the poles that are kept from G. Here we chose to modify C_r and D_r such that the following minimization problem is satisfied:

$$\begin{aligned} \min_{C_r, D_r} \quad & \gamma \\ & \textit{such that} \\ & \forall \omega \in (\underline{\omega}, \overline{\omega}),\ \overline{\sigma}\left(G_r(j\omega)^{-1}(G(j\omega) - G_r(j\omega))\right) < \gamma \end{aligned} \tag{4.28}$$

Remark. *The order of G is reduced only in the first step where we obtain G_r. The second step will not change the order because the dynamic matrix A_r stays the same.*

The major difficulty of Prob. (4.28) is the infinite number of constraints as it considers every frequency in a specified frequency band. However, it is possible to transform an infinite number of constraints into a finite number of constraints by introducing new matrix variables which defines a Linear Matrix Inequality (LMI) [31] constraint and there exist efficient algorithms to solve such LMI problem. However, we fail to transform Prob. (4.28) into an LMI optimization problem. Therefore, necessary approximation has to be made such that the approximation of Prob. (4.28) can be transformed into LMI problem and then be solved efficiently. For such an approximation, the following proposition is made:

Proposition 1. $\forall \omega$ such that $\overline{\sigma}\left(G(j\omega)^{-1}(G(j\omega) - G_r(j\omega))\right) \ll 1$ then:

$$\overline{\sigma}\left(G(j\omega)^{-1}(G(j\omega) - G_r(j\omega))\right) \approx \overline{\sigma}\left(G_r(j\omega)^{-1}(G(j\omega) - G_r(j\omega))\right) \ll 1 \tag{4.29}$$

Proof.

$$\begin{aligned}
&\overline{\sigma}\left(G(j\omega)^{-1}(G(j\omega)-G_r(j\omega))\right) = \overline{\sigma}\left(I - G(j\omega)^{-1}G_r(j\omega)\right) \ll 1 \\
\Leftrightarrow\ & G(j\omega)^{-1}G_r(j\omega) \approx I \\
\Leftrightarrow\ & \overline{\sigma}\left(G_r(j\omega)^{-1}G(j\omega)\right) = \frac{1}{\underline{\sigma}\left(G(j\omega)^{-1}G_r(j\omega)\right)} \approx 1
\end{aligned}$$

where I is identity. Then,

$$\begin{aligned}
&\overline{\sigma}\left(G_r(j\omega)^{-1}(G(j\omega)-G_r(j\omega))\right) \\
=\ & \overline{\sigma}\left(G_r^{-1}(j\omega)G(j\omega)G(j\omega)^{-1}(G(j\omega)-G_r(j\omega))\right) \\
\leqslant\ & \overline{\sigma}\left(G_r^{-1}(j\omega)G(j\omega)\right)\overline{\sigma}\left(G(j\omega)^{-1}(G(j\omega)-G_r(j\omega))\right) \\
\ll\ & 1
\end{aligned}$$

□

Using Proposition 1, Prob. (4.28) is approximated by:

$$\begin{aligned}
\min_{C_r,D_r}\ & \gamma \\
& \textit{such that} \\
& \forall\omega\in(\underline{\omega},\overline{\omega}),\ \overline{\sigma}\left(G(j\omega)^{-1}(G(j\omega)-G_r(j\omega))\right) < \gamma
\end{aligned} \tag{4.30}$$

In other words, the solution of Prob. (4.28) is approximately the solution of Prob. (4.30) which can be directly transformed into LMI constrains as described in the following theorem:

Theorem 2. *Consider G, the model of an LTI continuous system with the state-space representation denoted as (A,B,C,D), and G_r, a reduced model of G with the state-space representation denoted as (A_r,B_r,C_r,D_r) such that $\lambda(A_r)\subset\lambda(A)$. γ is a real positive number. The solution of Prob. (4.30) is given by solving the following LMI problem:*

$$\begin{aligned} \min_{C_r, D_r, P \in \mathbb{C}^{n_a \times n_a}} \quad & \gamma^2 \\ & \textit{such that} \\ & P + P^* < 0, \ K + K^* > 0 \end{aligned} \tag{4.31}$$

where

$$K = XN + Q \tag{4.32}$$

$$X = \left[\begin{array}{c|ccc} P & \multicolumn{3}{c}{0} \\ \hline 0 & C_r & D_r & 0 \\ & 0 & 0 & \gamma^2 I \end{array}\right], \ N = \left[\begin{array}{cc|cc} \multicolumn{2}{c|}{\widetilde{A}} & \multicolumn{2}{c}{\widetilde{B}} \\ \hline 0 & -E_{r\delta} & 0 & F_{r\delta} \\ 0 & 0 & 0 & -I \\ 0 & 0 & 0 & \frac{I}{2} \end{array}\right],$$

$$Q = \left[\begin{array}{cc|cc} B_\delta B_\delta^*/2 & 0 & 0 & 0 \\ 0 & 0 & 0 & 0 \\ \hline D_\delta B_\delta^* & 0 & D_\delta D_\delta^*/2 & D_\delta \\ B_\delta^* & 0 & 0 & 0 \end{array}\right],$$

$$\widetilde{A} = \begin{bmatrix} A_\delta^* & 0 \\ 0 & A_{r\delta} \end{bmatrix}, \ \widetilde{B} = \begin{bmatrix} C_\delta^* & 0 \\ 0 & B_{r\delta} \end{bmatrix}, \ E_{r\delta} = (I + \frac{j}{\underline{\omega}} A_r)^{-1}, \ F_{r\delta} = \frac{j}{\underline{\omega}} E_{r\delta} B_r$$

$$\begin{aligned} A_\delta &= -\overline{\omega} I - j(1 - \frac{\overline{\omega}}{\underline{\omega}}) A (I + \frac{j}{\underline{\omega}} A)^{-1}, & B_\delta &= -j(1 - \frac{\overline{\omega}}{\underline{\omega}})(I + \frac{j}{\underline{\omega}} A)^{-1} B, \\ C_\delta &= C(I + \frac{j}{\underline{\omega}} A)^{-1}, & D_\delta &= D - \frac{j}{\underline{\omega}} C (I + \frac{j}{\underline{\omega}} A)^{-1} B, \\ A_{r\delta} &= -\overline{\omega} I - j(1 - \frac{\overline{\omega}}{\underline{\omega}}) A_r (I + \frac{j}{\underline{\omega}} A_r)^{-1}, & B_{r\delta} &= -j(1 - \frac{\overline{\omega}}{\underline{\omega}})(I + \frac{j}{\underline{\omega}} A_r)^{-1} B_r, \\ C_{r\delta} &= C_r (I + \frac{j}{\underline{\omega}} A_r)^{-1}, & D_{r\delta} &= D_r - \frac{j}{\underline{\omega}} C_r (I + \frac{j}{\underline{\omega}} A_r)^{-1} B_r. \end{aligned} \tag{4.33}$$

and n_a the dimension of $\widetilde{A}$.

Prob. (4.31) is a linear cost minimization problem. There exist efficient algorithms to solve this problem, see [31]. The proof of **Theorem 2** is as follows.

Proof.

The constrain defined by Prob. (4.30) can be interpreted as below by using the Schur complement [31]:

$$\begin{aligned}
&\forall \omega \in (\underline{\omega}, \overline{\omega}), \\
&\overline{\sigma}\left(G(j\omega)^{-1}(G(j\omega) - G_r(j\omega))\right) < \gamma \\
\Leftrightarrow &\left((G(j\omega)^* - G_r(j\omega)^*)G(j\omega)^{-*}\right)\left(G(j\omega)^{-1}(G(j\omega) - G_r(j\omega))\right) < \gamma^2 I \\
\Leftrightarrow &\gamma^2 I - \left(G(j\omega) - G_r(j\omega)\right)^*\left(G(j\omega)G(j\omega)^*\right)^{-1}\left(G(j\omega) - G_r(j\omega)\right) > 0 \\
\Leftrightarrow &\begin{bmatrix} G(j\omega)G(j\omega)^* & G(j\omega) - G_r(j\omega) \\ G(j\omega)^* - G_r(j\omega)^* & \gamma^2 I \end{bmatrix} > 0
\end{aligned} \tag{4.34}$$

Let us define:

$$\Phi(j\omega) = \left[\begin{array}{cc} G(j\omega)^* & I \\ 0 & G_r(j\omega) \\ 0 & (\gamma^2 - 1)\frac{I}{2} \\ \hline I & 0 \\ 0 & I \end{array}\right], \quad H = \left[\begin{array}{ccc|cc} I & 0 & 0 & 0 & 0 \\ 0 & 0 & 0 & -I & 0 \\ 0 & 0 & 0 & 0 & I \\ \hline 0 & -I & 0 & 0 & 0 \\ 0 & 0 & I & 0 & 0 \end{array}\right], \tag{4.35}$$

then:

$$\Phi(j\omega)^* H \Phi(j\omega) = \begin{bmatrix} G(j\omega)G(j\omega)^* & G(j\omega) - G_r(j\omega) \\ G(j\omega)^* - G_r(j\omega)^* & \gamma^2 I \end{bmatrix}. \tag{4.36}$$

As a result, Eq. (4.34) is equivalent to:

$$\forall \omega \in (\underline{\omega}, \overline{\omega}), \Phi(j\omega)^* H \Phi(j\omega) > 0. \tag{4.37}$$

A lemma developed in [118] allows us to transform Eq. (4.37) into LMI constrains. This lemma is recalled below:

Lemma 3. *Consider* $\Psi(\delta) = \delta I \star \left[\begin{array}{c|c} A_\psi & B_\psi \\ \hline C_\psi & D_\psi \end{array}\right]$ *and* H *(an hermitian matrix), the two following propositions are equivalent:*

(1) $\forall \delta \in (0, +\infty)$,

$$\Psi(\delta)^* H \Psi(\delta) > 0 \tag{4.38}$$

(2) There exists a complex matrix P *such that* $P + P^* < 0$ *and:*

$$\begin{bmatrix} C_\psi^* \\ D_\psi^* \end{bmatrix} H \begin{bmatrix} C_\psi & D_\psi \end{bmatrix} + \begin{bmatrix} A_\psi^* P^* + P A_\psi & P B_\psi \\ B_\psi^* P^* & 0 \end{bmatrix} > 0 \tag{4.39}$$

By adding a finite variable P, the infinite constrains on δ is transformed into a finite LMI constrain. However, this lemma can not be directly applied because Φ is defined on $\omega \in (\underline{\omega}, \overline{\omega})$ while Ψ on $\delta \in (0, +\infty)$. In order to apply this lemma, variable substitution must be done to transform $\Phi(j\omega)$ into $\Psi(\delta)$. As Φ is computed by G and G_r, the objective is to transform $G(j\omega)|_{\omega\in(\underline{\omega},\overline{\omega})}$ and $G_r(j\omega)|_{\omega\in(\underline{\omega},\overline{\omega})}$ into $\mathcal{G}(\delta)|_{\delta\in(0,+\infty)}$ and $\mathcal{G}_r(\delta)|_{\delta\in(0,+\infty)}$. The transformation can be done through state-space representation.

The state-space representation of $G(s)$ with s the Laplace operator can be presented in block diagram as shown in Fig. 4.8a. Replacing s by $j\omega$ and then removing j from the upper block, we obtain Fig. 4.8b. The expression of $G(j\omega)$ becomes:

$$G(j\omega) = \frac{1}{\omega} I \star \left[\begin{array}{c|c} -jA & -jB \\ \hline C & D \end{array}\right], \tag{4.40}$$

where $\star$ denotes the Redheffer star product [32]. Variable substitution is done to $\dfrac{1}{\omega} I$ by defining $\dfrac{1}{\omega} I = \delta I \star T_\Omega$ as shown in Fig. 4.8c. Then $G(j\omega)$ becomes:

$$\mathcal{G}(\delta) = \delta I \star \left(T_\Omega \star \left[\begin{array}{c|c} -jA & -jB \\ \hline C & D \end{array}\right] \right) = \delta I \star \left[\begin{array}{c|c} A_\delta & B_\delta \\ \hline C_\delta & D_\delta \end{array}\right]. \tag{4.41}$$

Fig. 4.8d shows the block diagram of $\mathcal{G}(\delta)$. A_δ, B_δ, C_δ and D_δ are complex matrices. Similarly, the reduced model $G_r(s)$ also has the same form:

$$\mathcal{G}_r(\delta) = \delta I \star \left(T_\Omega \star \left[\begin{array}{c|c} -jA_r & -jB_r \\ \hline C_r & D_r \end{array}\right] \right) = \delta I \star \left[\begin{array}{c|c} A_{r\delta} & B_{r\delta} \\ \hline C_{r\delta} & D_{r\delta} \end{array}\right]. \tag{4.42}$$

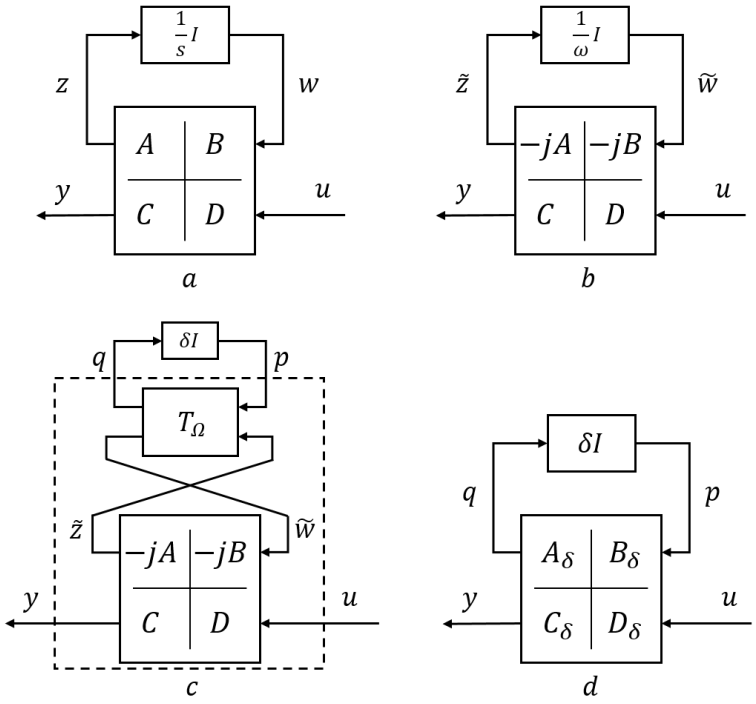

Figure 4.8: Block diagram of G in state-space representation

To transform $\omega \in (\underline{\omega}, \overline{\omega})$ into $\delta \in (0, +\infty)$, T_Ω is chosen as:

$$T_\Omega = \left[\begin{array}{c|c} -\overline{\omega}I & (1 - \frac{\overline{\omega}}{\underline{\omega}})I \\ \hline I & \frac{1}{\underline{\omega}}I \end{array}\right], \tag{4.43}$$

then:

$$\frac{1}{\omega}I = \delta I \star \left[\begin{array}{c|c} -\overline{\omega}I & (1 - \frac{\overline{\omega}}{\underline{\omega}})I \\ \hline I & \frac{1}{\underline{\omega}}I \end{array}\right] = \frac{1}{\underline{\omega}} + \delta(1+\delta\overline{\omega}I)^{-1}(1-\frac{\overline{\omega}}{\underline{\omega}})I = \frac{1+\delta\underline{\omega}}{\underline{\omega}(1+\delta\overline{\omega})}I. \tag{4.44}$$

The bounded variable $\delta \in (0, +\infty)$ implies exactly $\omega \in (\underline{\omega}, \overline{\omega})$. In this way, the system $G(j\omega)$ and $G_r(j\omega)$ with $\omega \in (\underline{\omega}, \overline{\omega})$ are tranformed into $\mathcal{G}(\delta)$ and $\mathcal{G}_r(\delta)$ with $\delta \in (0, +\infty)$. Substitute T_Ω into Eq. (4.41) and Eq. (4.42), we obtained exactly Eq. (4.33) in Theorem 2.

Taking H in Eq. (4.35) and defining $\Psi(\delta)$ as:

$$\Psi(\delta) = \left[\begin{array}{cc} \mathcal{G}(\delta)^* & I \\ 0 & \mathcal{G}_r(\delta) \\ 0 & (\gamma^2-1)\dfrac{I}{2} \\ \hline I & 0 \\ 0 & I \end{array}\right], \tag{4.45}$$

equivalence can be found between Eq. (4.37) and Eq. (4.38), and thus equivalence between the constrain in Prob. (4.30) and Eq. (4.38). According to Lemma 3, Eq. (4.38) is equivalent to Eq. (4.39) with $P + P^\star < 0$. Substitute Eq. (4.45), Eq. (4.41) and Eq. (4.42) into Eq. (4.39), we obtain $K + K^* > 0$ with K defined exactly by Eq. (4.32) in Theorem 2.

□

4.3.5 Application to the beam-piezo system model

The multi-variable model reduction method is applied on the full-order model $G^{full}(\theta_{id})$ obtained in Section 4.2.3 with state-space representation (4.18).

First, MFT is applied. The dynamic matrix A is transformed into a block diagonal matrix composed of two scalar (for the poles corresponding to the measurement circuit) and several 2×2 matrix (for the poles corresponding to the vibration modes). Consequently, it is rather straightforward to truncate those blocks corresponding to the modes outside the frequency band of interest $(600, 3000)$ rad/s, which yields the following reduced-order model[15] of order 24:

$$\left\{\begin{array}{rl} \dot{x} &= A^r \cdot x + B_f^r \cdot f + B_a^r \cdot V_a \\ \nu_{node} &= C_e^r \cdot x \\ V_s &= C_s^r \cdot x \end{array}\right. \tag{4.46}$$

[15]In fact, in order to have a maximum match between the full-order model and the reduced-order model, we finally choose to reserve one peak after 3000 rad/s which can be seen from Fig. 4.10. Thus, the reduced-order model will contain 12 modes with order 24, i.e. 11 to-be-controlled modes in $(600, 3000)$ rad/s and 1 mode after 3000 rad/s. However, this particular reserved mode will not be controlled if we choose proper weightings for the control outputs as explained in Section 5.2.2

The relative error between this reduced-order model (4.46) and $G^{full}(\theta_{id})$ is shown in solid blue in Fig. 4.9, where we focus on the dynamics between V_a and V_s and the maximum singular value of the error is drawn. We observe a high maximum error over $(600, 3000)$ rad/s: up to almost 20 dB. This high maximum error will fail the robust stability criterion which is explained later, see **Remark** of criterion **b** in Section 5.2.2. Relative error minimization is thus necessary.

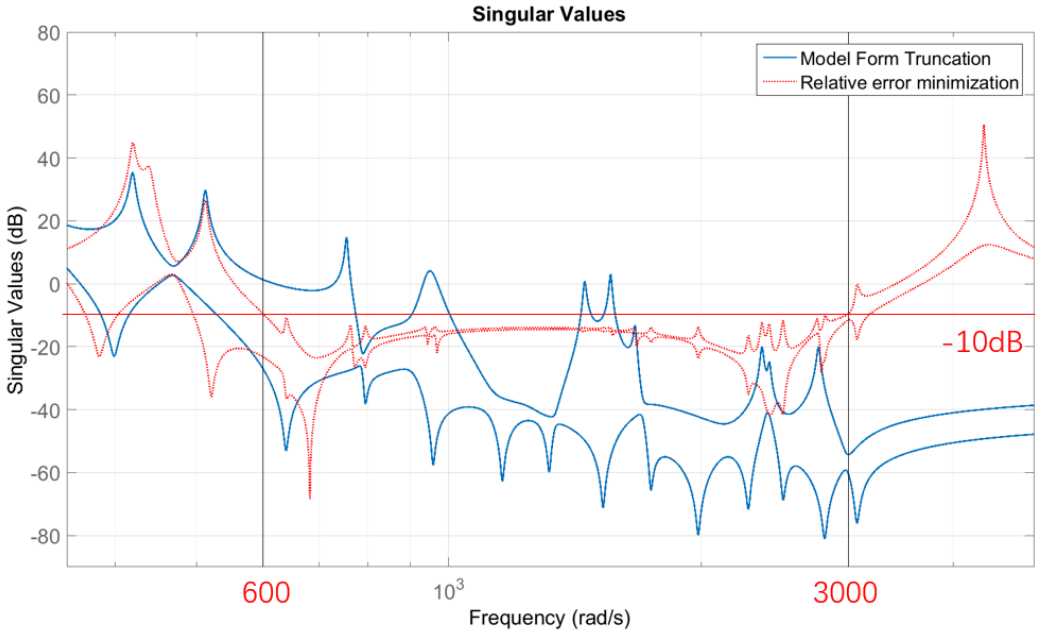

.

Figure 4.9: Singular value of the error for dynamics between V_a and V_s: MFT (solid blue) vs MFT and relative error minimization (dotted red)

Second, relative error minimization is performed. Instead of minimizing the relative error between model Eq. (4.46) and $G^{full}(\theta_{id})$, we will only focus on the relative error pertaining to the part of Eq. (4.46) between V_a and V_s, denoted $G_{V_a \to V_s}$. The main reasons for this are simplicity and the fact that $G_{V_a \to V_s}$ is the part of model which is directly involved in the closed-loop system. The error at the anti-resonances is indeed only required to be small for the reduced-order model to be a good model for control purpose. Consequently, the actual considered relative error in our specific case is:

$$\Delta(j\omega) = G^{-1}_{V_a \to V_s}(j\omega) \left(G^{full}_{V_a \to V_s}(j\omega) - G_{V_a \to V_s}(j\omega) \right). \tag{4.47}$$

As explained in Section 4.3.4, for $G_{V_a \to V_s}$, we will determine a modified C_s^r, denoted $C_s^{r,new}$, and add a direct term $D_s^{r,new}$ to increase the degrees of freedom. This gives a modified $G_{V_a \to V_s}$ in the following state-space representation:

$$\begin{cases} \dot{x} = A^r \cdot x + B_a^r \cdot V_a \\ V_s = C_s^{r,new} \cdot x + D_s^{r,new} \cdot V_a \end{cases} \tag{4.48}$$

where A^r and B_a^r are the same as the ones obtained after MFT (see Eq. (4.46)) and where $C_s^{r,new}$ and $D_s^{r,new}$ will be determined by solving the following minimization problem:

$$\min_{C_s^{r,new}, D_s^{r,new}} \sup_{\omega \in (600,3000)} \overline{\sigma} \left(G_{V_a \to V_s}^{-1}(j\omega)(G_{V_a \to V_s}^{full}(j\omega) - G_{V_a \to V_s}(j\omega)) \right). \tag{4.49}$$

The reduction of the relative error $\Delta(j\omega)$ (i.e. Eq. (4.47)) for the modified $G_{V_a \to V_s}$ (i.e. Eq. (4.48)) can be clearly seen from Fig. 4.9. When looking at the dynamics between V_a and V_s in the frequency band of interest, we observe in Fig. 4.10 that, with respect to the model obtained after MFT, the frequency response of the reduced-order model obtained after relative error minimization is closer to the one of the full-order model, especially at the anti-resonances.

The reduced-order model after this two-step procedure is thus finally given by the following state-space model, which will be used in the next section to design the controller:

$$\begin{cases} \dot{x} = A^r \cdot x + B_f^r \cdot f + B_a^r \cdot V_a \\ \nu_{node} = C_e^r \cdot x \\ V_s = C_s^{r,new} \cdot x + D_s^{r,new} \cdot V_a \end{cases} \tag{4.50}$$

Similarly as in Eq. (4.19), this reduced-order model (order 24) can be transformed into a matrix of transfer functions that will be denoted by G. In the next section, we will show how to design the controller based on G. Note that, by construction, the reduced-order model G will typically have low gain outside $(600, 3000)$ rad/s. See e.g. Fig. 4.10 for a confirmation of this observation.

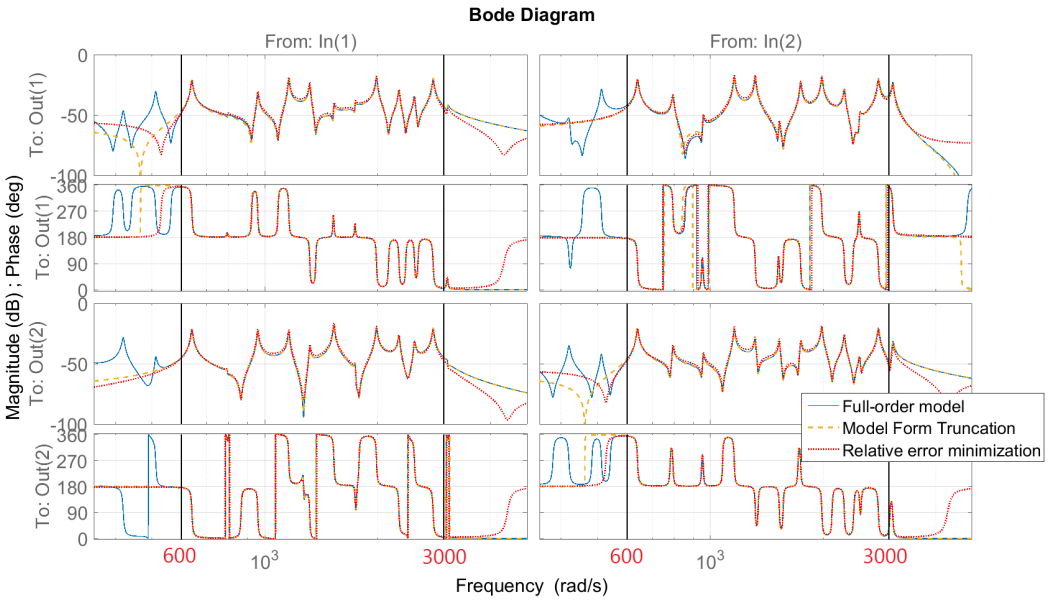

Figure 4.10: Frequency response of $G^{full}_{V_a \to V_s}$ (solid blue), of $G_{V_a \to V_s}$ after MFT (dashed yellow) and of this model after relative error minimization (dotted red)

4.4 Summary

This chapter focuses on building an accurate state-space model of the beam-piezo system used for centralized controller design. We first perform Finite Element Modeling to the structure using COMSOL which gives us a global governing equation that contains the beam dynamics and the electromechanical coupling between the beam and the PZT pairs. This governing equation is then simplified and corrected to approximate the global behaviour of the structure. Then, we deduce a mathematical expression of the vibration energy in the central zone using a constructed velocity vector. The dynamics of the measurement circuit are also taken into account. We finally deduce a state-space model of the beam-piezo system which takes the force disturbance, the actuation voltage vector as inputs and the constructed velocity vector, the sensing voltage vector as outputs. We also conclude that the central energy can be reduced by reducing the H_2 norm of the transfer function vector from the disturbance to the velocity vector. We validate this model and find discrepancies between its response and the response of the actual setup. We thus perform grey-box identification to correct specified parameters such that the response of the corrected model is close to the actual setup. Different experiments are carefully designed to correct the parameters

separately because we do not have the device to synchronously measure all the inputs/outputs from the setup. This corrected model is the so-called full-order model which covers a frequency band larger than the frequency band of the considered force disturbance. A new model reduction method is thus proposed to compute a reduced-order model that is close to the full-order model only in the frequency band of interest at both resonances and anti-resonances. The controller will be designed based on the reduced-order model.

Chapter 5

Centralized controller design

In this chapter, we will apply H_∞ control to compute a MIMO centralized controller based on the reduced-order model obtained through model improvement step (Section 4.2) and the model reduction step (Section 4.3), i.e. model (4.50), denoted G. First, the basic theorem of H_∞ control is introduced in terms of the performance and the robust stability. Then, H_∞ criterion is built according to our particular control objectives and considerations, which is to build the so-called augmented system. We aim at finding a controller that minimizes the H_∞ norm of the augmented system. This controller is then further reduced by neglecting the dynamics out of interest. This design process is then applied to our particular structure by properly choosing weighting transfer functions for H_∞ criterion. The validity of the obtained controller is verified by numerical simulations and by the experiment on the actual setup.

5.1 H_∞ control approach

The H_∞ control theory has experienced rapid development since it was first introduced into the control theory in 1981 by Zames [119]. Extensive investigation of the H_∞ control design procedures are available in [32, 120–122]. Here we briefly introduce the H_∞ approach with respect to performance criterion and then show some results in robust analysis. This is very important for understanding the proposed H_∞ criterion for solving our particular active vibration control problem.

5.1.1 Performance and criterion

Restricting attention to disturbance rejection, the objective of H_∞ control is to design a controller $K(s)$ ($u(s) = K(s)y(s)$) for a system of the type:

$$\begin{bmatrix} q(s) \\ y(s) \end{bmatrix} = \tilde{G}(s) \begin{bmatrix} p(s) \\ u(s) \end{bmatrix}, \tag{5.1}$$

where $u(s) \in \mathbb{C}^{n_u}$ is the (Laplace transform of the) vector of signals generated by the controller and $y(s) \in \mathbb{C}^{n_y}$ the input vector (sensor measurements) used by the controller $K(s)$. In the above system, we have also $p(s) \in \mathbb{C}^{n_p}$ which is a vector containing the to-be-rejected disturbances and $q(s) \in \mathbb{C}^{n_q}$ which is a vector containing the to-be-controlled outputs. It is to be noted that q does not need to be measured (this aspect will be important in our case because there are no sensors in the target zone). Finally, $\tilde{G}(s)$ is a matrix of transfer functions reflecting the dynamics between these signals. In our case, u will link to the actuation voltage V_a, y to the sensing voltage V_s. The to-be-rejected disturbance p will be made up of the disturbance f and the measurement noise. The to-be-controlled output q will be made up of the velocity vector ν_{node} (since we want to reduce the central energy) and the actuation V_a (since we want to limit control efforts), see Section 5.2.2 for more details.

In H_∞ control, the desired performance of the output q and the considered input p are presented in the frequency domain using weighing functions (specified transfer functions) which will describe the frequency content of q and p. For this purpose, let us introduce, for an arbitrary signal x of power spectral density (PSD) $\mathcal{S}_x(\omega)$, the following signal set defined using a stable and inversely stable transfer function $W(s)$:

$$\Omega_W = \left\{ x \middle| \forall \omega,\ \mathcal{S}_x(\omega) \leqslant |W(j\omega)|^2 \right\}. \tag{5.2}$$

Based on this expression, for considered inputs p, we specify transfer functions W_{p_j} ($j = 1...n_p$) such that each element p_j of p belongs to the signal set $\Omega_{W_{p_j}}$ and for the desired performance of the to-be-controlled output q, we choose transfer functions W_{q_k} ($k = 1...n_q$) such that each element q_k of q belongs to the signal set $\Omega_{W_{q_k}^{-1}}$. The objective of H_∞ control is then to compute a controller $K(s)$

that when applied to the system described by Eq. (5.1) (i.e. $u(s) = K(s)y(s)$), each element q_k of q will belong to $\Omega_{W_{q_k}^{-1}}$ $(q = 1...n_q)$ for well chosen W_{q_k} if each element p_j of p belongs to $\Omega_{W_{p_j}}$ $(j = 1...n_p)$. Generally, there is no need to define all these transfer functions W_{p_j} and W_{q_k}. Simplifications could be used which will generally based on the following interpretation of the H_∞ control problem in term of the loop-shaping of the closed-loop transfer functions: if a controller satisfying the above objectives is applied to Eq. (5.1), then the following inequality holds for the closed-loop transfer function $T_{p_j \to q_k}$ between any signal p_j $(j = 1...n_p)$ and any signal q_k $(q = 1...n_q)$:

$$\forall \omega, \ |T_{p_j \to q_k}(j\omega)| < \frac{1}{|W_{q_k}(j\omega) W_{p_j}(j\omega)|}. \tag{5.3}$$

The transfer functions W_{p_i} and W_{q_k} can thus be seen as weightings to shape the closed-loop transfer functions $T_{p_j \to q_k}$. In order to mathematically formalize the above control design problem, let us define the so-called augmented plant, denoted $P(s)$, as follows:

$$P(s) = diag(W_{q_1}, \cdots, W_{q_{n_q}}, I_{n_y}) \tilde{G}(s) diag(W_{p_1}, \cdots, W_{p_{n_p}}, I_{n_u}). \tag{5.4}$$

This augmented plant $P(s)$ can be presented by Fig. 5.1 where the signals e_j $(j = 1...n_p)$ and z_k $(k = 1...n_q)$ are fictive signals that all have a PSD smaller or equal to one (i.e. $e_j, z_k \in \Omega_1$) when $p_j \in \Omega_{W_{p_j}}$ $(j = 1...n_p)$ and $q_k \in \Omega_{W_{q_k}^{-1}}$ $(q = 1...n_q)$.

Denoting $e = [e_1, \cdots, e_{n_p}]^T$ and $z = [z_1, \cdots, z_{n_q}]^T$, the closed-loop system can then be rewritten as:

$$\begin{bmatrix} z(s) \\ y(s) \end{bmatrix} = P(s) \begin{bmatrix} e(s) \\ u(s) \end{bmatrix} = \begin{bmatrix} P_{ze}(s) & P_{zu}(s) \\ P_{ye}(s) & P_{yu}(s) \end{bmatrix} \begin{bmatrix} e(s) \\ u(s) \end{bmatrix}, \quad . \\ u(s) = K(s)y(s) \tag{5.5}$$

The transfer function from $e(s)$ to $z(s)$ in Eq. (5.5) (closed-loop transfer function) will be presented using the so-called Redheffer star product [32] as follows[1]

[1] As K will have less dimension than P, this expression is also called the lower Linear Fractional Transformation (LFT) $F_l(P, K)$ [123]

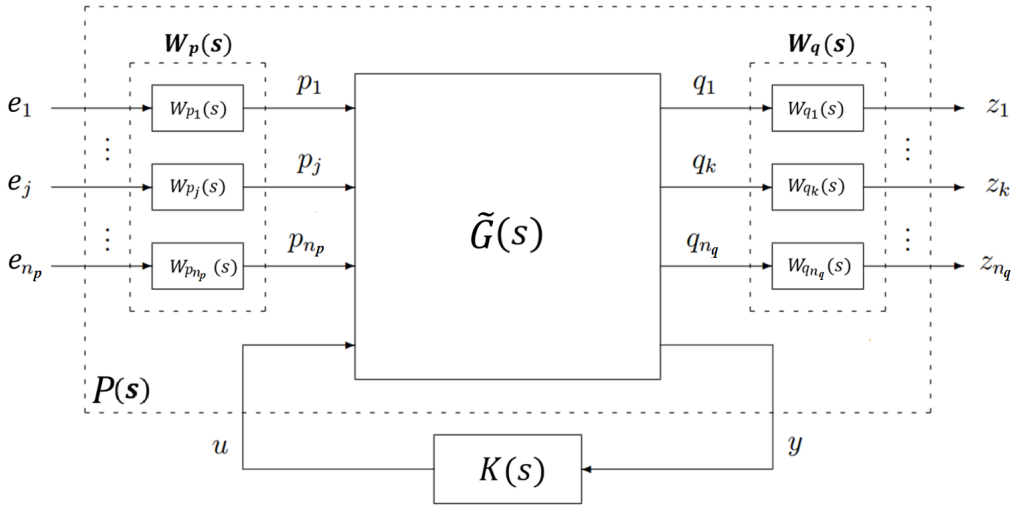

Figure 5.1: Standard form of H_∞ synthesis

$$P \star K = P_{ze} + P_{zu} K \left(I - P_{yu} K\right)^{-1} P_{ye}.$$

Using Eq. (5.5), the H_∞ control criterion described above can be mathematically formulated as the problem of determining a stabilizing controller $K(s)$ such that the following condition holds for the scalar $\gamma < 1$:

$$||P \star K||_\infty < \gamma, \tag{5.6}$$

where the H_∞ norm of an arbitrary stable LTI system T is defined as:

$$||T||_\infty = \sup_\omega \overline{\sigma}(T(j\omega)).$$

Moreover, for a transfer function matrix T, its H_∞ norm is larger than the H_∞ norm of each of its elements:

$$\left\|\begin{bmatrix} T_1 \\ T_2 \end{bmatrix}\right\|_\infty \geqslant \left\|T_1\right\|_\infty \qquad \left\|\begin{bmatrix} T_1 \\ T_2 \end{bmatrix}\right\|_\infty \geqslant \left\|T_2\right\|_\infty$$
$$\left\|\begin{bmatrix} T_1 & T_2 \end{bmatrix}\right\|_\infty \geqslant \left\|T_1\right\|_\infty \qquad \left\|\begin{bmatrix} T_1 & T_2 \end{bmatrix}\right\|_\infty \geqslant \left\|T_2\right\|_\infty$$

Using the above property, Eq. (5.6) implies that each entry of $P \star K$ has an H_∞ norm smaller than $\gamma < 1$:

$$||W_{q_k} T_{p_j \to q_k} W_{p_j}||_\infty \leqslant ||P \star K||_\infty < \gamma < 1, \;\; j = 1...n_p, \;\; k = 1...n_q, \tag{5.7}$$

which in turn implies Eq. (5.3) when W_{p_j} and W_{q_k} are chosen as scalar or SISO transfer function. Note that the H_∞ controller K designed in this way will have the same order as the augmented plant P.

5.1.2 Robust stability

H_∞ control allows us to impose robust stability. This is realized by using an important result in robust analysis which is the so-called Weighted Small Gain Theorem (a corollary of the Small Gain Theorem in [32, 33]). This is also the most important reason why we choose H_∞ control over H_2 control which seems to be a more direct way for central energy reduction (see the expression of the central energy, i.e. Eq. (4.17)). To explain the Weighted Small Gain Theorem, let us define the following uncertainty set $\mathbf{\Delta}$ containing stable LTI transfer matrices $\Delta(s)$ such that:

$$\mathbf{\Delta} = \left\{ \Delta(s) \mid \Delta(s) = W_1(s) \hat{\Delta}(s) W_2(s) \text{ with } \left\| \hat{\Delta} \right\|_\infty \leqslant 1 \right\}, \tag{5.8}$$

with W_1 and W_2 two given stable transfer matrices. Then, for a stable transfer matrix $M_d(s)$ (with no uncertainty), the loop represented in Fig. 5.2 is stable for all Δ in $\mathbf{\Delta}$ if and only if the following condition holds:

$$||W_2 M_d W_1||_\infty < 1. \tag{5.9}$$

The two transfer matrices W_1 and W_2 are used to limit the frequency content of the uncertainty Δ (in which case, this uncertainty is called the unstructured uncertainty in [32, 33]). As it was discussed before (see Section 4.3.4.1), we have considered the relative error between the reduced-order model and the full-order model as the unstructured uncertainty Δ and now we will choose a proper

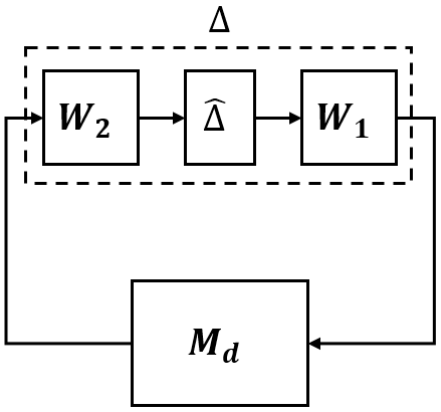

Figure 5.2: Weighted Small Gain Theorem (WSGT)

weighting function for it. The nominal part M_d will be composed of the reduced-order model and the controller such that the system family (M_d, Δ) (with a structure of Fig. 5.2) is a representation of the closed-loop full-order model. The application of the Weighted Small Gain Theorem will then guarantee the robust stability.

5.2 H_∞ controller design for the vibration reduction in the central zone

In this section, we will present the particular H_∞ control design (an application of the above presented H_∞ control approach) for our active vibration reduction problem.

5.2.1 Vibration reduction problem statement

First, let us recall the control objectives discussed in Section 3.2. They are summarized for a general case as follows:

Excitation: We consider a force disturbance f (vibration source in z direction applied by the shaker at the excitation point as shown in Fig. 3.2) which has high PSD in a specified frequency band Ω.

Performance: We aim to particularly reduce the vibration in the central zone of the beam where there is no PZT pairs, see Fig. 3.2. According to the discussion in the modeling part (see Section 4.1.4), this leads to reduce the H_2 norm of the transfer function vector from force f to velocity vector ν_{node}. As discussed in the sequel, this will be realized by minimizing the H_∞ norm.

Control signal: First, the controller should be able to filter a certain level of measurement noise (usually located at high frequencies) which means that the controller should have roll-off at higher frequencies. Second, the control energy consumption should be limited which requires that the controller should have high magnitude in the frequency band of interest Ω and low magnitude outside Ω.

Robust stability: The designed controller based on the reduced-order model G must also be able to guarantee the stability when applied on the full-order model[2], i.e. $G^{full}(\theta_{id})$ (see Section 4.2).

5.2.2 Augmented system and control criterion

We are now ready to present the H_∞ criterion to tackle our vibration reduction problem. According to the above objectives, we build an augmented system P as shown in Fig. 5.3. In this figure, G is the reduced-order model obtained from model reduction step (see Section 4.3, Eq. (4.50)), K the to-be-determined controller. This controller generates a signal u that will be applied as voltage V_a to the PZT actuators after an amplification by a factor A_p and uses a signal y obtained after filtering the sensor voltage V_s by a transfer function $F_d(s)$ which is a model of pure time delay using Pade Approximation [124]. The factor A_p and the transfer function $F_d(s)$ represent respectively the gain and the time delay introduced by power amplifiers, the digital conversion mechanism[3] and the anti-aliasing filters[4] (see Fig. 3.5 and we suppose that the gain/time delay is the same in each control channel). Recall that N_a and N_s are respectively the number of PZT actuators and sensors used for control ($N_a = N_s = 2$ in our case).

[2]This is to avoid the so-called spill-over problem
[3]The controller will thus be implemented digitally
[4]The phase shift in the anti-aliasing filter can be approximated by a pure time delay

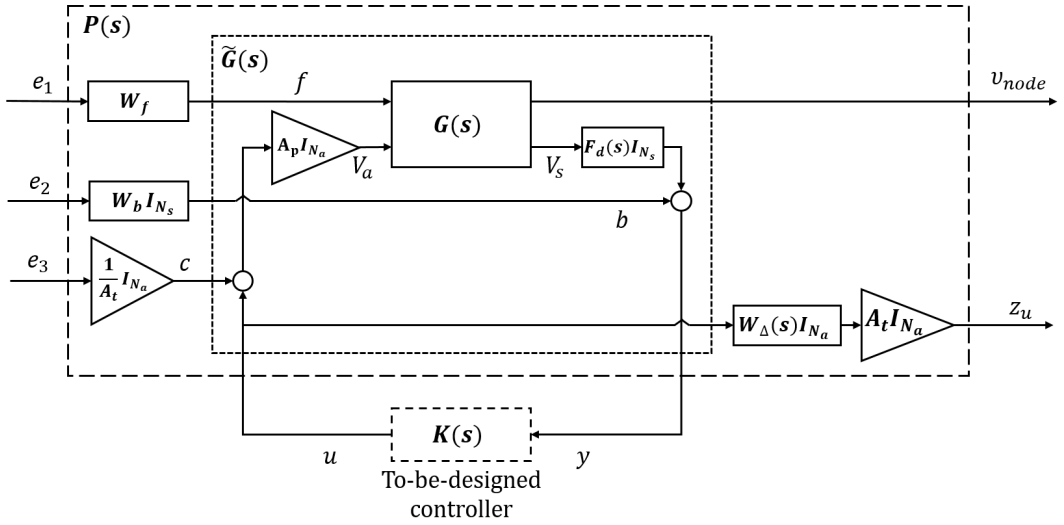

Figure 5.3: Block diagram of H_∞ synthesis

Remark: *As discussed in Section 4.2, the data used for identification is carefully measured such that the effect of the control devices can be considered as pure gain or time delay. It is thus reasonable to choose A_p as a scalar and F_d as a transfer function that models the delay introduced by the digital conversion mechanism and the anti-aliasing filters.*

Fig. 5.3 is indeed an interpretation of the standard form of H_∞ synthesis (i.e. Fig. 5.1) by considering the specified control objectives for our active vibration reduction problem. We see that the vector z (Fig. 5.1, corresponding to the to-be-controlled variables q) is made up of the velocity vector ν_{node} and of a weighted version z_u of u (Fig. 5.3) and that the vector e (Fig. 5.1, corresponding to the disturbance signals p) is made up of $[e_1, e_2, e_3]^T$ (Fig. 5.3) where e_1 is a weighted version of the disturbance f generated by the shaker, e_2 a weighted version of the output measurement noise b and e_3 a weighted version of a signal c that will allows us to deal with the modeling error introduced by the model reduction step (see Section 4.3). Finally, W_f, W_b, W_Δ and A_t are weighting functions (under the form of a SISO transfer function for W_Δ and of constants for W_f, W_b and A_t) which have to be determined in order to realize the specifications described in Section 5.2.1.

Mathematically, Fig. 5.3 corresponds to Fig. 5.1 with $P(s) = W_q(s)\tilde{G}(s)W_p(s)$ where:

$$\tilde{G}(s) = \begin{bmatrix} I_{N_z} & 0 & 0 & 0 \\ 0 & 0 & 0 & I_{N_a} \\ 0 & F_d(s)I_{N_s} & I_{N_s} & 0 \end{bmatrix} \left[\begin{array}{cc|cc} & & 0 & 0 \\ \multicolumn{2}{c|}{\mathrm{G(s)}} & 0 & 0 \\ \hline 0 & 0 & I_{N_s} & 0 \\ 0 & 0 & 0 & I_{N_a} \end{array}\right] \begin{bmatrix} 1 & 0 & 0 & 0 \\ 0 & 0 & A_p I_{N_a} & A_p I_{N_a} \\ 0 & I_{N_s} & 0 & 0 \\ 0 & 0 & 0 & I_{N_a} \end{bmatrix},$$

$$W_q(s) = \begin{bmatrix} I_{N_z} & 0 \\ 0 & A_t W_\Delta(s) I_{N_a} \end{bmatrix}, \quad W_p(s) = \begin{bmatrix} W_f(s) & 0 & 0 \\ 0 & W_b(s) I_{N_s} & 0 \\ 0 & 0 & \dfrac{1}{A_t} I_{N_a} \end{bmatrix}.$$

Consequently, the controller K determined using H_∞ synthesis will be such that $||P \star K||_\infty < \gamma$ holds for the smallest possible $\gamma < 1$. The latter in particular implies:

a. $||T_{e_1 \to \nu_{node}}||_\infty < \gamma < 1$

b. $||T_{e_3 \to z_u}||_\infty < \gamma < 1$

c. $||T_{e_1 \to z_u}||_\infty < \gamma < 1$ and $||T_{e_2 \to z_u}||_\infty < \gamma < 1$

The above criterion are sufficient of ensuring all the control objectives described in Section 5.2.1 if we properly choose the constant weighting W_f, W_b, A_t and the transfer function weighting W_Δ. These criterion are detailed as follows:

a. $||T_{e_1 \to \nu_{node}}||_\infty < \gamma < 1$

The vector of transfer functions $T_{e_1 \to \nu_{node}}$ is equal to $T_{f \to \nu_{node}} W_f$. As already mentioned, we will here choose W_f as a constant weighting. Consequently, the constraint $||T_{e_1 \to \nu_{node}}||_\infty < 1$ in fact means:

$$\forall \omega, \quad \overline{\sigma}(T_{f \to \nu_{node}}(j\omega)) < \frac{\gamma}{\left|W_f\right|} < \frac{1}{\left|W_f\right|} \tag{5.10}$$

or equivalently:

$$\forall \omega, \quad \sqrt{T^*_{f \to \nu_{node}}(j\omega) T_{f \to \nu_{node}}(j\omega)} < \frac{\gamma}{\left|W_f\right|} < \frac{1}{\left|W_f\right|} \tag{5.11}$$

This criterion will ensure a good performance with respect to the specified disturbance (i.e. **Performance** and **Excitation** mentioned in Section 5.2.1). To justify this, let us first consider the open-loop case i.e. the case where $K = 0$. The transfer vector $T_{f\to\nu_{node}}$ then reduces to $G_{f\to\nu_{node}}$. Due to the resonant nature of the considered system, the largest singular value $\overline{\sigma}(G_{f\to\nu_{node}})$ of the transfer vector between f and ν_{node} will be made up of sharp peaks (as will be seen in e.g. Fig. 5.5). This will of course remain the case when a controller $K \neq 0$ will be applied to the system. However, since the controller K will be designed in such a way that Eq. (5.10) (and other constraints) holds with the smallest γ, the amplitude of these sharp peaks can be made smaller by a smart choice of the constant W_f (the larger W_f, the larger the peak reduction). Recall now the expression for the central energy, Eq. (4.17), given in Section 4.1.4. Using this expression and the sharp peak nature of the considered system, it is clear that a reduction of the peak amplitudes in $\overline{\sigma}(T_{f\to\nu_{node}})$ implies a reduction of the central energy[5].

For the PSD of the disturbance f, seen from Fig. 5.3 and using the definition (5.2), we have $f \in \Omega_{W_f}$. Thus, f has high PSD over the frequency band of interest Ω implies that W_f should be chosen as a band-pass filter focusing on Ω. However, due to the model reduction step of Section 4.3, $\overline{\sigma}(G_{f\to\nu_{node}})$ will only present peaks in Ω and will have low gain outside Ω which in turn implies that a such band-pass filter has already been applied via model reduction step. As a result, it is sufficient to only choose constant for W_f. Consequently, by imposing Eq. (5.10), we will only reduce the peaks in Ω.

b. $||T_{e_3\to z_u}||_\infty < \gamma < 1$

[5]This statement can be mathematically proved when $T_{f\to\nu_{node}}$ is a vector of transfer functions. Denote $T_{e_1\to\nu_{node}} = [T_{e_1\to\nu_{node},1}, T_{e_1\to\nu_{node},2}, \cdots, T_{e_1\to\nu_{node},N_z}]^T$. The definition of H_2 norm and H_∞ norm [125, 126] gives:

$$\left\|T_{e_1\to\nu_{node}}\right\|_2^2 = \frac{1}{2\pi} tr \int_{-\infty}^{+\infty} T^*_{e_1\to\nu_{node}}(j\omega) T_{e_1\to\nu_{node}}(j\omega) d\omega = \frac{1}{2\pi}\int_{-\infty}^{+\infty}\left(\sum_{i=1}^{N_z}\left|T_{e_1\to\nu_{node},i}(j\omega)\right|^2\right) d\omega$$

$$\left\|T_{e_1\to\nu_{node}}\right\|_\infty = \sup_\omega \overline{\sigma}\left(T_{e_1\to\nu_{node}}(j\omega)\right) = \sup_\omega \max \sqrt{\lambda\left(T^*_{e_1\to\nu_{node}}(j\omega) T_{e_1\to\nu_{node}}(j\omega)\right)} = \sup_\omega \sqrt{\sum_{i=1}^{N_z}\left|T_{e_1\to\nu_{node},i}(j\omega)\right|^2}.$$

The quantity $||T_{e_1\to\nu_{node}}||_2^2$ is in fact the surface below $\overline{\sigma}(T_{e_1\to\nu_{node}}(j\omega))^2$. Considering the sharp peak nature of $\overline{\sigma}(T_{e_1\to\nu_{node}}(j\omega))$, the controller that minimizes $||T_{e_1\to\nu_{node}}||_\infty$ will surely leads to a small $||T_{e_1\to\nu_{node}}||_2^2$.

Even though the model reduction has been done with care (see Section 4.3), an H_∞ controller designed on the reduced-order model G could still destabilize the full-order model G^{full} which is the so-called spill-over problem [17]. Ensuring that $||T_{e_3 \to z_u}||_\infty < \gamma$ with $\gamma < 1$ will prevent this spill-over problem to happen (i.e. **Robust stability** mentioned in Section 5.2.1). Indeed, from Fig. 5.3, we see that $T_{e_3 \to z_u}$ is equal to $W_\Delta T_{c \to u}$ where $T_{c \to u}$ is (if we compute its expression) the complementary sensitivity function (for a positive feedback K):

$$T_{c \to u} = (1 - K G_{V_a \to V_s})^{-1} K G_{V_a \to V_s} \tag{5.12}$$

To optimally choose the weighting function W_Δ, recall the robust stability result presented in Section 5.1.2. Using this result, if we choose W_Δ in such a way that the following holds:

$$\forall \omega, \ \overline{\sigma}(\Delta(j\omega)) \leqslant |W_\Delta(j\omega)| \tag{5.13}$$

where Δ is the relative error defined by Eq. (4.47) in the application of the model reduction step (see Section 4.3.5), an H_∞ controller satisfying $||T_{e_3 \to z_u}||_\infty = ||W_\Delta T_{c \to u}||_\infty < 1$ will be guaranteed not only to stabilize G, but also G^{full}.

To justify this, let us first note that the part of the full-order model between V_a and V_s can be written for the Δ defined in Eq. (4.47) and satisfying Eq. (5.13) as

$$G^{full}_{V_a \to V_s} = G_{V_a \to V_s}(I + \Delta).$$

Then, the closed-loop family $G^{full}_{V_a \to V_s} \star K$ can be recast in a closed-loop (Δ, M_d) (see Fig. 5.2) with $M_d = T_{c \to u}$. Consequently, the desired stability property, guaranteed by $||W_\Delta T_{c \to u}||_\infty < 1$, is a direct result of the robust stability result presented in Section 5.1.2. It is to be noted that, by virtue of this same robust stability result, the H_∞ controller will also stabilize all systems $\bar{G}$ that can be expressed as $\bar{G} = G_{V_a \to V_s}(I + \Delta)$ with a transfer matrix Δ satisfying Eq. (5.13).

Remark. *The above approach will only lead to satisfactory results if the relative error Δ in Eq. (4.47) satisfies the following constraint:*

$$\sup_{\omega\in\Omega} \ \overline{\sigma}(\Delta(j\omega)) \leqslant 1. \tag{5.14}$$

Otherwise, if $\overline{\sigma}(\Delta(j\omega)) > 1$*, according to Eq. (5.13) we will have* $|W_\Delta(j\omega)| > 1$ *in* Ω*. Thus, the condition* $||W_\Delta T_{c\to u}||_\infty < 1$ *will imply that* $\overline{\sigma}(T_{c\to u}(j\omega)) < 1$ *in* Ω*, which in turn implies that* $G_{V_a\to V_s}K$ *is small in* Ω*. This contradicts the fact that* $G_{V_a\to V_s}K$ *should be large in* Ω *in order to have enough control effect. The expression Eq. (5.14) also gives a quality tag for the reduced-order model. As an example, the second step of the model reduction technique proposed in Section 4.3 is only necessary if Eq. (5.14) is not satisfied after the first step.*

c. $||T_{e_1\to z_u}||_\infty < \gamma < 1$ and $||T_{e_2\to z_u}||_\infty < \gamma < 1$

These parts of the H_∞ criterion pertain to the limitation of the control effort (i.e. **Control signal** in mentioned in Section 5.2.1). More precisely, they shape the transfer matrices between the external signals (the force f and the measurement noise vector b) and the vector of control inputs u. We have indeed that $T_{e_1\to z_u} = A_t W_\Delta T_{f\to u} W_f$ and $T_{e_2\to z_u} = A_t W_\Delta T_{b\to u} W_b$. Due to the scalar nature of the weightings, these parts of the criterion ensure:

$$\forall\omega, \ \overline{\sigma}(T_{f\to u}(j\omega)) < \frac{1}{|A_t W_\Delta(j\omega) W_f|} \tag{5.15}$$

$$\forall\omega, \ \overline{\sigma}(T_{b\to u}(j\omega)) < \frac{1}{|A_t W_b W_\Delta(j\omega)|} \tag{5.16}$$

As already mentioned, we will choose A_t and W_b as constant weightings. This simple choice is made possible by the shape of the frequency response of the transfer function weighting $W_\Delta(s)$ which will generally have high amplitude outside the frequency band of interest Ω since it must satisfy Eq. (5.13). The presence of $|W_\Delta(j\omega)|$ in the above equations ensures that the control input u will have roll-off at higher frequencies which eliminates the influence of (high frequency content) noise b on u and also ensures that u will have high PSD mainly located in Ω which limits the control efforts.

The constant weightings A_t and W_b can be used to limit the amplitude of the control effort (whose frequency content will be concentrated in Ω via $|W_\Delta(j\omega)|$)

and we can make a distinction between the contribution of f and b in this control effort by independently tuning A_t and W_b. A good practice is to increase these constants as long as the H_∞ criterion remains solvable for a constant $\gamma < 1$. As already mentioned, the required control efforts (and thus the extent with which the constants can be increased) depend on the desired central energy reduction (i.e. the choice of W_f, see criterion **a.** above).

Remark. *A controller that is stable itself is preferred. Otherwise, for actual implementation, as long as the control loop is broken for some reason when the controller is functioning (for example the sensor failure, the interruption of physical connections, etc), the presence of an unstable controller may lead to signal explosion and thus damage the equipment. However, the H_∞ synthesis will not guarantee the stability of the obtained controller. If excessive constraints are imposed, it is possible that we obtain an unstable controller. Thus, we will check the stability of the obtained controller. If it is unstable, we re-tune the weightings.*

5.2.3 Controller reduction and discretization

As mentioned in Section 3.4, for the ease of the implementation, the obtained H_∞ controller will be reduced without degrading the performance. Due to the choice of the weighting functions discussed in the previous subsection (especially for the choice of W_Δ), the obtained H_∞ controller will have low gain dynamics outside the frequency band of interest. Moreover, these dynamics outside the frequency band of interest are not/less important for the control objectives and can therefore be removed in the reduced-order controller. Consequently, the simple and widely used Balanced Truncation method [34, 35] can be applied to perform controller reduction. More precisely, we determine the controller with the lowest order that nevertheless preserve the stability and the level of performance with the full-order model. In addition, as mentioned above, a stable controller is preferred and Balanced Truncation method is able to preserve the stability of the to-be-reduced controller.

Since the controller will be implemented in a digital control board[6], the obtained reduced-order controller has finally to be discretized. The sampling time should

[6] *DSpace DS1104* in our case

be chosen small enough to guarantee that the frequency response of the discrete-time controller remains close to the continuous-time controller over the frequency band of interest Ω. This consideration is discussed in Section 5.2.4.5.

5.2.4 Application to the beam-piezo system

We will now apply the proposed H_∞ criterion on our specific beam-piezo system.

5.2.4.1 Augmented system

According to Section 3.2, we focus on a force disturbance f which has high PSD in $\Omega = (600, 3000)\ rad/s$ where it covers 11 to-be-controlled modes. Referring to Fig. 5.3, the to-be-controlled system G is the reduced-order model obtained in Section 4.3.5, i.e. model (4.50), which is reduced from the identified full-order model $G^{full}(\theta_{id})$ obtained in Section 4.2.3. The power amplifiers used to drive the PZT actuators have the same gain -10. Thus the scalar factor A_p is set to -10. The phase shift (tested using the frequency analyzer *HP 35652B*) in the anti-aliasing filters is approximated by a pure time delay of $T_{anti} = 1.6 \times 10^{-4} s$. Moreover, as discussed by Section 5.2.3, the obtained controller will be in continuous time and then be discretized for implementation in the control board *DSpace DS1104* with a small enough sampling time T_s and we will see in the sequel that $T_s = 2 \times 10^{-4} s$. In reality, the discretization and the digital conversion mechanism of the control board will together introduce a pure time delay of one sampling time. In order to take into account this phenomenon, we will add a pre-delay of T_s into the to-be controlled system. These two time delays (i.e. $T_{anti} + T_s$) will be approximated by the transfer function $F_d(s)$ using Pade approximation of order 2 with the following expression[7]:

$$F_d(s) = \frac{s^2 - 1.667 \times 10^4 s + 9.259 \times 10^7}{s^2 + 1.667 \times 10^4 s + 9.259 \times 10^7}.$$

The choice of the weightings (i.e. W_f, W_b, A_t and W_Δ) is detailed as follows.

[7]The order is chosen such that there will be almost no difference in phase response between the approximated transfer function and the pure time delay before 3000 rad/s

5.2.4.2 Weightings and results

First, let us discuss the choice of the weighting $W_\Delta(s)$ as it is the only weighting that does not have trade-off with other weightings and will not be tuned over the entire design process. W_Δ is chosen as a simple transfer function that satisfies Eq. (5.13). The modulus of the frequency response of the chosen W_Δ is represented in Fig. 5.4 and we observe that Eq. (5.13) is indeed satisfied. The details for the construction of W_Δ can be found in Appendix B.

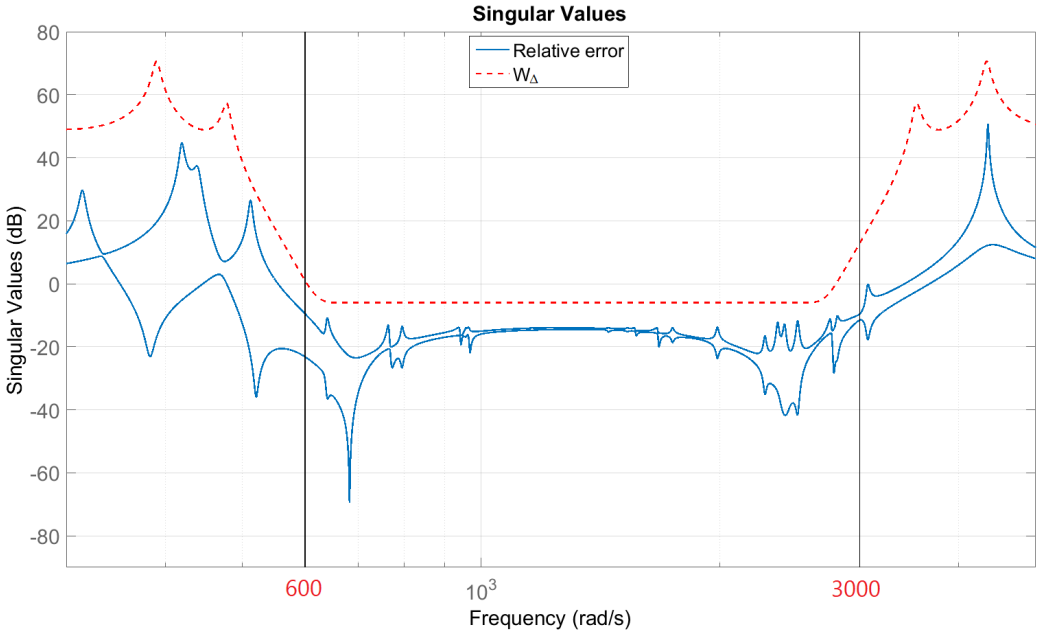

Figure 5.4: $\sigma(\Delta(j\omega))$ (solid blue) and $|W_\Delta(j\omega)|$ (dashed red)

For other weightings, there exists the trade-off. The weighting W_f relates to the level of the disturbance and as discussed in Section 5.2.2, the larger W_f, the larger the peak reduction. This requires more control effort which implies a smaller A_t, see Eq. (5.15). However, we will have the risk of obtaining $\gamma > 1$ if A_t is too small. Therefore, for a given W_f, we try to find A_t that ensures the existence of a controller with $\gamma < 1$ with the largest energy reduction rate. The choice of W_b has little effect on the result. After several iterations, we finally choose $W_f = 6.9$, $A_t = 3.9 \times 10^{-2}$ and $W_b = 1$. Together with the other weightings[8], we obtain a controller K of order 52 for which the H_∞ criterion holds with $\gamma = 0.9923$. Fig. 5.6 shows the singular values of all the transfer

[8]The gain of the power amplifier $A_p = -10$ and the Pade filter F_d approximating a pure delay of $T_{anti} + T_s = 3.6 \times 10^{-4}$ s (see Fig. 5.3).

functions from inputs f, b, c to outputs ν_{node}, u in open-loop and closed-loop case[9] and the corresponding weightings. From which we observe that the closed-loop transfer functions (respectively corresponding to the performance, the control energy consumption, the measurement noise and the robust stability) are well saturated which means that all the criterion are well imposed. The frequency response of this controller K is given in solid blue in Fig. 5.8.

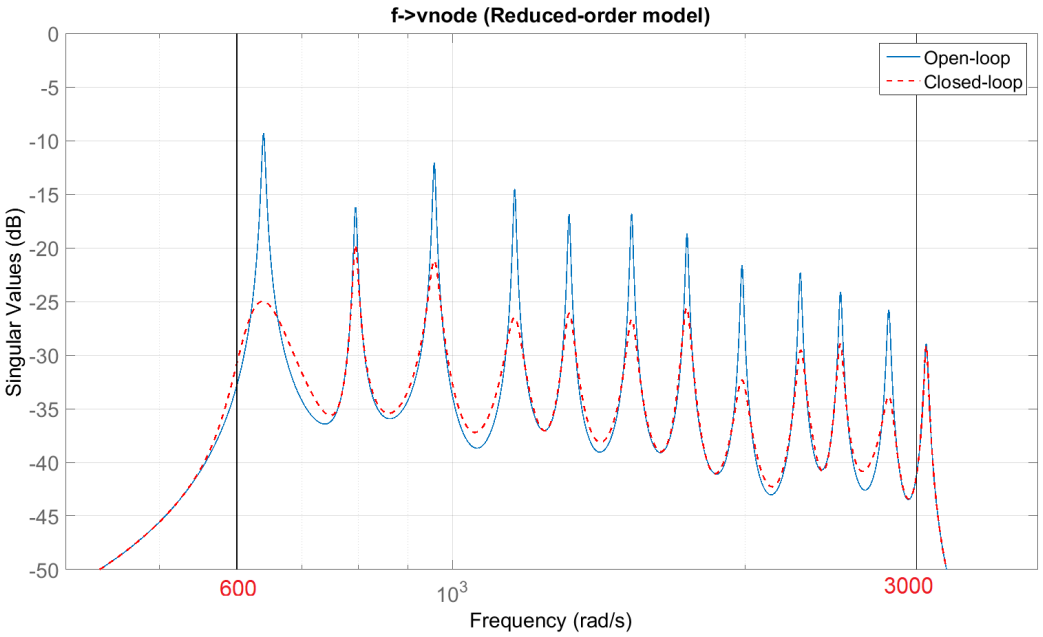

Figure 5.5: $\overline{\sigma}(G_{f\to\nu_{node}}(j\omega))$ (solid blue) and $\overline{\sigma}(T_{f\to\nu_{node}}(j\omega))$ (dashed red) when the controller K is applied to the reduced-order model G

To illustrate the control effect in terms of H_∞ norm, we compare the closed-loop quantity $\overline{\sigma}(T_{f\to\nu_{node}}(j\omega))$ with the open-loop quantity $\overline{\sigma}(G_{f\to\nu_{node}}(j\omega))$ in Fig. 5.5 and we observe that all the peaks in $(600, 3000)$ rad/s are severely reduced as imposed, i.e. $\forall\omega$, $\overline{\sigma}(T_{f\to\nu_{node}}(j\omega)) < -19$ dB. As will be seen later, this peak reduction is performed with an acceptable control action for typical disturbance force f. Further reduction would of course be possible, but at the cost of higher control actions (and thus more energy consumption).

As imposed in the H_∞ criterion, the controller K designed with the reduced-order model G indeed stabilizes the full-order model $G^{full}(\theta_{id})$ and, when this controller is applied to $G^{full}(\theta_{id})$, we obtain a very similar peak reduction as with the reduced-order model G (compare Fig. 5.7 and Fig. 5.5). Note that,

[9]It can be seen from Fig. 5.3 that $T_{b\to\nu_{node}}$, $T_{f\to u}$, $T_{b\to u}$ and $T_{c\to u}$ have no open-loop responses.

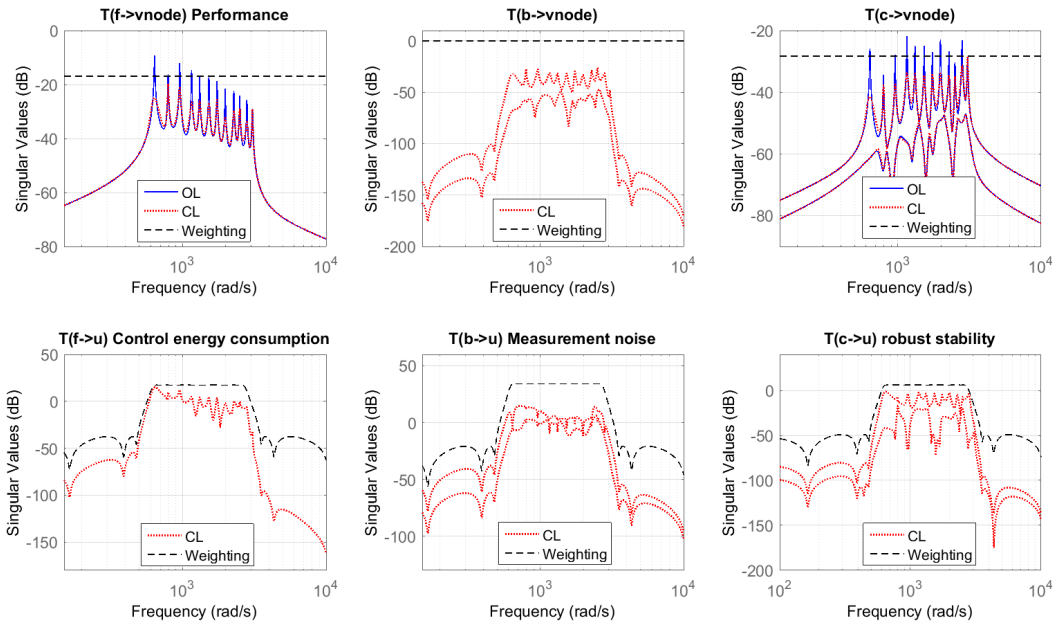

Figure 5.6: Singular value of all the transfer functions and the corresponding weightings: Open-loop (solid blue) vs Closed-loop (dotted red) vs Weightings (dashed black)

as expected, only the modes in $(600, 3000)$ rad/s are reduced in the closed-loop made up of K and $G^{full}(\theta_{id})$ (see Fig. 5.7).

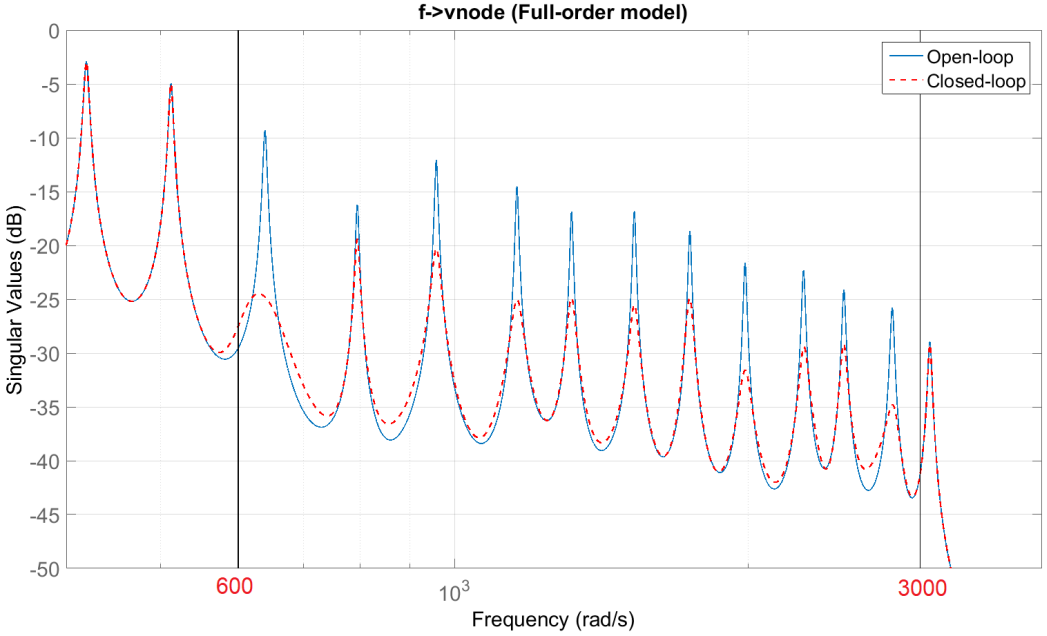

Figure 5.7: $\overline{\sigma}(G^{full}_{f\to\nu_{node}}(j\omega))$ (solid blue) and $\overline{\sigma}(T_{f\to\nu_{node}}(j\omega))$ (dashed red) when the controller K is applied to the full-order model $G^{full}(\theta_{id})$

5.2.4.3 Reduced-order controller

The obtained controller K of order 52 has several low gain dynamics outside $(600, 3000)$ rad/s as shown in solid blue in Fig. 5.8. By ignoring these low gain dynamics, the controller K can be further reduced. As discussed in Section 5.2.3, we apply Balanced Truncation method and gradually reduce the order[10] of the controller K without destabilizing the system and without significant change in the closed-loop performance. After some trial and error, we finally stop at a reduced-order controller of order 30, denoted K_{red}. Fig. 5.9 indeed shows the almost perfect match between the closed-loop quantities $\overline{\sigma}(T_{f\rightarrow\nu_{node}}(j\omega))$ obtained when applying the full-order controller K (dashed green) and the reduced-order controller K_{red} (dotted red) to the full-order model $G^{full}(\theta_{id})$ (solid blue). The frequency response of K_{red} is represented in dotted red in Fig. 5.8 and compared with K. It is to be noted that both K and K_{red} are stable transfer functions.

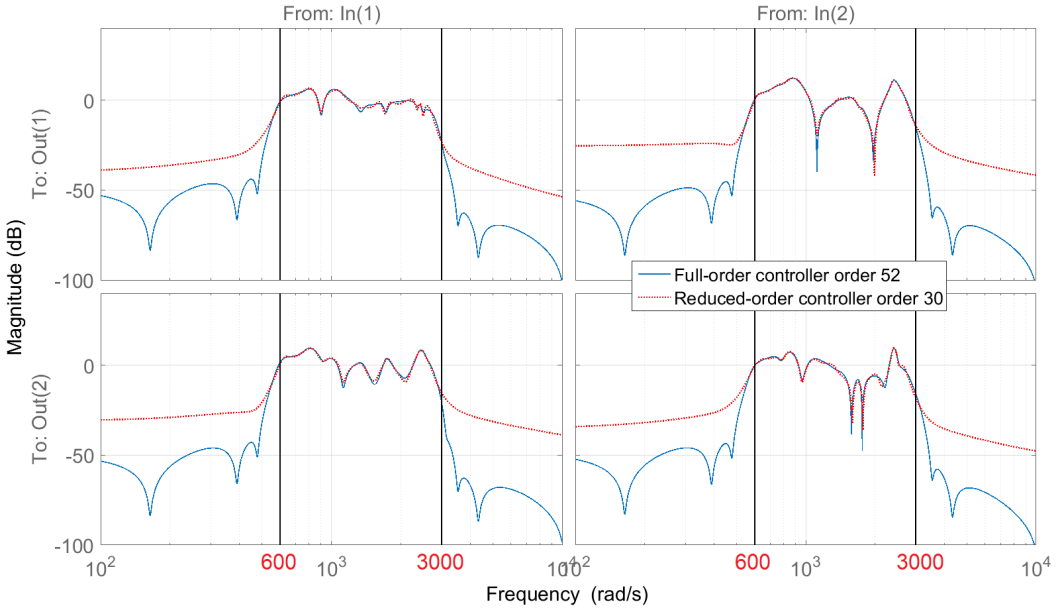

Figure 5.8: Modulus of the frequency response of the full-order controller K (solid blue) and of the reduced-order controller K_{red} (dotted red)

5.2.4.4 Performance — Central energy reduction rate

Here, we discuss the performance of the closed-loop system made up of the full-order model G^{full} and the reduced-order controller K_{red}. The performance is

[10] We gradually truncate the states that correspond to smaller Hankel singular values

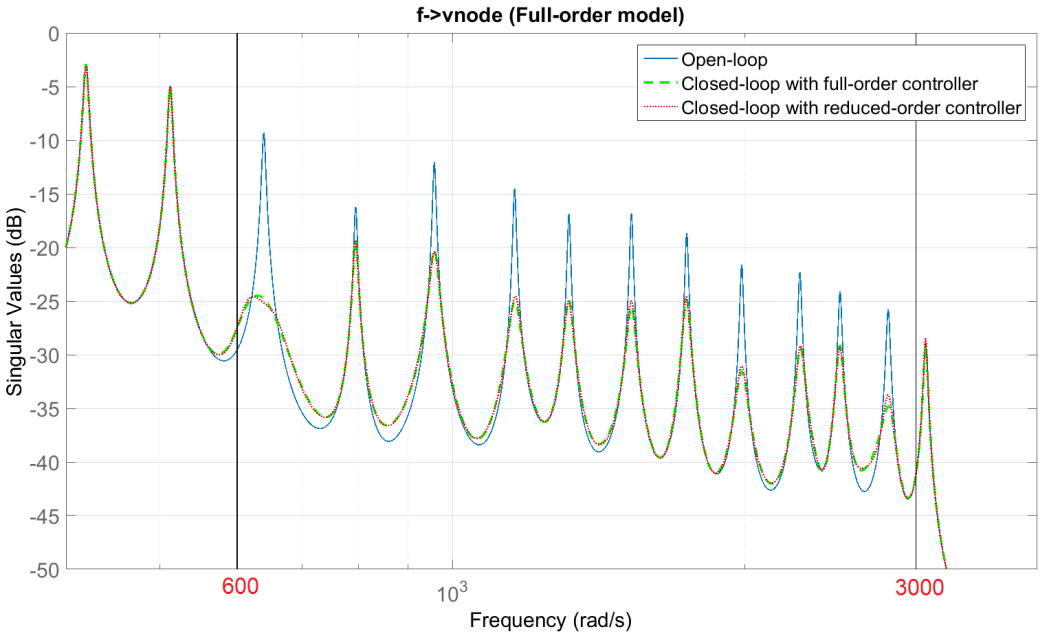

Figure 5.9: $\overline{\sigma}(G^{full}_{f\to\nu_{node}}(j\omega))$ (solid blue) vs $\overline{\sigma}(T_{f\to\nu_{node}}(j\omega))$ with full-order controller K (dashed green) vs $\overline{\sigma}(T_{f\to\nu_{node}}(j\omega))$ with reduced-order controller K_{red} (dotted red)

characterized by the reduction rate of the vibration energy in the central zone (central energy) which is equal to the reduction rate of the average proportional central energy[11] $\overline{E^p_{cent}}$ (see Section 4.1.4 for its definition). Intuitively, by comparing the solid blue and the dotted red curves in Fig. 5.9, we can expect that the reduction of the proportional central energy will be important. Using Eq. (4.17), the reduction rate of $\overline{E^p_{cent}}$ can be deduced as follows:

$$r^p_e = \left(1 - \frac{\left(\overline{E^p_{cent}}\right)_{CL}}{\left(\overline{E^p_{cent}}\right)_{OL}}\right) \times 100\% = \left(1 - \frac{||T_{f\to\nu_{node}} L_f||_2^2}{||G^{full}_{f\to\nu_{node}} L_f||_2^2}\right) \times 100\% \qquad (5.17)$$

where $T_{f\to\nu_{node}}$ is here the closed-loop transfer vector between f and ν_{node} and where $L_f(s)$ is a transfer function such that the PSD of f is given by $|L_f(j\omega)|^2$. When L_f is given by a band-pass filter in the frequency band of interest $(600, 3000)$ rad/s, the reduction rate r^p_e is equal to 59.6%. When L_f corresponds to the PSD of the actual disturbance force f generated by the shaker, the reduction rate r^p_e is then equal to 62.5%. It should be noted that the above expression (i.e.

[11] We mainly focus on the reduction rate instead of the exact value of the central energy

Eq. (5.17)) neglects the effect of the measurement noise b in the closed-loop situation.

5.2.4.5 Numerical simulation

In order to numerically verify the effectiveness of the obtained reduced-order controller K_{red} and also to investigate the effect of the measurement noise b on the performance, we have performed simulations.

As explained in Section 5.2.3, the actual implemented controller will be the discretization of K_{red}, denoted K_{red}^d, and K_{red}^d will thus be the controller applied in simulations. Here, we use Zero-Order-Hold [127] to perform the discretization. The choice of the sampling time T_s should be relatively small (i.e. the Nyquist frequency [127] should be much larger[12] than the maximum frequency of the frequency band of interest) and should also consider the computing power of the digital control board (*DSpace DS1104* in our case). Thus, we finally choose $T_s = 2 \times 10^{-4} s$ with the Nyquist frequency equals to $\frac{1}{2Ts} = 2500Hz = 1.57 \times 10^4\ rad/s$ which is much larger than 3000 rad/s. Fig. 5.10 compares the frequency response of K_{red} and K_{red}^d which shows that this choice T_s is small enough as we observe a perfect match between K_{red} and K_{red}^d before 3000 rad/s in both modulus and phase. We also remove the pre-delay of one sampling time from $F_d(s)$ and thus take a new $F_d(s)$ which only approximates a pure time delay of $T_{anti} = 1.6 \times 10^{-4} s$ (instead of $T_{anti} + T_s$ in the controller design section, see Section 5.2.4.1). We also add white noise to the outputs of $F_d(s)$ (inputs of the controller) as the measurement noise. The Signal-to-Noise Ratio is the same as that in the controller design, which is the ratio between the weighting for the disturbance f and the weighting for the measurement noise W_b, i.e. W_b/W_f. The PSD of the disturbance f is given by $|L_f(j\omega)|^2$ with L_f a band-pass filter in $(600, 3000)\ rad/s$.

We then simulate the real-time proportional central energy $E_{cent}^p(t)$ using the following expression (referring to Eq. (4.16)):

$$E_{cent}^p(t) = \nu_{node}^T(t) \cdot \nu_{node}(t) \tag{5.18}$$

[12] This is to avoid that the discretized controller has large phase shift near the Nyquist frequency which is close to the frequency band of interest

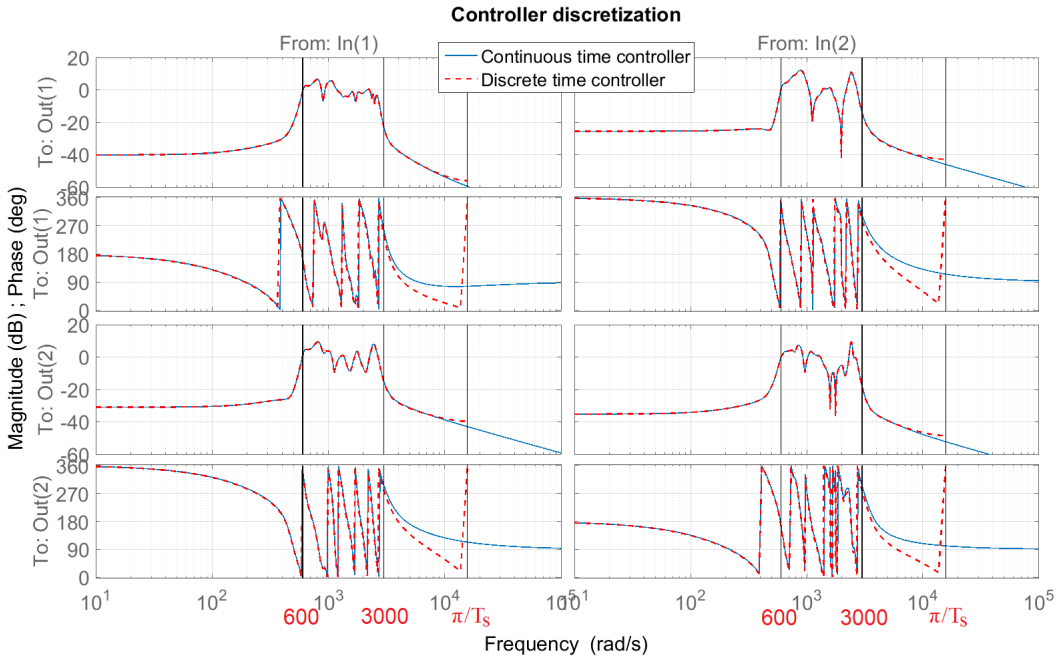

Figure 5.10: K_{red} (solid blue) vs K^d_{red} (dashed red)

Fig. 5.11 shows the result of the simulation where we observe a stable closed-loop system and a significant reduction of the energy $E^p_{cent}(t)$. Using Eq. (4.16) and Eq. (5.17), the reduction rate r^p_e given by this simulation is 60.12%. It should be noted that this result is under the presence of the measurement noise. We also perform simulation without the measurement noise and obtain a reduction rate of 61.28%, very close to 60.12% (with measurement noise). This means that the controller is indeed able to effectively filter the measurement noise such that it has ignorable effect on the global performance. These simulations have also allowed us to verify that the control efforts (due to the presence of both f and b) remain at all time in the working range of the digital control board and the actuators.

5.3 Experimental validation

Let us now verify whether this control performance (in particular the large reduction rate) can also be achieved in practice when the obtained controller is applied on the real setup.

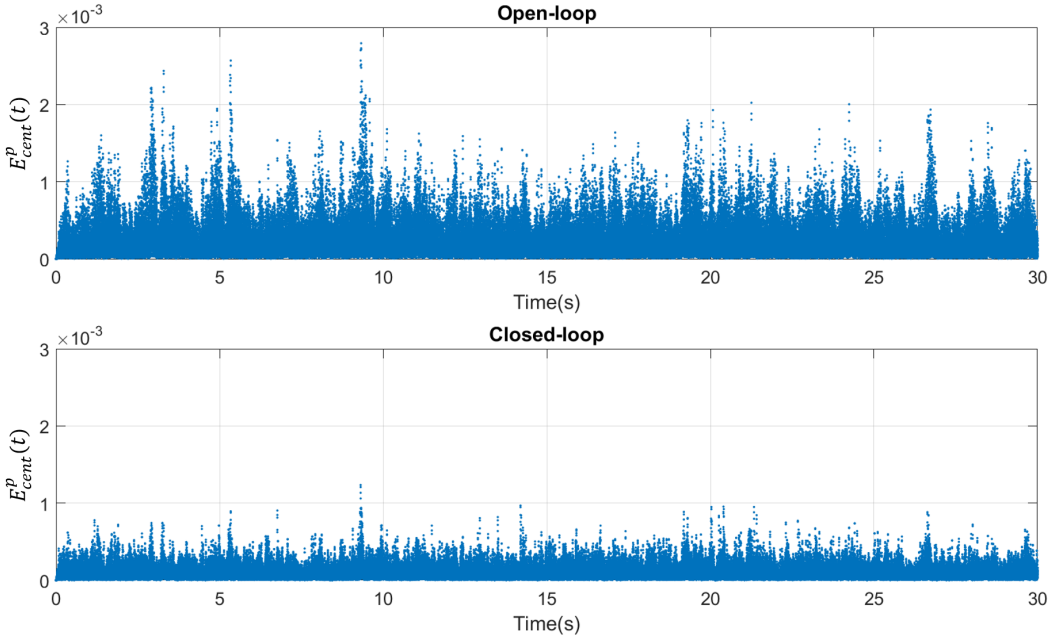

Figure 5.11: Real-time proportion central energy simulation: Open-loop (upper figure) vs Closed-loop (lower figure)

The digital control board used to implement the controller (i.e. the discrete time controller K^d_{red} obtained in Section 5.2.4.5 with sampling time $T_s = 2 \times 10^{-4} s$) is *DSpace DS1104*. The force disturbance is applied by an electrodynamical shaker (see the top right figure of Fig. 3.1) which requires an input reference signal to characterize the frequency band of the output force. We thus use the control board (a different channel from those for control outputs) as a signal generator where a filtered white noise signal[13] is generated and then sent to the shaker as the reference such that the output force of the shaker (the force disturbance f applied to the beam) will only have high PSD in $(600, 3000)$ rad/s. The effect of the mechanism and the signal processing between the white noise and the force disturbance f is represented by a transfer function $L_f(j\omega)$ so that the PSD of f is characterized by $|L_f(j\omega)|^2$. The gain of the power amplifier is -10 (the value of A_p) and the cutoff frequency of the anti-aliasing filter is set to 1000 Hz (about 6.3×10^3 rad/s)[14].

To evaluate the actual reduction rate obtained on the experimental setup, we

[13] We set up a digital band-pass filter inside *DSpace DS1104* which has a pass-band of $(600, 3000)$ rad/s

[14] The cutoff frequency 1000 Hz is smaller than the Nyquist frequency, i.e. $\frac{1}{2T_s} = 2500$ Hz

will compare the open-loop (without control actions, i.e. $V_a = 0$) and the closed-loop (with controller K_{red} activated) situation where the same disturbance f (of PSD $|L_f(j\omega)|^2$) is applied to the beam. In both situations, $\nu_{node_i}(t) = \nu(x_i, t)$ is measured via the laser velocimeter at the $N_z = 19$ nodes x_i that have been chosen in the central zone[15].

First, let us see the vibration state of a point in the central zone, which will intuitively demonstrate the vibration reduction. In the top part of Fig. 5.12, we represent, as a function of the time, the vibration velocity $\nu_{node_i}(t) = \nu(x_i, t)$ of one of these nodes during an experiment where the controller is kept inactive (open-loop situation) from $t = 0$ till $t = 10$ seconds and then the controller is activated (closed-loop situation) for 10 seconds, etc.(the middle/bottom part of Fig. 5.12 represents the real-time actuation voltage of the PZT actuators). We can clearly observe the velocity reduction when the controller is active. Evaluating the (proportional) vibration energy $\overline{E^p_{node_i}}$ at node i as the average value of $\nu^2_{node_i}(t)$ in the open-loop and closed-loop situation, the reduction of the vibration energy at this particular node is equal to 65.4%. For comparing with the theoretical value, we also simulate the real-time velocity of the same node which gives consistent reduction rate: 63.1% with measurement noise and 65.1% without measurement noise. In Fig. 5.12, the voltages applied on the two actuators (i.e. V_a) are also represented and they remain at all time within the working limits of the control board and piezo-actuators.

Second, let us formally evaluate the reduction rate of the central energy using the measurements $\nu_{node_i}(t) = \nu(x_i, t)$ at all 19 nodes. For this purpose, we will estimate the central energy $\overline{E^p_{cent}}$ in the open-loop and the closed-loop situations as (see Eq. (4.16)):

$$\overline{E^p_{cent}} = \sum_{i=1}^{19} \overline{E^p_{node_i}}. \tag{5.19}$$

Based on the central energy obtained in this way in open-loop and closed-loop[16], we obtain a reduction rate of 58.9%. This estimate of the experimental reduction

[15] in fact, 19 different experiments have to be performed to obtain this result since only one laser velocimeter is available

[16] It is to be noted that, as opposed to what is done for $\left(\overline{E^p_{cent}}\right)_{CL}$ in Eq. (5.17), the above manner to evaluate the central energy in the closed-loop situation considers the influence of both the disturbance force f and the measurement noise b.

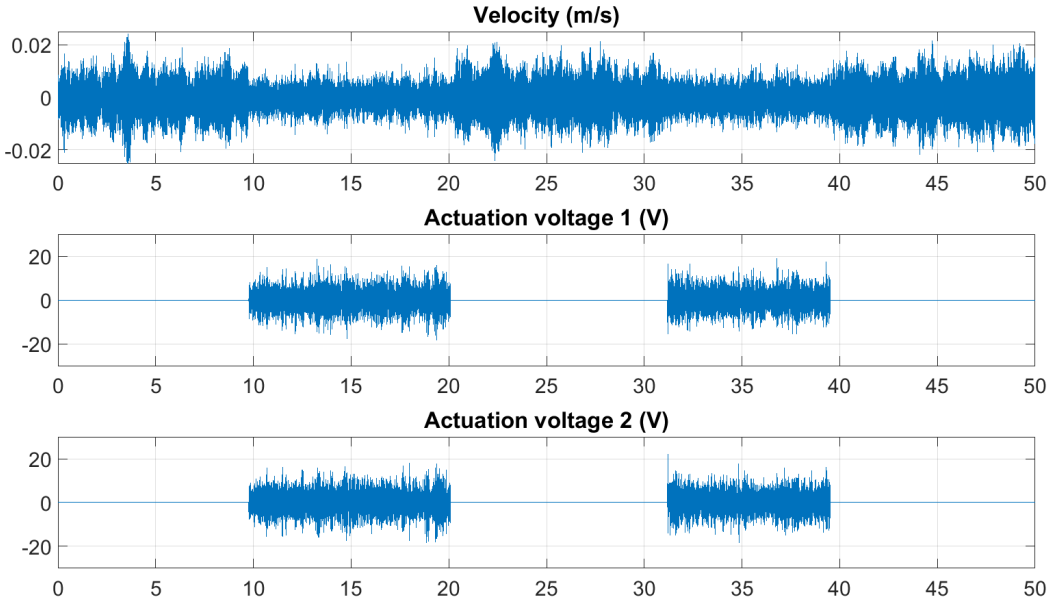

Figure 5.12: Velocity of an arbitrary point in the central zone (top figure) for an experiment consisting of switching on and off the controller every 10 seconds, the first element of V_a (mid-figure) and the second element of V_a (bottom figure)

rate is very close to the one that is theoretically computed on the loop made up of the controller K_{red} and of the full-order model $G^{full}(\theta_{id})$ (i.e. 62.5%, see Section 5.2.4.4).

It can therefore be concluded that the model $G^{full}(\theta_{id})$ deduced from grey-box identification was a reliable model of the actual setup for control purpose. It is also to be stressed that the model improvement step, i.e. the grey-box identification, is necessary. Indeed, if the H_∞ controller is designed based on the initial model $G^{full}(\theta_{init})$ and then applied on $G^{full}(\theta_{id})$, the obtained central energy reduction rate would go down to only 46%.

Let us further illustrate the energy reduction rate of 58.9%. Using the measurements $\nu_{node_i}(t) = \nu(x_i, t)$ obtained at all 19 nodes and the applied disturbance force f, we use the frequency analyzer to estimate the frequency responses of the transfer functions between f and ν_{node_i} $(i = 1...19)$ in the open-loop and the closed-loop situations, denoted respectively $G_{f\to\nu_{node_i},m}(j\omega)$ and $T_{f\to\nu_{node_i},m}(j\omega)$. For $(i = 1...19)$, we obtain the open-loop transfer vector $G_{f\to\nu_{node},m}(j\omega)$ and the closed-loop transfer vector $T_{f\to\nu_{node},m}(j\omega)$. We subsequently compute the largest

singular value of these two transfer vectors and the result are plotted, as a function of the frequency, in Fig. 5.13. Even though we can see some discrepancies between this figure and Fig. 5.9 (that can be due among other things to the inherent difficulties in this validation step of pointing the laser velocimeter at exactly the same 19 positions as during the identification procedure), we also clearly observe that the 11 modes in the frequency band of interest $(600, 3000)$ rad/s are effectively controlled (reduced). The peak reduction in dB of each of these 11 modes is listed in Table 5.1 where the average peak reduction is 8 dB with 15 dB being the maximum. Such peak reductions can also be observed in other papers (see e.g. [11, 70, 71, 73, 128]), but on fewer resonance peaks (meaning that the reduction rate will be smaller). Note moreover that the control problem is here more complex since the energy reduction is achieved in a zone where there are no actuators and no sensors.

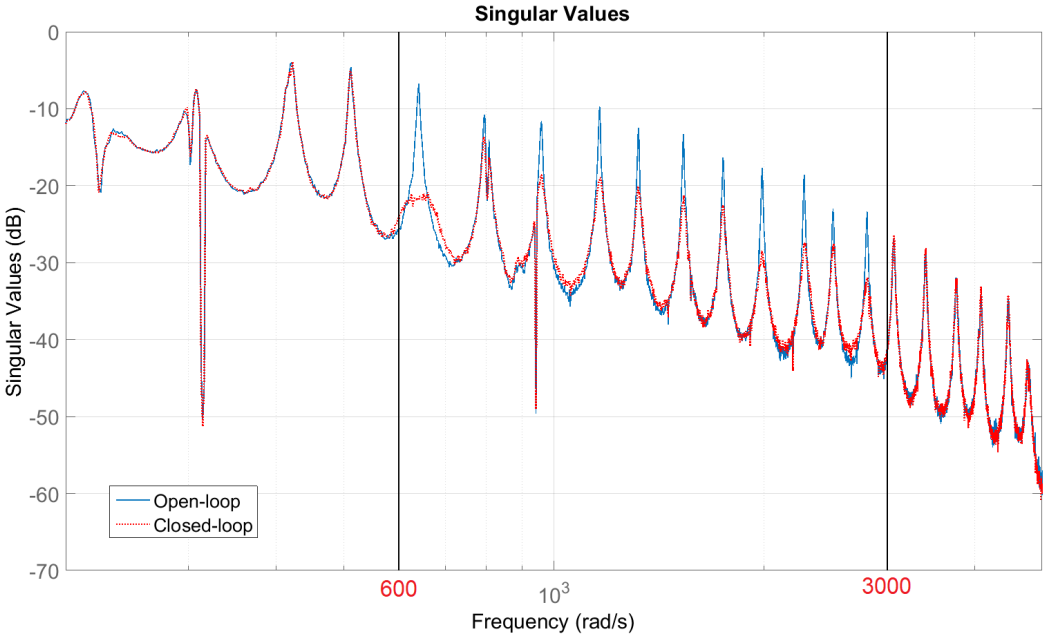

Figure 5.13: $\overline{\sigma}(G_{f\to\nu_{node},m}(j\omega))$ (solid blue) and $\overline{\sigma}(T_{f\to\nu_{node},m}(j\omega))$ (dotted red) measured on the experimental set-up

Table 5.1: Peak reduction (dB) of the 11 controlled modes

Mode frequency (rad/s)	641	795	960	1163	1322	1533
Peak reduction (dB)	15	3	7	8	8	8
Mode frequency (rad/s)	1747	1987	2282	2510	2808	
Peak reduction (dB)	6	11	9	5	8	

Our objective was thus to reduce the vibration in the central zone of the beam. One could wonder what happens in the other parts of the beam. We have therefore also measured the velocity at one point on the left side and at one point on the right side of the central zone (see Fig. 5.14) and we have observed that the vibration at these two points is also reduced in closed-loop: the reduction of the vibration energy at these two nodes are respectively equal to 56.8% and 49.8%, however smaller than that of the measured point in the central zone (i.e. 65.4%).

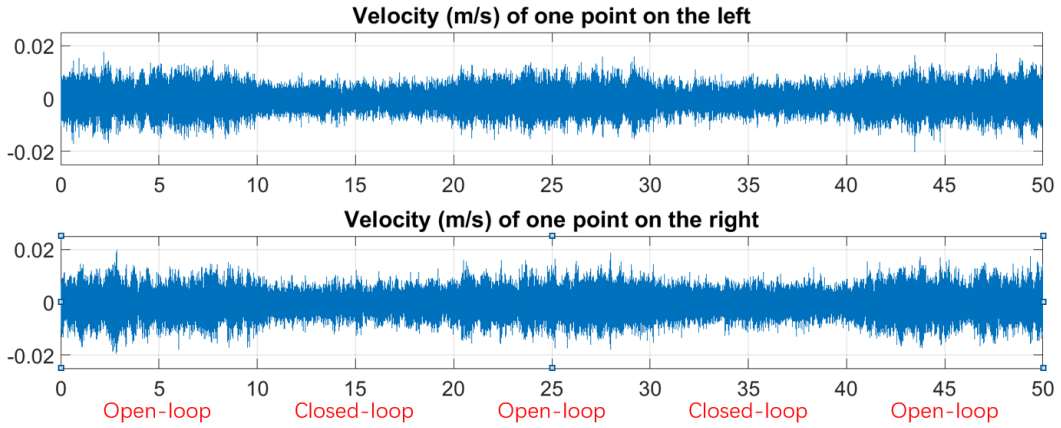

Figure 5.14: Velocity of one point on the left (top figure), velocity of one point on the right (bottom figure)

5.4 Discussion in single-variable case — Limitation of SISO controllers

In Section 3.3, we have pointed out that a SISO controller is not sufficient for effectively controlling all the 11 modes in $(600, 3000)$ rad/s, which is the most important limitation of a SISO controller. This limitation can be explained by the position of the PZT pairs. In particular, if a PZT pair is located close to the node of a certain mode shape, it cannot effectively excite or detect this mode so that this mode cannot be controlled as efficiently as other modes, see Appendix A for detailed explanations. The objective of this part is to verify this discussion.

In this work, we illustrate the reduction of different modes by comparing the maximum singular value of the transfer function vector from the force disturbance f to the velocity vector ν_{node} in both open-loop and closed-loop case (i.e.

$\overline{\sigma}(G^{full}_{f\to\nu_{node}}(j\omega))$ and $\overline{\sigma}(T_{f\to\nu_{node}}(j\omega)))$, see for example Fig. 5.7 where we clearly see the reduction of each mode (peak). If the discussion of Section 3.3 was right, by comparing the same quantity in both open-loop case and closed-loop case with a SISO controller, there must exist peaks (modes) with little or even no reduction, which in turn leads to lower reduction rate. To verify this, we will apply the proposed H_∞ criterion with the same choice of weighting functions to the model with only one actuation input and one sensing output. This model will be obtained by truncating the ignored input and output of the reduced-order model G obtained in Section 4.3.5. Similarly, the corresponding full-order model will be obtained by truncating the full-order model G^{full} obtained in Section 4.2.3. As an example, we here consider the SISO case with 10^{th} PZT pair as actuator and 5^{th} PZT pair as sensor (respectively the first element of actuation inputs and sensing outputs). Consequently, the input relating to the 16^{th} PZT pair and the output relating to the 11^{th} PZT pair (respectively the second element of actuation inputs and sensing outputs) are truncated from G and G^{full}, which gives a reduced-order model $G^{v_{10}\to v_5}$ and a corresponding full-order model $G^{full,v_{10}\to v_5}$. The H_∞ synthesis based on $G^{v_{10}\to v_5}$ gives us a SISO controller $K^{v_5\to v_{10}}$. Then we compute the closed-loop singular value $\overline{\sigma}(T^{v_{10}\to v_5}_{f\to\nu_{node}}(j\omega))$ made up of the full-order model $G^{full,v_{10}\to v_5}$ and the controller $K^{v_5\to v_{10}}$. Fig. 5.15 shows the comparison between the open-loop singular value $\overline{\sigma}(G^{full,v_{10}\to v_5}_{f\to\nu_{node}}(j\omega))$ (solid blue) and the closed-loop singular value $\overline{\sigma}(T^{v_{10}\to v_5}_{f\to\nu_{node}}(j\omega))$ (dotted red). As expected, we observe the phenomenon that there are several peaks with little or even no reduction. Moreover, in Fig. 5.15, we also show (in dashed yellow) the response from the 10^{th} PZT pair to the 5^{th} PZT pair measured from the setup (a copy of the blue line in Fig. A.2). We observe that the peaks with little or no reduction are exactly where the setup shows low response between the chosen actuator and sensor, for example at about 800 rad/s, 1500 rad/s and 1700 rad/s. This observation fully proves the discussion in Appendix A that if the modes cannot be effectively detected or excited, they cannot be controlled. Finally, we compute the reduction rate of the central energy and obtain 38.54%. The simulation gives a similar reduction rate of 41.81%. As expected, the reduction rate of a SISO controller is much smaller than that of the MIMO controller K_{red} which is around 60%. In addition, we have also designed other SISO controllers using the same procedure described above which gives $K^{v_{11}\to v_{10}}$, $K^{v_5\to v_{16}}$ and $K^{v_{11}\to v_{16}}$. They all show similar results with $K^{v_5\to v_{10}}$.

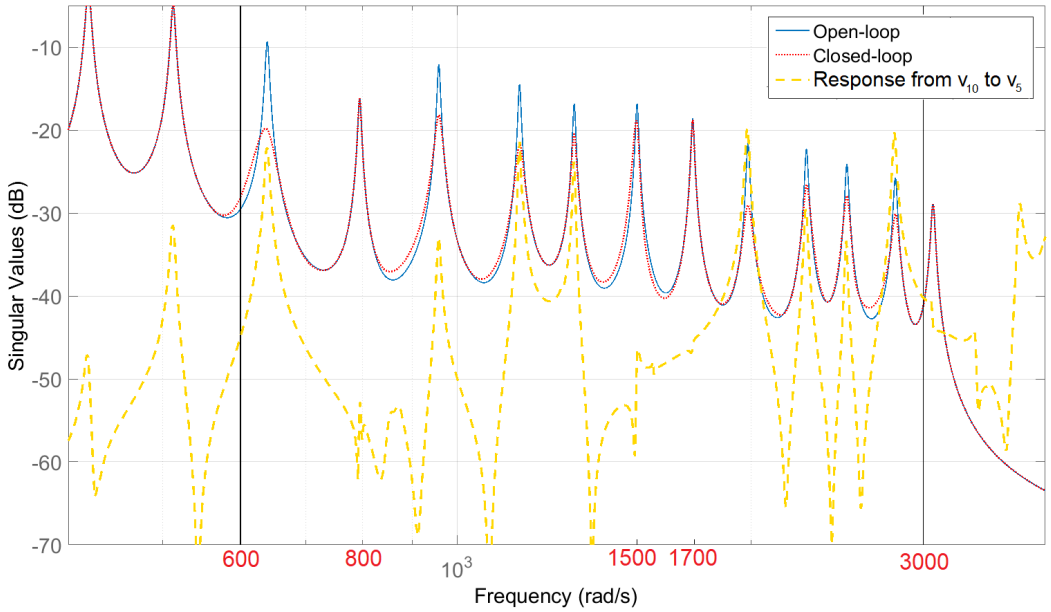

Figure 5.15: Performance of the SISO controller with the 10^{th} PZT pair as actuator and 5^{th} PZT pair as sensor

In conclusion, a SISO controller indeed has the limitation, it is not able to effectively control all the 11 modes in $(600, 3000)$ rad/s, which leads to a small central energy reduction rate. A MIMO controller is indeed necessary.

5.5 Summary

This chapter proposes a particular H_∞ criterion to tackle our vibration reduction problem which allows us to compute a multi-variable H_∞ controller under multiple control objectives: reduce the central energy, limit the control energy consumption and guarantee the robust stability. The proposed H_∞ criterion is then applied on the to-be-controlled model. By properly choosing the weightings, we obtain a MIMO controller which is able to effectively reduce the vibration energy (with a large energy reduction rate) in the central zone of the beam under a force disturbance over the specified large frequency band. The obtained controller is then further reduced without destabilizing the closed-loop stability or degrading the performance. The effectiveness of the controller is validated by simulations and the measurements on the actual setup as we obtain good match between the theoretical value and the measurement result. These results also prove that the obtained model is very close to the actual experimental setup.

The obtained controller is indeed also able to reduce the vibration energy in other zones however with smaller reduction rate than the central zone which implies that the control effort is concentrated in the central zone as expected. Based on the full-order model, we also verify that a SISO controller is not sufficient to control all the modes in the frequency band of interest. A MIMO controller is thus necessary.

It should be noted that the obtained controller is centralized, i.e. it processes all sensor data to generate all feedback control signals. The drawback of a centralized controller is the complexity of the controller which gives high computational burden to the centralized processor, and the complexity of the physical connections. Distributed controller may be a solution for these drawbacks as it allows us to use a number of simpler localized controllers which will work together to achieve a global performance. The next chapter will introduce how to build a distributed model of the same setup for the purpose of distributed control.

Chapter 6

Modeling for distributed control

In the centralized control, it has been demonstrated in Section 3.3 that two PZT actuators and two PZT sensors are necessary to control all the modes in the frequency band of interest (see, Appendix A) and a good performance has been achieved (see, Section 5.3). In fact, using more PZT pairs are also possible by applying the proposed methodology and better performance could be obtained. However, more PZT means more complicated system and controller, which will put higher demand on the processing capability and the power consumption of the controller. On the other hand, the centralized controller needs more complicated physical connections because it collects all the sensor signals and outputs all the control signals at the same time. Therefore, we finally turn to distributed control.

Distributed control strategy is to use several simpler controllers to achieve a global performance. Each controller reacts only with a small number of actuators and sensors that are locally located on the structure. This local part of the structure with the sensors is considered as a subsystem with much lower order and the entire structure is thus considered as the interconnection of several such subsystems. Each subsystem only has information exchange with neighbor subsystems. The objective of distributed control is to find proper feedback controller for each subsystem such that the vibration in a particular zone of the global mechanical structure is reduced (referring to Section 3.2). For this purpose, an interconnected model for these subsystems should first be built in form of state-space representation. This chapter presents how to build the state-space model of such subsystems.

6.1 Distributed modeling overview

In distributed control, we consider the entire structure as the interconnection of several LTI subsystems. These subsystems have information exchange with their neighbors and also additional inputs and outputs for distributed controllers. Fig. 6.1 shows an example of such interconnected systems. Thus, the objective of the distributed modeling of the beam-piezo system is to build these LTI subsystems G^s such that the interconnection of these subsystems gives the model of the entire structure.

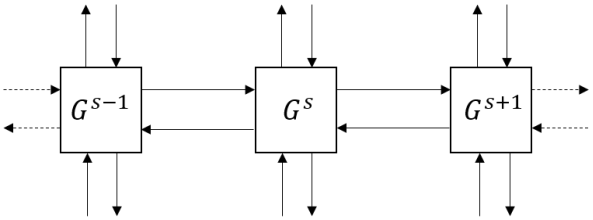

Figure 6.1: Example of interconnected system

The idea is to first spatially decompose the structure into cells and then transform the model of each cell (governing equation) into a simpler LTI subsystem (i.e. G^s in Fig. 6.1). This allows us to design simple distributed controller for each subsystem. In addition, as the subsystems correspond to different parts of the structure, it is possible to particularly control the vibration in a specific zone.

The modeling process is as follows. First, the governing equation of each cell is deduced from Finite Element Modeling. This step is similar with the modeling for centralized control (referring to Eq. (4.1) in Section 4.1.1.1) except that the displacement vector should contain the displacement along all the directions (i.e. x, y and z axis). Note that although only the displacement in z direction is of interest, the boundary condition of a single cell, which relates to the constraints applied by neighbor cells, is actually in three directions. More importantly, these constraints are necessary for building the subsystem[1] (i.e. G^s). Second, as in the modeling for centralized control, the obtained governing equation will have a large number of degree of freedom (DOF) and should thus be simplified as much as possible for the ease of controller design. The simplification should necessarily keep the constrains between neighbor cells for the purpose of constructing

[1]The constraints applied by neighbor cells are actually considered as the communication between neighbor subsystems

subsystems, and also keep the dynamics at lower frequencies for the purpose of controlling the vibration with respect to a disturbance over a specified frequency band. Therefore, we introduce Guyan condensation [129] and Euler-Bernoulli kinematic assumption. Third, according to the simplified governing equations, the information exchanged between neighbor subsystems is defined and, according to which, we finally construct the state-space representation of G^s. At last, in order to validate G^s, at least two steps of verification are needed. First, we need to verify that the governing equations deduced for each cell are correct. This is very important because G^s will be constructed based on these equations. In other words, we need to make sure that grouping together these cells can correctly reflect the global dynamics of the entire beam. For this purpose, we will perform assembly to the cells such that a complete model of the entire structure could be obtained and compare the dynamic of this assembled model with the previous global model (the beam-piezo system model built by using COMSOL in Section 4.1). Second, we need to make sure that G^s is correctly constructed from the governing equations of cells which means that if we interconnect all the G^s, we will find exactly the same model as the assembled model obtained in the first verification step.

Remark. *Modal Displacement Method, which is applied to simplify the governing equation in centralized control (see Section 4.1.1.2) is not applicable here. Modal Displacement Method decomposes the governing equation directly obtained from Finite Element Analysis into modes. However, the modes of the vibration of a cell do not represent the modes of the global vibration of the entire structure.*

The principle of Guyan condensation and Euler-Bernoulli kinematic assumption are presented in Section 6.2. Then, they are applied to our specific beam-piezo system in Section 6.3, and we obtain the simplified governing equations of the cells. According to these governing equations, we construct the state-space representations of all the subsystems, see Section 6.4.

6.2 Governing equation simplification for structural cells

6.2.1 Guyan condensation

Guyan condensation [36] is a common used primal method that reduces a complex structural model with a great number of DOF, aiming at finding an equivalent, simpler model which allows us to compute the approximate behavior of the initial structure. For this purpose, we define two sets of DOF: the set of master DOF, denoted q_m, which is composed of the DOF under external constrains, and the set of slave DOF, denoted q_e, which is composed of free DOF (no constraints). Consider the governing equation of a complex structure (with a great number of DOF from Finite Element Analysis) partitioned master DOF and slave DOF as:

$$\begin{bmatrix} M_{mm} & M_{me} \\ M_{em} & M_{ee} \end{bmatrix} \begin{bmatrix} \ddot{q}_m \\ \ddot{q}_e \end{bmatrix} + \begin{bmatrix} K_{mm} & K_{me} \\ K_{em} & K_{ee} \end{bmatrix} \begin{bmatrix} q_m \\ q_e \end{bmatrix} = \begin{bmatrix} g_m \\ 0 \end{bmatrix} \tag{6.1}$$

where $g_m \neq 0$ represents the constraints related to q_m and the constraints relating to q_e are zeros.

The idea of Guyan condensation is to neglect the kinetic energy before the strain energy with respect to the slave DOF q_e, which means that the second-order derivative terms in the second line of Eq. (6.1) are neglected[2]. Then we can directly write the static relation existing between q_m and q_e:

$$q_e = -K_{ee}^{-1} K_{em} \cdot q_m \tag{6.2}$$

Variable substitution is introduced here as below:

$$\begin{bmatrix} q_m \\ q_e \end{bmatrix} = T \cdot q_m, \tag{6.3}$$

[2]This constrains the model to be used in the low frequency band before a half of the eigen frequency of the first internal mode

where $T = \begin{bmatrix} I \\ -K_{ee}^{-1} K_{em} \end{bmatrix}$. Then, a simplified governing equation can be obtained as below [36]:

$$\bar{M} \cdot \ddot{q}_m + \bar{K} \cdot q_m = T^T \cdot \begin{bmatrix} g_m \\ 0 \end{bmatrix} \tag{6.4}$$

where[3]

$$\bar{M} = T^T \begin{bmatrix} M_{mm} & M_{me} \\ M_{em} & M_{ee} \end{bmatrix} T, \quad \bar{K} = T^T \begin{bmatrix} K_{mm} & K_{me} \\ K_{em} & K_{ee} \end{bmatrix} T.$$

Comparing to Eq. (6.1), Eq. (6.4) is simpler since it has less number of DOF.

Remark. *The error introduced by this simplification will depend on the choice of the master DOF [130] (i.e. q_m) . Of course, the more DOF are kept in q_m, the less error there will be. On the other hand, the error trends to increase at higher modes (frequencies) which means that Eq. (6.4) is only capable of well keeping the initial dynamics at low frequencies (before a half of the eigen frequency of the first eigne mode). The reason is that, as the frequency goes higher, the kinetic energy, which corresponds to the second-order derivative terms in Eq. (6.1), increases and thus becomes less neglectable. That is also the reason why the first step verification explained in Section 6.1 is important. We need to make sure that when the simplified cell models are assembled, we can find relatively correct dynamics over a frequency band that covers the disturbance.*

6.2.2 Euler-Bernoulli kinematic assumption

Euler-Bernoulli kinematic assumption[4] is used to represent the displacement field of a surface (displacement of all the points on the surface) by the displacement and the rotation of that surface against a single point (e.g. the central point of the a cross-section) under the assumption that the displacement is small.

[3]The mass matrix and the stiff matrix should be square and symmetric. We multiply T^T on the left to keep the symmetric property of these two matrices after simplification.

[4]The kinematic assumption in Euler-Bernoulli beam theory [129]

Consider that, in the generalized coordinate system $x-y-z$ (see Fig. 6.2), there is a surface S in yz plane. Denote $y_S - z_S$ the coordinate system attached to S and O_S its original point. The displacement under $x-y-z$, denoted $[u,v,w]^T$, of a point on S with coordinate (y_S, z_S) under $y_S - z_S$ can be computed as follow:

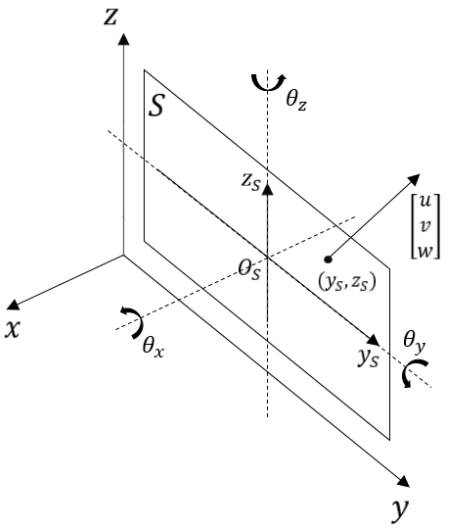

Figure 6.2: Coordinate system $x-y-z$, surface S, coordinate system $y_S - z_S$ attached to S and a point on S with coordinate (y_s, z_s) and displacement $[u,v,w]^T$

$$\begin{bmatrix} u \\ v \\ w \end{bmatrix} = \begin{bmatrix} 1 \\ 0 \\ 0 \end{bmatrix} u_0 + \begin{bmatrix} 0 \\ 1 \\ 0 \end{bmatrix} v_0 + \begin{bmatrix} 0 \\ 0 \\ 1 \end{bmatrix} w_0 + \begin{bmatrix} 0 \\ -z_S \\ y_S \end{bmatrix} \theta_x + \begin{bmatrix} z_S \\ 0 \\ 0 \end{bmatrix} \theta_y + \begin{bmatrix} -y_S \\ 0 \\ 0 \end{bmatrix} \theta_z, \tag{6.5}$$

where u_0, v_0, w_0 and θ_x, θ_y, θ_z are respectively the displacements of O_S and the rotations of S against O_S in $x-y-z$ along axis x, y and z. Using Eq. (6.5) allows us to reduce the number of DOF on a surface to only 6.

In our specific case, Eq. (6.5) could be further simplified. According to Section 3.2, only the bending mode in z direction is of interest. Fig. 6.3 presents an example of this bending deformation where S is a cross-section of the bending beam. In this bending deformation, S will never have rotation along x and z axis. The displacement of an arbitrary point on S will never have displacement

in y direction. Thus, it is enough to express the displacement of a point using u_0, w_0 and θ_y [5]:

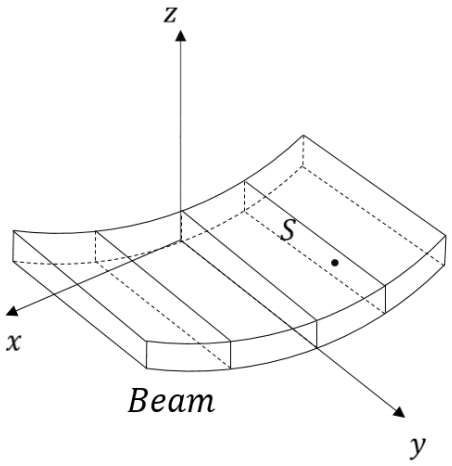

Figure 6.3: Bending deformation

$$\begin{bmatrix} u \\ v \\ w \end{bmatrix} = \begin{bmatrix} 1 \\ 0 \\ 0 \end{bmatrix} u_0 + \begin{bmatrix} 0 \\ 0 \\ 1 \end{bmatrix} w_0 + \begin{bmatrix} z_S \\ 0 \\ 0 \end{bmatrix} \theta_y, \tag{6.6}$$

By using Eq. (6.6), the number of DOF on a surface can thus be further reduced to only 3.

The next section will explain how to apply Guyan condensation and Euler-Bernoulli kinematic assumption on the considered beam-piezo structure and build simple cell models (governing equations).

6.3 Application to the structural cells

First, let us cut the structure into cells. Fig. 6.4 shows the virtual 3D model of the structure in COMSOL. It can be observed that not all the parts are the same. By discretizing the parts with length L_3 (the parts with PZT), we obtain cells with piezos. By discretizing the parts with length L_1 and L_2 (parts with no PZT), we obtain homogeneous cells. The entire structure is obviously the

[5] Indeed, if we ignore any DOF from u_0, w_0 and θ_y, there will be large discrepancies in frequency response between the initial model and the simplified model.

combination of these two kinds of cells. The following parts will explain how to build the model of these cells.

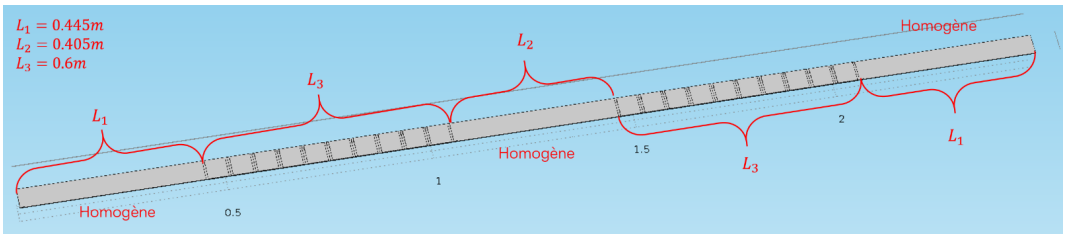

Figure 6.4: Different cells of the beam-piezo system

Remark. *If we aim to obtain more accurate global behavior from assembling the cells, it is obvious that the smaller the cell is, the more accuracy there will be. However, the dimension and position of the PZT limit the minimum length of the cell with piezos. For example, if we use two neighbor PZT pairs as a local control unit, the part with length L_3 can only be divided into 5 cells.*

6.3.1 Cells with piezos

6.3.1.1 Simplified governing equation

Two neighbor PZT pairs are used as actuator and sensor. We thus cut the parts with length L_3 (Fig. 6.4) between every two PZT pairs and 5 cells with piezos are obtained.

The governing equation of the cell with piezos can be deduced in the way similar to how we deduce the global model (referring to Section 4.1.1.1). First, a virtual 3D model of a such cell is built in COMSOL as shown in Fig. 6.5.

Then, the 3D model of the cell with piezos is spatially discretised into elements as shown in Fig. 6.6, called mesh, for the purpose of performing Finite Element Analysis.

Remark. *The mesh should be thin enough so that the solution converges*

The mesh generates the nodes. The displacement of a node under the generalized coordinate system $x - y - z$ is denoted as W:

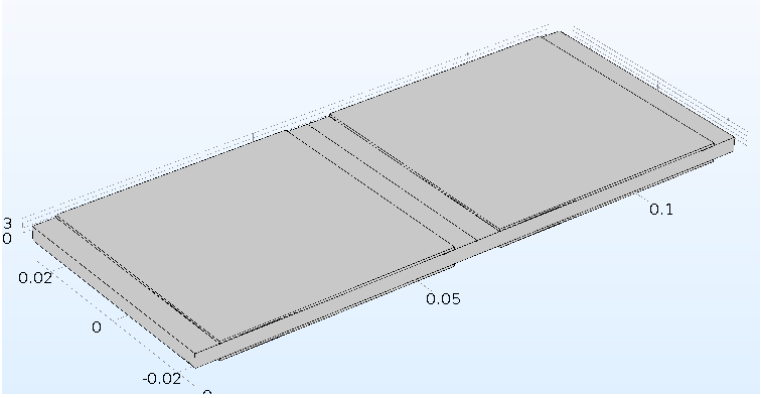

Figure 6.5: 3D model of a cell with piezos

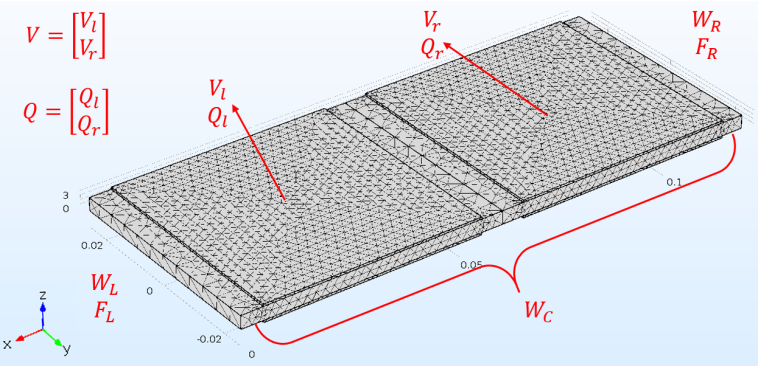

Figure 6.6: Mesh of a cell with piezos created by FEA

$$W = \begin{bmatrix} u \\ v \\ w \end{bmatrix} \tag{6.7}$$

where u, v and w denote respectively the displacement in directions x, y and z. To simplify the notation, we divide, according to the position, all the nodes into 3 groups and denote W_L, W_R and W_C respectively the column vector of the displacement of the nodes in the left surface, right surface and the central domain, see Fig. 6.6. Denote also V_l and V_r, Q_l and Q_r respectively the voltage and the charge on the left and right PZT pair, F_L and F_R respectively the force applied on W_L and W_R. The governing equation of this cell obtained from Finite Element Analysis will be in the following form:

$$\begin{bmatrix} M_{LL} & M_{LR} & M_{LC} & 0 \\ M_{LR}^T & M_{RR} & M_{RC} & 0 \\ M_{LC}^T & M_{RC}T & M_{CC} & 0 \\ 0 & 0 & 0 & 0 \end{bmatrix} \begin{bmatrix} \ddot{W}_L \\ \ddot{W}_R \\ \ddot{W}_C \\ \ddot{V} \end{bmatrix} + \begin{bmatrix} K_{LL} & K_{LR} & K_{LC} & E_L \\ K_{LR}^T & K_{RR} & K_{RC} & E_R \\ K_{LC}^T & K_{RC}T & K_{CC} & E_C \\ -E_L^T & -E_R^T & -E_C^T & R \end{bmatrix} \begin{bmatrix} W_L \\ W_R \\ W_C \\ V \end{bmatrix} = \begin{bmatrix} F_L \\ F_R \\ 0 \\ Q \end{bmatrix}, \tag{6.8}$$

$$V = \begin{bmatrix} V_l \\ V_r \end{bmatrix}, \quad Q = \begin{bmatrix} Q_l \\ Q_r \end{bmatrix}$$

Eq. (6.8) contains hundreds of DOF because of the large number of nodes. If it is transformed into state-space, there will be a huge order, which will lead to a much complex distributed controller for one cell, even more complex than the centralized controller. We need a much simpler governing equation. For this purpose, we first apply Guyan condensation.

In the case of one cell, the external constraint applied on it should only be on the left and right surface which means that all the DOF in W_C are free. This can also be seen from Eq. (6.8) as we have zero on the right part of the third line. Thus, W_C should be considered as slave DOF and others as master DOF. Eq. (6.8) can be simplified by neglecting the kinetic energy relating to W_C (second-order derivative terms in the third line).

Following the procedure of Guyan condensation (see Section 6.2.1), the static relation between W_C and other DOF is first computed:

$$W_C = -K_{CC}^{-1} \begin{bmatrix} K_{LC}^T & K_{RC}^T & E_C \end{bmatrix} \begin{bmatrix} W_L \\ W_R \\ V \end{bmatrix}. \tag{6.9}$$

Then, variable substitution is introduced as follow:

$$\begin{bmatrix} W_L \\ W_R \\ W_C \\ V \end{bmatrix} = \begin{bmatrix} I & 0 & 0 \\ 0 & I & 0 \\ -K_{CC}^{-1}K_{LC}^T & -K_{CC}^{-1}K_{RC}^T & -K_{CC}^{-1}E_C \\ 0 & 0 & I \end{bmatrix} \begin{bmatrix} W_L \\ W_R \\ V \end{bmatrix} = T \begin{bmatrix} W_L \\ W_R \\ V \end{bmatrix} \tag{6.10}$$

Substitute Eq. (6.10) into Eq. (6.8) and a simpler governing equation of the cell with piezos is obtained in the following form:

$$\begin{bmatrix} \bar{M}_{LL} & \bar{M}_{LR} & 0 \\ \bar{M}_{LR}^T & \bar{M}_{RR} & 0 \\ 0 & 0 & 0 \end{bmatrix} \begin{bmatrix} \ddot{W}_L \\ \ddot{W}_R \\ \ddot{V} \end{bmatrix} + \begin{bmatrix} \bar{K}_{LL} & \bar{K}_{LR} & \bar{E}_L \\ \bar{K}_{LR}^T & \bar{K}_{RR} & \bar{E}_R \\ -\bar{E}_L^T & -\bar{E}_R^T & \bar{R} \end{bmatrix} \begin{bmatrix} W_L \\ W_R \\ V \end{bmatrix} = \begin{bmatrix} \bar{F}_L \\ \bar{F}_R \\ Q \end{bmatrix}. \tag{6.11}$$

Remark. *As mentioned by the **Remark** in Section 6.2.1, the simplified governing equation obtained from Guyan condensation will keep the initial dynamics at low frequencies. Whether the assembled model will have correct dynamics over the frequency band of the disturbance will be discussed in Section 6.3.3 by comparing the frequency response of the global model and the assembled model. Here, we just assume that the previous statement is true.*

It can be observed that Eq. (6.11) still contains many DOF because the discretization by Finite Element Analysis also generates lots of nodes on the left and right surface (referring to Fig. 6.6) and each node needs 3 DOF to describe its displacement under the generalized coordinate system $x-y-z$ (see Eq. (6.7)). Thus, Eq. (6.11) needs to be further simplified without loosing the constraints on the left and right surface. For this purpose, we apply Euler-Bernoulli kinematic assumption.

We first apply Eq. (6.6) to all the nodes in W_L and W_R and we are thus able to obtain two corresponding transmission matrices, denoted H_L and H_R, such that:

$$W_L = H_L \widehat{W}_L, \quad W_R = H_R \widehat{W}_R, \tag{6.12}$$

with

$$\widehat{W}_L = [u_{0L}, w_{0L}, \theta_{yL}]^T, \quad \widehat{W}_R = [u_{0R}, w_{0R}, \theta_{yR}]^T, \tag{6.13}$$

where u_{0L}, w_{0L}, θ_{yL} are the displacements (x and z axis) and the rotations (y axis) of the left surface against its central point and u_{0R}, w_{0R}, θ_{yR} those of the right surface.

Then, similar to what we did in Guyan condensation, we here introduce another variable substitution as bellow:

$$\begin{bmatrix} W_L \\ W_R \\ V \end{bmatrix} = \begin{bmatrix} H_L & 0 & 0 \\ 0 & H_R & 0 \\ 0 & 0 & I \end{bmatrix} \begin{bmatrix} \widehat{W}_L \\ \widehat{W}_R \\ V \end{bmatrix} = \widehat{T} \begin{bmatrix} \widehat{W}_L \\ \widehat{W}_R \\ V \end{bmatrix}. \tag{6.14}$$

Substitute Eq. (6.14) into Eq. (6.11), the final governing equation of a cell with piezos with much less DOF is obtained in the following form:

$$\begin{bmatrix} \widehat{M}_{LL} & \widehat{M}_{LR} & 0 \\ \widehat{M}_{LR}^T & \widehat{M}_{RR} & 0 \\ 0 & 0 & 0 \end{bmatrix} \begin{bmatrix} \ddot{\widehat{W}}_L \\ \ddot{\widehat{W}}_R \\ \ddot{V} \end{bmatrix} + \begin{bmatrix} \widehat{K}_{LL} & \widehat{K}_{LR} & \widehat{E}_L \\ \widehat{K}_{LR}^T & \widehat{K}_{RR} & \widehat{E}_R \\ -\widehat{E}_L^T & -\widehat{E}_R^T & \widehat{R} \end{bmatrix} \begin{bmatrix} \widehat{W}_L \\ \widehat{W}_R \\ V \end{bmatrix} = \begin{bmatrix} \widehat{F}_L \\ \widehat{F}_R \\ Q \end{bmatrix}. \tag{6.15}$$

Till now, we reduce the DOF of the governing equation from a few hundreds to only a dozen. For the computation of the parameters in Eq. (6.15), we can still use COMSOL however in a particular way. This is explained in Section 6.3.1.2.

6.3.1.2 COMSOL solutions

Computing the parameters in Eq. (6.15) is to find $\widehat{M} = \begin{bmatrix} \widehat{M}_{LL} & \widehat{M}_{LR} \\ \widehat{M}_{LR}^T & \widehat{M}_{RR} \end{bmatrix}$, $\widehat{K} = \begin{bmatrix} \widehat{K}_{LL} & \widehat{K}_{LR} \\ \widehat{K}_{LR}^T & \widehat{K}_{RR} \end{bmatrix}$, $\widehat{E} = \begin{bmatrix} \widehat{E}_L \\ \widehat{E}_R \end{bmatrix}$ and $\widehat{R}$. For this purpose, we build a new cell model and compute these parameters using COMSOL. In order to reduce computational complexity, instead of solving (compute matrix parameters using COMSOL) Eq. (6.8) and then doing the calculations (impose Guyan condensation and Euler-Bernoulli kinematic assumption), we directly solve Eq. (6.15). The solutions are obtained by two steps:

Remark. *It is not possible to reuse the global finite element model (4.1) obtained in Section 4.1.1.1 to extract these parameters because model (4.1) does not have the same DOF as model (6.15).*

(1) Static solutions – Compute $\widehat{K}$, $\widehat{E}$ and $\widehat{R}$

COMSOL is able to compute the constraints or the actuation voltage on the structure or the piezo that are necessary to generate a predefined deformation or a resulting charge change. The constraints could be the force or the torque (moment of force). A predefined deformation could be a displacement or a rotation. With only a predefined deformation or a static actuation voltage, there will be no kinetic energy, which means that the inertial terms (second-order derivative terms) should be zero. In this case, Eq. (6.15) can be simplified as below:

$$\begin{bmatrix} \widehat{K}_{LL} & \widehat{K}_{LR} & \widehat{E}_L \\ \widehat{K}_{LR}^T & \widehat{K}_{RR} & \widehat{E}_R \\ -\widehat{E}_L^T & -\widehat{E}_R^T & \widehat{R} \end{bmatrix} \begin{bmatrix} \widehat{W}_L \\ \widehat{W}_R \\ V \end{bmatrix} = \begin{bmatrix} \widehat{F}_L \\ \widehat{F}_R \\ Q \end{bmatrix}. \tag{6.16}$$

Each value we chose for $\begin{bmatrix} \widehat{W}_L \\ \widehat{W}_R \\ V \end{bmatrix}$ represents a predefined deformation and an static actuation voltage. The constraints and the resulting charge change are exactly represented by $\begin{bmatrix} \widehat{F}_L \\ \widehat{F}_R \\ Q \end{bmatrix}$. Therefore, if we chose $\begin{bmatrix} \widehat{W}_L \\ \widehat{W}_R \\ V \end{bmatrix}$ as a unit vector whose i^{th} line equals to 1, the constraint vector computed by COMSOL is exactly the i^{th} column of $\begin{bmatrix} \widehat{K}_{LL} & \widehat{K}_{LR} & \widehat{E}_L \\ \widehat{K}_{LR}^T & \widehat{K}_{RR} & \widehat{E}_R \\ -\widehat{E}_L^T & -\widehat{E}_R^T & \widehat{R} \end{bmatrix}$.

(2) Equivalent mass matrix – Compute $\widehat{M}$

COMSOL is also able to compute the displacement field of the structure under a predefined deformation. Denote φ_i the displacement field when choosing $\begin{bmatrix} \widehat{W}_L \\ \widehat{W}_R \\ V \end{bmatrix}$ with $V = 0$ as a unit vector whose i^{th} line equals to 1. Then we have:

$$\widehat{M}_{ij} = \iiint_M \rho_m \varphi_i^T \varphi_j dV + \iiint_P \rho_p \varphi_i^T \varphi_j dV \tag{6.17}$$

where ρ_m and ρ_p are respectively the density of the beam and the piezo. The integration corner mark 'M' and 'P' represent the volume integration in mechanical domain (beam) and the piezo-electric domain (piezo).

6.3.2 Homogeneous cells

The homogeneous cells are discretized from the parts with length L_1 and L_2, see Fig. 6.4. The modelization of the homogeneous cells is similar to that of the cells with piezos except that there are no piezos on homogeneous cells. This means that there is no electro-mechanical coupling between the beam and the piezos. There will thus be no more coupling terms in the governing equation which will be in the following form (after introducing Guyan condensation and Euler-Bernoulli kinematic assumption):

$$\begin{bmatrix} \widehat{M}_{LL} & \widehat{M}_{LR} \\ \widehat{M}_{LR}^T & \widehat{M}_{RR} \end{bmatrix} \begin{bmatrix} \ddot{\widehat{W}}_L \\ \ddot{\widehat{W}}_R \end{bmatrix} + \begin{bmatrix} \widehat{K}_{LL} & \widehat{K}_{LR} \\ \widehat{K}_{LR}^T & \widehat{K}_{RR} \end{bmatrix} \begin{bmatrix} \widehat{W}_L \\ \widehat{W}_R \end{bmatrix} = \begin{bmatrix} \widehat{F}_L \\ \widehat{F}_R \end{bmatrix}. \tag{6.18}$$

We also use COMSOL to compute $\widehat{M}$ and $\widehat{K}$ by applying the same procedure explained in Section 6.3.1.2.

Remark. *In this work, the parts with length L_1 and L_2 are all cut into 5 cells of the same size. It should be noticed that L_1 and L_2 are different. We thus have to build two different homogeneous cells in COMSOL respectively with length $L_1/5$ and $L_2/5$ which leads to different $\widehat{M}$ and $\widehat{K}$.*

6.3.3 Assembly

Assembly is to group together the governing equations of the cells to form a global equation system of the entire structure. The objective of the assembly is to validate the model of the cells. If the cells are correctly modeled, we can find very close dynamics between the assembled model and the previous beam-piezo system model built for centralized control (see Section 4.1). Besides, the distributed controllers must work together to obtain a global performance. It is therefore necessary to first verify if the cells grouping together can correctly reflect the global dynamics.

As explained in previous sections, each part of the structure (parts with length L_1, L_2 and L_3) is discretized into 5 identical parts. The entire structure is thus divided into 25 cells in total which results in 26 cross-sections. Denote i the number of the cells. It should be noticed that $i = 1, \cdots, 5, 11, \cdots, 15, 21, \cdots, 25$

represents the homogeneous cells and $i = 6, \cdots, 10, 16, \cdots, 20$ the cells with piezos, the matrices used in the governing equations of the 25 cells are denoted as follows:

$$\begin{aligned}
\widehat{M}^i &= \begin{bmatrix} \widehat{M}^i_{LL} & \widehat{M}^i_{LR} \\ \widehat{M}^i_{LR}{}^T & \widehat{M}^i_{RR} \end{bmatrix} (i = 1, \cdots, 25) \\
\widehat{K}^i &= \begin{bmatrix} \widehat{K}^i_{LL} & \widehat{K}^i_{LR} \\ \widehat{K}^i_{LR}{}^T & \widehat{K}^i_{RR} \end{bmatrix} (i = 1, \cdots, 25) \\
\widehat{F}^i &= \begin{bmatrix} \widehat{F}^i_L \\ \widehat{F}^i_R \end{bmatrix} (i = 1, \cdots, 25) \\
\widehat{W}^i &= \begin{bmatrix} \widehat{W}^i_L \\ \widehat{W}^i_R \end{bmatrix} (i = 1, \cdots, 25) \\
\widehat{E}^i &= \begin{bmatrix} \widehat{E}^i_L \\ \widehat{E}^i_R \end{bmatrix} (i = 6, \cdots, 10, 16, \cdots, 20) \\
\widehat{C}^i &= \begin{bmatrix} \widehat{C}^i_{ll} & \widehat{C}^i_{lr} \\ \widehat{C}^i_{lr}{}^T & \widehat{C}^i_{rr} \end{bmatrix} (i = 6, \cdots, 10, 16, \cdots, 20) \\
V^i &= \begin{bmatrix} V^i_l \\ V^i_r \end{bmatrix} (i = 6, \cdots, 10, 16, \cdots, 20) \\
Q^i &= \begin{bmatrix} Q^i_l \\ Q^i_r \end{bmatrix} (i = 6, \cdots, 10, 16, \cdots, 20).
\end{aligned} \tag{6.19}$$

In addition, as the cells are physically connected, the total DOF of all the cells $\widehat{W}^i, i = 1, \cdots, 25$ has thus duplication at every contact surface. For example, when two cells are assembled, the contact surface of each cell becomes one cross-section of the assembled structure with only one DOF vector. In addition, each surface has internal constraint. If the surface is not under extra constraints, the constrain applied on the right surface of the cell on the left and the constraint applied on the left surface of the cell on the right are always opposite. Denoted $\widetilde{W}_j$ and $\widetilde{F}_j$ the DOF and the extra constraint at the j^{th} surface ($j = 1, \cdots, 26$), then we have the following algebraic relations:

$$\widehat{W}^i_R = \widehat{W}^{i+1}_L = \widetilde{W}_{j+1}, \quad \widehat{F}^i_R + \widehat{F}^{i+1}_L = \widetilde{F}_{j+1} = 0 \tag{6.20}$$

for $i = j = 1, \cdots 24$. It should be noticed that the disturbance is applied on the right end of the beam, which is at the 26^{th} surface where the extra constraint

will no longer be zero. This will be discussed later.

Considering the above algebraic relations, the governing equation of the assembled system is in the following form:

$$\begin{bmatrix} \widetilde{M} & 0 \\ 0 & 0 \end{bmatrix} \begin{bmatrix} \ddot{\widetilde{W}} \\ \ddot{V} \end{bmatrix} + \begin{bmatrix} \widetilde{K} & \widetilde{E} \\ -\widetilde{E}^T & \widetilde{C} \end{bmatrix} \begin{bmatrix} \widetilde{W} \\ V \end{bmatrix} = \begin{bmatrix} \widetilde{F} \\ Q \end{bmatrix} \tag{6.21}$$

where

$$\widetilde{W} = \left[\widetilde{W}_1, \widetilde{W}_1, \cdots, \widetilde{W}_{26}\right]^T, \quad \widetilde{F} = \left[\widetilde{F}_1, 0, \cdots, 0, \widetilde{F}_{26}\right]^T,$$

$$\widetilde{M} = \begin{bmatrix} \widetilde{M}^1 & & & \\ & \widetilde{M}^2 & & \\ & & \widetilde{M}^3 & \\ & & & \ddots \\ & & & & \widetilde{M}^{25} \end{bmatrix} \qquad \widetilde{K} = \begin{bmatrix} \widetilde{K}^1 & & & \\ & \widetilde{K}^2 & & \\ & & \widetilde{K}^3 & \\ & & & \ddots \\ & & & & \widetilde{K}^{25} \end{bmatrix}$$

$$\widetilde{E} = \begin{bmatrix} 0 \\ \hat{E}^6 & & \\ & \hat{E}^7 & \\ & & \ddots \\ & & & \hat{E}^{10} \\ 0 \\ & & & \hat{E}^{16} \\ & & & & \hat{E}^{17} \\ & & & & & \ddots \\ & & & & & & \hat{E}^{20} \\ 0 \end{bmatrix} \begin{matrix} \\ \\ \\ \\ \\ \\ \\ \\ \\ \\ \\ \end{matrix} \begin{matrix} 5 \times 3 \text{ lines} \\ \\ \\ \\ \\ 4 \times 3 \text{ lines} \\ \\ \\ \\ \\ 5 \times 3 \text{ lines} \end{matrix}$$

$$\tilde{C} = \begin{bmatrix} \hat{C}^6 & & & \\ & \hat{C}^{10} & & \\ & & \hat{C}^{16} & \\ & & & \ddots \\ & & & & \hat{C}^{20} \end{bmatrix}$$

$$V = \begin{bmatrix} V^6 \\ \vdots \\ V^{10} \\ V^{16} \\ \vdots \\ V^{20} \end{bmatrix} \qquad Q = \begin{bmatrix} Q^6 \\ \vdots \\ Q^{10} \\ Q^{16} \\ \vdots \\ Q^{20} \end{bmatrix}$$

and

$$\widetilde{M}^1 = \begin{bmatrix} \widehat{M}^1_{LL} & \widehat{M}^1_{LR} \\ {\widehat{M}^1_{LR}}^T & \widehat{M}^2_{LL} + \widehat{M}^1_{RR} \end{bmatrix}, \quad \widetilde{M}^{25} = \begin{bmatrix} \widehat{M}^{25}_{LL} + \widehat{M}^{24}_{RR} & \widehat{M}^{25}_{LR} \\ {\widehat{M}^{25}_{LR}}^T & \widehat{M}^{25}_{RR} \end{bmatrix},$$
$$\widetilde{M}^i = \begin{bmatrix} \widehat{M}^i_{LL} + \widehat{M}^{i-1}_{RR} & \widehat{M}^i_{LR} \\ {\widehat{M}^i_{LR}}^T & \widehat{M}^{i+1}_{LL} + \widehat{M}^i_{RR} \end{bmatrix} (i = 2, \cdots, 24),$$
$$\widetilde{K}^1 = \begin{bmatrix} \widehat{K}^1_{LL} & \widehat{K}^1_{LR} \\ {\widehat{K}^1_{LR}}^T & \widehat{K}^2_{LL} + \widehat{K}^1_{RR} \end{bmatrix}, \quad \widetilde{K}^{25} = \begin{bmatrix} \widehat{K}^{25}_{LL} + \widehat{K}^{24}_{RR} & \widehat{K}^{25}_{LR} \\ {\widehat{K}^{25}_{LR}}^T & \widehat{K}^{25}_{RR} \end{bmatrix},$$
$$\widetilde{K}^i = \begin{bmatrix} \widehat{K}^i_{LL} + \widehat{K}^{i-1}_{RR} & \widehat{K}^i_{LR} \\ {\widehat{K}^i_{LR}}^T & \widehat{K}^{i+1}_{LL} + \widehat{K}^i_{RR} \end{bmatrix} (i = 2, \cdots, 24)$$

The boundary condition can be found in $\widetilde{F}_1$ and $\widetilde{F}_{26}$ which represent extra constraints at the left and right end of the beam. We consider the beam as free-free and the excitation is applied at the right end with only a force disturbance in z direction. Thus, $\widetilde{F}_1$ and $\widetilde{F}_{26}$ are given by:

$$\widetilde{F}_1 = [0, 0, 0]^T, \quad \widetilde{F}_{26} = [0, f, 0]^T \tag{6.22}$$

where f is the applied force disturbance.

For the damping effect, we use the same damping constants as explained in Section 4.1.2 which adds a first derivative term in Eq. (6.21). It then becomes:

$$\begin{bmatrix} \widetilde{M} & 0 \\ 0 & 0 \end{bmatrix} \begin{bmatrix} \ddot{\widetilde{W}} \\ \ddot{V} \end{bmatrix} + \begin{bmatrix} \widetilde{\mathcal{X}} & 0 \\ 0 & 0 \end{bmatrix} \begin{bmatrix} \dot{\widetilde{W}} \\ \dot{V} \end{bmatrix} + \begin{bmatrix} \widetilde{K} & \widetilde{E} \\ -\widetilde{E}^T & \widetilde{C} \end{bmatrix} \begin{bmatrix} \widetilde{W} \\ V \end{bmatrix} = \begin{bmatrix} \widetilde{F} \\ Q \end{bmatrix} \tag{6.23}$$

where

$$\widetilde{\mathcal{X}} = \kappa_a \widetilde{M} + \kappa_s \widetilde{K}. \tag{6.24}$$

In order to verify the assembled model, we compare its frequency response with the previous beam-piezo system model (before identification step) between the same actuator and sensor (from the 10^{th} to the 11^{th} PZT pair) and from the force disturbance to the same sensor (the 11^{th} PZT pair), with the same κ_a and κ_s (whose optimal value is obtained from identification). The result is respectively shown in Fig. 6.7 and Fig. 6.8 where we observe that the response of the assembled

model (dashed red) and the beam-piezo system model (solid blue) are quite similar below the maximum frequency of the disturbance (i.e. 3000 rad/s). This means that the cells are correctly modeled. It should be noticed that the shifting at resonances is not due to modeling error. It is in fact due to the condensation as we neglect W_C which has a large dimension. In addition, the length of the cell is not small enough. However, as mentioned by the **Remark** at the beginning of Section 6.3, the minimum length of the cell is limited by the dimension and the position of the PZT pairs. In any case, model correction on the cell models is still necessary such that the assembled model matches the benchmark.

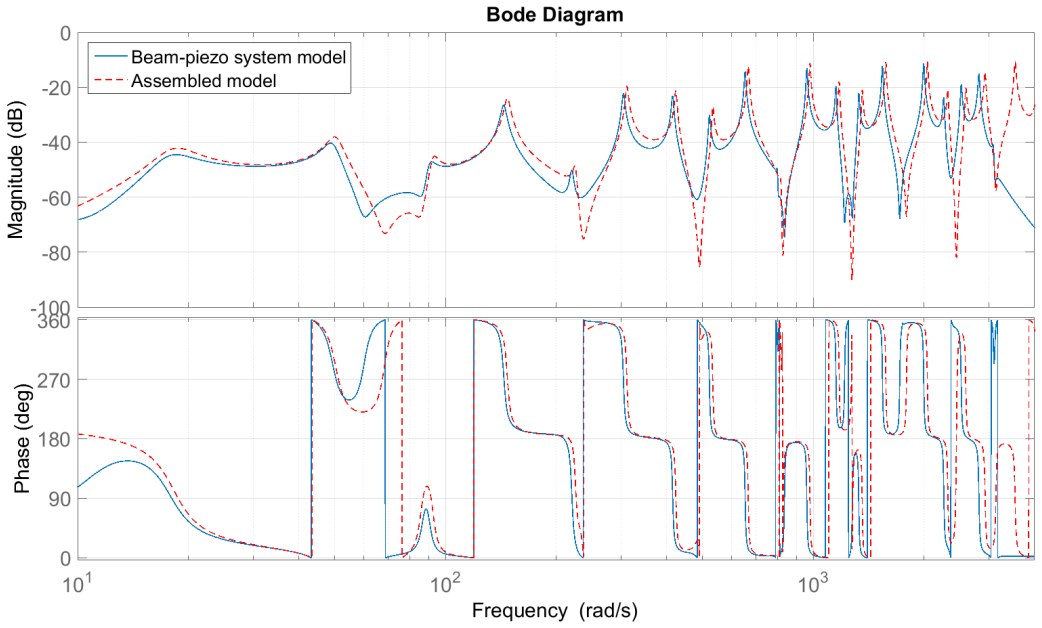

Figure 6.7: Frequency response comparison (from the 10^{th} to the 11^{th} PZT pair): Beam-piezo system model (solid blue) vs Assembled model (dashed red)

6.4 State-space modeling of interconnected LTI subsystems

The objective of this section is to deduce interconnected LTI subsystems (i.e. G^s) from the results obtained in Section 6.3. Before we start, the following discussions are necessary.

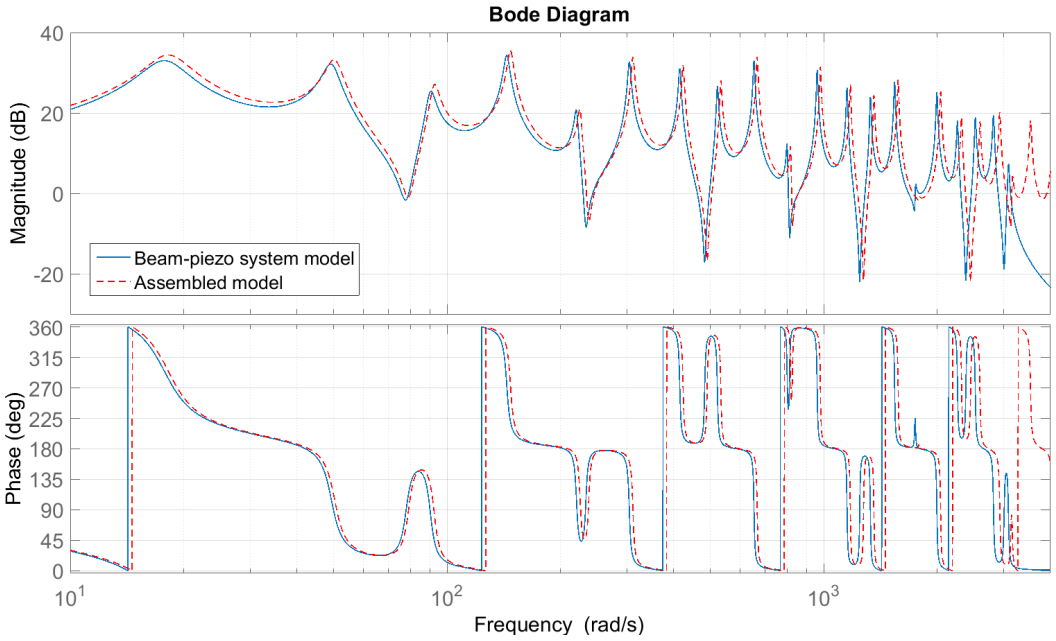

Figure 6.8: Frequency response comparison (from the force disturbance to the 11^{th} PZT pair): Beam-piezo system model (solid blue) vs Assembled model (dashed red)

6.4.1 Discussions

To build the state-space representations for interconnected subsystems, it seems to be easier to start from model (6.23) because the parameters corresponding to the beam dynamics (i.e. $\widetilde{M}$, $\widetilde{\mathcal{X}}$ and $\widetilde{K}$) have particular form, see their definitions in Eq. (6.21) and Eq. (6.24). In particular, for a dynamic system in the state-space representation $\dot{X} = A \cdot X$ with A in the following particular form:

$$A = \begin{bmatrix} A_{11} & A_{12} & & & \\ A_{21} & A_{22} & A_{23} & & \\ & A_{32} & A_{33} & \ddots & \\ & & \ddots & \ddots & A_{n-1n} \\ & & & A_{nn-1} & A_{nn} \end{bmatrix}, \tag{6.25}$$

this system can be decomposed into several interconnected subsystems (see Fig. 6.1 for an example of such interconnected subsystems) with $A_{ii}(i = 1, 2, \cdots, n)$ the dynamic matrix of the i^{th} subsystem. The matrix $A_{ij}(i \neq j)$ represents the communication between neighbor subsystems i and j.

Now let us discuss model (6.23). It is reasonable to choose $X = \begin{bmatrix} \dot{\widetilde{W}} \\ \widetilde{W} \end{bmatrix}$ as the state vector and model (6.23) can thus be transformed into $\dot{X} = A \cdot X$ (if we ignore the input matrix B of state-space representation) where:

$$A = \begin{bmatrix} -\widetilde{M}^{-1}\widetilde{\mathcal{X}} & -\widetilde{M}^{-1}\widetilde{K} \\ I & 0 \end{bmatrix}. \tag{6.26}$$

Here we face the problem that if a matrix with the form of Eq. (6.25) is reversed, the original form will no longer exist[6]. As we observe $\widetilde{M}^{-1}$ in A, A will thus lose this particular form which means that we cannot directly decompose model Eq. (6.25) into such interconnected subsystems as illustrated by Fig. 6.1. In this case, particular investigations in details of cell governing equations must be done to achieve such objective. The following sections will explain our method.

6.4.2 Architecture of the interconnected system

Before we start constructing the subsystems, we should first have a general understand of the architecture of the interconnected system representing the considered setup, which helps us classify different subsystems and then construct them. For this purpose, we start from the cells.

It should be noted that, by cutting the structure (setup), we obtain two kinds of cells: homogeneous cell and cell with piezos. They have different governing equations with different values for the mass matrix and the stiffness matrix. In addition, the homogeneous cells in the central zone and other homogeneous zones have different length (respectively $L_2/5$ and $L_1/5$), referring to the **Remark** in Section 6.3.2. This also results in different mass matrices and stiffness matrices. In summary, the entire structure is composed of cells with in total three different governing equations that represents respectively the homogeneous cell with length $L_1/5$, the homogeneous cell with length $L_2/5$ and the cell with piezos.

Denote M^a, M^b and M^c respectively the mass matrices of the above three types of cell and K^a, K^b and K^c respectively their stiffness matrices. Denote W_L, W_R

[6]The inverse of A with the form of Eq. (6.25) becomes an unstructured square matrix with full element

the DOF vector (referring to Eq. (6.13)) of a cell on the left and right surface and F_L, F_R the corresponding constraint vector[7]. Recall the governing equations (with damping effect) for these three types of cell as follows.

Type a. Homogeneous cell with length $L_1/5$:

$$\begin{bmatrix} M^a_{LL} & M^a_{LR} \\ {M^a_{LR}}^T & M^a_{RR} \end{bmatrix} \begin{bmatrix} \ddot{W}_L \\ \ddot{W}_R \end{bmatrix} + \begin{bmatrix} \mathcal{X}^a_{LL} & \mathcal{X}^a_{LR} \\ {\mathcal{X}^a_{LR}}^T & \mathcal{X}^a_{RR} \end{bmatrix} \begin{bmatrix} \dot{W}_L \\ \dot{W}_R \end{bmatrix} + \begin{bmatrix} K^a_{LL} & K^a_{LR} \\ {K^a_{LR}}^T & K^a_{RR} \end{bmatrix} \begin{bmatrix} W_L \\ W_R \end{bmatrix} = \begin{bmatrix} F_L \\ F_R \end{bmatrix}, \tag{6.27}$$

Type b. Homogeneous cell with length $L_2/5$:

$$\begin{bmatrix} M^b_{LL} & M^b_{LR} \\ {M^b_{LR}}^T & M^b_{RR} \end{bmatrix} \begin{bmatrix} \ddot{W}_L \\ \ddot{W}_R \end{bmatrix} + \begin{bmatrix} \mathcal{X}^b_{LL} & \mathcal{X}^b_{LR} \\ {\mathcal{X}^b_{LR}}^T & \mathcal{X}^b_{RR} \end{bmatrix} \begin{bmatrix} \dot{W}_L \\ \dot{W}_R \end{bmatrix} + \begin{bmatrix} K^b_{LL} & K^b_{LR} \\ {K^b_{LR}}^T & K^b_{RR} \end{bmatrix} \begin{bmatrix} W_L \\ W_R \end{bmatrix} = \begin{bmatrix} F_L \\ F_R \end{bmatrix}, \tag{6.28}$$

Type c. Cell with piezos:

$$\begin{bmatrix} M^c_{LL} & M^c_{LR} & 0 \\ {M^c_{LR}}^T & M^c_{RR} & 0 \\ 0 & 0 & 0 \end{bmatrix} \begin{bmatrix} \ddot{W}_L \\ \ddot{W}_R \\ \ddot{V} \end{bmatrix} + \begin{bmatrix} \mathcal{X}^c_{LL} & \mathcal{X}^c_{LR} & 0 \\ {\mathcal{X}^c}^T_{LR} & \mathcal{X}^c_{RR} & 0 \\ 0 & 0 & 0 \end{bmatrix} \begin{bmatrix} \dot{W}_L \\ \dot{W}_R \\ \dot{V} \end{bmatrix} + \begin{bmatrix} K^c_{LL} & K^c_{LR} & E_L \\ {K^c_{LR}}^T & K^c_{RR} & E_R \\ -E_L^T & -E_R^T & C \end{bmatrix} \begin{bmatrix} W_L \\ W_R \\ V \end{bmatrix} = \begin{bmatrix} F_L \\ F_R \\ Q \end{bmatrix}. \tag{6.29}$$

Therefore, unlike the standard form of an interconnected system presented by Fig. 6.1 where all the subsystems G^s are the same, the considered beam-piezo

[7] To simplify the notation, we here remove the mark '$\widehat{\ }$'. Consequently, W_L, W_R will refer to $\widehat{W}_L$, $\widehat{W}_R$ in Eq. (6.13) and F_L, F_R will refer to $\widehat{F}_L$, $\widehat{F}_R$ (i.e. the constraint vectors corresponding to $\widehat{W}_L$ and $\widehat{W}_R$). In addition, we will not number the parameters and the variables of different cell equations using i or j as we did in Section 6.3.3 because cells of the same type have the same governing equation. We just use W_L to present the DOF on the left surface of one cell and W_R those on the right surface

system is in fact a particular interconnected system composed of subsystems with different types. Considering the position of the PZT pairs and the force disturbance, the free-free boundary condition and the velocity output in the central zone, etc., this particular interconnected system can be represented by the bock diagram illustrated in Fig. 6.9.

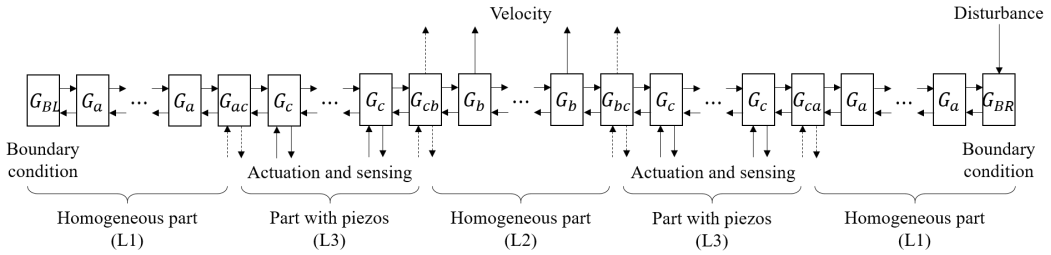

Figure 6.9: General architecture of the interconnected system for the setup

In general, the interconnected system should contain at least 9 different subsystems denoted respectively G_a, G_b, G_c, G_{BL}, G_{BR}, G_{ac}, G_{ca}, G_{bc} and G_{cb}. In particular, G_a, G_b and G_c are the subsystems which have themselves as neighbors and respectively deduced from the cells of **Type a**, **Type b** and **Type c**. In addition to the communication with neighbor subsystems, G_b should also have velocity output in order to construct the central energy and G_c should have actuation input and sensing output for distributed controller. G_{BL} and G_{BR} are the subsystems deduced from the cell of **Type a** and represent the boundary condition on the left and right surface of the beam. The force disturbance is considered as one boundary condition on the right surface and thus also considered in G_{BR}. G_{ac} and G_{ca} are the intermediate subsystems that connect G_a and G_c. For example, on the left of G_{ac} connects with G_a and on the right with G_c. As G_a and G_c are different subsystems which means that the communication signals with neighbors are different, G_{ac} should thus have to be particularly considered as a new subsystem different from both G_a and G_c, and should have to be deduced using cells of both **Type a** and **Type c**. In addition, whether G_{ac} or G_{ca} has actuation and sensing capabilities depends on the choice of the state vector. This will be further discussed in the Section 6.4.3. The same situation also happens for G_{bc} and G_{cb}.

The next section will discuss how to deduce these 9 subsystems from the cells of **Type a**, **Type b** and **Type c**.

6.4.3 Construction of LTI subsystems

First, it is very important to notice that a subsystem does not strictly represent a cell. When two cells are physically connected (assembled), they actually share one surface (cross-section of the assembled structure). If we directly consider a cell as a subsystem, there will exist algebraic relations in the interconnected LTI system because two neighbor subsystems will share part of their states. For example, if we simply consider G_a equals to the cell of **Type a**, it can be observed from Eq. (6.27) that G_a should have W_L (DOF on the left surface) and W_R (DOF on the right surface) as states. When two G_a are interconnected left and right, the W_R of the left one and the W_L of the right one contain exactly the same DOF. To avoid this phenomenon, we will first assemble several cells so that a more general governing equation that contains all the considered DOF is obtained. We will then reasonably regroup the DOF and finally construct subsystems such that each one has its proper states.

Before we start, it is also necessary to first define the notation of communication signals between neighbor subsystems, see Fig. 6.10 where G represents one subsystem and s its position. Denote u and y respectively the communication input and output vector between neighbor subsystems. The symbols '+' and '−' represent the direction of the signals with '+' to the right and '−' to the left. For example, $u^{s,+}$ means the input of G^s from G^{s-1}, and $y^{s,-}$ the output of G^s into G^{s-1}. Thus, we also have: $u^{s,+} = y^{s-1,+}$, $u^{s-1,-} = y^{s,-}$.

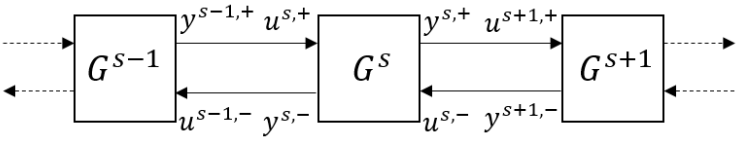

Figure 6.10: Definition of communication signals

In fact, the process for constructing these 9 subsystems are quit similar. In the sequel, we just take the most typical case as an example which is the construction of G_c as G_c is considered as a local control unit which has actuation and sensing capabilities. For details of constructing all the other 8 subsystems (i.e. G_a, G_b, G_{BL}, G_{BR}, G_{ac}, G_{ca}, G_{bc} and G_{cb}), see Section 6.5 at the end of this chapter.

Now let us discuss the construction of G_c. G_c is in the part with piezo cells composed of cells of **Type c**. In addition to the communications with its neighbors,

G_c also has actuation and sensing capabilities as it will be connected with the distributed controller, see Fig. 6.9. This means that each G_c should contain the voltages of the two PZT pairs on one cell of **Type c** respectively as actuation input and sensing output. We will here use the PZT pair on the left as actuator.

First, we perform assembly to two cells of **Type c** as shown in Fig. 6.11 where W_i and F_i $(i = 1, 2, 3)$ denote the DOF and the corresponding constraints on different cross-sections and which gives us the following governing equation:

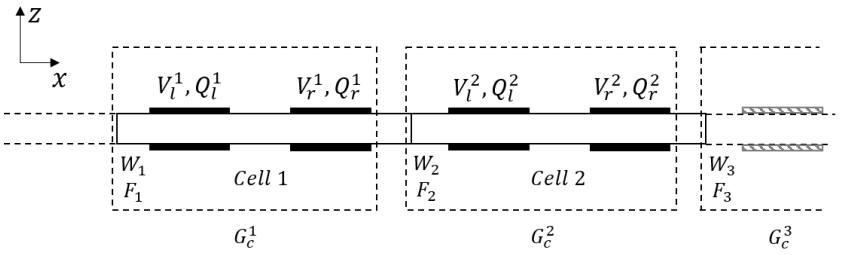

Figure 6.11: Assemble two cells of **Type c**

$$\begin{bmatrix} M_{LL}^c & M_{LR}^c & \\ {M_{LR}^c}^T & M_{LL}^c + M_{RR}^c & M_{LR}^c \\ & {M_{LR}^c}^T & M_{RR}^c \end{bmatrix} \begin{bmatrix} \ddot{W}_1 \\ \ddot{W}_2 \\ \ddot{W}_3 \end{bmatrix} + \begin{bmatrix} \mathcal{X}_{LL}^c & \mathcal{X}_{LR}^c & \\ {\mathcal{X}_{LR}^c}^T & \mathcal{X}_{LL}^c + \mathcal{X}_{RR}^c & \mathcal{X}_{LR}^c \\ & {\mathcal{X}_{LR}^c}^T & \mathcal{X}_{RR}^c \end{bmatrix} \begin{bmatrix} \dot{W}_1 \\ \dot{W}_2 \\ \dot{W}_3 \end{bmatrix} +$$

$$\begin{bmatrix} K_{LL}^c & K_{LR}^c & \\ {K_{LR}^c}^T & K_{LL}^c + K_{RR}^c & K_{LR}^c \\ & {K_{LR}^c}^T & K_{RR}^c \end{bmatrix} \begin{bmatrix} W_1 \\ W_2 \\ W_3 \end{bmatrix} = \begin{bmatrix} F_1 \\ 0 \\ F_3 \end{bmatrix} + \begin{bmatrix} -E_{Ll} & -E_{Lr} & & \\ -E_{Rl} & -E_{Rr} & -E_{Ll} & -E_{Lr} \\ & & -E_{Rl} & -E_{Rr} \end{bmatrix} \begin{bmatrix} V_l^1 \\ V_r^1 \\ V_l^2 \\ V_r^2 \end{bmatrix}, \tag{6.30}$$

$$\begin{bmatrix} -{E_{Ll}}^T & -{E_{Rl}}^T & & \\ -{E_{Lr}}^T & -{E_{Rr}}^T & & \\ & -{E_{Ll}}^T & -{E_{Rl}}^T & \\ & -{E_{Lr}}^T & -{E_{Rr}}^T & \end{bmatrix} \begin{bmatrix} W_1 \\ W_2 \\ W_3 \end{bmatrix} + \begin{bmatrix} C_l & & & \\ & C_r & & \\ & & C_l & \\ & & & C_r \end{bmatrix} \begin{bmatrix} V_l^1 \\ V_r^1 \\ V_l^2 \\ V_r^2 \end{bmatrix} = \begin{bmatrix} Q_l^1 \\ Q_r^1 \\ Q_l^2 \\ Q_r^2 \end{bmatrix}, \tag{6.31}$$

with

$$E_L = \begin{bmatrix} E_{Ll} & E_{Lr} \end{bmatrix}, \; E_R = \begin{bmatrix} E_{Rl} & E_{Rr} \end{bmatrix}, \; C = \begin{bmatrix} C_l & \\ & C_r \end{bmatrix},$$

where V_l^s, V_r^s $(s = 1, 2)$ denote the voltage of the left and right PZT pair on a cell and Q_l^s, Q_r^s $(s = 1, 2)$ their charges.

As already mentioned at the beginning of this section, in order to avoid algebraic relations between neighbor subsystems, we should regroup the DOF such that each subsystem has its proper states. When we assemble two cells of **Type c**, we obtain two sets of actuator-sensor pair (i.e. V_l^s, V_r^s for $s = 1, 2$) while three cross-sections (i.e. $W_i, i = 1, 2, 3$). Suppose that W_i only belongs to the state of one subsystem, we construct G_c such that it only contains the left cross-section of a cell (e.g. W_1) and the two PZT pairs (e.g. V_l^1, V_r^1) on the same cell[8], see for example $G_c^s, s = 1, 2, 3$ in Fig. 6.11.

The sensing voltage (i.e. V_r^s) will be measured by the controller through a measurement circuit, referring to Fig. 4.1 in Section 4.1.3. Denote Y the internal resistance of the controller. According to Ohm's law:

$$-YV_r^s = \dot{Q}_r^s. \tag{6.32}$$

Now let us deduce G_c from Eq. (6.30)-(6.32). If we define the communication signal as follows:

$$\begin{aligned}
u^{2,-} &= y^{3,-} = -M_{LR}^c\ddot{W}_3 - \mathcal{X}_{LR}^c\dot{W}_3 - K_{LR}^cW_3\\
y^{2,-} &= u^{1,-} = -M_{LR}^c\ddot{W}_2 - \mathcal{X}_{LR}^c\dot{W}_2 - K_{LR}^cW_2\\
u^{2,+} &= y^{1,+} = -{M_{LR}^c}^T\ddot{W}_1 - {\mathcal{X}_{LR}^c}^T\dot{W}_1 - {K_{LR}^c}^TW_1 - E_{Rl}V_l^1 - E_{Rr}V_r^1\\
y^{2,+} &= u^{3,+} = -{M_{LR}^c}^T\ddot{W}_2 - {\mathcal{X}_{LR}^c}^T\dot{W}_2 - {K_{LR}^c}^TW_2 - E_{Rl}V_l^2 - E_{Rr}V_r^2,
\end{aligned} \tag{6.33}$$

the following differential equations relating to G_c^1, G_c^2 and G_c^3 could be deduced from Eq. (6.30):

$$G_c^1: \ M_{LL}^c\ddot{W}_1 + \mathcal{X}_{LL}^c\dot{W}_1 + K_{LL}^cW_1 = y^{2,-} + F_1 - E_{Ll}V_l^1 - E_{Lr}V_r^1, \tag{6.34}$$

$$G_c^2: \ \bar{M}^c\ddot{W}_2 + \bar{\mathcal{X}}^c\dot{W}_2 + \bar{K}^cW_2 = u^{2,+} + u^{2,-} - E_{Ll}V_l^2 - E_{Lr}V_r^2, \tag{6.35}$$

$$G_c^3: \ M_{RR}^c\ddot{W}_3 + \mathcal{X}_{RR}^c\dot{W}_3 + K_{RR}^cW_3 = y^{2,+} + F_3, \tag{6.36}$$

where:

[8]Chosing two PZT pairs and the right cross-section is also possible.

$$\bar{M}^c = M^c_{LL} + M^c_{RR},\ \bar{\mathcal{X}}^c = \mathcal{X}^c_{LL} + \mathcal{X}^c_{RR},\ \bar{K}^c = K^c_{LL} + K^c_{RR}.$$

Eq. (6.31) and Eq. (6.32) give another two differential equations relating to V_r^1 and V_r^2, the voltage of the PZT sensor (dynamic of the measurement circuit):

$$-YV_r^1 = \dot{Q}_r^1 = -E_{Lr}^T\dot{W}_1 - E_{Rr}^T\dot{W}_2 + C_r\dot{V}_r^1 \tag{6.37}$$

$$-YV_r^2 = \dot{Q}_r^2 = -E_{Lr}^T\dot{W}_2 - E_{Rr}^T\dot{W}_3 + C_r\dot{V}_r^2. \tag{6.38}$$

It should also be noticed that, in this example, the effect of other cells of **Type c** connecting with W_1 on the left and W_3 on the right are not included in Eq. (6.30). Therefore, Eq. (6.34) and (6.36) do not represent the complete dynamics of G_c^1 and G_c^3. If more cells are assembled, the deduced differential equations for G_c^1, G_c^2 and G_c^3 will have the same form as Eq. (6.35). As a result, we now focus on G_c^2 and try to build the state space representation of G_c out of G_c^2.

It could be observed from Eq. (6.34)-(6.36) and Eq. (6.38) that G_c^2, which is considered as G_c, has $u^{2,+}$, $u^{2,-}$, $\dot{W}_3$, V_l^2 as inputs, $y^{2,+}$, $y^{2,-}$, $\dot{W}_2$, V_r^2 as outputs and W_2, V_r^2 belonging to its state. Accordingly, in a more general case, denote $u^+ = u^{2,+}$, $u_1^- = u^{2,-}$, $u_2^- = \dot{W}_3$, $V_{act} = V_l^2$ the inputs of G_c, $y^+ = y^{2,+}$, $y_1^- = y^{2,-}$, $y_2^- = \dot{W}_2$, $V_{sen} = V_r^2$ the outputs and $W^c = W_2$, V_{sen} belonging to its state. The state-space representation of $G_c(A, B, C, D)$, is thus deduced from Eq. (6.33), Eq. (6.35) and Eq. (6.38) as follows (Fig. 6.12):

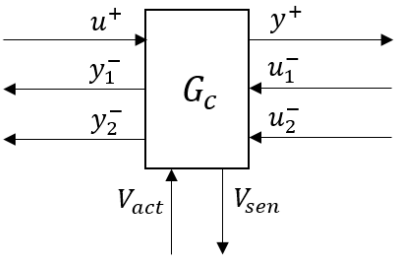

Figure 6.12: Block diagram of G_c

$$\left[\begin{array}{c} y^+ \\ \hline y_1^- \\ y_2^- \\ \hline V_{sen} \end{array}\right] = G_c \left[\begin{array}{c} u^+ \\ \hline u_1^- \\ u_2^- \\ \hline V_{act} \end{array}\right], \tag{6.39}$$

with $\begin{bmatrix} W^c \\ \dot{W}^c \\ V_{sen} \end{bmatrix}$ the state vector (order 7) and:

$$A = \begin{bmatrix} 0 & I & 0 \\ -(\bar{M}^c)^{-1}\bar{K}^c & -(\bar{M}^c)^{-1}\bar{\mathcal{X}}^c & -(\bar{M}^c)^{-1}E_{Lr} \\ 0 & C_r^{-1}E_{Lr}^T & -C_r^{-1}Y \end{bmatrix},$$

$$B = \begin{bmatrix} 0 & 0 & 0 & 0 \\ (\bar{M}^c)^{-1} & -(\bar{M}^c)^{-1} & 0 & -(\bar{M}^c)^{-1}E_{Ll} \\ 0 & 0 & C_r^{-1}E_{Rr}^T & 0 \end{bmatrix},$$

$$C = \begin{bmatrix} {M_{LR}^c}^T(\bar{M}^c)^{-1}\bar{K}^c - {K_{LR}^c}^T & {M_{LR}^c}^T(\bar{M}^c)^{-1}\bar{\mathcal{X}}^c - {\mathcal{X}_{LR}^c}^T & {M_{LR}^c}^T(\bar{M}^c)^{-1}E_{Lr} - E_{Rr} \\ M_{LR}^c(\bar{M}^c)^{-1}\bar{K}^c - K_{LR}^c & M_{LR}^c(\bar{M}^c)^{-1}\bar{\mathcal{X}}^c - \mathcal{X}_{LR}^c & M_{LR}^c(\bar{M}^c)^{-1}E_{Lr} \\ 0 & I & 0 \\ 0 & 0 & 1 \end{bmatrix},$$

$$D = \begin{bmatrix} -{M_{LR}^c}^T(\bar{M}^c)^{-1} & -{M_{LR}^c}^T(\bar{M}^c)^{-1} & 0 & {M_{LR}^c}^T(\bar{M}^c)^{-1}E_{Ll} - E_{Rl} \\ -M_{LR}^c(\bar{M}^c)^{-1} & -M_{LR}^c(\bar{M}^c)^{-1} & 0 & M_{LR}^c(\bar{M}^c)^{-1}E_{Ll} \\ 0 & 0 & 0 & 0 \\ 0 & 0 & 0 & 0 \end{bmatrix}.$$

Following the same procedure, the state-space representation of all the 9 subsystems could be obtained. Their state-space matrices are summarized in Table 6.1-6.2 and the corresponding block diagrams with input/output signals are summarized in Table 6.3.

It should be noticed that the force disturbance is considered as the boundary condition (constraints) at the right surface of the structure (i.e. F_{BR}) and the corresponding subsystem is G_{BR}, see Table 6.3. In fact, F_{BR} contains the constraints along 3 DOF and only the second DOF is the displacement in z direction (referring to Eq. (6.22)). Denote f the force disturbance applied by the shaker, we thus have:

$$F_{BR} = \begin{bmatrix} 0 \\ 1 \\ 0 \end{bmatrix} f \tag{6.40}$$

If we consider a subsystem representing the boundary condition at the right surface with only u^+ and f as input, denoted G_{BL}^f, we thus have (Fig. 6.13):

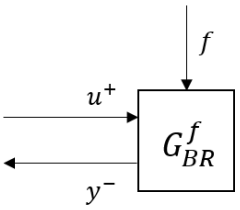

Figure 6.13: Block diagram of G^f_{BR}

$$y^- = G^f_{BR} \begin{bmatrix} u^+ \\ \hline f \end{bmatrix} = G_{BR} \left[\begin{array}{cc} I & 0 \\ 0 & 0 \\ 0 & 1 \\ 0 & 0 \end{array}\right] \begin{bmatrix} u^+ \\ \hline f \end{bmatrix} \tag{6.41}$$

With the particular constructed subsystems, we can update the architecture of the interconnected system (i.e. Fig. 6.9) to Fig. 6.14.

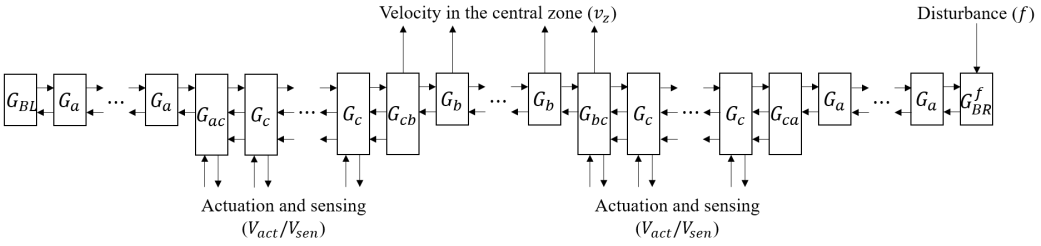

Figure 6.14: Architecture of the interconnected system for the setup

At last, we need to verify that this interconnected model equals to the assembled model obtained in Section 6.3.3 (the second verification step mentioned in Section 6.1). For this purpose, we interconnect these 9 subsystems as illustrated in Fig. 6.14, knowing that G_{ca} and G_{cb} do not have actuation input and sensing output. Then, we compute the response from all the actuators to all the sensors for both the assembled model and the interconnected model. The maximum singular value along the frequency of the absolute error between the two responses is shown in Fig. 6.15. The error always stays below $-190\ dB$ which means that the assembled model and the interconnected model are the same. In conclusion, all the 9 subsystems are correctly constructed.

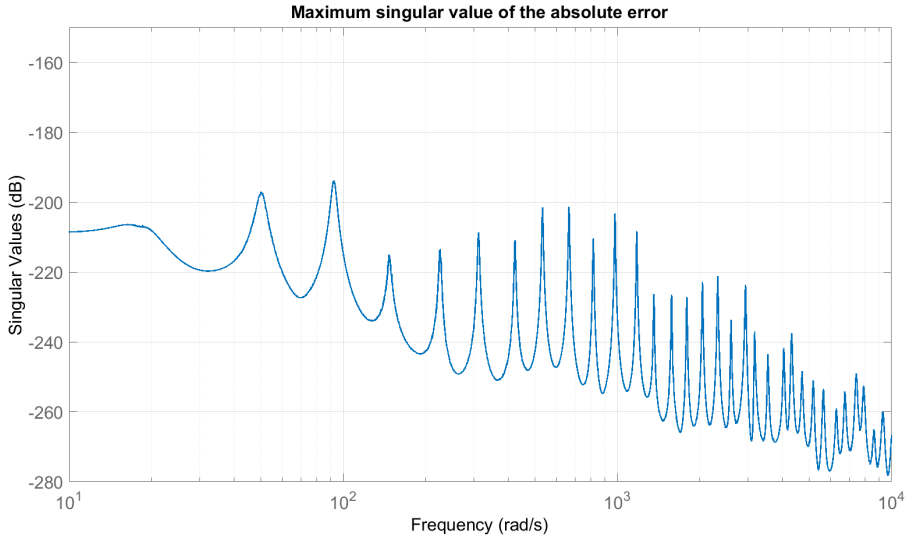

Figure 6.15: Maximum singular value of the absolute error between Assembled model and Interconnected model

6.5 Appendix

(1) Construction of G_a and G_b

The subsystem G_a is in the homogeneous part with cells of **Type a** where there is no electro-mechanical coupling and all of its inputs/outputs are the communication signals with its neighbors (see Fig. 6.9). Fig. 6.16 shows the definition of signals when we interconnect three G_a, respectively denoted G_a^1, G_a^2 and G_a^3.

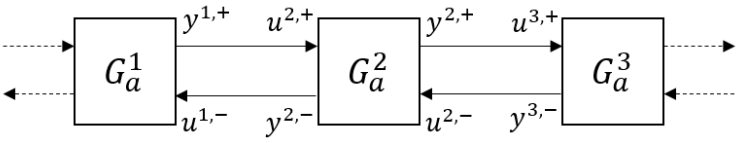

Figure 6.16: Notation of communication signals for G_a

To deduce G_a, let us first assemble two cells of **Type a** (ignoring other cells) as shown in Fig. 6.17 which gives us the governing equation as follow:

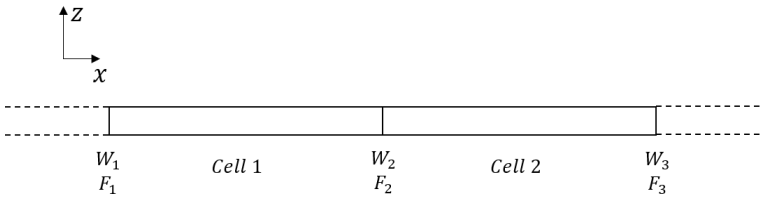

Figure 6.17: Assemble two cells of **Type a**

$$\begin{bmatrix} M^a_{LL} & M^a_{LR} & \\ {M^a_{LR}}^T & M^a_{LL}+M^a_{RR} & M^a_{LR} \\ & {M^a_{LR}}^T & M^a_{RR} \end{bmatrix} \begin{bmatrix} \ddot{W}_1 \\ \ddot{W}_2 \\ \ddot{W}_3 \end{bmatrix} + \begin{bmatrix} \mathcal{X}^a_{LL} & \mathcal{X}^a_{LR} & \\ {\mathcal{X}^a_{LR}}^T & \mathcal{X}^a_{LL}+\mathcal{X}^a_{RR} & \mathcal{X}^a_{LR} \\ & {\mathcal{X}^a_{LR}}^T & \mathcal{X}^a_{RR} \end{bmatrix} \begin{bmatrix} \dot{W}_1 \\ \dot{W}_2 \\ \dot{W}_3 \end{bmatrix} + \begin{bmatrix} K^a_{LL} & K^a_{LR} & \\ {K^a_{LR}}^T & K^a_{LL}+K^a_{RR} & K^a_{LR} \\ & {K^a_{LR}}^T & K^a_{RR} \end{bmatrix} \begin{bmatrix} W_1 \\ W_2 \\ W_3 \end{bmatrix} = \begin{bmatrix} F_1 \\ 0 \\ F_3 \end{bmatrix}. \tag{6.42}$$

Suppose that W_i only belongs to the state of G^i_a for $i = 1, 2, 3$, which means that G^i_a actually represents the i^{th} cross-section of the assembled structure shown in Fig. 6.17. If we define the communication signals as follows:

$$\begin{aligned} u^{2,-} &= y^{3,-} = -M^a_{LR}\ddot{W}_3 - \mathcal{X}^a_{LR}\dot{W}_3 - K^a_{LR}W_3 \\ y^{2,-} &= u^{1,-} = -M^a_{LR}\ddot{W}_2 - \mathcal{X}^a_{LR}\dot{W}_2 - K^a_{LR}W_2 \\ u^{2,+} &= y^{1,+} = -{M^a_{LR}}^T\ddot{W}_1 - {\mathcal{X}^a_{LR}}^T\dot{W}_1 - {K^a_{LR}}^T W_1 \\ y^{2,+} &= u^{3,+} = -{M^a_{LR}}^T\ddot{W}_2 - {\mathcal{X}^a_{LR}}^T\dot{W}_2 - {K^a_{LR}}^T W_2, \end{aligned} \tag{6.43}$$

the following differential equations relating to G^1_a, G^2_a and G^3_a could be deduced from Eq. (6.42):

$$G^1_a: \ M^a_{LL}\ddot{W}_1 + \mathcal{X}^a_{LL}\dot{W}_1 + K^a_{LL}W_1 = y^{2,-} + F_1, \tag{6.44}$$

$$G^2_a: \ \bar{M}^a\ddot{W}_2 + \bar{\mathcal{X}}^a\dot{W}_2 + \bar{K}^a W_2 = u^{2,+} + u^{2,-}, \tag{6.45}$$

$$G^3_a: \ M^a_{RR}\ddot{W}_3 + \mathcal{X}^a_{RR}\dot{W}_3 + K^a_{RR}W_3 = y^{2,+} + F_3, \tag{6.46}$$

where:

$$\bar{M}^a = M^a_{LL} + M^a_{RR},\ \bar{\mathcal{X}}^a = \mathcal{X}^a_{LL} + \mathcal{X}^a_{RR},\ \bar{K}^a = K^a_{LL} + K^a_{RR}.$$

It should be noticed that, in this example, the assembly is only performed to two cells. The effect of other cells of **Type a** connecting with W_1 on the left and with W_3 on the right are not included in Eq. (6.42). Therefore, Eq. (6.44) and (6.46) do not represent the complete dynamics of G^1_a and G^3_a. If more cells are assembled, the deduced differential equations for G^1_a, G^2_a and G^3_a will have the same form as Eq. (6.45). As a result, we now focus on G^2_a and try to build the state space representation of G_a out of G^2_a.

It could be clearly seen from Eq. (6.44)-(6.46) that G^2_a, which is considered as G_a, has $u^{2,+}$, $u^{2,-}$ as inputs, $y^{2,+}$, $y^{2,-}$ as outputs and W_2 belonging to its state. Accordingly, denote $u^+ = u^{2,+}$, $u^- = u^{2,-}$ the inputs of G_a, $y^+ = y^{2,+}$, $y^- = y^{2,-}$ the outputs and $W^a = W_2$ belonging to its state. The state-space representation of $G_a(A, B, C, D)$, is thus deduced from Eq. (6.43) and Eq. (6.45) as follows (Fig. 6.18):

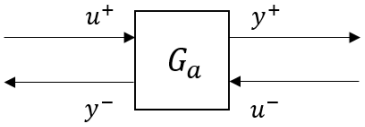

Figure 6.18: Block diagram of G_a

$$\begin{bmatrix} y^+ \\ \hline y^- \end{bmatrix} = G_a \begin{bmatrix} u^+ \\ \hline u^- \end{bmatrix}, \tag{6.47}$$

with $\begin{bmatrix} W^a \\ \dot{W}^a \end{bmatrix}$ the state vector (order 6) and:

$$A = \begin{bmatrix} 0 & I \\ -(\bar{M}^a)^{-1}\bar{K}^a & -(\bar{M}^a)^{-1}\bar{\mathcal{X}}^a \end{bmatrix},\quad B = \begin{bmatrix} 0 & 0 \\ (\bar{M}^a)^{-1} & (\bar{M}^a)^{-1} \end{bmatrix},$$

$$C = \begin{bmatrix} {M^a_{LR}}^T(\bar{M}^a)^{-1}\bar{K}^a - {K^a_{LR}}^T & {M^a_{LR}}^T(\bar{M}^a)^{-1}\bar{\mathcal{X}}^a - {\mathcal{X}^a_{LR}}^T \\ M^a_{LR}(\bar{M}^a)^{-1}\bar{K}^a - K^a_{LR} & M^a_{LR}(\bar{M}^a)^{-1}\bar{\mathcal{X}}^a - \mathcal{X}^a_{LR} \end{bmatrix},$$

$$D = \begin{bmatrix} -{M^a_{LR}}^T(\bar{M}^a)^{-1} & -{M^a_{LR}}^T(\bar{M}^a)^{-1} \\ -M^a_{LR}(\bar{M}^a)^{-1} & -M^a_{LR}(\bar{M}^a)^{-1} \end{bmatrix}.$$

As to G_b, it is in the central zone which is the homogeneous part with cells of **Type b** (see Fig. 6.9). The procedure for constructing G_b is exactly the same as that for constructing G_a, except that the assembled cells (*Cell 1* and *Cell 2* in Fig. 6.17) are of **Type b** and G_b will have to output the velocity in z direction in order to compute the central energy. If we denote W^b the DOF vector of an cross-section in the central zone that belongs to G_b, according to the definition of the DOF vector, (referring to Eq. (6.13)), the second element of $\dot{W}^b$ is exactly the velocity in z direction, denoted v_z. As a result, the state-space representation of G_b should be as follows (Fig. 6.19):

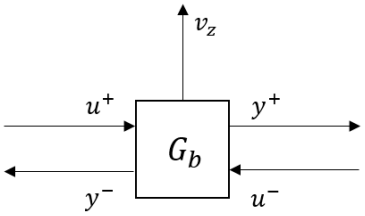

Figure 6.19: Block diagram of G_b

$$\left[\begin{array}{c} y^+ \\ \hline y^- \\ \hline v_z \end{array}\right] = G_b \left[\begin{array}{c} u^+ \\ \hline u^- \end{array}\right], \tag{6.48}$$

with $\begin{bmatrix} W^b \\ \dot{W}^b \end{bmatrix}$ the state vector (order 6) and:

$$A = \begin{bmatrix} 0 & I \\ -(\bar{M}^b)^{-1}\bar{K}^b & -(\bar{M}^b)^{-1}\bar{\mathcal{X}}^b \end{bmatrix}, \quad B = \begin{bmatrix} 0 & 0 \\ (\bar{M}^b)^{-1} & (\bar{M}^b)^{-1} \end{bmatrix},$$

$$C = \begin{bmatrix} {M^b_{LR}}^T(\bar{M}^b)^{-1}\bar{K}^b - {K^b_{LR}}^T & {M^b_{LR}}^T(\bar{M}^b)^{-1}\bar{\mathcal{X}}^b - {\mathcal{X}^b_{LR}}^T \\ M^b_{LR}(\bar{M}^b)^{-1}\bar{K}^b - K^b_{LR} & M^b_{LR}(\bar{M}^b)^{-1}\bar{\mathcal{X}}^b - \mathcal{X}^b_{LR} \\ 0 & \begin{bmatrix} 0 & 1 & 0 \end{bmatrix} \end{bmatrix},$$

$$D = \begin{bmatrix} -{M^b_{LR}}^T(\bar{M}^b)^{-1} & -{M^b_{LR}}^T(\bar{M}^b)^{-1} \\ -M^b_{LR}(\bar{M}^b)^{-1} & -M^b_{LR}(\bar{M}^b)^{-1} \\ 0 & 0 \end{bmatrix},$$

where:

$$\bar{M}^b = M^b_{LL} + M^b_{RR},\ \bar{\mathcal{X}}^b = \mathcal{X}^b_{LL} + \mathcal{X}^b_{RR},\ \bar{K}^b = K^b_{LL} + K^b_{RR}.$$

(2) Construction of G_{BL} and G_{BR}

These two subsystems represent the boundary conditions at the left and right end (surface) of the setup, except that G_{BR} also takes into account the force disturbance applied at the right end in z direction. As the cells at the boundary are also of **Type a**, we can reuse the differential equations from which we deduce G_a.

First, let us discuss the construction of G_{BL}. If we assemble two cells close to the left surface, we will obtain exactly the same structure as shown in Fig. 6.17, except that there will be no more other cells on the left side of W_1. The assembly also leads to Eq. (6.43)-(6.46) where G^1_a should be considered as G_{BL} with F_1 equals to zero because the boundary condition is free which means that there is no constraint on the left surface. Knowing that $y^{2,-} = u^{1,+}$ and $u^{2,+} = y^{1,+}$, (see Eq. (6.43)), it could be clearly seen from Eq. (6.44)-(6.45) that G^1_a has $u^{1,-}$ as input, $y^{1,+}$ as output and W_1 belonging to the its state. Accordingly, denote $u^- = u^{1,-}$ the input of G_{BL}, $y^+ = y^{1,+}$ the output and $W^a = W_1$ belonging to its state. The state-space representation of $G_{BL}(A, B, C, D)$ is thus deduced from Eq. (6.43) and Eq. (6.44) as follows (Fig. 6.20):

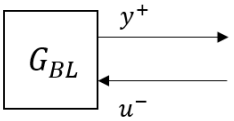

Figure 6.20: Block diagram of G_{BL}

$$y^+ = G_{BL}u^-, \tag{6.49}$$

with $\begin{bmatrix} W^a \\ \dot{W}^a \end{bmatrix}$ the state vector (order 6) and:

$$A = \begin{bmatrix} 0 & I \\ -(M^a_{LL})^{-1}K^a_{LL} & -(M^a_{LL})^{-1}\mathcal{X}^a_{LL} \end{bmatrix},\quad B = \begin{bmatrix} 0 \\ (M^a_{LL})^{-1} \end{bmatrix},$$

$$C = \begin{bmatrix} {M^a_{LR}}^T(M^a_{LL})^{-1}K^a_{LL} - {K^a_{LR}}^T & {M^a_{LR}}^T(M^a_{LL})^{-1}\mathcal{X}^a_{LL} - {\mathcal{X}^a_{LR}}^T \end{bmatrix},$$

$$D = -{M^a_{LR}}^T (M^a_{LL})^{-1}.$$

For G_{BR}, similar with the discussion on G_{BL}, we will also obtain, by assembly, Fig. 6.17 and Eq. (6.43)-(6.46), except that there is no more other cells on the right side of W_3. Thus, G^3_a should be considered as G_{BR} with F_3 the constraints applied on the right surface. F_3 is not zero because it contains the force disturbance in z direction. Knowing that $y^{2,+} = u^{3,+}$ and $u^{2,-} = y^{3,-}$, (see Eq. (6.43)), it could be clearly seen from Eq. (6.45)-(6.46) that G^3_a has $u^{3,+}$, F_3 as inputs, $y^{3,-}$ as output and W_3 belonging to the its state. Accordingly, denote $u^+ = u^{3,+}$, $F_{BR} = F_3$ the input of G_{BR}, $y^+ = y^{3,-}$ the output and $W^a = W_3$ belonging to its state. The state-space representation of $G_{BR}(A, B, C, D)$ is thus deduced from Eq. (6.43) and Eq. (6.46) as follows (Fig. 6.21):

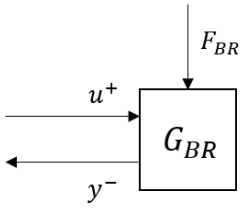

Figure 6.21: Block diagram of G_{BR}

$$y^- = G_{BR} \begin{bmatrix} u^+ \\ \hline F_{BR} \end{bmatrix}, \tag{6.50}$$

with $\begin{bmatrix} W^a \\ \dot{W}^a \end{bmatrix}$ the state vector (order 6) and:

$$A = \begin{bmatrix} 0 & I \\ -(M^a_{RR})^{-1} K^a_{RR} & -(M^a_{RR})^{-1} \mathcal{X}^a_{RR} \end{bmatrix}, \quad B = \begin{bmatrix} 0 & 0 \\ (M^a_{RR})^{-1} & (M^a_{RR})^{-1} \end{bmatrix},$$

$$C = \begin{bmatrix} M^a_{LR}(M^a_{RR})^{-1} K^a_{RR} - K^a_{LR} & M^a_{LR}(M^a_{RR})^{-1} \mathcal{X}^a_{RR} - \mathcal{X}^a_{LR} \end{bmatrix},$$

$$D = \begin{bmatrix} -M^a_{LR}(M^a_{RR})^{-1} & -M^a_{LR}(M^a_{RR})^{-1} \end{bmatrix}.$$

(3) Construction of G_c

Already discussed in Section 6.4.3 as an example.

(4) Construction of G_{ac} and G_{bc}

These two subsystems are the particular ones that connect on the left and right respectively the homogeneous part and the part with piezos, see Fig. 6.9. The procedure of construction is always the same.

For G_{ac}, we assemble one cell of **Type a** (*Cell 1*) and one cell of **Type c** (*Cell 2*) as shown in Fig. 6.22 where G^2 is considered as G_{ac} which will have actuation and sensing capabilities. This leads to the following governing equation:

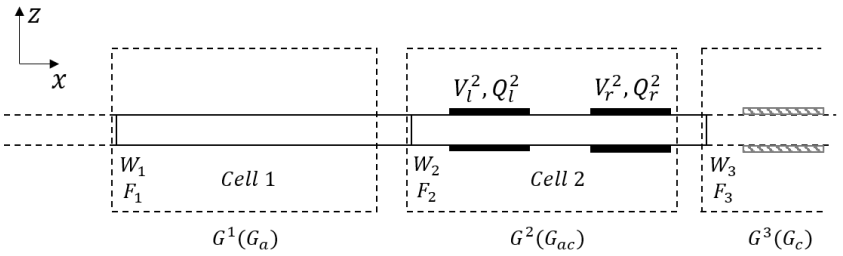

Figure 6.22: Assemble two cells of **Type a** (*Cell 1*) and **Type c** (*Cell 2*)

$$\begin{bmatrix} M^a_{LL} & M^a_{LR} & \\ {M^a_{LR}}^T & M^c_{LL}+M^a_{RR} & M^c_{LR} \\ & {M^c_{LR}}^T & M^c_{RR} \end{bmatrix} \begin{bmatrix} \ddot{W}_1 \\ \ddot{W}_2 \\ \ddot{W}_3 \end{bmatrix} + \begin{bmatrix} \mathcal{X}^a_{LL} & \mathcal{X}^a_{LR} & \\ {\mathcal{X}^a_{LR}}^T & \mathcal{X}^c_{LL}+\mathcal{X}^a_{RR} & \mathcal{X}^c_{LR} \\ & {\mathcal{X}^c_{LR}}^T & \mathcal{X}^c_{RR} \end{bmatrix} \begin{bmatrix} \dot{W}_1 \\ \dot{W}_2 \\ \dot{W}_3 \end{bmatrix} + \begin{bmatrix} K^a_{LL} & K^a_{LR} & \\ {K^a_{LR}}^T & K^c_{LL}+K^a_{RR} & K^c_{LR} \\ & {K^c_{LR}}^T & K^c_{RR} \end{bmatrix} \begin{bmatrix} W_1 \\ W_2 \\ W_3 \end{bmatrix} = \begin{bmatrix} F_1 \\ 0 \\ F_3 \end{bmatrix} + \begin{bmatrix} 0 & 0 \\ -E_{Ll} & -E_{Lr} \\ -E_{Rl} & -E_{Rr} \end{bmatrix} \begin{bmatrix} V_l^2 \\ V_r^2 \end{bmatrix}. \tag{6.51}$$

and the measurement circuit of G^2 also satisfy Eq. (6.38). Eq. (6.51) thus gives us the following differential equations relating to G^1, G^2 and G^3:

$$G^1: \quad M^a_{LL}\ddot{W}_1 + \mathcal{X}^a_{LL}\dot{W}_1 + K^a_{LL}W_1 = y^{2,-} + F_1, \tag{6.52}$$

$$G^2: \quad \bar{M}^{ac}\ddot{W}_2 + \bar{\mathcal{X}}^{ac}\dot{W}_2 + \bar{K}^{ac}W_2 = u^{2,+} + u^{2,-} - E_{Ll}V_l^2 - E_{Lr}V_r^2, \tag{6.53}$$

$$G^3: \quad M^c_{RR}\ddot{W}_3 + \mathcal{X}^c_{RR}\dot{W}_3 + K^c_{RR}W_3 = y^{2,+} + F_3, \tag{6.54}$$

with:

$$\begin{aligned}
u^{2,-} &= y^{3,-} = -M^c_{LR}\ddot{W}_3 - \mathcal{X}^c_{LR}\dot{W}_3 - K^c_{LR}W_3 \\
y^{2,-} &= u^{1,-} = -M^a_{LR}\ddot{W}_2 - \mathcal{X}^a_{LR}\dot{W}_2 - K^a_{LR}W_2 \\
u^{2,+} &= y^{1,+} = -{M^a_{LR}}^T\ddot{W}_1 - {\mathcal{X}^a_{LR}}^T\dot{W}_1 - {K^a_{LR}}^T W_1 \\
y^{2,+} &= u^{3,+} = -{M^c_{LR}}^T\ddot{W}_2 - {\mathcal{X}^c_{LR}}^T\dot{W}_2 - {K^c_{LR}}^T W_2 - E_{Rl}V_l^2 - E_{Rr}V_r^2,
\end{aligned} \tag{6.55}$$

where:

$$\bar{M}^{ac} = M^c_{LL} + M^a_{RR},\ \bar{\mathcal{X}}^{ac} = \mathcal{X}^c_{LL} + \mathcal{X}^a_{RR},\ \bar{K}^{ac} = K^c_{LL} + K^a_{RR}.$$

Denote $u^+ = u^{2,+}$, $u^-_1 = u^{2,-}$, $u^-_2 = \dot{W}_3$, $V_{act} = V_l^2$ as inputs of G_{ac}, $y^+ = y^{2,+}$, $y^- = y^{2,-}$, $V_{sen} = V_r^2$ as outputs and $W^{ac} = W_2$, V_{sen} belonging to its state. The state-space representation of $G_{ac}(A, B, C, D)$, is thus deduced from Eq. (6.55), Eq. (6.53) and Eq. (6.38) as follows (Fig. 6.23):

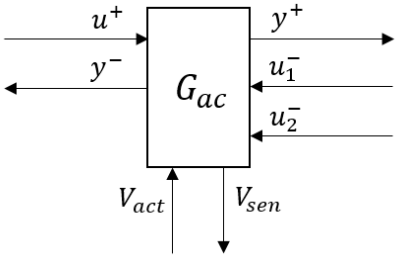

Figure 6.23: Block diagram of G_{ac}

$$\left[\begin{array}{c} y^+ \\ \hline y^- \\ \hline V_{sen} \end{array}\right] = G_{ac} \left[\begin{array}{c} u^+ \\ \hline u^-_1 \\ u^-_2 \\ \hline V_{act} \end{array}\right], \tag{6.56}$$

with $\begin{bmatrix} W^{ac} \\ \dot{W}^{ac} \\ V_{sen} \end{bmatrix}$ the state vector (order 7) and:

$$A = \begin{bmatrix} 0 & I & 0 \\ -(\bar{M}^{ac})^{-1}\bar{K}^{ac} & -(\bar{M}^{ac})^{-1}\bar{\mathcal{X}}^{ac} & -(\bar{M}^{ac})^{-1}E_{Lr} \\ 0 & C_r^{-1}E_{Lr}^T & -C_r^{-1}Y \end{bmatrix},$$

$$B = \begin{bmatrix} 0 & 0 & 0 & 0 \\ (\bar{M}^{ac})^{-1} & -(\bar{M}^{ac})^{-1} & 0 & -(\bar{M}^{ac})^{-1}E_{Ll} \\ 0 & 0 & C_r^{-1}E_{Rr}^T & 0 \end{bmatrix},$$

$$C = \begin{bmatrix} M_{LR}^{c\,T}(\bar{M}^{ac})^{-1}\bar{K}^{ac} - K_{LR}^{c\,T} & M_{LR}^{c\,T}(\bar{M}^{ac})^{-1}\bar{\mathcal{X}}^{ac} - \mathcal{X}_{LR}^{c\,T} & M_{LR}^{c\,T}(\bar{M}^{ac})^{-1}E_{Lr} - E_{Rr} \\ M_{LR}^{a}(\bar{M}^{ac})^{-1}\bar{K}^{ac} - K_{LR}^{a} & M_{LR}^{a}(\bar{M}^{ac})^{-1}\bar{\mathcal{X}}^{ac} - \mathcal{X}_{LR}^{a} & M_{LR}^{a}(\bar{M}^{ac})^{-1}E_{Lr} \\ 0 & 0 & 1 \end{bmatrix},$$

$$D = \begin{bmatrix} -M_{LR}^{c\,T}(\bar{M}^{ac})^{-1} & -M_{LR}^{c\,T}(\bar{M}^{ac})^{-1} & 0 & M_{LR}^{c\,T}(\bar{M}^{ac})^{-1}E_{Ll} - E_{Rl} \\ -M_{LR}^{a}(\bar{M}^{ac})^{-1} & -M_{LR}^{a}(\bar{M}^{ac})^{-1} & 0 & M_{LR}^{a}(\bar{M}^{ac})^{-1}E_{Ll} \\ 0 & 0 & 0 & 0 \end{bmatrix}.$$

The procedure for constructing G_{bc} is exactly the same as that for constructing G_{ac}, except that *Cell 1* in Fig. 6.22 is replaced by the cell of **Type b** and G_{bc} will have to output the velocity in z direction (the left surface of *Cell 2* is located in the central zone) in order to compute the central energy. Denote W^{bc} the DOF vector of the cross-section belonging to G_{bc} (i.e. W_2 in Fig. 6.22), The second element of $\dot{W}^{bc}$ is exactly the velocity in z direction, denoted v_z. The state-space representation of G_{bc} should be as follows (Fig. 6.24):

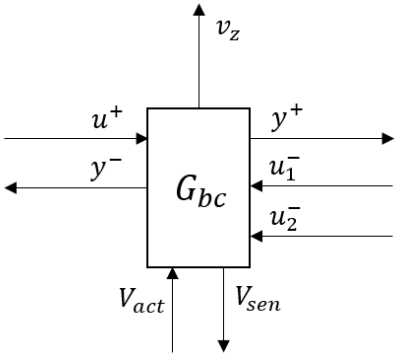

Figure 6.24: Block diagram of G_{bc}

$$\left[\begin{array}{c} y^+ \\ \hline y^- \\ \hline v_z \\ V_{sen} \end{array}\right] = G_{bc} \left[\begin{array}{c} u^+ \\ \hline u_1^- \\ u_2^- \\ \hline V_{act} \end{array}\right], \tag{6.57}$$

with $\begin{bmatrix} W^{bc} \\ \dot{W}^{bc} \\ V_{sen} \end{bmatrix}$ the state vector (order 7) and:

$$A = \begin{bmatrix} 0 & I & 0 \\ -(\bar{M}^{bc})^{-1}\bar{K}^{bc} & -(\bar{M}^{bc})^{-1}\bar{\mathcal{X}}^{bc} & -(\bar{M}^{bc})^{-1}E_{Lr} \\ 0 & C_r^{-1}E_{Lr}^T & -C_r^{-1}Y \end{bmatrix},$$

$$B = \begin{bmatrix} 0 & 0 & 0 & 0 \\ (\bar{M}^{bc})^{-1} & -(\bar{M}^{bc})^{-1} & 0 & -(\bar{M}^{bc})^{-1}E_{Ll} \\ 0 & 0 & C_r^{-1}E_{Rr}^T & 0 \end{bmatrix},$$

$$C = \begin{bmatrix} {M_{LR}^c}^T(\bar{M}^{bc})^{-1}\bar{K}^{bc} - {K_{LR}^c}^T & {M_{LR}^c}^T(\bar{M}^{bc})^{-1}\bar{\mathcal{X}}^{bc} - {\mathcal{X}_{LR}^c}^T & {M_{LR}^c}^T(\bar{M}^{bc})^{-1}E_{Lr} - E_{Rr} \\ M_{LR}^b(\bar{M}^{bc})^{-1}\bar{K}^{bc} - K_{LR}^b & M_{LR}^b(\bar{M}^{bc})^{-1}\bar{\mathcal{X}}^{bc} - \mathcal{X}_{LR}^b & M_{LR}^b(\bar{M}^{bc})^{-1}E_{Lr} \\ 0 & \begin{bmatrix} 0 & 1 & 0 \end{bmatrix} & 0 \\ 0 & 0 & 1 \end{bmatrix},$$

$$D = \begin{bmatrix} -{M_{LR}^c}^T(\bar{M}^{bc})^{-1} & -{M_{LR}^c}^T(\bar{M}^{bc})^{-1} & 0 & {M_{LR}^c}^T(\bar{M}^{bc})^{-1}E_{Ll} - E_{Rl} \\ -M_{LR}^b(\bar{M}^{bc})^{-1} & -M_{LR}^b(\bar{M}^{bc})^{-1} & 0 & M_{LR}^b(\bar{M}^{bc})^{-1}E_{Ll} \\ 0 & 0 & 0 & 0 \\ 0 & 0 & 0 & 0 \end{bmatrix}.$$

where:

$$\bar{M}^{bc} = M_{LL}^c + M_{RR}^b,\ \bar{\mathcal{X}}^{bc} = \mathcal{X}_{LL}^c + \mathcal{X}_{RR}^b,\ \bar{K}^{bc} = K_{LL}^c + K_{RR}^b.$$

(5) Construction of G_{ca} and G_{cb}

The construction of G_{ca} and G_{cb} is similar to that of G_{ac} and G_{bc}. We first assemble one cell of **Type c** (*Cell 1*) and one cell of **Type a** or **Type b** (*Cell 2*) as shown in Fig. 6.25 where G_2 is of interest. It can be clearly observed from Fig. 6.25 that G_{ca} and G_{cb} will not have actuation and sensing capabilities and G_{cb} will also have a velocity output. Following the procedure for constructing G_{ac} and G_{bc}, G_{ca} and G_{cb} could be obtained.

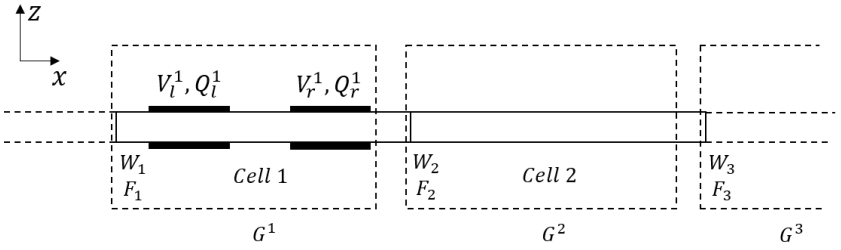

Figure 6.25: Assemble two cells of **Type c** (*Cell 1*) and **Type a** or **Type b** (*Cell 2*)

The state-space representation of $G_{ca}(A, B, C, D)$ is as follows (Fig. 6.26):

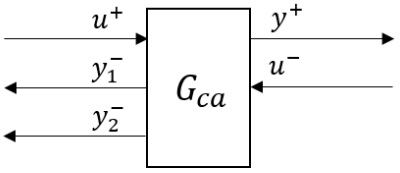

Figure 6.26: Block diagram of G_{ca}

$$\begin{bmatrix} y^+ \\ \hline y_1^- \\ y_2^- \end{bmatrix} = G_{ca} \begin{bmatrix} u^+ \\ \hline u^- \end{bmatrix}, \tag{6.58}$$

with $\begin{bmatrix} W^{ca} \\ \dot{W}^{ca} \end{bmatrix}$ the state vector (order 6) and:

$$A = \begin{bmatrix} 0 & I \\ -(\bar{M}^{ca})^{-1}\bar{K}^{ca} & -(\bar{M}^{ca})^{-1}\bar{\mathcal{X}}^{ca} \end{bmatrix},$$

$$B = \begin{bmatrix} 0 & 0 \\ (\bar{M}^{ca})^{-1} & -(\bar{M}^{ca})^{-1} \end{bmatrix},$$

$$C = \begin{bmatrix} {M^a_{LR}}^T(\bar{M}^{ca})^{-1}\bar{K}^{ca} - {K^a_{LR}}^T & {M^a_{LR}}^T(\bar{M}^{ca})^{-1}\bar{\mathcal{X}}^{ca} - {\mathcal{X}^a_{LR}}^T \\ M^c_{LR}(\bar{M}^{ca})^{-1}\bar{K}^{ca} - K^c_{LR} & M^c_{LR}(\bar{M}^{ca})^{-1}\bar{\mathcal{X}}^{ca} - \mathcal{X}^c_{LR} \\ 0 & I \end{bmatrix},$$

$$D = \begin{bmatrix} -{M^a_{LR}}^T(\bar{M}^{ca})^{-1} & -{M^a_{LR}}^T(\bar{M}^{ca})^{-1} \\ -M^c_{LR}(\bar{M}^{ca})^{-1} & -M^c_{LR}(\bar{M}^{ca})^{-1} \\ 0 & 0 \end{bmatrix}.$$

where:

$$\bar{M}^{ca} = M^a_{LL} + M^c_{RR},\ \bar{\mathcal{X}}^{ca} = \mathcal{X}^a_{LL} + \mathcal{X}^c_{RR},\ \bar{K}^{ca} = K^a_{LL} + K^c_{RR}.$$

The state-space representation of $G_{cb}(A, B, C, D)$ is as follows (Fig. 6.27):

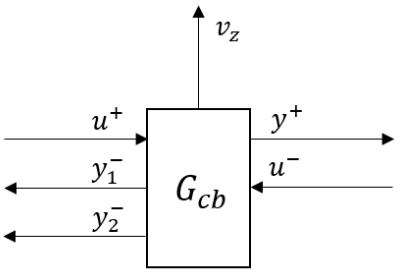

Figure 6.27: Block diagram of G_{cb}

$$\left[\begin{array}{c} y^+ \\ \hline y_1^- \\ y_2^- \\ v_z \end{array}\right] = G_{cb} \left[\begin{array}{c} u^+ \\ \hline u^- \end{array}\right], \tag{6.59}$$

with $\begin{bmatrix} W^{cb} \\ \dot{W}^{cb} \end{bmatrix}$ the state vector (order 6) and:

$$A = \begin{bmatrix} 0 & I \\ -(\bar{M}^{cb})^{-1}\bar{K}^{cb} & -(\bar{M}^{cb})^{-1}\bar{\mathcal{X}}^{cb} \end{bmatrix},$$

$$B = \begin{bmatrix} 0 & 0 \\ (\bar{M}^{cb})^{-1} & -(\bar{M}^{cb})^{-1} \end{bmatrix},$$

$$C = \begin{bmatrix} {M_{LR}^b}^T(\bar{M}^{cb})^{-1}\bar{K}^{cb} - {K_{LR}^b}^T & {M_{LR}^b}^T(\bar{M}^{cb})^{-1}\bar{\mathcal{X}}^{cb} - {\mathcal{X}_{LR}^b}^T \\ M_{LR}^c(\bar{M}^{cb})^{-1}\bar{K}^{cb} - K_{LR}^c & M_{LR}^c(\bar{M}^{cb})^{-1}\bar{\mathcal{X}}^{cb} - \mathcal{X}_{LR}^c \\ 0 & I \\ 0 & \begin{bmatrix} 0 & 1 & 0 \end{bmatrix} \end{bmatrix},$$

$$D = \begin{bmatrix} -{M_{LR}^b}^T(\bar{M}^{cb})^{-1} & -{M_{LR}^b}^T(\bar{M}^{cb})^{-1} \\ -M_{LR}^c(\bar{M}^{cb})^{-1} & -M_{LR}^c(\bar{M}^{cb})^{-1} \\ 0 & 0 \\ 0 & 0 \end{bmatrix}.$$

where:

$$\bar{M}^{cb} = M_{LL}^b + M_{RR}^c,\ \bar{\mathcal{X}}^{cb} = \mathcal{X}_{LL}^b + \mathcal{X}_{RR}^c,\ \bar{K}^{cb} = K_{LL}^b + K_{RR}^c.$$

6.6 Summary

This chapter introduces our method to build interconnected LTI subsystems that will be used in the future for distributed controller design. We first discretize the structure (beam with piezo patches) into cells. There are cells with PZT pairs (one actuator and one sensor) which will be used as a local control unit. There are also homogeneous cells free of PZT pairs which contribute to the global dynamics of the beam. Then we perform Finite Element Modeling to these cells using COMSOL and deduce the governing equation for each cell, similar to the modeling process for the centralized beam-piezo system. However, we apply different method to reduce the governing equation such that the governing equation of each cell has the least number of DOF. We validate the cell models (governing equations) by assembling them and comparing the response of the assembled model with the response of the centralized beam-piezo model obtained for centralized control. Good match was found. Based on these cell models, we finally construct the state-space representations of interconnected LTI subsystems. It is very important to note that one subsystem and one cell are not identical. This is to avoid algebraic relation between neighbor subsystems. We finally validate these subsystems by interconnecting them and comparing the global response with the assembled model obtained in the first validation step. Perfect match was found which means that all the LTI subsystems are correctly constructed.

Table 6.1: State-space matrices of subsystems (1)

Subsystem	(A,B,C,D)
$y^+ = G_{BL}u^-$	$A = \begin{bmatrix} 0 & I \\ -(M^a_{LL})^{-1}K^a_{LL} & -(M^a_{LL})^{-1}\mathcal{X}^a_{LL} \end{bmatrix}$, $B = \begin{bmatrix} 0 \\ (M^a_{LL})^{-1} \end{bmatrix}$, $C = \begin{bmatrix} {M^a_{LR}}^T(M^a_{LL})^{-1}K^a_{LL} - {K^a_{LR}}^T & {M^a_{LR}}^T(M^a_{LL})^{-1}\mathcal{X}^a_{LL} - {\mathcal{X}^a_{LR}}^T \end{bmatrix}$, $D = -{M^a_{LR}}^T(M^a_{LL})^{-1}$.
$\begin{bmatrix} y^+ \\ \hline y^- \end{bmatrix} = G_a \begin{bmatrix} u^+ \\ \hline u^- \end{bmatrix}$	$A = \begin{bmatrix} 0 & I \\ -(\bar{M}^a)^{-1}\bar{K}^a & -(\bar{M}^a)^{-1}\bar{\mathcal{X}}^a \end{bmatrix}$, $B = \begin{bmatrix} 0 & 0 \\ (\bar{M}^a)^{-1} & (\bar{M}^a)^{-1} \end{bmatrix}$, $C = \begin{bmatrix} {M^a_{LR}}^T(\bar{M}^a)^{-1}\bar{K}^a - {K^a_{LR}}^T & {M^a_{LR}}^T(\bar{M}^a)^{-1}\bar{\mathcal{X}}^a - {\mathcal{X}^a_{LR}}^T \\ M^a_{LR}(\bar{M}^a)^{-1}\bar{K}^a - K^a_{LR} & M^a_{LR}(\bar{M}^a)^{-1}\bar{\mathcal{X}}^a - \mathcal{X}^a_{LR} \end{bmatrix}$, $D = \begin{bmatrix} -{M^a_{LR}}^T(\bar{M}^a)^{-1} & -{M^a_{LR}}^T(\bar{M}^a)^{-1} \\ -M^a_{LR}(\bar{M}^a)^{-1} & -M^a_{LR}(\bar{M}^a)^{-1} \end{bmatrix}$, $\bar{M}^a = M^a_{LL} + M^a_{RR}$, $\bar{\mathcal{X}}^a = \mathcal{X}^a_{LL} + \mathcal{X}^a_{RR}$, $\bar{K}^a = K^a_{LL} + K^a_{RR}$.
$\begin{bmatrix} y^+ \\ \hline y^- \\ \hline V_{sen} \end{bmatrix} = G_{ac} \begin{bmatrix} u^+ \\ \hline u^-_1 \\ u^-_2 \\ \hline V_{act} \end{bmatrix}$	$A = \begin{bmatrix} 0 & I & 0 \\ -(\bar{M}^{ac})^{-1}\bar{K}^{ac} & -(\bar{M}^{ac})^{-1}\bar{\mathcal{X}}^{ac} & -(\bar{M}^{ac})^{-1}E_{Lr} \\ 0 & C_r^{-1}E_{Lr}^T & -C_r^{-1}Y \end{bmatrix}$, $B = \begin{bmatrix} 0 & 0 & 0 & 0 \\ (\bar{M}^{ac})^{-1} & -(\bar{M}^{ac})^{-1} & 0 & -(\bar{M}^{ac})^{-1}E_{Ll} \\ 0 & 0 & C_r^{-1}E_{Rr}^T & 0 \end{bmatrix}$, $C = \begin{bmatrix} {M^c_{LR}}^T(\bar{M}^{ac})^{-1}\bar{K}^{ac} - {K^c_{LR}}^T & {M^c_{LR}}^T(\bar{M}^{ac})^{-1}\bar{\mathcal{X}}^{ac} - {\mathcal{X}^c_{LR}}^T & {M^c_{LR}}^T(\bar{M}^{ac})^{-1}E_{Lr} - E_{Rr} \\ M^a_{LR}(\bar{M}^{ac})^{-1}\bar{K}^{ac} - K^a_{LR} & M^a_{LR}(\bar{M}^{ac})^{-1}\bar{\mathcal{X}}^{ac} - \mathcal{X}^a_{LR} & M^a_{LR}(\bar{M}^{ac})^{-1}E_{Lr} \\ 0 & 0 & 1 \end{bmatrix}$, $D = \begin{bmatrix} -{M^c_{LR}}^T(\bar{M}^{ac})^{-1} & -{M^c_{LR}}^T(\bar{M}^{ac})^{-1} & 0 & {M^c_{LR}}^T(\bar{M}^{ac})^{-1}E_{Ll} - E_{Rl} \\ -M^a_{LR}(\bar{M}^{ac})^{-1} & -M^a_{LR}(\bar{M}^{ac})^{-1} & 0 & M^a_{LR}(\bar{M}^{ac})^{-1}E_{Ll} \\ 0 & 0 & 0 & 0 \end{bmatrix}$, $\bar{M}^{ac} = M^c_{LL} + M^a_{RR}$, $\bar{\mathcal{X}}^{ac} = \mathcal{X}^c_{LL} + \mathcal{X}^a_{RR}$, $\bar{K}^{ac} = K^c_{LL} + K^a_{RR}$.
$\begin{bmatrix} y^+ \\ \hline y^-_1 \\ y^-_2 \\ \hline V_{sen} \end{bmatrix} = G_c \begin{bmatrix} u^+ \\ \hline u^-_1 \\ u^-_2 \\ \hline V_{act} \end{bmatrix}$	$A = \begin{bmatrix} 0 & I & 0 \\ -(\bar{M}^c)^{-1}\bar{K}^c & -(\bar{M}^c)^{-1}\bar{\mathcal{X}}^c & -(\bar{M}^c)^{-1}E_{Lr} \\ 0 & C_r^{-1}E_{Lr}^T & -C_r^{-1}Y \end{bmatrix}$, $B = \begin{bmatrix} 0 & 0 & 0 & 0 \\ (\bar{M}^c)^{-1} & -(\bar{M}^c)^{-1} & 0 & -(\bar{M}^c)^{-1}E_{Ll} \\ 0 & 0 & C_r^{-1}E_{Rr}^T & 0 \end{bmatrix}$, $C = \begin{bmatrix} {M^c_{LR}}^T(\bar{M}^c)^{-1}\bar{K}^c - {K^c_{LR}}^T & {M^c_{LR}}^T(\bar{M}^c)^{-1}\bar{\mathcal{X}}^c - {\mathcal{X}^c_{LR}}^T & {M^c_{LR}}^T(\bar{M}^c)^{-1}E_{Lr} - E_{Rr} \\ M^c_{LR}(\bar{M}^c)^{-1}\bar{K}^c - K^c_{LR} & M^c_{LR}(\bar{M}^c)^{-1}\bar{\mathcal{X}}^c - \mathcal{X}^c_{LR} & M^c_{LR}(\bar{M}^c)^{-1}E_{Lr} \\ 0 & I & 0 \\ 0 & 0 & 1 \end{bmatrix}$, $D = \begin{bmatrix} -{M^c_{LR}}^T(\bar{M}^c)^{-1} & -{M^c_{LR}}^T(\bar{M}^c)^{-1} & 0 & {M^c_{LR}}^T(\bar{M}^c)^{-1}E_{Ll} - E_{Rl} \\ -M^c_{LR}(\bar{M}^c)^{-1} & -M^c_{LR}(\bar{M}^c)^{-1} & 0 & M^c_{LR}(\bar{M}^c)^{-1}E_{Ll} \\ 0 & 0 & 0 & 0 \\ 0 & 0 & 0 & 0 \end{bmatrix}$, $\bar{M}^c = M^c_{LL} + M^c_{RR}$, $\bar{\mathcal{X}}^c = \mathcal{X}^c_{LL} + \mathcal{X}^c_{RR}$, $\bar{K}^c = K^c_{LL} + K^c_{RR}$.
$\begin{bmatrix} y^+ \\ \hline y^-_1 \\ y^-_2 \\ v_z \end{bmatrix} = G_{cb} \begin{bmatrix} u^+ \\ \hline u^- \end{bmatrix}$	$A = \begin{bmatrix} 0 & I \\ -(\bar{M}^{cb})^{-1}\bar{K}^{cb} & -(\bar{M}^{cb})^{-1}\bar{\mathcal{X}}^{cb} \end{bmatrix}$, $B = \begin{bmatrix} 0 & 0 \\ (\bar{M}^{cb})^{-1} & -(\bar{M}^{cb})^{-1} \end{bmatrix}$, $C = \begin{bmatrix} {M^b_{LR}}^T(\bar{M}^{cb})^{-1}\bar{K}^{cb} - {K^b_{LR}}^T & {M^b_{LR}}^T(\bar{M}^{cb})^{-1}\bar{\mathcal{X}}^{cb} - {\mathcal{X}^b_{LR}}^T \\ M^c_{LR}(\bar{M}^{cb})^{-1}\bar{K}^{cb} - K^c_{LR} & M^c_{LR}(\bar{M}^{cb})^{-1}\bar{\mathcal{X}}^{cb} - \mathcal{X}^c_{LR} \\ 0 & I \\ 0 & \begin{bmatrix} 0 & 1 & 0 \end{bmatrix} \end{bmatrix}$, $D = \begin{bmatrix} -{M^b_{LR}}^T(\bar{M}^{cb})^{-1} & -{M^b_{LR}}^T(\bar{M}^{cb})^{-1} \\ -M^c_{LR}(\bar{M}^{cb})^{-1} & -M^c_{LR}(\bar{M}^{cb})^{-1} \\ 0 & 0 \\ 0 & 0 \end{bmatrix}$, $\bar{M}^{cb} = M^b_{LL} + M^c_{RR}$, $\bar{\mathcal{X}}^{cb} = \mathcal{X}^b_{LL} + \mathcal{X}^c_{RR}$, $\bar{K}^{cb} = K^b_{LL} + K^c_{RR}$.
$\begin{bmatrix} y^+ \\ \hline y^- \\ \hline v_z \end{bmatrix} = G_b \begin{bmatrix} u^+ \\ \hline u^- \end{bmatrix}$	$A = \begin{bmatrix} 0 & I \\ -(\bar{M}^b)^{-1}\bar{K}^b & -(\bar{M}^b)^{-1}\bar{\mathcal{X}}^b \end{bmatrix}$, $B = \begin{bmatrix} 0 & 0 \\ (\bar{M}^b)^{-1} & (\bar{M}^b)^{-1} \end{bmatrix}$, $C = \begin{bmatrix} {M^b_{LR}}^T(\bar{M}^b)^{-1}\bar{K}^b - {K^b_{LR}}^T & {M^b_{LR}}^T(\bar{M}^b)^{-1}\bar{\mathcal{X}}^b - {\mathcal{X}^b_{LR}}^T \\ M^b_{LR}(\bar{M}^b)^{-1}\bar{K}^b - K^b_{LR} & M^b_{LR}(\bar{M}^b)^{-1}\bar{\mathcal{X}}^b - \mathcal{X}^b_{LR} \\ 0 & \begin{bmatrix} 0 & 1 & 0 \end{bmatrix} \end{bmatrix}$, $D = \begin{bmatrix} -{M^b_{LR}}^T(\bar{M}^b)^{-1} & -{M^b_{LR}}^T(\bar{M}^b)^{-1} \\ -M^b_{LR}(\bar{M}^b)^{-1} & -M^b_{LR}(\bar{M}^b)^{-1} \\ 0 & 0 \end{bmatrix}$, $\bar{M}^b = M^b_{LL} + M^b_{RR}$, $\bar{\mathcal{X}}^b = \mathcal{X}^b_{LL} + \mathcal{X}^b_{RR}$, $\bar{K}^b = K^b_{LL} + K^b_{RR}$.

Table 6.2: State-space matrices of subsystems (2)

Subsystem	(A,B,C,D)
$\begin{bmatrix} y^+ \\ \hline y^- \\ \hline v_z \\ \hline V_{sen} \end{bmatrix} = G_{bc} \begin{bmatrix} u^+ \\ \hline u_1^- \\ \hline u_2^- \\ \hline V_{act} \end{bmatrix}$	$A = \begin{bmatrix} 0 & I & 0 \\ -(\bar{M}^{bc})^{-1}\bar{K}^{bc} & -(\bar{M}^{bc})^{-1}\bar{\mathcal{X}}^{bc} & -(\bar{M}^{bc})^{-1}E_{Lr} \\ 0 & C_r^{-1}E_{Lr}^T & -C_r^{-1}Y \end{bmatrix}$, $B = \begin{bmatrix} 0 & 0 & 0 & 0 \\ (\bar{M}^{bc})^{-1} & -(\bar{M}^{bc})^{-1} & 0 & -(\bar{M}^{bc})^{-1}E_{Ll} \\ 0 & 0 & C_r^{-1}E_{Rr}^T & 0 \end{bmatrix}$, $C = \begin{bmatrix} M_{LR}^{c\,T}(\bar{M}^{bc})^{-1}\bar{K}^{bc} - K_{LR}^{c\,T} & M_{LR}^{c\,T}(\bar{M}^{bc})^{-1}\bar{\mathcal{X}}^{bc} - \mathcal{X}_{LR}^{c\,T} & M_{LR}^{c\,T}(\bar{M}^{bc})^{-1}E_{Lr} - E_{Rr} \\ M_{LR}^{b}(\bar{M}^{bc})^{-1}\bar{K}^{bc} - K_{LR}^{b} & M_{LR}^{b}(\bar{M}^{bc})^{-1}\bar{\mathcal{X}}^{bc} - \mathcal{X}_{LR}^{b} & M_{LR}^{b}(\bar{M}^{bc})^{-1}E_{Lr} \\ 0 & \begin{bmatrix} 0 & 1 & 0 \end{bmatrix} & 0 \\ 0 & 0 & 1 \end{bmatrix}$, $D = \begin{bmatrix} -M_{LR}^{c\,T}(\bar{M}^{bc})^{-1} & -M_{LR}^{c\,T}(\bar{M}^{bc})^{-1} & 0 & M_{LR}^{c\,T}(\bar{M}^{bc})^{-1}E_{Ll} - E_{Rl} \\ -M_{LR}^{b}(\bar{M}^{bc})^{-1} & -M_{LR}^{b}(\bar{M}^{bc})^{-1} & 0 & M_{LR}^{b}(\bar{M}^{bc})^{-1}E_{Ll} \\ 0 & 0 & 0 & 0 \\ 0 & 0 & 0 & 0 \end{bmatrix}$, $\bar{M}^{bc} = M_{LL}^{c} + M_{RR}^{b},\ \bar{\mathcal{X}}^{bc} = \mathcal{X}_{LL}^{c} + \mathcal{X}_{RR}^{b},\ \bar{K}^{bc} = K_{LL}^{c} + K_{RR}^{b}.$
$\begin{bmatrix} y^+ \\ \hline y_1^- \\ \hline y_2^- \end{bmatrix} = G_{ca} \begin{bmatrix} u^+ \\ \hline u^- \end{bmatrix}$	$A = \begin{bmatrix} 0 & I \\ -(\bar{M}^{ca})^{-1}\bar{K}^{ca} & -(\bar{M}^{ca})^{-1}\bar{\mathcal{X}}^{ca} \end{bmatrix}$, $B = \begin{bmatrix} 0 & 0 \\ (\bar{M}^{ca})^{-1} & -(\bar{M}^{ca})^{-1} \end{bmatrix}$, $C = \begin{bmatrix} M_{LR}^{a\,T}(\bar{M}^{ca})^{-1}\bar{K}^{ca} - K_{LR}^{a\,T} & M_{LR}^{a\,T}(\bar{M}^{ca})^{-1}\bar{\mathcal{X}}^{ca} - \mathcal{X}_{LR}^{a\,T} \\ M_{LR}^{c}(\bar{M}^{ca})^{-1}\bar{K}^{ca} - K_{LR}^{c} & M_{LR}^{c}(\bar{M}^{ca})^{-1}\bar{\mathcal{X}}^{ca} - \mathcal{X}_{LR}^{c} \\ 0 & I \end{bmatrix}$, $D = \begin{bmatrix} -M_{LR}^{a\,T}(\bar{M}^{ca})^{-1} & -M_{LR}^{a\,T}(\bar{M}^{ca})^{-1} \\ -M_{LR}^{c}(\bar{M}^{ca})^{-1} & -M_{LR}^{c}(\bar{M}^{ca})^{-1} \\ 0 & 0 \end{bmatrix}$, $\bar{M}^{ca} = M_{LL}^{a} + M_{RR}^{c},\ \bar{\mathcal{X}}^{ca} = \mathcal{X}_{LL}^{a} + \mathcal{X}_{RR}^{c},\ \bar{K}^{ca} = K_{LL}^{a} + K_{RR}^{c}.$
$y^- = G_{BR} \begin{bmatrix} u^+ \\ \hline F_{BR} \end{bmatrix}$	$A = \begin{bmatrix} 0 & I \\ -(M_{RR}^{a})^{-1}K_{RR}^{a} & -(M_{RR}^{a})^{-1}\mathcal{X}_{RR}^{a} \end{bmatrix}$, $B = \begin{bmatrix} 0 & 0 \\ (M_{RR}^{a})^{-1} & (M_{RR}^{a})^{-1} \end{bmatrix}$, $C = \begin{bmatrix} M_{LR}^{a}(M_{RR}^{a})^{-1}K_{RR}^{a} - K_{LR}^{a} & M_{LR}^{a}(M_{RR}^{a})^{-1}\mathcal{X}_{RR}^{a} - \mathcal{X}_{LR}^{a} \end{bmatrix}$, $D = \begin{bmatrix} -M_{LR}^{a}(M_{RR}^{a})^{-1} & -M_{LR}^{a}(M_{RR}^{a})^{-1} \end{bmatrix}$.

Table 6.3: Block diagrams of subsystems

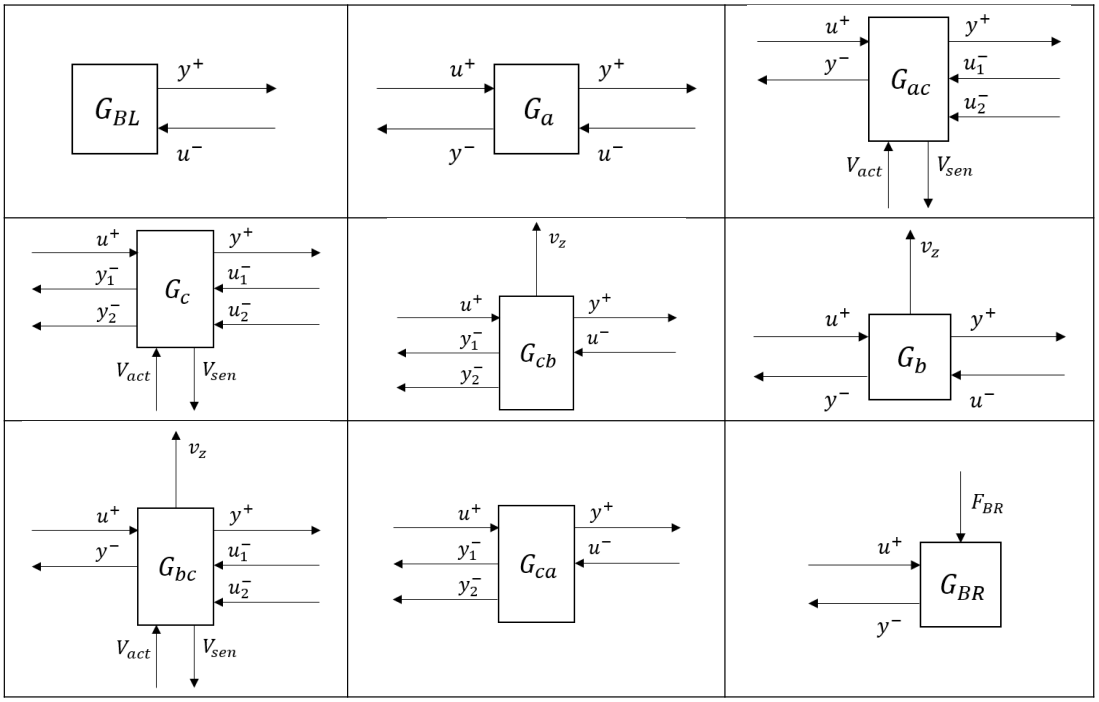

Chapter 7

Conclusions and future research

This research aims at solving a particular active vibration control problem that is to reduce the vibration of smart structures in a specific zone where neither actuation nor sensing is possible. Thus, the challenge is that we want to control a part of the structure while only have access to measurements at other parts. Another challenge is that the disturbance is over a wide frequency band (covering 11 modes) such that a SISO controller is not sufficient for controlling all the modes in this bandwidth. A MIMO controller is thus necessary which requires modern control methods. Such methods will allow us to efficiently synthesize MIMO controllers that satisfy multiple control objectives. Moreover, the spillover instability must also be avoided which guarantees that the model-based design could also work as expected on actual setup.

To tackle all these challenges, we first propose a methodology for centralized control. This methodology first allows us to build a reliable model of the smart structure as only a reliable model can result in guaranteed performance. Here, reliable means that the response of the model, mainly in frequency domain, is close to the actual setup. Therefore, in the modeling process, the effects of the actual control devices are also taken into account which makes sure that the model is close to the reality as much as possible. Based on this reliable model, an H_∞ control based synthesis method with particular criterion is proposed. This criterion is a mathematical interpretation of all the challenges considered in this research. By applying a standard H_∞ framework, we could obtain a controller that satisfies the proposed criterion. At last, for the ease of implementation, the

obtained H_∞ controller is further reduced without losing the closed-loop stability or degrading the performance.

In particular, for the first challenge, we construct, in the model, a to-be-controlled output signal which allows us to deduce an expression of the vibration energy in a specific zone of the smart structure. By controlling this output signal, we control the vibration in that specific zone. Second, the H_∞ based synthesis method is applicable for computing both SISO and MIMO controllers. In addition, this methodology allows us to flexibly specify the frequency band of the disturbance. However, in different circumstances, the number and position of actuators/sensors should be carefully chosen such that the to-be-controlled modes can be effectively excited/detected. Third, the spillover problem is avoided by guaranteeing the robust stability. In fact, this methodology first gives a reliable full-order model which will contain a larger frequency band than the bandwidth of the disturbance. Then, a proposed multi-variable model reduction method is applied to obtain a reduced -order model which only focuses on the bandwidth of the disturbance. The reduced-order model is used to design the controller while the full-order model, as it is a good representation of the actual setup, is used as a reference to validate the closed-loop stability of the reduced-order model based controller, which is the so-called robust stability. As a result, the proposed multi-variable model reduction method is also an important contribution of this research.

This methodology is validated by applying it on an experimental setup composed of an aluminum beam where a number of piezoelectric transducers (PZT) have already been patched except in the central zone. We finally obtain a MIMO controller that particularly reduces the vibration energy in the central zone with a high reduction rate. This high reduction rate is validated by both simulations and experiments. Besides, the application of this methodology will not be limited in the vibration reduction of beam structures. It can also be applied on other structures such as flexible plates and shells.

It should be noted that the above methodology belongs to centralized control. Considering the high computational cost and the high level of physical connectivity in the presence of a large number of actuators and sensors, we then turn to distributed control. We consider the same beam structure and aims at computing

distributed controllers such that the same control objectives are satisfied. For distributed control, the smart structure should first be spatially discretized and thus will be considered as the so-called spatially interconnected systems (the interconnection of multiple LTI subsystems). The to-be-designed distributed controllers will connect with the subsystems with actuation and sensing capabilities to form a local control unit. Multiple controllers work together to achieve a global performance. As a result, the spatially discretization of the smart structure and the modeling for these interconnected subsystems are of great importance. This research proposes a FEM based modeling method which gives the state-space representation of all subsystems. In particular, this method first decomposes the structure into cells and FEM is performed to each cell which gives their governing equations. Then, several local cells are assembled which gives a larger governing equation whose variables are regrouped and then decomposed to obtain the model of LTI subsystems. The decomposition allows to avoid that two subsystems share a part of their states. This makes sure that the states of different subsystems are orthogonal which is important for distributed controller synthesis.

This modeling method has been proved correct with respect to the finite element model obtained for centralized control (before model improvement step by grey-box identification) which has discrepancies compared with the actual setup. Thus, the future works will be focused on two aspects. First, the identification of LTI subsystems such that the global behaviour matches the actual setup. Second, the design of distributed controllers for such interconnected systems such that all the objectives are satisfied.

Part II

Résumé en français

Chapitre 1

Introduction

1.1 Motivation de cette recherche

Les structures légères et les manipulateurs flexibles ont de plus en plus attiré l'attention pour de nombreuses applications dans de nombreux domaines industriels (aérospatial, automobile, industrie manufacturière, etc.). Les avantages principaux des structures légères sont le poids léger et le coût faible de production. Cependant, les structures légères sont généralement moins rigides et donc souffrent du problème de vibration important quand elles sont excitées aux fréquences de résonance par des perturbations externes. Par conséquent, le contrôle efficace de vibration de telles structures aura une grande importance économique, ce qui a motivé beaucoup de recherches dans ce domaine [1–4].

Pour le contrôle de vibration des structures flexibles, le contrôle actif [8] a attiré l'attention des chercheurs durant ces dernières années. Les méthodes actives utilisent généralement un ensemble d'actionneurs et de capteurs (structures actives) qui se connectent comme une boucle de réaction. Le développement rapide des technologies électroniques rend les actionneurs/capteurs plus intelligentes et efficaces. De tels actionneurs/capteurs sont appelés les matériaux intelligentes. Les structures intelligentes correspondent aux structures actives qui intègrent les matériaux intelligents (utilisés comme actionneurs et capteurs). Bien qu'il y ait plusieurs types de matériaux intelligentes, une grande partie des recherches du contrôle actif de vibration utilisent des matériaux piézoélectriques comme actionneurs/capteurs [10] en raison de la grande précision et performance.

Dans cette recherche, on se concentre sur un problème de vibration particulier qui reflète des applications principalement dans les domaines de l'aérospatial et de l'automobile. Premièrement, l'énergie vibratoire doit être particulièrement réduite dans des endroits spécifiques. Par exemple, au niveau d'une antenne ou d'un capteur sur l'enveloppe de l'avion, au niveau du siège de passager dans une voiture (Fig. 1.1), etc.. De telles applications nous permettent de réaliser des objectifs précis, par exemple en donnant plus de confort aux passagers dans une voiture. Deuxièmement, nous ne pouvons pas placer d'actionneurs ou de capteurs à ces endroits spécifiques. Comme il existe déjà nombreux dispositifs connectés entre eux, il sera donc difficile d'ajouter des dispositifs d'actionnement et de détection supplémentaires. Le défi sera de réduire la vibration à des endroits spécifiques tout en ayant accès aux mesures des autres endroits. Cet objectif a besoin de l'utilisation des méthodes multivariables modernes permettant de traiter les variables de performance non mesurable. Troisièmement, nous visons à réduire la vibration dans une gamme de fréquence la plus large possible. Plus la bande passante est large, plus le système sera applicable. Quatrièmement, il faut éviter le problème de spill-over [17] qui est l'instabilité causée par les dynamiques négligées du modèle lorsque le contrôleur est appliqué sur l'installation expérimentale.

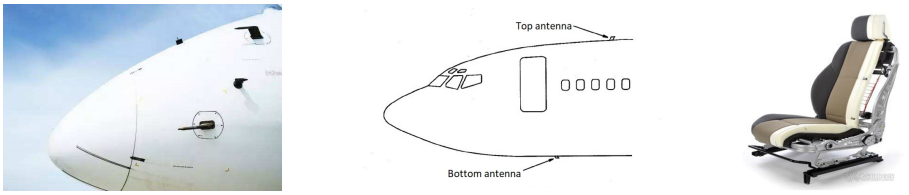

Figure 1.1: Applications particulières des problèmes du contrôle de vibration

Pour reproduire le problème ci-dessus, nous construisons une installation expérimentale composée d'une poutre d'aluminium libre-libre[1] sur laquelle un certain nombre de matériaux intelligents (on utilise ici des transducteurs piézoélectriques) est déjà été collés, sauf dans la zone centrale. L'objectif est de calculer des contrôleurs pour rétroaction qui réduisent l'énergie vibratoire dans la zone centrale. Dans cette recherche, nous proposerons d'abord une méthodologie permettant de concevoir un contrôleur centralisé. Ensuite, on passe au contrôle distribué où on propose une méthode de modélisation de la structure pour des

[1] Il n'y pas de contraintes aux deux extrémités de la poutre

sous-systèmes interconnectés permettant à l'avenir de synthétiser des contrôleurs distribués.

1.2 Contexte

Le matériel intelligent le plus couramment utilisées dans le contrôle actif de vibration est le matériel piézoélectrique à cause de sa simplicité mécanique, sa légèreté, sa large bande passante, sa haute précision, et sa capacité d'intégration de haut niveau dans la structure. Pour les recherches sur le contrôle actif de vibration des structures flexibles, plusieurs méthodes ont été développées durant ces dernières années.

Pour la partie modélisation, de nombreuses recherches dans ce domaine appliquent la technique d'éléments finis (FEM — Finite Element Modeling) et d'identification des systèmes [45–51]. La FEM est basée sur des principes mécaniques et des lois physiques qui permet d'obtenir des équations différentielles partielles. Cependant, telles équations ont un grand nombre de degré de liberté (DOF — Degree of Freedom). Il existe plusieurs méthodes de réduction permettant de réduire de tels modèles comme la méthode de déplacement modal [27], de sous-espace Krylov [52], de Rayleigh – Ritz [53], etc.. De façon différente, l'identification permet de construire un modèle à partir de données expérimentales dans la perspective des systèmes et du contrôle. Une fonction de transfert (ou une représentation d'état) qui reflète le comportement entrée-sortie de la structure est directement obtenue. Il existe également des méthodes pour réduire de tels modèles comme presenté dans [54]. En outre, il est également possible de combiner ces deux techniques.

Pour la partie du contrôle centralisé, il existe de nombreuses lois de commande appliquées dans les circonstances différentes permettant de contrôler différents types des systèmes. Pour être précis, la structure étudiée ici est considérée comme un système LTI (Linear Time Invariant) et on se concentre sur la loi de commande pour rétroaction. Dans la littérature sur le contrôle actif des vibrations pour les systèmes LTI, des méthodes ont d'abord été développées pour un système SISO (Single Input Sinlge Output), par exemple PID [55–57], Retour de vitesse [9, 16, 58–60], Retour d'accélération [13, 61, 62], Retour positif de position [63–66], etc.. De telles méthodes ont des inconvénients. Premièrement, elles

ne peuvent que contrôler qu'un mode de résonance. Pour en contrôler plusieurs, différents contrôleurs doivent être calculés séparément et connectés en parallèle ce qui a une faible efficacité et performance. Deuxièmement, ces méthodes requièrent des actionneur et des capteurs co-localisés, ce qui limite l'applicabilité. Troisièmement, si trop de modes sont concernés, l'utilisation d'un contrôleur MIMO (Multi Input Multi Output) est obligatoire. L'application des méthodes de contrôle modernes permettent de surmonter ces inconvénients. Ces méthodes incluent le Placement des Pôles [69], le Linéaire quadratique Gaussien/Régulateur (LQG/LQR) [70–75], la Synthèse H_2 [76], la Synthèse H_∞ [77–82], etc.. Ces méthodes modernes sont applicables aux systèmes SISO et MIMO et n'ont pas besoin des actionneurs et des capteurs co-localisés. En particulier, le contrôle H_∞ fournit des propriétés de robustesse satisfaisantes en présence d'incertitudes paramétriques et dynamiques [32] qui ne sont pas facile à obtenir par d'autres méthodes. La prise en compte de la robustesse nous permet d'éviter le problème de spill-over [83, 84] qui est la motivation principale de l'application du contrôle H_∞ dans cette recherche. De plus, nous visons à réduire la vibration dans une zone spécifique où il n'y a pas d'actionneur ou de capteur par rapport à une perturbation dans une large gamme de fréquences. À notre connaissance, cette recherche est la première qui propose une technique traitant d'un tel problème. L'adaptation du contrôle H_∞ à ces objectifs particuliers est donc un grand défi et constitue la contribution principale de ce travail.

Cependant, en présence d'un grand nombre d'actionneurs et de capteurs[2], le contrôle centralisé entraîne des coûts de calcul élevés et une connectivité physique complexe. Ceu motive la conception des contrôleurs distribués où chaque contrôleur réagit uniquement avec une partie locale de la structure. Plusieurs contrôleurs travaillent ensemble pour obtenir un effet global. Pour cet objectif, la structure intelligente sera discrétisée et pourra donc être considérée comme l'ensemble des sous-systèmes spatialement interconnecté (ou un système spatialement distribué) [85]. Fig. 1.2 présente l'architecture d'un système distribué avec G notant le sous-système d'interconnexion[3] et K le contrôleur distribué. Dans ces dernières années, plusieurs méthodes ont été développées pour concevoir tels contrôleurs. Raffaello et Geir [88] proposent un cadre d'espace d'état

[2]En utilisant plus d'actionneur et de capteur, on est capable de contôler plus de modes avec une meilleur performance

[3]Un sous-système fait partir de la structure et a des capacités d'actionnement et de détection

permettant de contrôler des systèmes avec une topologie d'interconnexion structurée de haut niveau. Les conditions d'analyse et de synthèse sont formulées en termes de LMI (Linear Matrix Inequality). Tous les sous-systèmes sont considérés comme identiques. Cependant dans les applications réelles, l'architecture pourrait être spatialement variante. Ainsi, des méthodes étendues sont développées pour des systèmes spatialement variants [92–94] ou des systèmes hétérogènes [95–97]. Pour obtenir le modèle d'un système distribué, plusieurs techniques sont disponibles incluant l'identification distribuée [98, 99], le FEM [90], la combinaison d'identification distribuée et de FEM [100], etc..

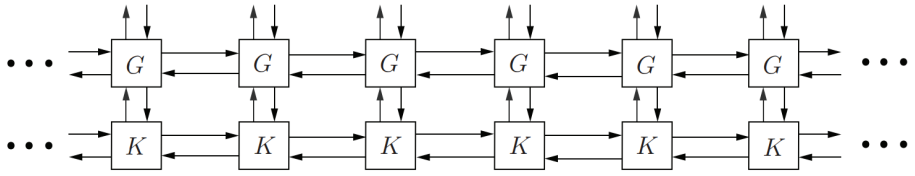

Figure 1.2: Architecture d'un système distribué contrôlé

1.3 Organisation de la thèse

Le Chapitre 2 présent le banc expérimental étudié dans cette recherche. Les objectifs de contrôle globale sont donnés. Le Chapitre 3 explique en détail la méthodologie proposée pour concevoir un contrôleur MIMO. Le Chapitre 4 discute la modélisation du modèle distribué (l'interconnexion des sous-systèmes). La conclusion est donnée dans Chapitre 5.

Notations: Notons $G_{x\to y}$ et $T_{x\to y}$ respectivement la fonction de transfert en boucle ouverte et en boucle fermée de x à y, $\mathcal{S}_u$ la Densité Spectrale de Puissance (DSP) d'un signal u, $||G||_2$ et $||G||_\infty$ respectivement la norme H_2 et la norme H_∞ d'un system (LTI) G, $\overline{\sigma}(A)$ la valeur singulière maximale d'une matrice A, $diag(A_1, A_2, \cdots, A_n)$ une matrice diagonale ou bloc-diagonale avec $A_i, i = 1, 2, \cdots, n$ les termes ou les blocs diagonales, A^T la transposé d'une matrice réelle A, et A^* la transposé conjuguée d'une matrice complexe A. '$\star$' représente la Produit étoile de Redheffer.

Chapitre 2

Description du système

2.1 Installation expérimentale

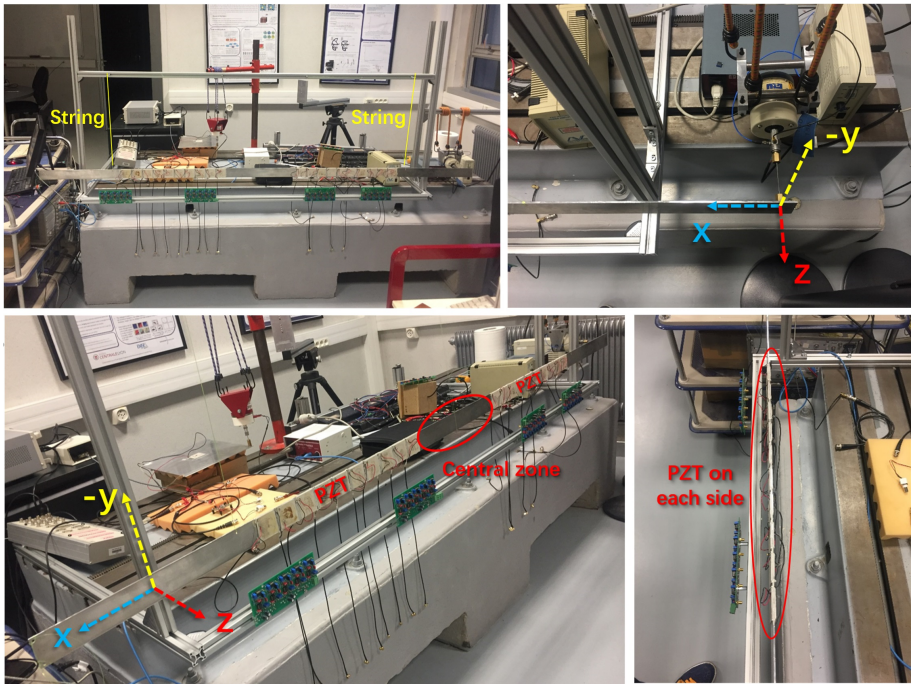

Figure 2.1: Installation expérimentale : vue générale (en haut à gauche), shaker (en haut à droite), zone centrale et localisations des PZT (en bas à gauche), pairs de PZT (en pas à droite)

On considère une structure flexible intégrée avec les matériaux intelligentes. On vise à réduire la vibration dans une zone particulière où les matériaux intelligents ne peuvent pas être placés. Ce qui veut dire qu'on va contrôler la vibration d'une

zone en effectuant des mesures dans une autre zone. Pour cela, on considère l'installation expérimentale montrée Fig. 2.1. L'installation se compose d'une poutre d'aluminium longue et mince avec plusieurs transducteurs piézoélectriques (PZT). La perturbation vient d'un shaker électrodynamique localisé à l'extrémité droite de la poutre. Fig. 2.2 est le diagramme schématique de cette installation qui donne plus de détails.

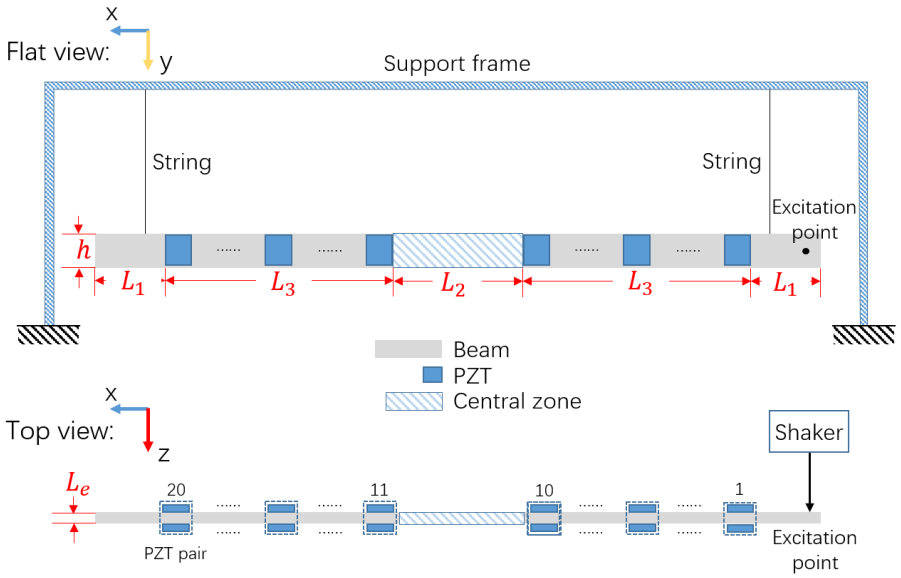

Figure 2.2: Diagramme schématique de l'installation : vue plate (en haut); vue d'en haut (en bas)

La poutre est suspendu à une étagère solide, ce qui crée une condition de limite libre-libre. Deux fois 10 paires de PZT couvrent deux zones L_3 autour de la zone centrale (zone L_2). Une paire de PZT (deux PZT situés au même endroit mais sur des côtés différents de la poutre) est utilisé comme un actionneur (ou capteur) afin de générer une force inversée sur les deux côtés de la poutre, ce qui donne un couple de commande équilibré comme illustrée dans Fig. 2.3. Il y a au total 20 paires de PZT numérotées de 1 à 20 (10 paires dans chaque côté de la zone centrale). La perturbation en force (appliqué par le shaker) est dans l'axis z à l'extrémité droite au point d'excitation au milieu de hauteur (h). Les dimensions et les paramètres matériaux sont présentés dans Table 2.1.

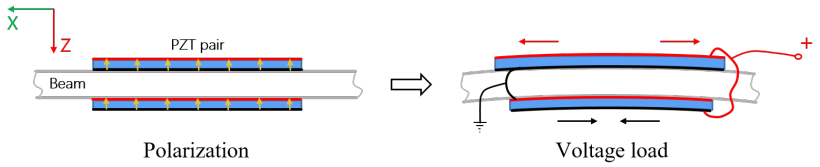

Figure 2.3: Polarisation des PZT et couple de commande équilibré résultant généré par l'excitation d'une tension

Table 2.1: Dimensions et paramètres de l'installation

Propriété	**Valeur**
Densité de la poutre (Aluminium), ρ	$2720\,kg/m^3$
Longueur totale de la poutre, L	$2.5\,m$
Zone sans PZT, L_1	$0.45\,m$
Zone centrale, L_2	$0.42\,m$
Zone avec PZT, L_3	$0.59\,m$
Hauteur de la poutre, h	$0.053\,m$
Épaisseur de la poutre, L_e	$0.003\,m$
PZT type	FerroPerm Pz26
PZT dimensions	$0.05m \times 0.05m \times 0.0005m$
Distance entre PZT	$0.01\,m$
Tension maximale de PZT (guideline)	$200\,VAC/mm$
Surface transversale de la poutre, A_S	$159\,mm^2$
Module d'Young (Aluminium), Y_{ang}	$69\,GPa$

2.2 Objectifs et considérations

L'objectif général est de réduire les vibrations dans une zone spécifique lorsqu'on a seulement accès aux mesures dans d'autres zones. Pour notre installation expérimentale, cet objectif s'interprète de réduire l'énergie vibratoire dans la zone centrale (la zone avec longueur L_2) quand la poutre est excitée par une perturbation de force au long de l'axis z. On vise aussi à contrôler le plus grand nombre de modes possible. On choisit donc une large gamme de fréquence $(600, 3000)$[1] rad/s. Cette gamme de fréquence est dans la plage sensible du Pz26 (le type de PZT qu'on choisit, voir Table 2.1) et couvre 11 modes vibratoires. Les modes en dehors de cette gamme ne seront pas être contrôlés.

Pour contrôler tellement beaucoup de modes et des variables de performance non-mesurables, on a besoin d'appliquer les méthodes de conception multi-variable moderne. De plus, on est obligé d'utiliser plusieurs actionneurs et capteurs pour que tous les 11 modes soient contrôlées. Ce qui conduit à concevoir un contrôleur

[1] Environ $(95, 477)$ Hz

MIMO pour le contrôle centralisé et plusieurs contrôleurs SISO pour le contrôle distribué.

Certaines autres considérations doivent également être prises en compte. Premièrement, lorsque le modèle n'est pas assez précis, la technique d'identification doit être appliquée. Deuxièmement, pour concevoir à la fin un contrôleur simple, il est important d'avoir d'abord un modèle simple. Ce qui signifie dans notre cas un modèle d'ordre réduit où les dynamiques apparaissaient uniquement dans l'intervalle $(600, 3000)$ rad/s. Cela introduit une exigence de stabilité robuste. Le contrôleur obtenu doit également stabiliser le modèle complet. Ceu peut être interprèté comme éviter le problème de spill-over[2]. Troisièmement, les gains du contrôleur doivent être élevés dans $(600, 3000)$ rad/s pour assurer un rapport de réduction élevé. En dehors de $(600, 3000)$ rad/s, l'amplitude doit être faible pour limiter la consommation d'énergie. Pour la même raison, on doit également faire attention à ce que le bruit de mesure (généralement situé en hautes fréquences) ait un effet limité sur la sortie du contrôleur.

2.3 Implémentation du contrôleur

On discute ici l'implémentation du contrôleur centralisé. La conception des contrôleurs distribués sera un travail à effectuer dans le futur. Pour concevoir un contrôleur simple, on doit choisir le nombre minimal d'actionneurs et de capteurs qui permettent de garantir une performance maximale accessible. Dans notre cas, on choisit deux actionneurs et deux capteurs. En particulier, on choisit la $10^{ème}$ et la $16^{ème}$ paires de PZT comme actionneurs, la $5^{ème}$ et la $11^{ème}$ paires de PZT comme capteurs[3]. Fig. 2.4 présente les positions de ces paires de PZT.

Les dispositifs utilisés pour implémenter le contrôleur sont listés dans Table 2.2. Le contrôleur est implémenté dans une carte de contrôle numérique. Cette carte est équipé d'un convertisseur ADC (DAC) dans chaque canal d'entrée (de sortie). Les tensions des capteurs sont d'abord filtrées par les filtres anti-repliements et puis collectées par la carte via son convertisseur ADC. Les amplificateurs de

[2]Problème d'instabilité dû à l'effet de l'actionnement sur les dynamiques non modélisées de la structure [17]

[3]Ce choix est expérimentalement montré raisonnable pour contrôler tous les 11 modes avec un grand rapport de réduction.

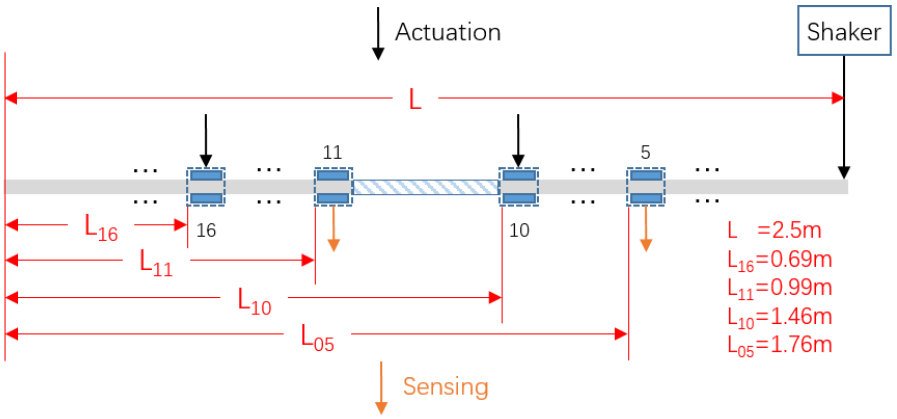

Figure 2.4: Les positions des actionneurs et capteurs utilisé pour le contrôle centralisé

puissance sont utilisés pour prendre les sorties de la carte et puis conduire les actionneurs. Le shaker a besoin d'un signal d'entrée comme une référence pour caractériser la bande passante et l'amplitude de la perturbation. En général, le système en boucle fermée est présenté par la figure Fig. 2.5 où f représente la perturbation de force, V_s le vecteur de tension induite dans les capteurs (le $5^{ème}$ et le $11^{ème}$ paires de PZT) et V_a le vecteur de tension appliqué sur les actionneurs (le $10^{ème}$ et le $16^{ème}$ paires de PZT).

Table 2.2: List of the control devices

Dispositifs	**Type**
Carte de contrôle numérique	DSpace DS1104
Filtre anti-repliement	Nexus Conditioning Amplifier Type 2692
Amplificateur de puissance	PCB 790 Series Power Amplifier
Shaker électrodynamique	DP V4

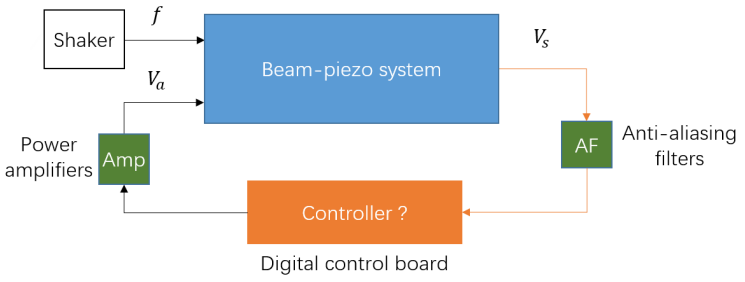

Figure 2.5: Système en boucle fermée

Chapitre 3

Contrôle centralisé

3.1 Méthodologie

La méthodologie qu'on propose pour remplir les objectifs décrits dans Section 2.2 est présentée par la figure Fig. 3.1. Cette méthodologie permet de concevoir un contrôleur MIMO centralisé simple avec une performance garantie sur l'installation expérimentale.

En résumé, on construit d'abord un modèle précis. Plusieurs techniques sont appliquées. On applique la FEM à l'aide de COMSOL qui donne un modèle par éléments finis qui est ensuite transformé en une représentation d'espace d'état. Ce modèle contient les dynamiques inférieur à une fréquence donnée. Dans notre cas, cette fréquence est choisie un peu plus grande que 3000 rad/s. De plus, on construit dans ce modèle une sortie (un vecteur) composé des vitesses des nombreux points dans la zone centrale. À part de celle-là, on peut déduire une expression d l'énergie vibratoire de cette zone. Les paramètres du modèle sont ensuite réglés en appliquant l'identification boite-grise qui donne un modèle plus précis (modèle complet). Évidemment, ce modèle complet couvre une gamme de fréquence plus large que $(600, 3000)$ rad/s. On propose donc une méthode de réduction de modèle. En appliquant cette méthode, on obtient un modèle réduit proche au modèle complet uniquement dans $(600, 3000)$ rad/s. Ce modèle réduit est ensuite utilisé pour concevoir le contrôleur en appliquant la synthèse H_∞. Un critère H_∞ particulier est proposé afin de minimiser l'énergie dans la zone centrale et afin de garantir la stabilité en boule fermée du modèle complet. Le

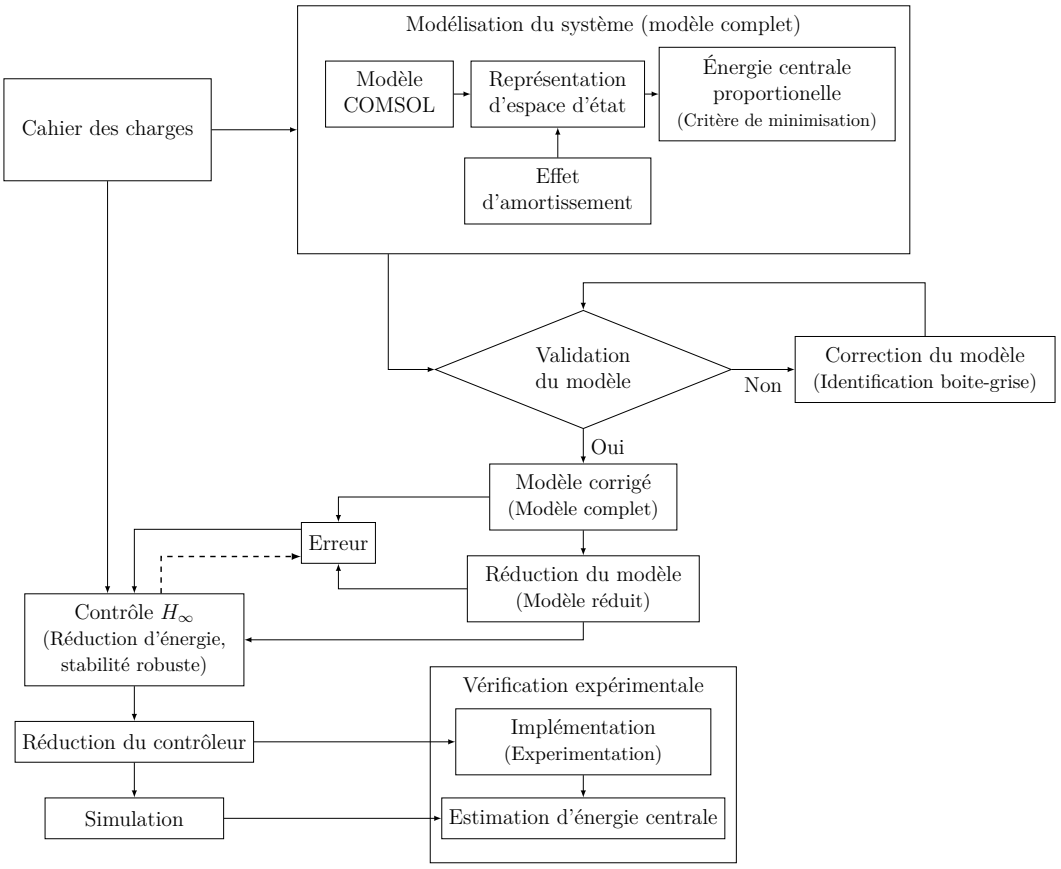

Figure 3.1: Présentation générale de la méthodologie

dernier objectif est abordé en considérant la différence entre le modèle complet et le modèle réduit comme une incertitude. Le contrôleur obtenu est encore réduit sans détruire la stabilité ni dégrader les performances. On fait à la fin la validation numérique et expérimentale.

3.2 Modélisation

L'objectif de la modélisation est d'obtenir une représentation d'espace d'état de l'installation expérimentale. Le modèle doit avoir la perturbation de force $f \in \mathbf{R}$ et la tension des actionneurs $V_a \in \mathbf{R}^{N_a \times 1}$ comme entrées, la tension des capteurs $V_s \in \mathbf{R}^{N_s \times 1}$ comme sortie, comme illustré par Fig. 2.5[1]. De plus, on construit

[1]Les effets des dispositifs pour l'implémentation (amplificateur de puissance, filtre anti-repliement, DAC/ADC convertisseur dans la carte de contrôle) sont considérés comme des gains constants et des déphasages. Ces derniers seront approximés par des retards purs.

aussi une autre sortie de vitesse qui permet d'exprimer l'énergie vibratoire dans la zone centrale (énergie centrale).

La modélisation est basée sur les hypothèses suivantes. On considère que la poutre est homogène, isotrope transverse et élastique. L'effet des moments de flexion et des déplacements latéraux sera pris en compte, mais la déformation en cisaillement et l'inertie de rotation seront négligées. Il n'y a pas de moment de flexion ou d'effort en cisaillement aux deux extrémités de la poutre (condition limite). À l'aide de COMSOL, on effectue l'analyse par éléments finis basée sur des éléments 3D standard. On applique aussi le déplacement modal [27] qui permet de simplifier ce modèle par éléments finis en négligeant les modes hautes fréquences. L'erreur introduite par cette simplification est corrigée par l'analyse statique [28]. Pour l'effet d'amortissement, on choisit d'imposer le modèle de Rayleigh [105] qui introduit deux termes constantes[2]. Les dynamiques dans les circuits de mesure[3] sont aussi pris en compte. Toutes les opérations ci-dessus nous permet de déduire une représentation d'état de la forme suivante qui contient les premières N mode :

$$\begin{cases} \dot{x}(t) = A \cdot x(t) + B_f \cdot f(t) + B_a \cdot V_a(t) \\ \nu_{node}(t) = C_e \cdot x(t) \\ V_s(t) = C_s \cdot x(t) \end{cases}, \quad x(t) = \begin{bmatrix} \eta(t) \\ \dot{\eta}(t) \\ V_s(t) \end{bmatrix} \tag{3.1}$$

avec

$$A = \begin{bmatrix} 0 & I & 0 \\ -K_{mode} & -\kappa_a I - \kappa_s K_{mode} & -E_s \\ 0 & R_s^{-1} \cdot E_s^T & -R_s^{-1} \cdot Y_s \end{bmatrix}, \quad B_a = \begin{bmatrix} 0 \\ -E_a \\ 0 \end{bmatrix}, \quad B_f = \begin{bmatrix} 0 \\ F \\ 0 \end{bmatrix},$$
$$C_s = \begin{bmatrix} 0 & 0 & I \end{bmatrix}, \quad C_e = \varphi_{node} \cdot \begin{bmatrix} 0 & I & 0 \end{bmatrix}, \quad \varphi_{node} = [\varphi_{node_1}^T, \varphi_{node_2}^T, \cdots, \varphi_{node_{N_z}}^T]^T$$

où $K_{mode} = diag(\omega_1^2, \omega_2^2, \cdots, \omega_N^2)$ est la matrice de rigidité avec ω_i la fréquence de $i^{ème}$ mode[4], $R_s = diag(r_{s_1}, r_{s_2}, \cdots, r_{s_{N_s}})$ la matrice de capacité avec r_{s_j} la capacité de $j^{ème}$ paire de PZT utilisée comme capteur. E_s et E_a sont les matrices de couplage électromécanique entre la poutre et les PZT respectivement liées au

[2] Il existe des méthodes plus générales par exemple introduire pour chaque mode une terme d'amortissement modal, ce qui se complique le modèle lorsqu'il contient nombreux modes.

[3] La tension de capteur est mesurée par un circuit électrique en boule fermée.

[4] Dans notre cas, ω_N doit être choisie au moins plus grande que 3000 rad/s

capteurs et actionneurs. F est le vecteur de force lié à la perturbation et $Y_s = Y \cdot I_{N_s}$ l'impédance[5] interne de la carte de contrôle. $\eta(t) = [\eta_1(t), \eta_2(t), \cdots, \eta_N(t)]^T$ est un vecteur composé des coordonnées modales $\eta_i(t)$ $(i = 1...N)$ des premières N modes. On exprime la vibration dans la zone centrale par l'énergie centrale moyenne. Pour construire une expression mathématique simple de cette énergie dans une zone continue, on prend sa discrétisation spatiale qui est la somme d'énergie cinétique (carrée de vitesse) de plusieurs nœuds[6] dans cette zone. Une approche pratique est de choisir N_z nœuds uniformément répartis dans la zone centrale. Les vitesses de ces N_z nœuds sont représentées par le vecteur $\nu_{node}(t) = [\nu_{node_1}(t), \nu_{node_2}(t), \cdots, \nu_{node_{N_z}}(t)]^T$. Par conséquent, l'énergie centrale peut être représentée par la quantité suivante:

$$\begin{aligned} \overline{E^p_{cent}} &= \lim_{T\to\infty} \frac{1}{T} \int_0^T \nu_{node}(t)^T \cdot \nu_{node}(t) \cdot dt \\ &= \frac{1}{2\pi} \int_{-\infty}^{+\infty} H^*(j\omega) H(j\omega) |L_f(j\omega)|^2 \, d\omega = \left\| H(s) L_f(s) \right\|_2^2 \end{aligned} \tag{3.2}$$

où $H(s)$ est la fonction de transfère (vecteur) entre f et ν_{node}, $|L_f(j\omega)|^2$ la densité spectrale de puissance (DSP) de f. Pour notre système particulier, on peut montrer dans la suite que la réduction de $||HL_f||_\infty$ entraîne également la réduction de $||HL_f||_2$. Par conséquent, en réduisant $||HL_f||_\infty$, on réduit l'énergie centrale.

En appliquant la transformation de Laplace sur modèle (3.1), on obtient une matrice de fonction de transfert noté $G^{full}(s)$:

$$G^{full}(s) = \left[\begin{array}{c|c} G^{full}_{f\to\nu_{node}}(s) & G^{full}_{V_a\to\nu_{node}}(s) \\ \hline G^{full}_{f\to V_s}(s) & G^{full}_{V_a\to V_s}(s) \end{array} \right] \tag{3.3}$$

On applique maintenant le modèle (3.1) sur l'installation considérée. Selon l'objectif, la bande passante de la perturbation est $(600, 3000)$ rad/s. On choisit donc de garder les premières 20 modes ($N = 20$) où la fréquence de résonance maximale ω_{20} est plus large que 3000 rad/s. L'entrée V_a contient la tension de la $10^{ème}$ et de la $16^{ème}$ paire de PZT. La sortie V_s contient la tension du $5^{ème}$ et du $11^{ème}$ paire de PZT ($N_a = N_s = 2$). Pour le vecteur de vitesse ν_{node}, on choisit $N_z = 19$ points uniformément répartis dans la zone centrale. Ces choix

[5] L'impédance est l'inverse de résistance

[6] Les nœuds sont les points sur la structure. Ils sont générés par COMSOL pour effectuer l'analyse par éléments finis

nous donnent un modèle d'ordre 42 (modèle initial). Pour vérifier ce modèle, on compare sa réponse fréquentielle avec cela de l'installation réelle (benchmark) qui est mesuré en utilisant un analyseur de fréquence (*HP 35652B*). Pour l'exemple, on choisit ici de montrer la réponse entre V_a et V_s, i.e. $G^{full}_{V_a \to V_s}$, voir Fig. 3.2. Le trait jaune discontinu présente la réponse du modèle initial et le trait bleu solide celle du benchmark où on trouve décalage entre les deux. Les résultats similaires peuvent être aussi observés entre les autres entrées et sorties. Ce qui montre que ce modèle initial n'est pas assez précis et la correction est nécessaire.

3.3 Correction du modèle

Le modèle (3.1) est caractérisé par les paramètres suivant : K_{mode}, R_s, Y_s, κ_a, κ_s, E_a, E_s, F et φ_{node}. Pour R_s, Y_s et K_{mode}, on peut prendre les valeurs mesurées directement sur l'installation réelle. Les autres paramètres sont calculés par COMSOL. On les appelle les premières estimations de COMSOL. Cependant, les premières estimations ont une faible précision et donc doivent être corrigés. Pour la correction, on applique identification boite-grise qui nous permet de régler $\theta = (\kappa_a, \kappa_s, E_a, E_s, F, \varphi_{node})$. Évidement, sa valeur initial θ_{init} est données par les premières estimations de COMSOL.

Pour réduire la complexité du critère d'identification, on divise θ en 3 parties : $\theta_1 = (\kappa_a, \kappa_s, E_a, E_s)$, $\theta_2 = F$ et $\theta_3 = \varphi_{node}$. On les règle respectivement en effectuant 3 mesures. Pour la **mesure** 1, on applique seulement une tension (bruit blanc) en V_a ($f = 0$) où la relation entre V_a et V_s est seulement une fonction de θ_1, ce qui nous permet d'obtenir la valeur identifiée $\theta_{1,id}$. Pour la **mesure** 2, on applique seulement f (bruit blanc) ($V_a = 0$) où la relation entre f et V_s est une fonction de θ_2 ($\theta_1 = \theta_{1,id}$). Ce qui nous permet d'obtenir la valeur identifiée $\theta_{2,id}$. De la même façon, pour la **mesure** 3, on applique f (bruit blanc) et on mesure ν_{node} qui permet d'identifier $\theta_{3,id}$ ($\theta_1 = \theta_{1,id}$, $\theta_2 = \theta_{2,id}$)[7]. Finalement, on obtient un modèle identifié caractérisé par $\theta_{id} = (\theta_{1,id}, \theta_{2,id}, \theta_{3,id})$, noté $G^{full}(\theta_{id})$.

[7]Pour la mesure ν_{node}, on utilise un vélocimètre de laser. Chaque fois, ce laser peut mesurer la vitesse d'un seul point $\nu_{node_i} (i = 1, \cdots, N_z)$. Par conséquent, la mesure doit être répétée N_z fois. Chaque mesure permet d'identifier une partie de $\theta_{3,id}$ qui contient les paramètres dans φ_{node_i}.

Les étapes ci-dessus sont appliquées sur le modèle initial d'ordre 42 obtenu dans la Section 3.2 et afin d'obtenir un modèle identifié beaucoup plus précis. Fig. 3.2 montre l'amélioration de la réponse fréquentielle du modèle identifié entre V_a et V_s (trait rouge pointillé). Des résultats similaires peuvent être aussi observés entre les autres entrées et sorties. Il est à noter que ce modèle identifié $G^{full}(\theta_{id})$ couvre une plage de fréquence plus large que $(600, 3000)$ rad/s et donc va être appelé dans la suite le modèle complet. Ce modèle complet est aussi considéré comme une référence pour vérifier la stabilité robuste.

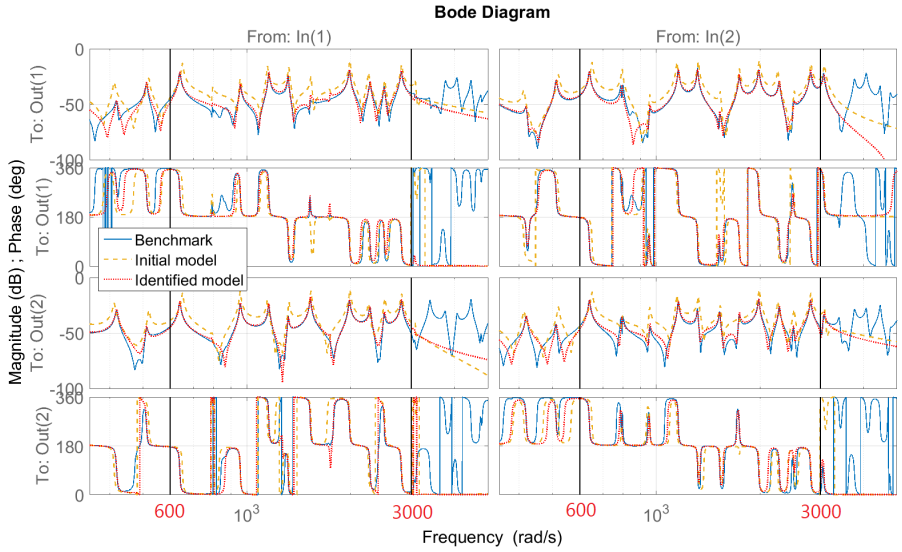

Figure 3.2: Frequency response : Benchmark (solid blue) vs $G^{full}_{V_a \to V_s}(\theta_{init})$ (dashed yellow) vs $G^{full}_{V_a \to V_s}(\theta_{id})$ (dotted red)

3.4 Réduction du modèle multi-variable

Le modèle complet $G^{full}(\theta_{id})$ contient les dynamiques en dehors de la gamme de fréquence ciblée $(600, 3000)$ rad/s parce qu'on applique le déplacement modale qui garde les 20 premiers modes. Pour obtenir un modèle plus simple contenant uniquement les dynamiques dans $(600, 3000)$ rad/s, d'autres méthodes doivent être développées. Pour cela, on cherche des méthodes au sens des systèmes et du contrôle. Plusieurs méthodes peuvent être trouvées dans [54]. L'idée générale est de simplifier un modèle en minimisant différents types de normes d'erreur qui permet de garder les dynamiques dans une gamme de fréquence choisie. En se lacant sur des processus similaires, on propose une méthode de réduction en

minimisant une erreur particulière qui n'a pas été discutée dans [54]. Cette méthode a deux étapes : la troncature de la forme modale et la minimisation de l'erreur relative.

3.4.1 Troncature de la forme modale

La troncature de la forme modale (MFT — Modal Form Truncation) est actuellement l'application de l'Agrégation [30] qui permet d'éliminer les pôles sans intérêt. Le processus est comme suit.

À partir du modèle complet $G = \left[\begin{array}{c|c} A & B \\ \hline C & D \end{array}\right]$ d'ordre n et de $\Lambda(A)$ l'ensemble de ses valeurs propres (pôles de G), on fait un changement de base qui permet de transformer G en forme modale (appelée également forme canonique diagonale dans [115]) comme suit :

$$G = \left[\begin{array}{c|c} \hat{A} & \hat{B} \\ \hline \hat{C} & \hat{D} \end{array}\right] = \left[\begin{array}{ccccccc|c} \hat{A}_1 & & & & & & & \hat{B}_1 \\ & \ddots & & & & & & \vdots \\ \hdashline & & \hat{A}_p & & & & & \hat{B}_p \\ & & & \ddots & & & & \vdots \\ & & & & \hat{A}_q & & & \hat{B}_q \\ \hdashline & & & & & \ddots & & \vdots \\ & & & & & & \hat{A}_n & \hat{B}_n \\ \hline \hat{C}_1 & \cdots & \hat{C}_p & \cdots & \hat{C}_q & \cdots & \hat{C}_n & \hat{D} \end{array}\right] \tag{3.4}$$

où $\hat{A}$ est bloc-diagonale et $\Lambda(\hat{A}) = \Lambda(A)$. Chaque bloc $\hat{A}_i, i = 1, 2, \cdots, n$ est un scalaire ou une matrice 2×2. Ces blocs sont dans un ordre croissant du module de valeur propre correspondant. Soit Ω la gamme de fréquences intéressantes qui couvre les pôles de $\hat{A}_i, i = p, \cdots, q$, le modèle réduit qui contient uniquement les pôles dans Ω peut être construit en tronquant le système (3.4), ce qui donne:

$$G_r = \left[\begin{array}{c|c} A_r & B_r \\ \hline C_r & D_r \end{array}\right] = \left[\begin{array}{ccc|c} \hat{A}_p & & & \hat{B}_p \\ & \ddots & & \vdots \\ & & \hat{A}_q & \hat{B}_q \\ \hline \hat{C}_p & \cdots & \hat{C}_q & \hat{D} \end{array}\right] \tag{3.5}$$

3.4.2 Minimisation de l'erreur relative

Il est à noter que la troncature va généralement introduire une erreur entre le modèle G et son modèle réduit G_r (après MFT). L'objectif est de modifier G_r pour que l'erreur entre G et G_r soit minimisée. Comme les pôles de G_r appartiennent à ceux de G, G_r sera très proche que G aux résonances dans Ω. L'erreur se présentera principalement aux anti-résonances. Pour capturer l'erreur aux anti-résonances, on choisit de minimiser l'erreur relative car sa définition donne des pondérations similaires sur les résonances et anti-résonances [116]. L'erreur relative est définie comme suit[8]:

$$\Delta(j\omega) = G_r(j\omega)^{-1}\left(G(j\omega) - G_r(j\omega)\right). \tag{3.6}$$

On ne modifie pas la matrice A_r qui est liée aux pôles. Ici, on choisit de modifier C_r et D_r. De plus, l'erreur doit être minimisée pour toutes les fréquences dans Ω. Donc, on propose le critère de minimisation suivant:

$$\min_{C_r,D_r} \quad \gamma \quad \textit{tel que} \quad \forall\omega \in \Omega,\ \overline{\sigma}\left(G_r(j\omega)^{-1}(G(j\omega) - G_r(j\omega))\right) < \gamma \tag{3.7}$$

Prob. (3.7) possède un nombre infini de contraintes car il considère toutes les fréquences dans Ω. Cependant, on peut transformer un nombre infini de contraintes en un nombre fini de contraintes en introduisant une nouvelle variable de matrice décision, ce qui définit la contrainte LMI (Linear Matrix Inequality) [31]. Malheureusement, on n'a pas pu transformer directement Prob. (3.7) en un problème LMI. Mais on peut approximer Prob. (3.7) par un autre problème similaire comme suivante :

$$\min_{C_r,D_r} \quad \gamma \quad \textit{tel que}\ \forall\omega \in \Omega,\ \overline{\sigma}\left(G(j\omega)^{-1}(G(j\omega) - G_r(j\omega))\right) < \gamma \tag{3.8}$$

On a montré que la solution de Prob. (3.7) est approximativement la solution de Prob. (3.8). On arrive finalement à transformer Prob. (3.8) en un problème d'optimisation LMI. Il existe des algorithmes efficaces pour résoudre ce type de

[8] Cette erreur sera considérée comme une incertitude liée à la stabilité robuste dans le contrôle H_∞.

problèmes, voir [31]. Cette méthode de réduction proposée, i.e. MFT et minimisation d'erreur relative, est présentée dans un article de conférence récemment publié (voir la Section 1.3, Part I) où vous pouvez trouver la formulation du problème LMI.

3.4.3 Application

On applique cette méthode de réduction multi-variable sur le modèle complet $G^{full}(\theta_{id})$ obtenu dans Section 3.3 avec la représentation d'état (3.1). D'abord, la MFT est appliquée. On transforme $G^{full}(\theta_{id})$ en forme modale où la matrice dynamique A est bloc-diagonale. On tronque les blocs correspondant aux modes en dehors de $(600, 3000)$ rad/s, ce qui donne un modèle réduit d'ordre 24 comme suit[9] :

$$\begin{cases} \dot{x} = A^r \cdot x + B_f^r \cdot f + B_a^r \cdot V_a \\ \nu_{node} = C_e^r \cdot x \\ V_s = C_s^r \cdot x \end{cases} \tag{3.9}$$

À titre d'exemple, on compare la réponse fréquentielle entre V_a et V_s du modèle (3.9) (trait jaune discontinu) et du modèle complet (trait bleu solide) Fig. 3.3. On observe que le modèle (3.9) conserve bien les dynamiques entre $(600, 3000)$ rad/s aux résonances (des résultats similaires peuvent être aussi trouvés entre d'autres entrées et sorties). Cependant, à certaines anti-résonances, il existe des décalages qui entraînent une grande erreur relative. La valeur singulière de l'erreur relative $\Delta(j\omega)$ (entre V_a et V_s) est présentée dans Fig. 3.4 où on observe de grandes erreurs à certaines fréquences (jusqu'à presque 20 dB).

Ensuite, on modifie le modèle (3.9) en minimisant l'erreur relative. Pour cette étape, on se concentre uniquement sur l'erreur relative liée à la partie du modèle (3.9) entre V_a et V_s, noté $G_{V_a \to V_s}$, par raison de simplicité. D'autre part, il s'agit de la fonction de transfert directement impliquée dans la boucle fermé. En plus de déterminer un nouveau C_s^r, noté $C_s^{r,new}$, on ajoute une terme directe $D_s^{r,new}$ pour augmenter le degré de liberté. En conséquence, le problème de minimisation est comme suit :

[9] En fait, on garde un autre mode juste après 3000 rad/s. Le modèle réduit contient 12 modes. C'est la compromis entre l'ordre et la qualité du modèle réduit.

$$\min_{C_s^{r,new},D_s^{r,new}} \sup_{\omega\in(600,3000)} \overline{\sigma}\left(G^{-1}_{V_a\to V_s}(j\omega)(G^{full}_{V_a\to V_s}(j\omega) - G_{V_a\to V_s}(j\omega))\right). \tag{3.10}$$

Le modèle réduit final, noté G, sera dans la forme suivante:

$$\begin{cases} \dot{x} = A^r \cdot x + B_f^r \cdot f + B_a^r \cdot V_a \\ \nu_{node} = C_e^r \cdot x \\ V_s = C_s^{r,new} \cdot x + D_s^{r,new} \cdot V_a \end{cases} \tag{3.11}$$

La minimisation de l'erreur relative nous permet de trouver $C_s^{r,new}$ et $D_s^{r,new}$. On observe la réduction de l'erreur dans Fig. 3.4 (le trait rouge pointillé). L'amélioration du modèle réduit finale G par rapport au modèle (3.9) peut être observée Fig. 3.3 où le trait rouge pointillé représente la réponse de G entre V_a et V_s. Le contrôleur sera conçu basé sur G.

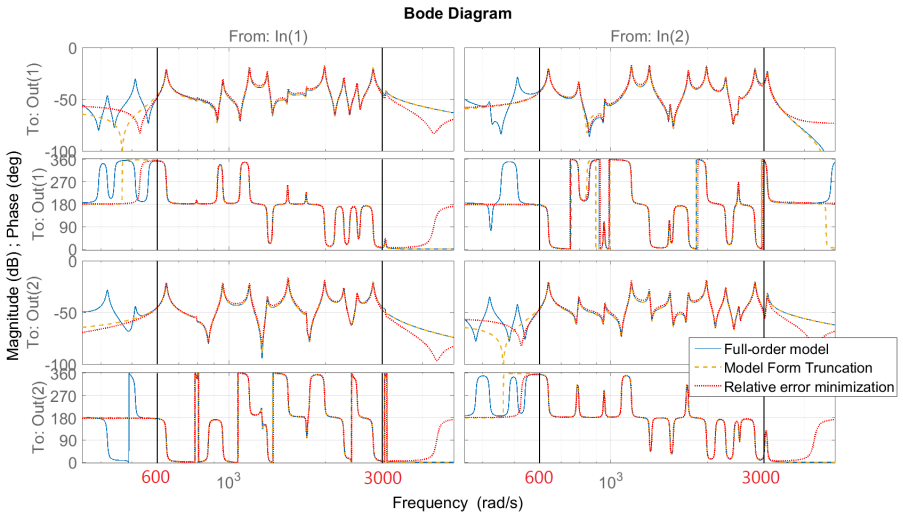

Figure 3.3: Réponse fréquentielle : modèle complet (trait bleu solide), modèle réduit par MFT (trait jaune discontinue) et modèle réduit modifié par LMI (trait rouge pointillé)

3.5 Conception du contrôleur par contrôle H_∞

3.5.1 Cahier des charges

On rappelle tout d'abord les objectifs du contrôle. Selon la discussion de Section 2.2, dans le cas général, le cahier des charges peut être résumé comme

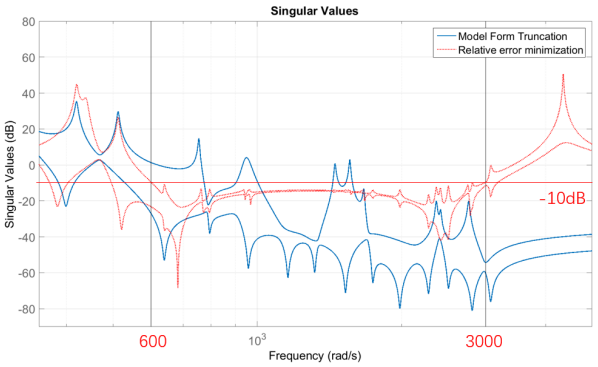

Figure 3.4: $\sigma(\Delta(j\omega))$ pour la partie entre V_a and V_s : MFT (trait bleu solide) vs MFT et minimisation de l'erreur relative (trait rouge pointillé)

suivante:

Perturbation : On considère une perturbation de force qui a une DSP importante dans une gamme de fréquence spécifiée, noté Ω.

Performance : On vise à réduire les vibrations dans la zone centrale de la poutre où il n'y pas de PZT (voir Fig. 2.2).

Signal du contrôle: Le contrôleur doit avoir du roll-off en hautes fréquences, ce qui permet de filtrer les bruits de mesure (qui normalement se trouvent en hautes fréquences). Le contrôleur doit avoir des gains importants dans Ω et des gains faibles en dehors de Ω. Ce qui permet de limiter la consommation d'énergie.

Stabilité robuste: Le contrôleur conçu à partir du modèle réduit G doit aussi garantir la stabilité lorsqu'il est appliqué au modèle complet G^{full}, ce qui permet d'évider le problème de spill-over.

3.5.2 Critère H_∞

La Fig. 3.5 montre le système augmenté proposé, noté $P(s)$. $\tilde{G}(s)$ est le système à contrôler composé du modèle réduit $G(s)$, du gain de l'amplificateur de puissance A_p et d'une fonction de transfert $F_d(s)$ qui approxime un retard pure en utilisant l'Approximation de Padé [124]. L'objectif de $F_d(s)$ est d'approximer les déphasages introduits par les amplificateurs de puissance, les filtres anti-repliements et le mécanisme de conversion numérique dans la carte de contrôle[10].

[10]Le contrôleur va être implémenté numériquement

$e = [e_1, e_2, e_3]^T$ est l'entrée générale composant des bruits blancs indépendants, b le bruit de mesure et z_u la sortie générale liée au signal du contrôle. W_f, W_b, W_Δ et A_t sont les pondérations choisies (constantes pour W_f, W_b et A_t, fonction de transfert SISO pour W_Δ). Le contrôle H_∞ permet de calculer un contrôleur $K(s)$ tel que le système en boucle fermée $P(s) \star K(s)$ soit stable et $||P \star K||_\infty < \gamma$ pour le plus petit $\gamma < 1$. Ce dernier implique :

Notation : Dans la suite, on note T le système en boucle fermée et G le système en boucle ouverte.

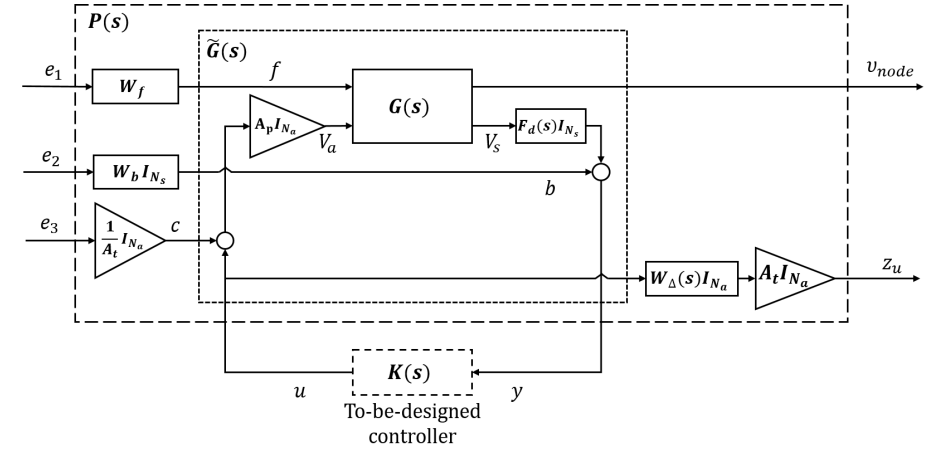

Figure 3.5: Bloc diagramme pour la synthèse H_∞

a. $||T_{e_1 \to \nu_{node}}||_\infty < \gamma < 1$

Ce critère remplit les objectifs de **Performance** et de **Perturbation** (voir Section 3.5.1). Selon Fig. 3.5, on a $T_{e_1 \to \nu_{node}} = T_{f \to \nu_{node}} W_f$. Ce critère implique :

$$\forall \omega, \quad \overline{\sigma}(T_{f \to \nu_{node}}(j\omega)) < \frac{\gamma}{|W_f|} < \frac{1}{|W_f|}. \tag{3.12}$$

En raison de la nature résonnante du système considéré, la valeur singulière maximale en boucle ouverte $\overline{\sigma}(G_{f \to \nu_{node}})$ tracée en fonction de la pulsation ω est composée de pics fin (comme on le verra par exemple dans Fig. 3.8). Ceci restera bien sûr le cas lorsqu'un contrôleur $K \neq 0$ est appliqué. Mais les amplitudes des pics deviendront plus petites en choisissant un W_f pertinent (plus W_f est grand, plus la réduction est importante). En utilisant l'expression de l'énergie centrale, c'est-à-dire Eq. (3.2), et la nature résonante du système considéré, on conclut

que la réduction d'amplitude des pics en $\overline{\sigma}(T_{f\to\nu_{node}})$ implique une réduction de l'énergie centrale. De plus, la DSP de f est bornée par W_f. Donc, W_f doit être choisie comme un filtre passe-bande concentré sur Ω. Cependant, à cause de l'étape de réduction de modèle, $\overline{\sigma}(G_{f\to\nu_{node}})$ présente déjà des amplitudes faibles en dehors de Ω. Par conséquent, on arrive à réduire les pics uniquement dans Ω en choisissant une constant pour W_f.

b. $||T_{e_3\to z_u}||_\infty < \gamma < 1$

Ce critère permet de garantir la **Stabilité Robuste** (voir Section 3.5.1). Selon la Fig. 3.5, on a $T_{e_3\to z_u} = W_\Delta T_{c\to u}$ où $T_{c\to u}$ est exactement la fonction de sensibilité complémentaire pour une boucle de rétroaction positive. En utilisant l'erreur relative Δ définie par Eq. (3.6), la partie du modèle complet G^{full} entre V_a et V_s peut être écrite comme suit :

$$G^{full}_{V_a\to V_s} = G_{V_a\to V_s}(I+\Delta).$$

Si on considère Δ comme une incertitude qui représente une matrices de transfert LTI stable appartenant à un ensemble $\mathbf{\Delta}$ tel que:

$$\mathbf{\Delta} = \left\{\Delta(s) \mid \Delta(s) = \hat{\Delta}(s)W_\Delta(s) \text{ avec } \left\|\hat{\Delta}\right\|_\infty \leqslant 1\right\}, \tag{3.13}$$

alors la boucle fermée $G^{full}_{V_a\to V_s} \star K$ peut être réécrite comme une boucle fermée composée d'une partie incertaine Δ et d'une partie nominale $T_{c\to u}$, ce qui définit pour tous les $\Delta \in \mathbf{\Delta}$ une famille du système en boucle fermée $(\Delta, T_{c\to u})$. D'après le Théorème du Petit Gain Pondéré, une telle famille $(\Delta, T_{c\to u})$ est stable pour tous les $\Delta \in \mathbf{\Delta}$ si et seulement si $||W_\Delta T_{c\to u}||_\infty < 1$. Par conséquent, si on choisit la pondération W_Δ telle que :

$$\forall\omega,\ \overline{\sigma}(\Delta(j\omega)) \leqslant |W_\Delta(j\omega)| \tag{3.14}$$

le critère $||T_{e_3\to z_u}||_\infty < 1$ va garantir que le contrôleur K stabilise aussi le modèle complet G^{full}.

c. $||T_{e_1\to z_u}||_\infty < \gamma < 1$ et $||T_{e_2\to z_u}||_\infty < \gamma < 1$

Ces deux critères bornent la DSP du **Signal du contrôle** (voir Section 3.5.1), c'est-à-dire signal u dans Fig. 3.5. On a en effet :

$$\forall\omega,\ \overline{\sigma}(T_{f\to u}(j\omega)) < \frac{1}{|A_t W_\Delta(j\omega) W_f|} \quad et \quad \overline{\sigma}(T_{b\to u}(j\omega)) < \frac{1}{|A_t W_b W_\Delta(j\omega)|}. \tag{3.15}$$

Le choix de A_t et W_b permet de limiter respectivement l'amplitude d'effort de contrôle et le niveau de bruit de mesure. Comme A_t, W_b et W_f sont choisie comme constantes, le choix de $W_\Delta(s)$ (satisfaisant Eq. (3.14)) assure que $\overline{\sigma}(T_{f\to u}(j\omega))$ et $\overline{\sigma}(T_{b\to u}(j\omega))$ ont des amplitudes importantes sur Ω et du roll-off en dehors permettant respectivement de limiter la consommation d'énergie de contrôle et d'enlever l'effet du bruit de mesure (en hautes fréquences) sur le signal de contrôle.

3.5.3 Réduction et discrétisation du contrôleur

À cause des choix de pondérations (notamment pour le choix de W_Δ), le contrôleur obtenu aura des dynamiques faibles en dehors de la gamme de fréquences intéressantes. Ces dynamiques sont faibles importances par rapport aux objectifs de contrôle. On peut les enlever en utilisant la Troncature Équilibrée [34, 35]. En particulier, on détermine le contrôleur avec l'ordre le plus faible tout en préservant la stabilité et le niveau de performance. Comme le contrôleur va être implémenté numériquement, le contrôleur simplifié doit être aussi discrétisé avec un temps d'échantillonnage assez petit.

3.5.4 Application et résultats

L'application des critères H_∞ (Fig. 3.5) est de choisir les pondérations convenables par rapport au cahier des charges. W_Δ est tout d'abord choisi comme un filtre stoppe-bande qui satisfait Eq. (3.14). Fig. 3.6 montre bien que $\sigma(\Delta(j\omega))$ (trait bleu solide) est inférieur à $|W_\Delta(j\omega)|$ (trait rouge discontinu) pour $\forall\omega$. Pour les autres pondérations, comme discuté dans la Section 3.5.2, plus W_f est grand, plus la réduction est importante. Plus A_t est grand, plus la consommation est réduite. Cependant, plus de consommation d'énergie est vraiment nécessaire pour

avoir une plus grande réduction. Il existe donc un compromise entre le choix de W_f et de A_t. Après quelques essais et erreurs, on choisit finalement $W_f = 6.9$ et $A_t = 3.9 \times 10^{-2}$. La pondération pour le bruit de mesure est choisie comme $W_b = 1$. De plus, on prend le gain de l'amplificateur $A_p = -10$. Le déphasage total introduit par les mécanismes de contrôle est approximé par un retard de $3.6 \times 10^{-4}s$ (présenté par $F_d(s)$). Ces choix nous permettent d'obtenir un contrôleur K d'ordre 52 avec $\gamma = 0.9923$. La réponse fréquentielle de K est présenté Fig. 3.7 en trait bleu solide. Comme prévu, on observe des dynamiques faibles en dehors de $(600, 3000)$ rad/s. On réduit ensuite K en appliquant la Troncature Équilibrée jusqu'à l'ordre 30 et on obtient un contrôleur réduit K_{red} comme montré Fig. 3.7 en trait rouge pointillé.

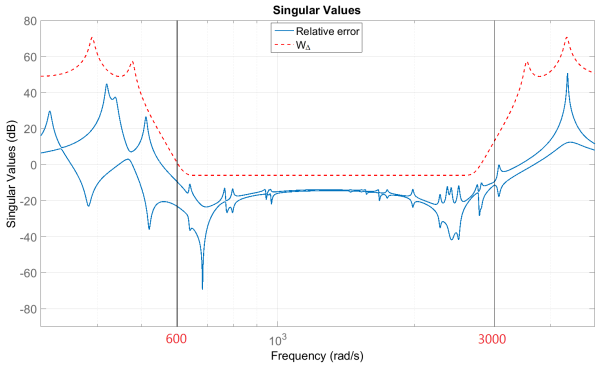

Figure 3.6: $\sigma(\Delta(j\omega))$ (trait bleu solide) et $|W_\Delta(j\omega)|$ (trait rouge discontinu)

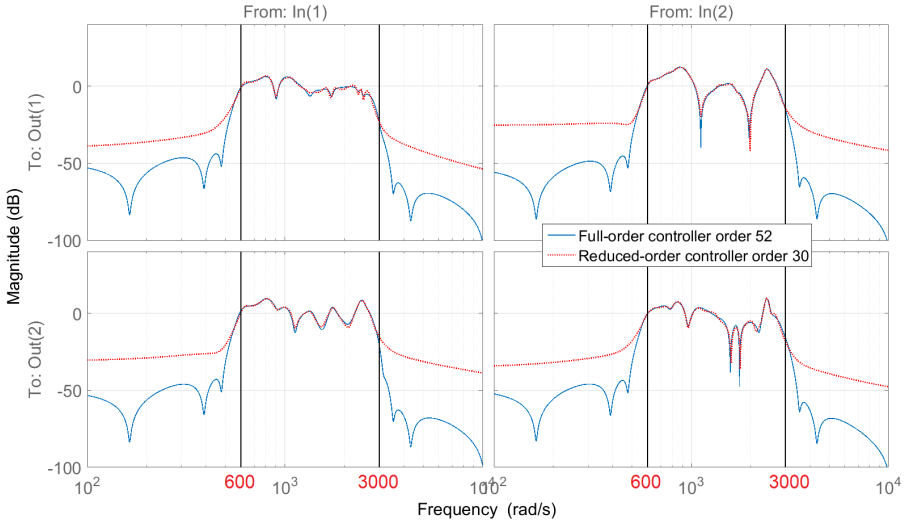

Figure 3.7: Module de la réponse fréquentielle du contrôleur K (trait bleu solide) et cela du contrôleur réduit K_{red} (trait rouge pointillé)

On présente l'effet du contrôle par rapport au modèle complet G^{full} en termes de norme H_∞. Fig. 3.8 compare la valeur singulière entre la perturbation f et le vecteur de vitesse ν_{node} en boucle ouverte $\overline{\sigma}(G_{f\to\nu_{node}}(j\omega))$ et en boucle fermée $\overline{\sigma}(T_{f\to\nu_{node}}(j\omega))$. En boucle fermée, on présente respectivement l'effet du K (trait vert discontinu) et K_{red} (trait rouge pointillé). On observe que seulement les pics dans $(600, 300)$ rad/s sont réduits et que K_{red} a un effet très proche que K. La performance finale est caractérisé par le rapport de réduction de $\overline{E^p_{cent}}$ (définit par Eq. (3.2)), noté r_p:

$$r_e^p = \left(1 - \frac{\left(\overline{E^p_{cent}}\right)_{CL}}{\left(\overline{E^p_{cent}}\right)_{OL}}\right) \times 100\% = \left(1 - \frac{||T_{f\to\nu_{node}} L_f||_2^2}{||G^{full}_{f\to\nu_{node}} L_f||_2^2}\right) \times 100\%, \tag{3.16}$$

où $|L_f(j\omega)|^2$ représente la DSP de f. Lorsque L_f correspond à la DSP de f réelle généré par le shaker, le rapport de réduction $r_p = 62.5\%$.

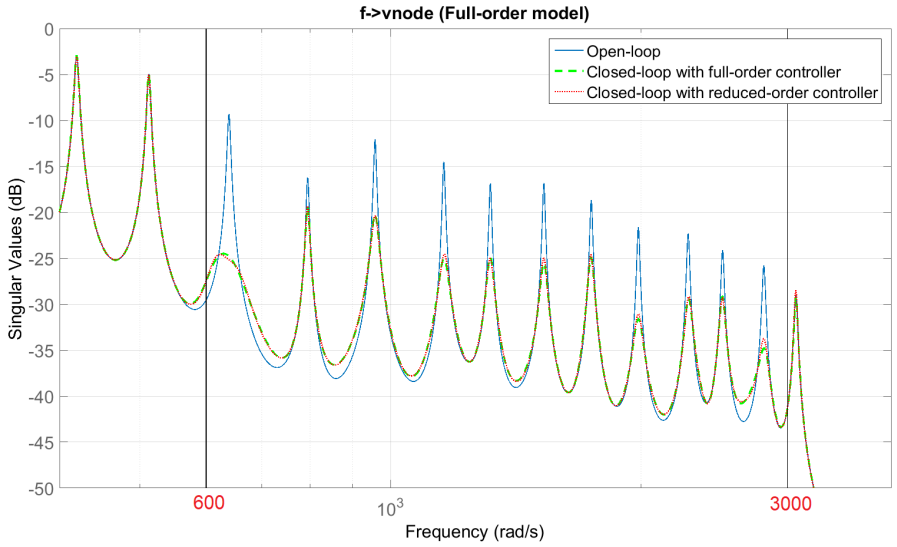

Figure 3.8: $\overline{\sigma}(G^{full}_{f\to\nu_{node}}(j\omega))$ (trait bleu solide) vs $\overline{\sigma}(T_{f\to\nu_{node}}(j\omega))$ avec le contrôleur K (trait vert discontinu) vs $\overline{\sigma}(T_{f\to\nu_{node}}(j\omega))$ avec le contrôleur réduit K_{red} (trait rouge pointillé)

La performance de K^d_{red} est aussi vérifié expérimentalement. En particulier, on implémente la discrétisation (Zero-Order-Hold [127]) du contrôleur réduit K_{red}, noté K^d_{red}, dans la carte de contrôle. La période d'échantillonnage est choisie à $T_s = 2 \times 10^{-4} s$. Le signal de référence du shaker (l'entrée du shaker) est un bruit blanc filtré par un filtre passe-bande, ce qui permet à f d'avoir une DSP importante uniquement dans $(600, 3000)$ rad/s. Les données en temps réel ($f(t)$ et

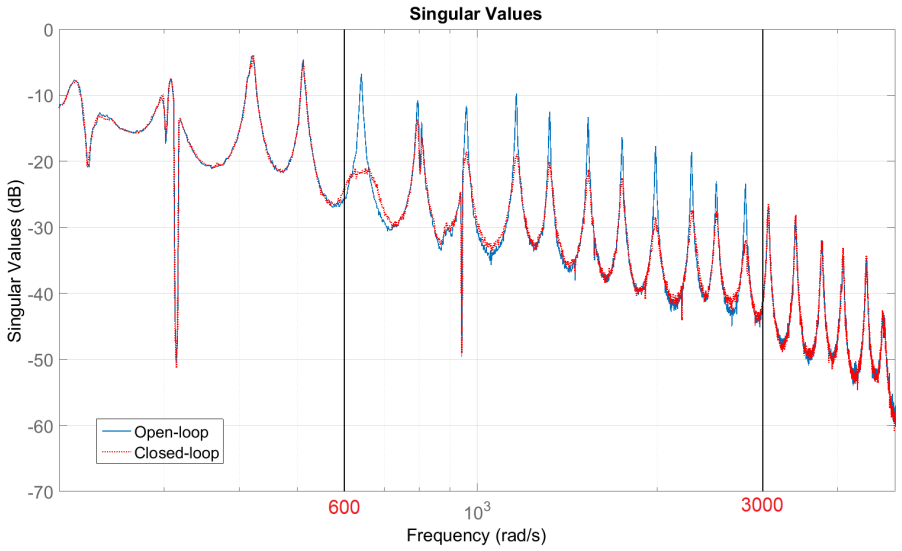

Figure 3.9: $\overline{\sigma}(G_{f\to\nu_{node},m}(j\omega))$ (trait bleu solide) rt $\overline{\sigma}(T_{f\to\nu_{node},m}(j\omega))$ (trait rouge pointillé) mesurés de l'installation expérimentale

$\nu_{node}(t)$) sont mesurées pour estimer les quantités en boucle ouverte ($(\overline{E^p_{cent}})_{OL}$ et $\overline{\sigma}(G_{f\to\nu_{node}}(j\omega))$) et en boucle fermée ($(\overline{E^p_{cent}})_{CL}$ et $\overline{\sigma}(T_{f\to\nu_{node}}(j\omega))$). Finalement, on obtient un rapport de réduction $r_p = 58.9\%$ qui est très poche de la valeur théorique. Fig. 3.9 présente $\overline{\sigma}(G_{f\to\nu_{node}}(j\omega))$ (trait bleu solide) et $\overline{\sigma}(T_{f\to\nu_{node}}(j\omega))$ (trait rouge pointillé) estimé en utilisant les données réelles. Comme prévu, les modes sont réduits uniquement dans $(600, 3000)$ rad/s.

Chapitre 4

Modélisation pour le contrôle distribué

Pour le contrôle distribué, on va utilisé tous les PZT de la poutre. En particulier, deux paires de PZT voisins connectées à un seul contrôleur forment une unité de contrôle locale. Plusieurs unités travaillent ensembles pour atteindre un effet global. Par conséquent, on considère le système à contrôler comme un ensemble des sous-systèmes interconnecté. L'objectif de la modélisation distribuée est de construire le modèle des sous-systèmes. Pour l'installation discutée ici, on va d'abord décomposer spatialement la structure en cellules. COMSOL peut nous donner les modèles par éléments finis des cellules. Ensuite, plusieurs techniques sont appliquées pour simplifier ces modèles de cellule. À la fin, on construit l'espace d'état (LTI) des sous-systèmes en faisant l'assemblage local.

4.1 Modélisation des cellules

La Fig. 4.1 montre le modèle 3D de la structure considérée. On observe qu'il y a des parties avec PZT (parties de longueur L_3) et des partie sans PZT (parties de longueur L_1 et L_2). Donc, en décomposant la structure, on obtient deux types de cellules : cellules avec PZT (Fig. 4.2) et cellules sans PZT (homogènes). En particulier, on décompose chaque partie en 5 cellules identiques (25 cellules au total). COMSOL permet de calculer la matrice d'équations différentielles de ces

cellules en effectuant l'analyse par éléments finis. L'équation de cellule avec PZT est de la forme suivante:

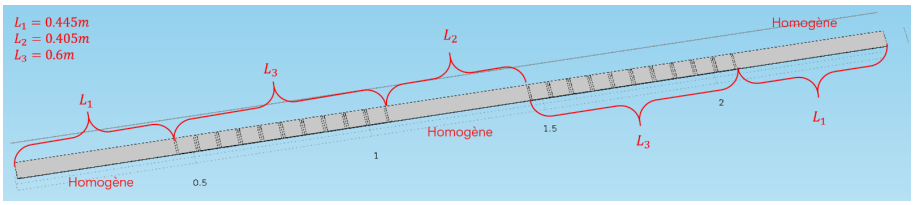

Figure 4.1: Modèle 3D de l'installation

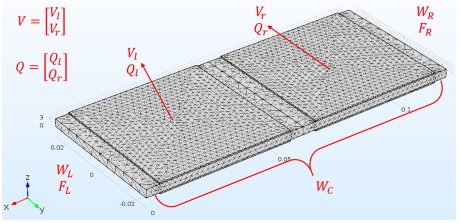

Figure 4.2: L'analyse par éléments finis de cellule avec PZT

$$\begin{bmatrix} M_{LL} & M_{LR} & M_{LC} & 0 \\ M_{LR}^T & M_{RR} & M_{RC} & 0 \\ M_{LC}^T & M_{RC}T & M_{CC} & 0 \\ 0 & 0 & 0 & 0 \end{bmatrix} \begin{bmatrix} \ddot{W}_L \\ \ddot{W}_R \\ \ddot{W}_C \\ \ddot{V} \end{bmatrix} + \begin{bmatrix} K_{LL} & K_{LR} & K_{LC} & E_L \\ K_{LR}^T & K_{RR} & K_{RC} & E_R \\ K_{LC}^T & K_{RC}T & K_{CC} & E_C \\ -E_L^T & -E_R^T & -E_C^T & R \end{bmatrix} \begin{bmatrix} W_L \\ W_R \\ W_C \\ V \end{bmatrix} = \begin{bmatrix} F_L \\ F_R \\ 0 \\ Q \end{bmatrix}, \quad (4.1)$$

où $W = (u, v, w)^T$ représente le déplacement d'un nœud dans 3 direction x, y et z. F est la contrainte appliquée sur W. Les indices 'L', 'R' et 'C' représentent respectivement la surface de la cellule à gauche, à droite et le domaine au milieu. Par exemple, W_L représente le champ de déplacement de tous les nœuds sur la surface à gauche. $V = [V_l, V_r]^T$ et $Q = [Q_l, Q_r]^T$ sont le vecteur de tension et de charge sur les PZT (voir Fig. 4.2). Pour la cellule homogène, il n'existe pas de couplage entre la poutre et les PZT. Son équation sera facilement obtenue en enlevant les lignes et les colonnes liées à V et Q dans l'Eq. (4.1). Le problème de ce modèle est le très grand nombre de degrés de liberté (DOF). Pour le simplifier, on impose la condensation de Guyan [36] et l'hypothèse cinématique d'Euler-Bernoulli.

4.1.1 Condensation de Guyan

La condensation de Gyuan permet de réduire le nombre de DOF d'un modèle complexe en négligeant certaines DOF qui ne subissent pas de contrainte. Pour cela, on sépare les DOF en deux ensembles : les DOF maîtres q_m et les DOF esclaves q_e. Soit une équation d'éléments finis d'une structure partitionnée en accord avec la définition des DOF maîtres et esclaves précédente :

$$\begin{bmatrix} M_{mm} & M_{me} \\ M_{em} & M_{ee} \end{bmatrix} \begin{bmatrix} \ddot{q}_m \\ \ddot{q}_e \end{bmatrix} + \begin{bmatrix} K_{mm} & K_{me} \\ K_{em} & K_{ee} \end{bmatrix} \begin{bmatrix} q_m \\ q_e \end{bmatrix} = \begin{bmatrix} g_m \\ 0 \end{bmatrix} \tag{4.2}$$

Si on néglige dans la deuxième ligne de l'Eq. (4.2) l'énergie cinétique (les termes inertiels) devant l'énergie de déformation, alors on obtient la relation statique : $q_e = -K_{ee}^{-1} K_{em} \cdot q_m$, ce qui permet d'appliquer un changement de variable comme suit :

$$\begin{bmatrix} q_m \\ q_e \end{bmatrix} = \begin{bmatrix} I \\ -K_{ee}^{-1} K_{em} \end{bmatrix} \cdot q_m = T \cdot q_m. \tag{4.3}$$

En conséquence, Eq. (4.2) devient une équation avec moins de DOF:

$$\bar{M} \cdot \ddot{q}_m + \bar{K} \cdot q_m = T^T \cdot \begin{bmatrix} g_m \\ 0 \end{bmatrix}, \tag{4.4}$$

$$\bar{M} = T^T \begin{bmatrix} M_{mm} & M_{me} \\ M_{em} & M_{ee} \end{bmatrix} T, \quad \bar{K} = T^T \begin{bmatrix} K_{mm} & K_{me} \\ K_{em} & K_{ee} \end{bmatrix} T.$$

4.1.2 Hypothèse cinématique d'Euler-Bernoulli

Selon l'hypothèse cinématique d'Euler-Bernoulli, le champ de déplacements d'une surface peut être exprimé par le déplacement et la rotation par rapport à un point sur cette surface si le déplacement est petit. On considère une surface S dans le plan yz du système de coordonnées global $x-y-z$, voir Fig. 4.3a. On note y_S-z_S le système de coordonnées attaché à S et O_S son origine. Le déplacement sous $x-y-z$, notant $[u, v, w]^T$, d'un point sur S avec la coordonnée (y_S, z_S) sous y_S-z_S peut être écrit comme une relation linéaire des déplacements et des rotations de

O_S au long des 3 directions x,y et z. Dans le cas où on s'intéresse uniquement une déformation particulière comme montré par Fig. 4.3b, le déplacement de ce point dans y et les rotations de S au long de x et z seront toujours zéros. Il est donc suffisant d'exprimer $[u, v, w]^T$ en utilisant le déplacement de O_S dans x et z, notant u_0 et w_0, et la rotation de S au long de y, notant θ_y:

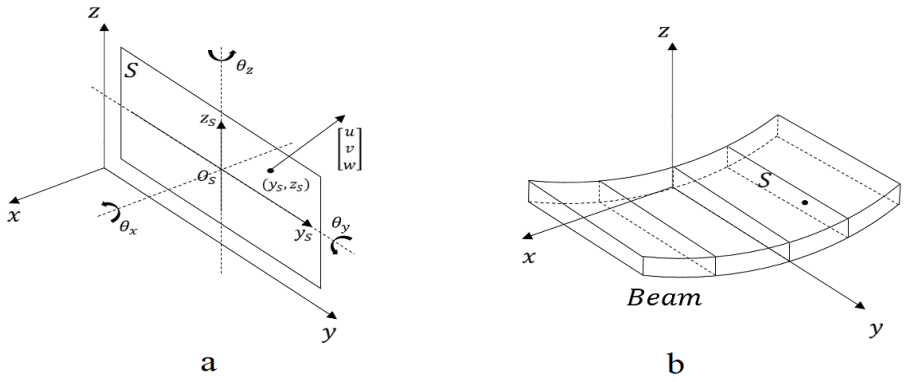

Figure 4.3: Cinématique

$$\begin{bmatrix} u \\ v \\ w \end{bmatrix} = \begin{bmatrix} 1 \\ 0 \\ 0 \end{bmatrix} u_0 + \begin{bmatrix} 0 \\ 0 \\ 1 \end{bmatrix} w_0 + \begin{bmatrix} z_S \\ 0 \\ 0 \end{bmatrix} \theta_y = \begin{bmatrix} 1 & 0 & z_S \\ 0 & 0 & 0 \\ 0 & 1 & 0 \end{bmatrix} \begin{bmatrix} u_0 \\ w_0 \\ \theta_y \end{bmatrix}. \tag{4.5}$$

4.1.3 Application

On prend l'équation de la cellule avec PZT comme un exemple. On observe dans l'Eq. (4.1) que W_C doit être défini comme le DOF esclaves. En appliquant la condensation de Guyan, W_C est supprimé et on obtient:

$$\begin{bmatrix} \bar{M}_{LL} & \bar{M}_{LR} & 0 \\ \bar{M}_{LR}^T & \bar{M}_{RR} & 0 \\ 0 & 0 & 0 \end{bmatrix} \begin{bmatrix} \ddot{W}_L \\ \ddot{W}_R \\ \ddot{V} \end{bmatrix} + \begin{bmatrix} \bar{K}_{LL} & \bar{K}_{LR} & \bar{E}_L \\ \bar{K}_{LR}^T & \bar{K}_{RR} & \bar{E}_R \\ -\bar{E}_L^T & -\bar{E}_R^T & \bar{R} \end{bmatrix} \begin{bmatrix} W_L \\ W_R \\ V \end{bmatrix} = \begin{bmatrix} \bar{F}_L \\ \bar{F}_R \\ Q \end{bmatrix}. \tag{4.6}$$

On impose ensuite l'hypothèse cinématique d'Euler-Bernoulli (i.e. Eq. (4.5)) sur W_L et W_R. On définit d'abord pour chaque surface de la cellule ('L' et 'R') un vecteur $\widehat{W}$ contenant deux déplacements (u_0 et w_0) et une rotation (θ_y):

$$\widehat{W}_L = [u_{0L}, w_{0L}, \theta_{yL}]^T, \quad \widehat{W}_R = [u_{0R}, w_{0R}, \theta_{yR}]^T, \tag{4.7}$$

Il existe sûrement deux matrices de transmission H_L et H_R tel que $W_L = H_L\widehat{W}_L$ et $W_R = H_R\widehat{W}_R$. Ce qui nous permet de faire le changement de variable comme suit :

$$\begin{bmatrix} W_L \\ W_R \\ V \end{bmatrix} = \begin{bmatrix} H_L & 0 & 0 \\ 0 & H_R & 0 \\ 0 & 0 & I \end{bmatrix} \begin{bmatrix} \widehat{W}_L \\ \widehat{W}_R \\ V \end{bmatrix} = \widehat{T} \begin{bmatrix} \widehat{W}_L \\ \widehat{W}_R \\ V \end{bmatrix}. \tag{4.8}$$

En injectant Eq. (4.8) dans Eq. (4.6), on obtient finalement une équation avec moins de DOF:

$$\begin{bmatrix} \widehat{M}_{LL} & \widehat{M}_{LR} & 0 \\ \widehat{M}_{LR}^T & \widehat{M}_{RR} & 0 \\ 0 & 0 & 0 \end{bmatrix} \begin{bmatrix} \ddot{\widehat{W}}_L \\ \ddot{\widehat{W}}_R \\ \ddot{V} \end{bmatrix} + \begin{bmatrix} \widehat{K}_{LL} & \widehat{K}_{LR} & \widehat{E}_L \\ \widehat{K}_{LR}^T & \widehat{K}_{RR} & \widehat{E}_R \\ -\widehat{E}_L^T & -\widehat{E}_R^T & \widehat{R} \end{bmatrix} \begin{bmatrix} \widehat{W}_L \\ \widehat{W}_R \\ V \end{bmatrix} = \begin{bmatrix} \widehat{F}_L \\ \widehat{F}_R \\ Q \end{bmatrix}. \tag{4.9}$$

COMSOL nous permet de calculer les paramètres dans l'Eq. (4.9). De plus, l'équation de la cellule homogène peut être aussi obtenue en simplement enlevant les lignes et les colonnes de l'Eq. (4.9) liée à V et Q.

Pour valider les modèles des cellules, on a assemblé les équations de toutes les 25 cellules, ce qui permet d'obtenir un modèle assemblé représentant la structure complète. Ensuite, on a comparé la réponse fréquentielle du modèle assemblé avec le modèle centralisé obtenu dans la Section 3.2 (avant identification). On a observé une bonne correspondance. À titre d'exemple, on montre ici la comparaison de la réponse entre la perturbation et la tension du $11^{ème}$ paire de PZT, voir Fig. 4.4. On conclut que le modèle assemblé est très proche du modèle centralisé, ce qui montre que les cellules sont correctement modélisées.

4.2 Modélisation des sous-systèmes

Dans un modèle distribué, les sous-systèmes communiquent, voir Fig. 1.2 à titre d'exemple. Cependant, les équations obtenues ci-dessus représentent uniquement les dynamiques des cellules. Elles n'expriment pas des communications entre les cellules voisines. Par conséquent, on ne peut pas simplement considérer le modèle d'une cellule comme un sous-système. L'objectif de cette section est de construire l'espace d'état des sous-systèmes (LTI) en utilisant les équations des

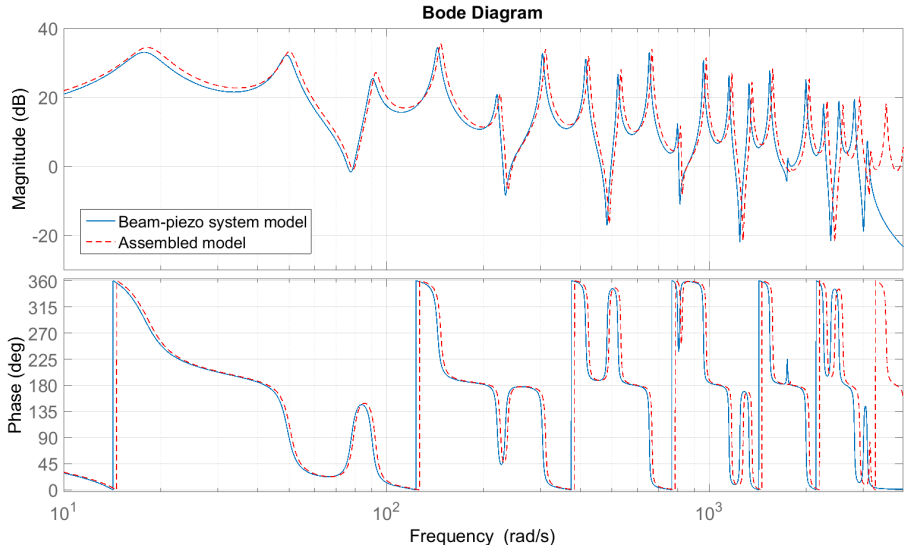

Figure 4.4: Réponses fréquentielles entre la perturbation et le $11^{ème}$ paire de PZT : Modèle centralisé (trait bleu solide) vs Modèle assemblé (trait rouge discontinu)

cellules. L'idée est d'abord d'assembler les équations d'un certain nombre de cellules voisines. Ensuite, on décompose l'équation assemblée pour construire les sous-systèmes, ce qui permet de garder les communications. Considérant que la structure est composée des cellules de différents types, les sous-systèmes ne seront pas identiques. Par exemple, on discute ici la construction du sous-système uniquement lié aux cellules avec PZT, noté G_c. En particulier, G_c sera connecté avec le contrôleur et il a seulement lui-même comme voisin. Les sous-systèmes liés aux autres cellules peuvent être construits dans la même façon.

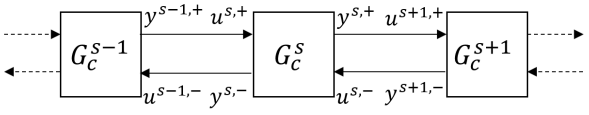

Figure 4.5: Définition des signaux de communication

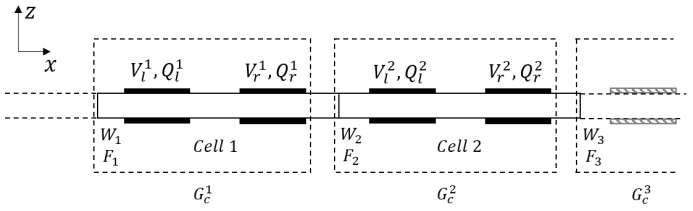

Figure 4.6: Assemblage locale de 3 cellules avec PZT

Tout d'abord, on définit les signaux de communication entre les sous-système voisins comme Fig. 4.5 où u est le signal d'entrée et y de sortie. '+' et '−'

indiquent la direction positive (à droite) et négative (à gauche) du signal. 's' indique la position de G_c et des signaux. On considère maintenant 3 cellules voisines. Les variables associées sont montrées Fig. 4.6 en notant que chaque cellule a une équation dans la forme d'Eq. (4.9) avec ses variables correspondantes. Fig. 4.6 montre aussi le choix des variables pour construire G_c, c'est-à-dire les variables liées à la surface à gauche et aux deux paires de PZT. En assemblant les 3 cellules, on obtient :

$$\begin{bmatrix} M_{LL} & M_{LR} & & \\ {M_{LR}}^T & M_{LL}+M_{RR} & M_{LR} & \\ & {M_{LR}}^T & M_{RR} & \end{bmatrix} \begin{bmatrix} \ddot{W}_1 \\ \ddot{W}_2 \\ \ddot{W}_3 \end{bmatrix} + \begin{bmatrix} \mathcal{X}_{LL} & \mathcal{X}_{LR} & & \\ {\mathcal{X}_{LR}}^T & \mathcal{X}_{LL}+\mathcal{X}_{RR} & \mathcal{X}_{LR} & \\ & {\mathcal{X}_{LR}}^T & \mathcal{X}_{RR} & \end{bmatrix} \begin{bmatrix} \dot{W}_1 \\ \dot{W}_2 \\ \dot{W}_3 \end{bmatrix} +$$
$$\begin{bmatrix} K_{LL} & K_{LR} & & \\ {K_{LR}}^T & K_{LL}+K_{RR} & K_{LR} & \\ & {K_{LR}}^T & K_{RR} & \end{bmatrix} \begin{bmatrix} W_1 \\ W_2 \\ W_3 \end{bmatrix} = \begin{bmatrix} F_1 \\ 0 \\ F_3 \end{bmatrix} + \begin{bmatrix} -E_{Ll} & -E_{Lr} & & \\ -E_{Rl} & -E_{Rr} & -E_{Ll} & -E_{Lr} \\ & & -E_{Rl} & -E_{Rr} \end{bmatrix} \begin{bmatrix} V_l^1 \\ V_r^1 \\ V_l^2 \\ V_r^2 \end{bmatrix}, \tag{4.10}$$

$$(E_L = [E_{Ll}, E_{Lr}],\ E_R = [E_{Rl}, E_{Rr}])$$

$$\begin{bmatrix} {-E_{Ll}}^T & {-E_{Rl}}^T & & \\ {-E_{Lr}}^T & {-E_{Rr}}^T & & \\ & {-E_{Ll}}^T & {-E_{Rl}}^T & \\ & {-E_{Lr}}^T & {-E_{Rr}}^T & \end{bmatrix} \begin{bmatrix} W_1 \\ W_2 \\ W_3 \end{bmatrix} + \begin{bmatrix} R_l & & & \\ & R_r & & \\ & & R_l & \\ & & & R_r \end{bmatrix} \begin{bmatrix} V_l^1 \\ V_r^1 \\ V_l^2 \\ V_r^2 \end{bmatrix} = \begin{bmatrix} Q_l^1 \\ Q_r^1 \\ Q_l^2 \\ Q_r^2 \end{bmatrix}, \tag{4.11}$$

$$(R = diag(R_l, R_r))$$

Si on définit les signaux de communication comme suit :

$$\begin{aligned} u^{2,-} &= y^{3,-} = -M_{LR}\ddot{W}_3 - \mathcal{X}_{LR}\dot{W}_3 - K_{LR}W_3, \\ y^{2,-} &= u^{1,-} = -M_{LR}\ddot{W}_2 - \mathcal{X}_{LR}\dot{W}_2 - K_{LR}W_2, \\ u^{2,+} &= y^{1,+} = -M_{LR}^T\ddot{W}_1 - \mathcal{X}_{LR}^T\dot{W}_1 - K_{LR}^TW_1 - E_{Rl}V_l^1 - E_{Rr}V_r^1, \\ y^{2,+} &= u^{3,+} = -M_{LR}^T\ddot{W}_2 - \mathcal{X}_{LR}^T\dot{W}_2 - K_{LR}^TW_2 - E_{Rl}V_l^2 - E_{Rr}V_r^2, \end{aligned} \tag{4.12}$$

alors on obtient les équations d'état pour G_c:

$$G_c^1 :\ M_{LL}\ddot{W}_1 + \mathcal{X}_{LL}\dot{W}_1 + K_{LL}W_1 = y^{2,-} + F_1 - E_{Ll}V_l^1 - E_{Lr}V_r^1, \tag{4.13}$$

$$G_c^2 :\ \bar{M}\ddot{W}_2 + \bar{\mathcal{X}}\dot{W}_2 + \bar{K}W_2 = u^{2,+} + u^{2,-} - E_{Ll}V_l^2 - E_{Lr}V_r^2, \tag{4.14}$$

$$G_c^3 :\ M_{RR}\ddot{W}_3 + \mathcal{X}_{RR}\dot{W}_3 + K_{RR}W_3 = y^{2,+} + F_3. \tag{4.15}$$

$$(\bar{M} = M_{LL} + M_{RR},\ \bar{\mathcal{X}} = \mathcal{X}_{LL} + \mathcal{X}_{RR},\ \bar{K} = K_{LL} + K_{RR})$$

Dans un sous-système, on choisit d'actionner V_l^s et de mesurer V_r^s. V_r^s sera mesurée via un circuit électrique fermé d'impédance Y. Selon la loi d'Ohm, on a :

$$-YV_r^s = \dot{Q}_r^s. \tag{4.16}$$

Les Eq. (4.11) et Eq. (4.16) nous donnent les équations de sortie :

$$-YV_r^1 = \dot{Q}_r^1 = -E_{Lr}^T\dot{W}_1 - E_{Rr}^T\dot{W}_2 + R_r\dot{V}_r^1 \tag{4.17}$$
$$-YV_r^2 = \dot{Q}_r^2 = -E_{Lr}^T\dot{W}_2 - E_{Rr}^T\dot{W}_3 + R_r\dot{V}_r^2. \tag{4.18}$$

Maintenant, on est près de construire G_c. En observant les Eq. (4.13)-(4.15) et Eq. (4.18), on trouve que G_c^2 doit avoir $u^{2,+}$, $u^{2,-}$, $\dot{W}_3$, V_l^2 comme les entrées, $y^{2,+}$, $y^{2,-}$, $\dot{W}_2$, V_r^2 comme les sorties et W_2, V_r^2 appartenant aux états. Dans un cas plus général, on note $u^+ = u^{2,+}$, $u_1^- = u^{2,-}$, $u_2^- = \dot{W}_3$, $V_{act} = V_l^2$ les entrées de G_c, $y^+ = y^{2,+}$, $y_1^- = y^{2,-}$, $y_2^- = \dot{W}_2$, $V_{sen} = V_r^2$ les soties et $W^c = W_2$, V_{sen} les états. L'espace d'état $G_c(A, B, C, D)$ est déduit d'Eq. (4.12), Eq. (4.14) et Eq. (4.18) comme suit (Fig. 4.7) :

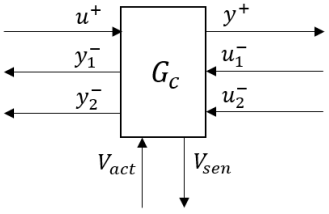

Figure 4.7: Diagramme de G_c

$$\begin{bmatrix} y^+ \\ \hline y_1^- \\ y_2^- \\ \hline V_{sen} \end{bmatrix} = G_c \begin{bmatrix} u^+ \\ \hline u_1^- \\ u_2^- \\ \hline V_{act} \end{bmatrix}, \tag{4.19}$$

avec l'état $x = \begin{bmatrix} W^c \\ \dot{W}^c \\ V_{sen} \end{bmatrix}$ (ordre 7) et:

$$A = \begin{bmatrix} 0 & I & 0 \\ -(\bar{M}^c)^{-1}\bar{K}^c & -(\bar{M}^c)^{-1}\bar{\mathcal{X}}^c & -(\bar{M}^c)^{-1}E_{Lr} \\ 0 & R_r^{-1}E_{Lr}^T & -R_r^{-1}Y \end{bmatrix}, B = \begin{bmatrix} 0 & 0 & 0 & 0 \\ (\bar{M}^c)^{-1} & -(\bar{M}^c)^{-1} & 0 & -(\bar{M}^c)^{-1}E_{Ll} \\ 0 & 0 & R_r^{-1}E_{Rr}^T & 0 \end{bmatrix},$$

$$C = \begin{bmatrix} {M_{LR}^c}^T(\bar{M}^c)^{-1}\bar{K}^c - {K_{LR}^c}^T & {M_{LR}^c}^T(\bar{M}^c)^{-1}\bar{\mathcal{X}}^c - {\mathcal{X}_{LR}^c}^T & {M_{LR}^c}^T(\bar{M}^c)^{-1}E_{Lr} - E_{Rr} \\ M_{LR}^c(\bar{M}^c)^{-1}\bar{K}^c - K_{LR}^c & M_{LR}^c(\bar{M}^c)^{-1}\bar{\mathcal{X}}^c - \mathcal{X}_{LR}^c & M_{LR}^c(\bar{M}^c)^{-1}E_{Lr} \\ 0 & I & 0 \\ 0 & 0 & 1 \end{bmatrix},$$

$$D = \begin{bmatrix} -{M_{LR}^c}^T(\bar{M}^c)^{-1} & -{M_{LR}^c}^T(\bar{M}^c)^{-1} & 0 & {M_{LR}^c}^T(\bar{M}^c)^{-1}E_{Ll} - E_{Rl} \\ -M_{LR}^c(\bar{M}^c)^{-1} & -M_{LR}^c(\bar{M}^c)^{-1} & 0 & M_{LR}^c(\bar{M}^c)^{-1}E_{Ll} \\ 0 & 0 & 0 & 0 \\ 0 & 0 & 0 & 0 \end{bmatrix}.$$

Comme discuté précédemment, les sous-systèmes ne sont pas identiques. Pour la structure étudiée, on est obligé de construire 9 types de sous-systèmes, notés respectivement G_a, G_b, G_c, G_{BL}, G_{BR}, G_{ac}, G_{ca}, G_{bc} et G_{cb}. Fig. 4.8 présente l'interconnexion des sous-systèmes où on trouve la perturbation, les tensions d'actionneurs et de capteurs, et aussi le vecteur de vitesse dans la zone centrale. La construction des 8 autres sous-systèmes suit le même processus que celle de G_c. Pour vérifier ce modèle distribué, on calcule la matrice de transfert du modèle distribué (interconnexion des sous-systèmes) et du modèle assemblé obtenu Section 4.1.3 (assemblage des cellules). Ensuite, on calcule la valeur singulière maximale de l'erreur absolue. L'erreur est toujours inférieure à -190 dB. Ce qui montre que les sous-systèmes sont correctement construits.

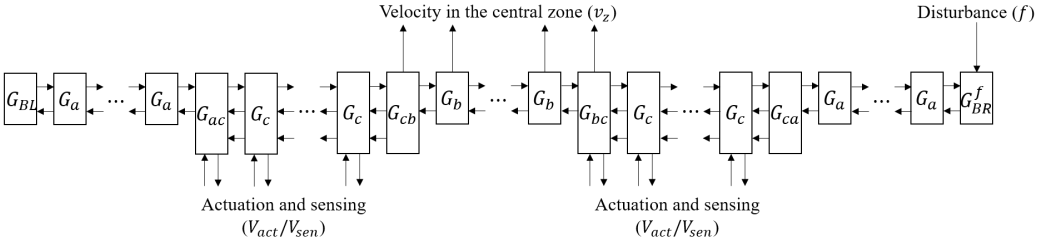

Figure 4.8: Architecture du système distribué, i.e. l'interconnexion des sous-système

Chapitre 5

Conclusions et recherches futures

Cette recherche vise à résoudre un problème de contrôler de vibration particulier. L'objectif est de réduire la vibration de la structure intelligente dans une zone spécifique où ni l'actionnement et ni la détection sont possibles. Le défi est donc de contrôler une partie de la structure lorsqu'on a uniquement accès aux mesures des autres parties. De plus, la perturbation couvre une large gamme de fréquence (11 modes) ce qui nécessite l'utilisation d'un contrôleur MIMO. Les méthodes de conception modernes doivent être appliquées pour synthétiser des contrôleurs MIMO. Le problème de spill-over doit être aussi évité.

Pour remplir ces objectifs, on propose une méthodologie qui permet de concevoir un contrôleur centralisé. Tout d'abord, un modèle fiable simple est construit en utilisant plusieurs techniques de modélisation, d'identification et de réduction. Ensuite, des critères H_∞ particuliers sont proposés. Le contrôleur est calculé en appliquant le cadre H_∞ standard. Ce contrôleur est ensuite simplifié tout en gardant la stabilité et la performance. Finalement, le contrôleur simplifié est expérimentalement validé. On obtient un grand rapport de réduction.

Considérant le coût de calcul élevé et la connectivité physique élevée en présence d'un grand nombre d'actionneurs et de capteurs, on passe au contrôle distribué. Dans cette recherche, on propose une méthode de modélisation qui permet de construire un modèle distribué (l'interconnexion de plusieurs sous-systèmes) de même structure. Cette méthode est basée sur la FEM et plusieurs techniques de réduction. Les travaux futurs seront l'identification du modèle distribué et la conception des contrôleurs distribués.

Appendix A

PZT selection

If a mode must be controlled, it should effectively be excited/detected by the actuator/sensor. This means that the peaks corresponding to all these modes must be clearly seen in the frequency response with a relatively high magnitude. Therefore, the frequency response, which can be measured by a frequency analyzer, between different actuators and sensors are compared and we found that the frequency response from one actuator to one sensor always has some peaks that can not be clearly seen or only have low magnitude. Such peaks are not always at the same frequencies in the response between other actuator and sensor. Fig. A.1 shows an example of this phenomenon. The blue line and red line are respectively the frequency response from the 10^{th} to the 11^{th} PZT pair and from the 16^{th} to the 11^{th} PZT pair. At the frequency circled by ellipse 1, the red line shows a much higher peak than the blue line while at the frequencies circled by ellipse 2 and 3, an opposite situation occurs. This phenomenon can be explained by the position of the PZT pair. If a PZT pair is located close to the node of a certain mode shape, this mode cannot be effectively excited or detected because the deformation at the node is very weak. Therefore, the corresponding peak in the frequency response will be very small or even disappear (it in fact depends on how close to the node the PZT pair is). As we will control as many as 11 modes, the distribution on the beam of all the nodes of the corresponding 11 mode shapes will be relatively intensive. Thus, there is a great probability that a PZT pair is close to one of these nodes. This also proves that a SISO controller is not enough to control all the modes. More PZT pairs must be used such that all the 11 modes can be effectively exited or detected. In particular, the PZT

pairs used for control are chosen in the way that when all the frequency responses between the chosen actuators and sensors are represented together in the same plot, all the peaks corresponding to the to-be-controlled modes can be clearly seen with a relatively high magnitude. At the same time, in order to balance the control effect, there should be at least one actuator and one sensor on each side of the central zone.

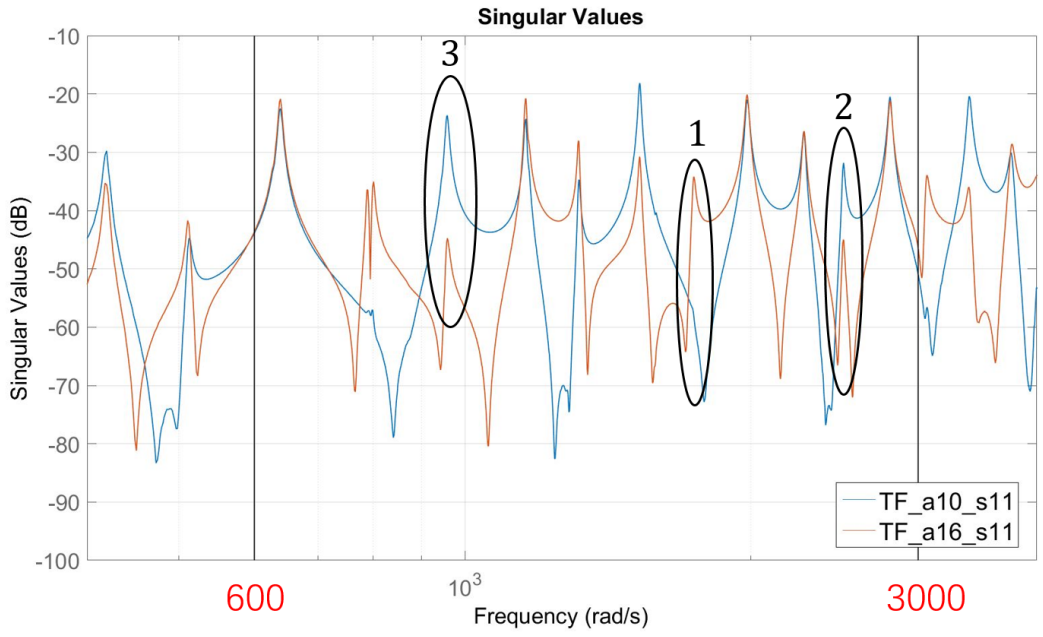

Figure A.1: Frequency response from the 10^{th} to the 11^{th} PZT pair (blue) and from the 16^{th} to the 11^{th} PZT pair (red)

Finally, in order to avoid local strain, the chosen actuators and sensors should not be too close to each other. Indeed, According to [131], when a piezoelectric patch is used as actuator, in addition to excite vibration modes, it also induces a local deformation. If the sensor is too close to the actuator, this local deformation can perturb the measurement of the vibration movement.

Considering all the above considerations and comparing different frequency responses, the 10^{th} and the 16^{th} PZT pairs are finally chosen as actuators, the 5^{th} and the 11^{th} PZT pairs as sensors (see Fig. 3.4). Indeed, as can be seen in Fig. A.2, all the peaks of interest are clearly seen. Moreover, the chosen actuators and sensors are not too close to each other and we have an actuator and a sensor on both sides of the central zone.

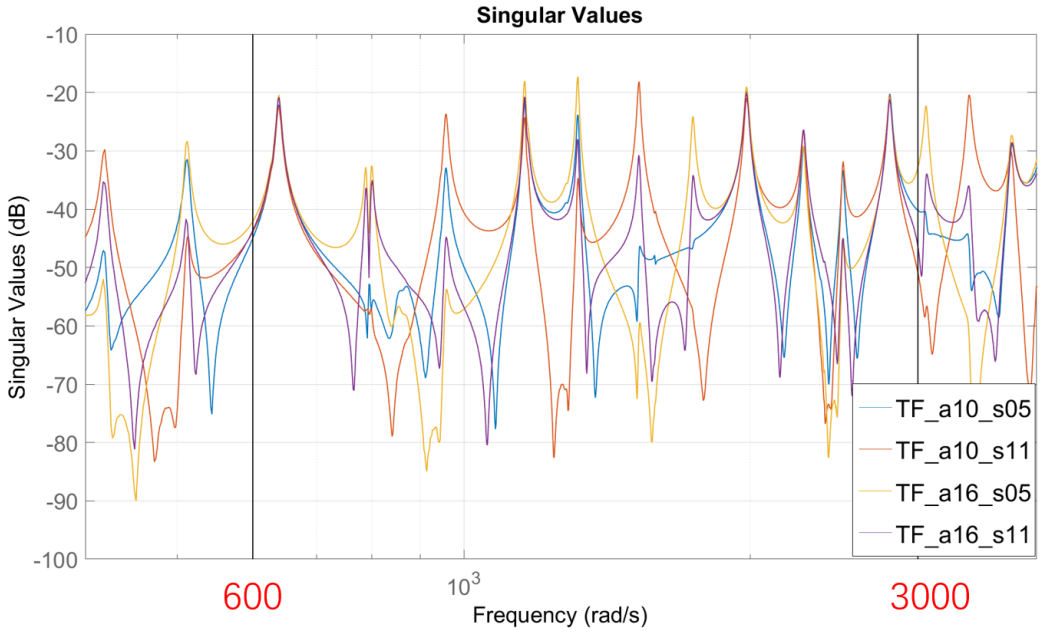

Figure A.2: Frequency response comparison: the 10^{th}, the 16^{th} to the 5^{th}, the 11^{th}

Remark. Even though more systematic approaches for the selection of the PZT pairs are available in the literature (see e.g. [132]), the simple approach above was satisfactory for our purpose.

Appendix B

Construction of the weighting for robust stability

The weighting for robust stability is the transfer function W_Δ, see Fig. 5.3. W_Δ should be chosen as simple as possible that satisfies Eq. (5.13) where Δ is defined by Eq. (4.47). Seen from Fig. 4.9 (red solid), as an upper bound of Δ, $W_\Delta(j\omega)$ should be small in $(600, 3000)$ rad/s and has rapid augmentation outside $(600, 3000)$ rad/s with a relatively lower order. For this purpose, we chose a band-stop Elliptic filter [133] of order 12 for W_Δ with a peak-to-peak stop-band ripple of 0.04 dB and a stop-band attenuation of 55 dB. The stop-band edge frequencies are respectively 650 rad/s and 2600 rad/s. We also modified the obtained band-stop filter by changing the damping ratio of each resonance frequency to 0.01 to avoid extremely low damped peaks. The modified band-stop Elliptic filter is considered as W_Δ (see Fig. 5.4 for the modulus of its frequency response) with the following expression:

$$W_\Delta(s) = \frac{\begin{array}{r}281.84(s^2+68.58s+3.87\times10^5)(s^2+281.8s+4.78\times10^5)\\(s^2+804.3s+9.26\times10^5)(s^2+1468s+3.08\times10^6)\\(s^2+995.6s+5.97\times10^6)(s^2+299.4s+7.38\times10^6)\end{array}}{\begin{array}{r}(s^2+3.28s+2.69\times10^4)(s^2+7.8s+1.52\times10^5)\\(s^2+9.56s+2.29\times10^5)(s^2+70.69s+1.25\times10^7)\\(s^2+86.69s+1.88\times10^7)(s^2+206.2s+1.06\times10^8)\end{array}}$$

References

[1] V. Ludovic and C. Philippe. Passive and active microvibration control for very high pointing accuracy space systems. *Smart materials and structures*, 8(6):719, 1999.

[2] M. Benosman and G. Le Vey. Control of flexible manipulators: A survey. *Robotica*, 22(5):533–545, 2004.

[3] S. Salapaka, A. Sebastian, J. P. Cleveland, and M. V. Salapaka. Design, identification and control of a fast nanopositioning device. In *American Control Conference, 2002. Proceedings of the 2002*, volume 3, pages 1966–1971. IEEE, 2002.

[4] Y. Wang and D. J. Inman. Comparison of control laws for vibration suppression based on energy consumption. *Journal of Intelligent Material Systems and Structures*, 22(8):795–809, 2011.

[5] D. Younesian, E. Esmailzadeh, and M. H. Kargarnovin. Passive control of vibration of elastically supported beams subjected to moving loads. In *ASME 2005 International Design Engineering Technical Conferences and Computers and Information in Engineering Conference*, pages 153–158. American Society of Mechanical Engineers, 2005.

[6] I. Zaman, M. M. Salleh, M. Ismon, B. Manshoor, A. Khalid, M. Sani, M. Shahrir, and S. Araby. Study of passive vibration absorbers attached on beam structure. *Applied Mechanics and Materials*, 660:511–515, 2014.

[7] X. Tong and X. Zhao. Passive vibration control of the scole beam system. *Structural Control and Health Monitoring*, 25(8):e2204, 2018.

[8] C. C. Fuller, S. Elliott, and P. A. Nelson. *Active control of vibration*. Academic Press, 1996.

[9] A. Preumont. *Vibration control of active structures, An Introduction 3rd Edition*. Springer, 2011.

[10] A. Luemchamloey and S. Kuntanapreeda. Active vibration control of flexible beams based on infinite-dimensional lyapunov stability theory: An experimental study. *Journal of Control, Automation and Electrical Systems*, 25(6):649–656, 2014.

[11] I. R. Petersen and H. R. Pota. Minimax LQG optimal control of a flexible beam. *Control Engineering Practice*, 11(11):1273–1287, 2003.

[12] S. V. Gosavi and A. G. Kelkar. Modelling, identification, and passivity-based robust control of piezo-actuated flexible beam. *Journal of vibration and acoustics*, 126(2):260–271, 2004.

[13] Z. Qiu, J. Han, X. Zhang, Y. Wang, and Z. Wu. Active vibration control of a flexible beam using a non-collocated acceleration sensor and piezoelectric patch actuator. *Journal of sound and vibration*, 326(3-5):438–455, 2009.

[14] Q. Hu. Robust adaptive sliding mode attitude control and vibration damping of flexible spacecraft subject to unknown disturbance and uncertainty. *Transactions of the Institute of Measurement and Control*, 34(4):436–447, 2012.

[15] L. A. Gagg Filho, S. M. Da Conceição, C. H. Vasques, G. L. C. M. De Abreu, V. Lopes Jr, and M. J. Brennan. Experimental identification and control of a cantilever beam using ERA/OKID with a LQR controller. *Journal of Control, Automation and Electrical Systems*, 25(2):161–173, 2014.

[16] D. Wu, L. Huang, B. Pan, Y. Wang, and S. Wu. Experimental study and numerical simulation of active vibration control of a highly flexible beam using piezoelectric intelligent material. *Aerospace Science and Technology*, 37:10–19, 2014.

[17] X. Dong, Z. Peng, W. Zhang, H. Hua, and G. Meng. Research on spillover effects for vibration control of piezoelectric smart structures by ansys. *Mathematical Problems in Engineering*, 2014, 2014.

[18] X. Q. Peng, K. Y. Lam, and G. R. Liu. Active vibration control of composite beams with piezoelectrics: a finite element model with third order theory. *Journal of sound and vibration*, 209(4):635–650, 1998.

[19] S. Narayanan and V. Balamurugan. Finite element modelling of piezolaminated smart structures for active vibration control with distributed sensors and actuators. *Journal of sound and vibration*, 262(3):529–562, 2003.

[20] L. Malgaca. Integration of active vibration control methods with finite element models of smart laminated composite structures. *Composite Structures*, 92(7):1651–1663, 2010.

[21] K. A. M. Nor, A. G. A. Muthalif, and A. N. Wahid. Optimization in active vibration control: Virtual experimentation using comsol multiphysics-matlab integration. In *Intelligent Systems, Modelling and Simulation (ISMS), 2014 5th International Conference on*, pages 385–389. IEEE, 2014.

[22] D. Guo, Z. Xie, and W. Cheng. Application of active damping control using piezoelectric material in modeling of a wind turbine blade. In *Applied Mechanics and Materials*, volume 598, pages 169–173. Trans Tech Publ, 2014.

[23] A. Sharma, A. Kumar, R. Kumar, Rahul Vaish, and V. S. Chauhan. Finite element analysis on active vibration control using lead zirconate titanate–Pt–based functionally graded piezoelectric material. *Journal of Intelligent Material Systems and Structures*, 27(4):490–499, 2016.

[24] R. Kandasamy and S. Dominique. Finite element based active vibration control of hierarchical honeycomb plates integrated with piezoelectric actuator. Technical report, SAE Technical Paper, 2018.

[25] E. M. Alawadhi. *Finite element simulations using ANSYS*. CRC Press, 2009.

[26] R. W. Pryor. *Multiphysics modeling using COMSOL: a first principles approach*. Jones & Bartlett Publishers, 2009.

[27] B. Besselink, U. Tabak, A. Lutowska, N. Van De Wouw, H. Nijmeijer, D.J. Rixen, M. E. Hochstenbach, and W. H. A. Schilders. A comparison of model reduction techniques from structural dynamics, numerical mathematics and systems and control. *Journal of Sound and Vibration*, 332(19):4403–4422, 2013.

[28] K. Yi, M. Monteil, M. Collet, and S. Chesné. Smart metacomposite-based systems for transient elastic wave energy harvesting. *Smart Materials and Structures*, 26(3):035040, 2017.

[29] H. Garnier, L. Wang, and P. C. Young. Direct identification of continuous-time models from sampled data: Issues, basic solutions and relevance. In *Identification of continuous-time models from sampled data*, pages 1–29. Springer, 2008.

[30] M. G. Singh. *Handbook of large scale systems engineering applications*. North Holland, North Holland, 1979.

[31] S. Boyd, L. El Ghaoui, E. Feron, and V. Balakrishnan. *Linear matrix inequalities in system and control theory*, volume 15 of *Studies in Applied Mathematics*. SIAM, Philadelphia, PA, jun 1994.

[32] K. Zhou, J. C. Doyle, and K. Glover. *Robust and optimal control*. Prentice Hall, 1996.

[33] U. Mackenroth. *Robust control systems: theory and case studies*. Springer Science & Business Media, 2013.

[34] C. Mullis and R. A. Roberts. Synthesis of minimum roundoff noise fixed point digital filters. *IEEE Transactions on Circuits and Systems*, 23(9):551–562, 1976.

[35] B. Moore. Principal component analysis in linear systems: Controllability, observability, and model reduction. *IEEE transactions on automatic control*, 26(1):17–32, 1981.

[36] R. J. Guyan. Reduction of stiffness and mass matrices. *AIAA journal*, 3(2):380–380, 1965.

[37] M. Yuvaraja and M. Senthilkumar. Vibration control of gfrp composite beam using smaflexinol actuators. *Annals of Faculty Engineering Hunedoara-International Journal of Engineering, Fascicule*, 3:288–295, 2010.

[38] S. J. Moon, C. W. Lim, B. H. Kim, and Y. Park. Structural vibration control using linear magnetostrictive actuators. *Journal of Sound and Vibration*, 302(4-5):875–891, 2007.

[39] Y. Shen, M. F. Golnaraghi, and G. R. Heppler. Semi-active vibration control schemes for suspension systems using magnetorheological dampers. *Journal of Vibration and Control*, 12(1):3–24, 2006.

[40] T. Bailey and J. E. Hubbard. Distributed piezoelectric-polymer active vibration control of a cantilever beam. *Journal of Guidance, Control, and Dynamics*, 8(5):605–611, 1985.

[41] K. Chandrashekhara and A. N. Agarwal. Active vibration control of laminated composite plates using piezoelectric devices: a finite element approach. *Journal of Intelligent Material Systems and Structures*, 4(4):496–508, 1993.

[42] W. P. Mason. Piezoelectricity, its history and applications. *The Journal of the Acoustical Society of America*, 70(6):1561–1566, 1981.

[43] A. Ballato. Piezoelectricity: history and new thrusts. In *Ultrasonics Symposium, 1996. Proceedings., 1996 IEEE*, volume 1, pages 575–583. IEEE, 1996.

[44] R. Alkhatib and M. F. Golnaraghi. Active structural vibration control: a review. *Shock and Vibration Digest*, 35(5):367, 2003.

[45] E. F. Crawley and J. De Luis. Use of piezoelectric actuators as elements of intelligent structures. *AIAA journal*, 25(10):1373–1385, 1987.

[46] N. W. Hagood, W. H. Chung, and A. Von Flotow. Modelling of piezoelectric actuator dynamics for active structural control. *Journal of Intelligent Material Systems and Structures*, 1(3):327–354, 1990.

[47] G. J. Balas and J. C. Doyle. Identification of flexible structures for robust control. *IEEE Control Systems Magazine*, 10(4):51–58, 1990.

[48] W. Chang, S. V. Gopinathan, V. V. Varadan, and V. K. Varadan. Design of robust vibration controller for a smart panel using finite element model. *Journal of vibration and acoustics*, 124(2):265–276, 2002.

[49] X. Dong, G. Meng, and J. Peng. Vibration control of piezoelectric smart structures based on system identification technique: Numerical simulation and experimental study. *Journal of sound and vibration*, 297(3-5):680–693, 2006.

[50] A. Koszewnik. The active vibration control of the smart plate by using piezo-patches. In *Carpathian Control Conference (ICCC), 2015 16th International*, pages 235–240. IEEE, 2015.

[51] X. Zhang, A. Takezawa, and Z. Kang. Topology optimization of piezoelectric smart structures for minimum energy consumption under active control. *Structural and Multidisciplinary Optimization*, 58(1):185–199, 2018.

[52] Z. Bai. Krylov subspace techniques for reduced-order modeling of large-scale dynamical systems. *Applied numerical mathematics*, 43(1-2):9–44, 2002.

[53] X. Si, W. Lu, and F. Chu. Modal analysis of circular plates with radial side cracks and in contact with water on one side based on the Rayleigh–Ritz method. *Journal of Sound and Vibration*, 331(1):231–251, 2012.

[54] P. Pognant-Gros. *De la réduction de modèles vers la commande robuste: application à la commande des canaux d'irrigation.* PhD thesis, Caen, 2003.

[55] J. Fei. Active vibration control of flexible steel cantilever beam using piezoelectric actuators. In *System Theory, 2005. SSST'05. Proceedings of the Thirty-Seventh Southeastern Symposium on*, pages 35–39. IEEE, 2005.

[56] S. M. Khot, N. P. Yelve, R. Tomar, S. Desai, and S. Vittal. Active vibration control of cantilever beam by using PID based output feedback controller. *Journal of Vibration and Control*, 18(3):366–372, 2012.

[57] S. Li, J. Li, Y. Mo, R. Zhao, and Z. Sun. Dob-based piezoelectric vibration control for stiffened plate considering accelerometer measurement noise. *Smart Structures and Systems*, 14(3):231–250, 2014.

[58] S. Y. Wang, S. T. Quek, and K. K. Ang. Vibration control of smart piezoelectric composite plates. *Smart materials and Structures*, 10(4):637, 2001.

[59] V. Gupta, M. Sharma, and N. Thakur. Active structural vibration control: robust to temperature variations. *Mechanical Systems and Signal Processing*, 33:167–180, 2012.

[60] P. Sood and M. Sharma. AVC of a smart plate with pzt sensor-actuator using direct method of model updating. *Ferroelectrics*, 510(1):184–195, 2017.

[61] C. J. Goh and W. Y. Yan. Approximate pole placement for acceleration feedback control of flexible structures. *Journal of guidance, control, and dynamics*, 19(1):256–259, 1996.

[62] F. An, W. Chen, and M. Shao. Study on discrete acceleration feedback control with time delay. *Journal of Vibration and Control*, 21(7):1267–1285, 2015.

[63] J. L. Fanson and T. K. Caughey. Positive position feedback control for large space structures. *AIAA journal*, 28(4):717–724, 1990.

[64] M. I. Friswell and D. J. Inman. The relationship between positive position feedback and output feedback controllers. *Smart Materials and Structures*, 8(3):285, 1999.

[65] T. Hegewald and D. J. Inman. Vibration suppression via smart structures across a temperature range. *Journal of Intelligent Material Systems and Structures*, 12(3):191–203, 2001.

[66] Z. Qiu, X. Zhang, H. Wu, and H. Zhang. Optimal placement and active vibration control for piezoelectric smart flexible cantilever plate. *Journal of Sound and Vibration*, 301(3-5):521–543, 2007.

[67] M. K. Kwak and S. Heo. Active vibration control of smart grid structure by multiinput and multioutput positive position feedback controller. *Journal of Sound and Vibration*, 304(1-2):230–245, 2007.

[68] E. Omidi and S. N. Mahmoodi. Multimode modified positive position feedback to control a collocated structure. *Journal of Dynamic Systems, Measurement, and Control*, 137(5):051003, 2015.

[69] T. Zhang and H. Li. Adaptive pole placement control for vibration control of a smart cantilevered beam in thermal environment. *Journal of Vibration and Control*, 19(10):1460–1470, 2013.

[70] A. Koszewnik. The optimal vibration control of the plate structure by using piezo-actuators. In *Carpathian Control Conference (ICCC), 2016 17th International*, pages 358–363. IEEE, 2016.

[71] A. Loghmani, M. Danesh, M. K. Kwak, and M. Keshmiri. Vibration suppression of a piezo-equipped cylindrical shell in a broad-band frequency domain. *Journal of Sound and Vibration*, 411:260–277, 2017.

[72] J. Maruani, I. Bruant, F. Pablo, and L. Gallimard. A numerical efficiency study on the active vibration control for a FGPM beam. *Composite Structures*, 182:478–486, 2017.

[73] M. A. Trindade, A. Benjeddou, and R. Ohayon. Piezoelectric active vibration control of damped sandwich beams. *Journal of Sound and Vibration*, 246(4):653–677, 2001.

[74] P. Bhattacharya, H. Suhail, and P. K. Sinha. Finite element analysis and distributed control of laminated composite shells using LQR/IMSC approach. *Aerospace Science and Technology*, 6(4):273–281, 2002.

[75] Z. Wang. Finite element modelling and LQG control of piezoelectric composite structure with distributed sensors and actuators. In *IEEE International Conference on Mechatronics and Automation (ICMA)*, pages 803–808. IEEE, 2016.

[76] G. E. Stavroulakis, G. Foutsitzi, E. Hadjigeorgiou, D. Marinova, and C. C. Baniotopoulos. Design and robust optimal control of smart beams with application on vibrations suppression. *Advances in Engineering Software*, 36(11):806–813, 2005.

[77] X. Zhang, Z. Dong, M. Hromcik, K. Hengster-Movric, C. Faria, H. D. Van der Auweraer, and W. Desmet. Reduced-order robust controller design for vibration reduction. Technical Report 2016-01-1845, SAE Technical Paper, 2016.

[78] W. H. Jee and C. W. Lee. H_∞ robust control of flexible manipulator vibration by using a piezoelectric-type servo-damper. *Control Engineering Practice*, 2(3):421–430, 1994.

[79] K. Zhang. *Mechatronic design under uncertainties*. PhD thesis, Ecully, Ecole centrale de Lyon, 2013.

[80] W. Symens, H. Van Brussel, and J. Swevers. Gain-scheduling control of machine tools with varying structural flexibility. *CIRP Annals-Manufacturing Technology*, 53(1):321–324, 2004.

[81] B. Paijmans, W. Symens, H. Van Brussel, and J. Swevers. A gain-scheduling-control technique for mechatronic systems with position-dependent dynamics. In *American Control Conference*, pages 6–pp. IEEE, 2006.

[82] L. Iorga, H. Baruh, and I. Ursu. A review of H_∞ robust control of piezoelectric smart structures. *Applied Mechanics Reviews*, 61(4):040802, 2008.

[83] X. Zhang, C. Shao, S. Li, D. Xu, and A. G. Erdman. Robust H_∞ vibration control for flexible linkage mechanism systems with piezoelectric sensors and actuators. *Journal of Sound and Vibration*, 243(1):145–155, 2001.

[84] F. J. Moreira, J. Roberto de França Arruda, and D. J. Inman. Design of a reduced–order H_∞ controller for smart structure satellite applications. *Philosophical Transactions of the Royal Society of London. Series A: Mathematical, Physical and Engineering Sciences*, 359(1788):2251–2269, 2001.

[85] Q. Liu. *Modelling, distributed identification and control of spatially-distributed systems with application to an actuated beam.* PhD thesis, Technische Universität Hamburg, 2015.

[86] W. P. Engels and S. J. Elliott. Optimal centralized and decentralized velocity feedback control on a beam. *Smart Materials and Structures*, 17(2):025009, 2008.

[87] K. D. Frampton, O. N. Baumann, and P. Gardonio. A comparison of decentralized, distributed, and centralized vibro-acoustic control. *The Journal of the Acoustical Society of America*, 128(5):2798–2806, 2010.

[88] R. D'Andrea and G. E. Dullerud. Distributed control design for spatially interconnected systems. *IEEE Transactions on automatic control*, 48(9):1478–1495, 2003.

[89] Q. Liu and H. Werner. Distributed identification and control of spatially interconnected systems with application to an actuated beam. *Control Engineering Practice*, 54:104–116, 2016.

[90] A. K. Schug and H. Werner. Active vibration control of an aluminum beam—an experimental testbed for distributed vs. centralized control. In *Decision and Control (CDC), 2017 IEEE 56th Annual Conference on*, pages 1876–1881. IEEE, 2017.

[91] Q. Liu, A. M. Gonzalez, and H. Werner. Distributed control of spatially-interconnected parameter-invariant and lpv models for actuated beams. In *American Control Conference (ACC), 2014*, pages 3381–3386. IEEE, 2014.

[92] S. Wollnack and H. Werner. Distributed fixed-structure control of spatially interconnected ltsv systems. In *Decision and Control (CDC), 2015 IEEE 54th Annual Conference on*, pages 1905–1910. IEEE, 2015.

[93] Q. Liu, C. Hoffmann, and H. Werner. Distributed control of parameter-varying spatially interconnected systems using parameter-dependent lyapunov functions. In *American Control Conference (ACC), 2013*, pages 3278–3283. IEEE, 2013.

[94] F. Wu and S. E. Yildizoglu. A distributed parameter dependent control design for a flexible beam problem. In *American Control Conference, 2002. Proceedings of the 2002*, volume 4, pages 3174–3179. IEEE, 2002.

[95] G. E. Dullerud and R. D'Andrea. Distributed control of heterogeneous systems. *IEEE Transactions on Automatic Control*, 49(12):2113–2128, 2004.

[96] J. K. Rice and M. Verhaegen. Distributed control: A sequentially semi-separable approach. In *Decision and Control, 2008. CDC 2008. 47th IEEE Conference on*, pages 2913–2919. IEEE, 2008.

[97] S. Wollnack, C. Kloock, A. K. Schug, and H. Werner. Well-posedness & stability analysis for spatially interconnected systems with finite extent. In *American Control Conference (ACC), 2017*, pages 1803–1808. IEEE, 2017.

[98] M. Ali, A. Ali, S. S. Chughtai, and H. Werner. Consistent identification of spatially interconnected systems. In *American Control Conference (ACC), 2011*, pages 3583–3588. IEEE, 2011.

[99] Q. Liu, J. Mohammadpour, R. Tóth, and N. Meskin. Non-parametric identification of linear parameter-varying spatially-interconnected systems using an LS-SVM approach. In *American Control Conference (ACC), 2016*, pages 4592–4597. IEEE, 2016.

[100] Q. Liu, J. Gross, and H. Werner. Distributed identification of spatially-distributed systems based on finite element modelling. In *Decision and Control (CDC), 2015 IEEE 54th Annual Conference on*, pages 1230–1235. IEEE, 2015.

[101] O. A. Bauchau and J. I. Craig. Euler-bernoulli beam theory. In *Structural analysis*, pages 173–221. Springer, 2009.

[102] T. Oomen, E. Grassens, and F. Hendriks. Inferential motion control: Identification and robust control framework for positioning an unmeasurable point of interest. *IEEE Transactions on control systems technology*, 23(4):1602–1610, 2015.

[103] V. Piefort and A. Preumont. Finite element modeling of piezoelectric structures. In *Samtech User's Conference*, Paris, France, 2001.

[104] J. Becker, O. Fein, M. Maess, and L. Gaul. Finite element-based analysis of shunted piezoelectric structures for vibration damping. *Computers & Structures*, 84(31-32):2340–2350, 2006.

[105] A. Erturk and D. J. Inman. *Piezoelectric Energy Harvesting*. Wiley, UK, 2011.

[106] L. Meirovitch. *Elements of vibration analysis*. McGraw-Hill, New York, 1975.

[107] S. O. R. Moheimani, D. Halim, and A. J. Fleming. *Spatial control of vibration: theory and experiments*, volume 10. World scientific, 2003.

[108] V. V. S. Malladi, M. I. Albakri, S. Gugercin, and P. A. Tarazaga. Application of projection-based model reduction to finite-element plate models for two-dimensional traveling waves. *Journal of Intelligent Material Systems and Structures*, 28(14):1886–1904, 2017.

[109] T. Örtel and J. F. Wagner. Integrated motion measurement for flexible structures using a modal and krylov subspace model reduction approach. *Journal of Intelligent Material Systems and Structures*, 20(15):1889–1898, 2009.

[110] R. W. Freund. Model reduction methods based on krylov subspaces. *Acta Numerica*, 12:267–319, 2003.

[111] A. C. Antoulas, C. A. Beattie, and S. Gugercin. Interpolatory model reduction of large-scale dynamical systems. In *Efficient modeling and control of large-scale systems*, pages 3–58. Springer, Boston, MA, 2010.

[112] C. A. Beattie and S. Gugercin. Model reduction by rational interpolation. *Model Reduction and Algorithms: Theory and Applications, P. Benner, A. Cohen, M. Ohlberger, and K. Willcox, eds., Comput. Sci. Engrg*, 15:297–334, 2014.

[113] U. Baur, P. Benner, and L. Feng. Model order reduction for linear and nonlinear systems: A system-theoretic perspective. *Archives of Computational Methods in Engineering*, 21(4):331–358, 2014.

[114] H. Lee and M. K. Kwak. Free vibration analysis of a circular cylindrical shell using the rayleigh–ritz method and comparison of different shell theories. *Journal of Sound and Vibration*, 353:344–377, 2015.

[115] R. L. Williams and D. A. Lawrence. *Linear state-space control systems*. John Wiley & Sons, Hoboken, New Jersey, 2007.

[116] M. G. Safonov and R. Y. Chiang. Model reduction for robust control: A schur relative error method. *International Journal of Adaptive Control and Signal Processing*, 2(4):259–272, 1988.

[117] J. Doyle. Robust and optimal control. In *Decision and Control, 1996., Proceedings of the 35th IEEE Conference on*, volume 2, pages 1595–1598. IEEE, 1996.

[118] L. Rossignol, G. Scorletti, and V. Fromion. Filter design under magnitude constraints is a finite dimensional convex optimization problem. In *Decision and Control, 2001. Proceedings of the 40th IEEE Conference on*, volume 4, pages 3575–3580. IEEE, 2001.

[119] G. Zames. Feedback and optimal sensitivity: Model reference transformations, multiplicative seminorms, and approximate inverses. *IEEE Transactions on automatic control*, 26(2):301–320, 1981.

[120] S. Font, G. Duc, and F. Carrere. Commande fréquentielle robuste. application aux paliers magnétiques. *Techniques de l'ingénieur. Informatique industrielle*, 2(R7432):R7432–1, 1997.

[121] G. Duc and S. Font. Commande H infinie et μ-analyse: des outils pour la robustesse. *Hermes*, 2000.

[122] G. Scorletti and V. Fromion. Automatique fréquentielle avancée. DEA, Ecole Centrale de Lyon, 2009. pp.216. <cel-00423848v1>.

[123] S. Hecker. *Generation of low order LFT representations for robust control applications*. PhD thesis, Technische Universität München, 2006.

[124] C. Glader, G. Högnäs, P. M. Mäkilä, and H. T. Toivonen. Approximation of delay systems—a case study. *International Journal of Control*, 53(2):369–390, 1991.

[125] H. Kwakernaak. H_2–optimization–Theory and applications to robust control design. *IFAC Proceedings Volumes*, 33(14):437–448, 2000.

[126] S. Skogestad and I. Postlethwaite. *Multivariable feedback control: Analysis and Design*. Wiley, New York, 2007.

[127] I. Kollar, G. Franklin, and R. Pintelon. On the equivalence of z-domain and s-domain models in system identification. In *Instrumentation and Measurement Technology Conference, 1996. IMTC-96. Conference Proceedings. Quality Measurements: The Indispensable Bridge between Theory and Reality., IEEE*, volume 1, pages 14–19. IEEE, 1996.

[128] D. Feliu-Talegon, A. San-Millan, and V. Feliu-Batlle. Fractional-order integral resonant control of collocated smart structures. *Control Engineering Practice*, 56:210–223, 2016.

[129] M. Géradin and D. J. Rixen. *Mechanical vibrations: theory and application to structural dynamics*. John Wiley & Sons, 2014.

[130] N. Bouhaddi and R. Fillod. Model reduction by a simplified variant of dynamic condensation. *Journal of Sound and Vibration*, 191(2):233–250, 1996.

[131] H. Ji, J. Qiu, Y. Wu, J. Cheng, and M. N. Ichchou. Novel approach of self-sensing actuation for active vibration control. *Journal of Intelligent Material Systems and Structures*, 22(5):449–459, 2011.

[132] W. Gawronski. *Advanced structural dynamics and active control of structures*. Springer Science & Business Media, 2004.

[133] M. D. Lutovac, D. V. Tošić, and B. L. Evans. *Filter design for signal processing using MATLAB and Mathematica*. Miroslav Lutovac, 2001.